THESE

Pour l'obtention du Grade de

DOCTEUR DE L'UNIVERSITE DE POITIERS

(Faculté des Sciences Fondamentales et Appliquées)
(Diplôme National - Arrêté du 25 mai 2016)

École Doctorale 649 :
« *Rosalind Franklin* » - Énergie – Environnement - Biosanté

Secteur de Recherche : Chimie Organique, Minérale, Industrielle
.....

Présentée par **Nathan Pichot**

.....

****

CONVERSION DU METHOXYBENZENE SUR ZEOLITHES PROTONIQUES : ROLE MAJEUR DES COMPOSES PHENOLIQUES DANS LA DESACTIVATION

METHOXYBENZENE CONVERSION ON ACID ZEOLITES: CRITICAL ROLE OF PHENOLIC COMPOUNDS IN DEACTIVATION

****
Directeur de Thèse : Yannick Pouilloux
Co-directeur de Thèse : Ludovic Pinard
Co-Encadrant de Thèse : Anthony Dufour
****

Soutenue le : 23/04/2024 devant la Commission d'Examen

****

JURY

Rapportrice : Dorothée Laurenti, Directrice de recherche CNRS, IRCELYON
Rapporteur : Frédéric Thibault-Starzyk, Directeur de recherche CNRS, LCS
Examinatrice : Camila Abreu Teles, Chargée de recherche CNRS, IC2MP
Examinatrice : Louwanda Lakiss, Ingénieure de recherche CNRS, Ecole Nationale Supérieure d'Ingénieurs de Caen, LCS
Examinatrice : Delphine Minoux, Ingénieure de recherche, TotalEnergies Feluy
Membre : Anthony Dufour, Directeur de recherche CNRS, LRGP
Membre : Ludovic Pinard, Professeur des Universités, Ecole Nationale Supérieure d'Ingénieurs de Caen, LCS
Membre : Yannick Pouilloux, Professeur des Universités, Université de Poitiers, IC2MP.

Remerciements

En premier lieu, je souhaite remercier mes superviseurs, pour avoir accepté de me faire confiance ces trois dernières années :

Ludovic, pour son encadrement constant et intensif, qui m'a fait énormément progresser, scientifiquement et professionnellement. Ta passion pour la science est évidente et infectieuse, et j'ai beaucoup appris à ton contact. Je ne t'en remercierai jamais assez.

Anthony, qui m'a accueilli à Nancy, n'hésitant pas à mettre les mains au cambouis lorsque nécessaire, tu es un exemple pour toute ton équipe, et je n'ai que de l'admiration pour ton engagement et ta passion.

Yannick, pour avoir accepté d'être mon « ancre » à Poitiers, ces quelques discussions et mises à jour m'ont tout de même permis de me sentir plus à l'aise sur mon sujet et j'apprécie le soutien que vous m'avez fourni. Merci beaucoup.

Je souhaite remercier les docteurs D. Laurenti, F. Thibault-Starzyk, C. Abreu Teles, L. Lakiss, D. Minoux pour avoir accepté de juger le travail effectué lors de mon doctorat.

Ensuite, je souhaite remercier mes collègues de bureaux dans les trois laboratoires, pour avoir supporté mes blagues intempestives et pour leur soutien, autant scientifique que personnel, et plus généralement, tous les membres des équipes de Poitiers, Nancy et Caen pour leur accueil et leur bonne humeur. Les étudiants (et post-docs) : Antoine, Thibaud, Santiago, Hugo, Valentin, Nuno, Mohammed B., Thilelli, Marwan, Charlotte, Sirine, Manon B., Saad, Mohammed A., Nabil, Eya, Jana, Thomas D.P., Camille R., Pierre-Alan, Thomas, Simone, Marcello, Marco F., Maya, Camille L., Thomas L., Nourrdine, Karen, et j'en oublie. Les personnels techniques sans qui la moitié du travail accompli n'aurait pas été, et que je ne remercierai jamais assez : Jean-Dominique Comparot pour ton amitié, pour l'infrarouge et la physisorption, ainsi que la bonne humeur et les manips de sauvetage d'urgence, le pôle ingénierie de Poitiers pour les innombrables interventions sur montages et réacteurs (M. Chauveau, C. Veit, C. Rouvier, J-J. Colin, B. Leroux), M. Tarighi pour la MS, de même Michel Mercy et Nicolas Mitre pour Nancy, et particulièrement Adrien Lanel à Caen, pour m'avoir accordé son temps et son expertise dans le re-design du réacteur, qui nous a à tous les deux fait gagner une précieuse heure par jour.

Merci à Marie, Benjamin, Pascal et Valérie à Caen. Enfin les permanents, pour les conseils et discussions sur divers sujets, scientifiques ou non, de l'équipe SAMCat de Poitiers, merci au reste de l'équipe GREENER pour leur accueil, Yann, Guillain et Julien, et merci au LCS dans son ensemble pour leur accueil et leur aide dans les moments difficiles.

Un merci tout particulier à M. Trochain, pour avoir avivé et entretenu mon amour des sciences et de la chimie.

Merci à mes amis du « vrai monde », pour m'avoir fait garder un pied sur terre lorsque ma tête était dans les sciences et les nuages : Yann, Diane, Marwan et Elsa, Alexis, André, Clémence, Gwenaëlle, Marion, Xavier, Célian, Sophie, et Loïc. Vous m'avez aidé à ne pas me prendre trop au sérieux. Merci à l'AFEP, pour tout ce que vous m'avez apporté, merci à Charline (jamais assez remerciée et jamais assez d'excuses présentées), Dorine, Marie, Marie-Sarah, et mention spéciale pour Anthony et Aymeric, cette aventure de deux ans en votre compagnie à tous m'a tellement apporté.

Brice et Thomas B., la Broloc toujours dans mon cœur.

Enfin, dernière mention, et non des moindres, merci à ma famille. Ceux qui sont partis et ceux qui restent. Maman, papa, Christèle et Gilles. Camille, Arthur et Maureen, Dylan et Marion. Votre soutien a été nécessaire et indéfectible. Merci et je vous aime.

Table des Matières

Introduction Générale

La science, sous toutes ses formes, doit participer à l'avancement des conditions de vie de l'humain et son environnement. A l'aube de la révolution industrielle, les sources de combustibles fossiles ont permis (via la domestication d'une énergie abondante et facile d'accès) l'accélération de la connectivité des régions du monde, ainsi que des partages d'idées, et de la recherche scientifique. En ont découlé des découvertes et inventions majeures telles que les moteurs, la démocratisation de l'électricité, électro-magnétisme, radioactivité, aviation, etc. En ce point, mission accomplie.

Cependant, les ressources pétrolières, devenues essentielles pour l'énergie et en tant que matières premières, se transforment en un point de contention. Ainsi, tel le cuivre et l'étain durant l'âge de bronze, lorsqu'une crise affecte les producteurs, elle s'étend rapidement aux utilisateurs. Conséquemment, suivant chaque crise touchant à l'approvisionnement de pétrole (crise de 1973, guerres du Golfe Persique, etc.), la réalisation de notre dépendance à ces centres névralgiques a dirigé l'attention de la recherche scientifique vers des moyens d'émancipation. Ainsi, régulièrement, des voies de recours alternatives pour produire les hydrocarbures tant convoités sont explorées, défrichées. A ces préoccupations géopolitiques s'ajoutent aujourd'hui autant de préoccupations environnementales (changement climatique, effet de serre, amenuisement des ressources, montée des eaux, etc.). Plus que jamais, les hydrocarbures sont nécessaires, et plus que jamais, leur mode de production doit évoluer.

La biomasse est utilisée depuis toujours comme source d'hydrocarbures utiles : combustibles, médicaments, fibres de textiles, etc. Désormais, elle offre une alternative intéressante pour la production plus ciblée d'hydrocarbures à haute valeur ajoutée : les BTX (Benzène, toluène, xylènes). Ces molécules plateformes, véritables piliers de l'industrie chimique, trouvent des applications dans la plupart des domaines : comme polymères pour les textiles, les emballages, le bâtiment, comme combustibles pour l'énergie, ou encore comme précurseurs de médicaments ou additifs alimentaires, etc. Plusieurs voies existent pour les produire à partir de la biomasse, chacune présentant avantages, inconvénients, et sélectivités différentes.

Le présent manuscrit s'inscrit dans le processus de recherche et développement du procédé de pyrolyse catalytiques de biomasse (CFP). Il consiste à pyrolyser rapidement (atmosphère inerte, hauts gradients de températures) la matière première (biomasse lignocellulosique sourcée dans

l'agriculture, l'aquaculture, la sylviculture) à haute température (500°C), ce qui produit, entre autres, des vapeurs d'huiles de pyrolyse. Ces huiles sont composées de composés organiques oxygénés et aromatiques, tels que les phénols, furanes ou le gaïacol. La forte teneur en oxygène est problématique, car elle produit plusieurs caractéristiques indésirables, parmi lesquelles une forte acidité et une faible capacité calorifique, qui interdissent à elles seules leur utilisation directe (dégradation des réacteurs/moteurs, mauvais combustible). Ainsi, ces huiles de pyrolyse sont transformées sur catalyseur acide ou bifonctionnel pour fournir les molécules cibles, ces hydrocarbures à haute valeur ajoutée.

Le procédé de pyrolyse catalytique de biomasse nécessite un catalyseur qui présente une forte sélectivité vers les BTX, fonctionnalisable et stable. En ce qui concerne les deux premiers points, la zéolithe H-ZSM-5 (MFI) a montré des résultats prometteurs, en raison de sa capacité de désoxygénation et sa forte sélectivité en aromatiques, apportées par l'encombrement stérique qu'induisent ses ouvertures de pores intermédiaires. Comme toutes les zéolithes, les caractéristiques de la ZSM-5 sont modifiables (force et concentration de l'acidité, ajout d'une fonction métallique, porosité secondaire, etc.), ce qui la rend idéale. Cependant, comme une majorité de catalyseurs hétérogènes pour la chimie organique, un facteur vient assombrir le tableau : la désactivation. Elle se manifeste sous plusieurs formes (empoisonnement des sites acides par des métaux alcalins ou des composés soufrés/azotés, attrition du catalyseur, etc.), mais sa principale cause reste le cokage. Cette formation, plus ou moins rapide, de composés organiques lourds et de faibles rapports H/C, peut provoquer le bouchage de la microporosité de la zéolithe et/ou l'empoisonnement de ses sites actifs, réduisant ou nullifiant l'activité, et modifiant possiblement la sélectivité du catalyseur. Ici aussi, la MFI est un candidat viable, grâce à ses canaux interconnectés sur trois dimensions, permettant une meilleur distribution et diffusion des précurseurs de coke et des produits de réaction. Néanmoins, le cokage reste un obstacle majeur à la mise en service à grande échelle du procédé de CFP, et plusieurs options existent pour mitiger ou ralentir ce processus. Ainsi, l'ajout de certains métaux (Ga, oxydes de Mg et de Zn, …), ou encore la hiérarchisation de la zéolithe (par désilication ou désalumination de la structure), ouvrant un système poreux secondaire aidant au raccourcissement du chemin diffusionnel, sont des solutions permettant de combattre la formation du coke, et ce faisant, la désactivation du catalyseur.

L'ouverture de ces voies de mitigation du coke n'est possible que par la compréhension des mécanismes intrinsèques de réaction et désactivation des catalyseurs avec les composants des bio-huiles. Ces dernières étant composées d'une multitude de ces hydrocarbures oxygénés, le choix de molécules modèles ciblées pour étudier leur comportement individuel dans les conditions de réaction s'est imposé. Ainsi, le travail de cette thèse se centre sur l'étude de l'anisole (le méthoxybenzène) comme molécule modèle décrivant le comportement des hydrocarbures substitués par la fonction methoxy dans les conditions d'upgrading des huiles de pyrolyse. L'anisole est un composant mineur des huiles de pyrolyse, et sa transformation sur zéolithe acide produit des composés phénoliques (phénol, crésols, xylénols, mésitols, etc.), qui sont également retrouvés dans les bio-huiles.

Le chapitre I présente une vision d'ensemble du contexte dans lequel s'inscrit cette thèse : il résume d'abord l'importance, et une partie des applications industrielles, des BTX, les produits cibles de cette thématique. Le choix de la biomasse comme matière première est expliqué, et les différentes voies d'exploitations sont brièvement explorées. La pyrolyse est explorée plus avant, ses conditions, ses produits et ses avantages et inconvénients. Par processus d'élimination, la pyrolyse rapide est choisie, pour maximiser la production de bio-huiles. Les différentes options de traitement (upgrading) de ces huiles sont brièvement explorées, avec un focus sur la pyrolyse catalytique, qui ne nécessite pas de forte pression, ni d'ajout d'hydrogène, pour désoxygéner la biomasse et produire les BTX cibles. Le catalyseur retenu, la zéolithe H-ZSM-5 (structure MFI), est présentée et ses caractéristiques qui sont pertinentes à la pyrolyse catalytique de biomasse sont explorées plus avant. Enfin, le choix de la molécule d'anisole comme modèle pour la pyrolyse catalytique de biomasse est expliqué, ses propriétés et applications sont brièvement abordées et les précédentes études menées sur elle sont présentées en base du travail présenté dans les chapitres suivants.

Dans le chapitre II, les protocoles expérimentaux appliqués lors de ces travaux sont présentés, des expériences de réactions aux techniques analytiques, permettant un suivi cinétique des activités et du cokage, ainsi que l'identification et quantification des produits de réactions et coke retenu sur les catalyseurs. Les différents catalyseurs utilisés dans ces travaux sont également présentés et étudiés en détail (acidité, volume poreux, cristallinité, teneur en aluminium, etc.).

Le chapitre III présente les travaux publiés dans Appl. Catal. A, 2023, 665, 119352, DOI : 10.1016/j.apcata.2023.119352 . Une étude cinétique, de sélectivité et mécanistique est menée sur la transformation de l'anisole sur la zéolithe H-ZSM-5 (43) de Zeolyst (CBV8014). Le mécanisme de transformation par transalkylation est formalisé, l'existence d'un état quasi-stationnaire de conversion en fin de réaction est mise au jour, et la contribution du coke (et sa composition inhabituelle, oxygénée) à la désactivation est explorée. Une étude est menée sur les énergies d'adsorption des principaux produits de réaction sur les sites actifs, par le biais de calculs DFT (calculs réalisés par les co-auteurs de l'article). Enfin, le mode de désactivation de la zéolithe par « fouling » des surfaces du catalyseur est mis en évidence.

Le chapitre IV présente les travaux publiés dans Appl. Catal. A, 2024, 671, 119565, DOI : 10.1016/j.apcata.2024.119565 . Cette étude étend le champ de recherche à l'effet de l'acidité sur l'activité initiale de la zéolithe H-ZSM-5 pour la dismutation de l'anisole, et par extension sur la « turnover frequency » de ses sites acides. Il y est montré que l'augmentation de la densité des sites acides provoque l'apparition d'un effet auto-inhibiteur, qui nullifie l'activité des sites. La suite de l'étude sur les énergies d'adsorption des réactifs et produits sur les sites acides montre l'importance de la position de ces sites dans les pores de la zéolithe, et la forte augmentation de ces énergies dès lors que les atomes d'aluminium sont appariés.

Le chapitre V présente les travaux soumis à Appl. Catal. A, (n° de soumission XXXXXXXXXX). Cette étude étend encore le champ de recherche à l'effet de la structure de zéolithe (2D, 3D, 10 MR vs 12 vs 16 MR) sur la dismutation de l'anisole. Ainsi, des zéolites MFI, *BEA, MOR, FAU et JZO sont testées sur la réaction modèle, avec différentes acidités. L'effet auto-inhibiteur montré dans le chapitre précédent est retrouvé ici, fortement influencé par l'interconnectivité des canaux des zéolithes, et par la taille des pores. Une étude cinétique est menée sur ces zéolithes, et les facteurs de la loi de désactivation sont mis en relation avec les propriétés intrinsèques des catalyseurs. Une étude sur l'évolution de la sélectivité en fonction du temps de réaction apporte plus de précisions sur les mécanismes de réaction mis en jeu. Puis, une explication de l'inhibition du mécanisme de formation de coke « classique » (réaction « d'épluchage », mécanisme de Sullivan) est proposée, reposant sur les effets mésomères en jeu pour les composants du coke. Enfin, il est montré que le mode de désactivation du catalyseur lors de la dismutation de l'anisole est indifférent

aux tailles de pores, mais dépendant de l'interconnectivité des systèmes poreux de la zéolithe.

Finalement, le chapitre VI présente les travaux réalisés en collaboration entre les laboratoires IC2MP et LRGP portant sur la pyrolyse catalytique de biomasse (chêne) sur des zéolithes MFI, *BEA et MOR, et présente l'effet majeur de sélectivité de forme que chaque zéolithe possède vers des composés « empreintes ». Cette étude présente également l'effet de la hiérarchisation (et des différentes techniques employées) des catalyseurs sur la stabilité. Une fois encore, cette étude souligne l'impact de la connectivité des réseaux poreux sur la stabilité (et donc sur la désactivation) des catalyseurs pour les procédés de pyrolyse catalytique de biomasse.

Chapitre I

Etude Bibliographique

I – Contexte

Les hydrocarbures, et à plus forte raison les BTX (Benzène, Toluène, Xylène), font partie intégrante de la base irremplaçable de produits chimiques utilisée depuis le milieu du XX^{e} siècle. On appelle les BTX des molécules plateformes, qui trouvent des applications, après transformation, dans l'agro-alimentaire, les médicaments, les carburants, matériaux plastiques, etc. (**Figure I.1**, **Figure I.2**, **Figure I.3**)[1].

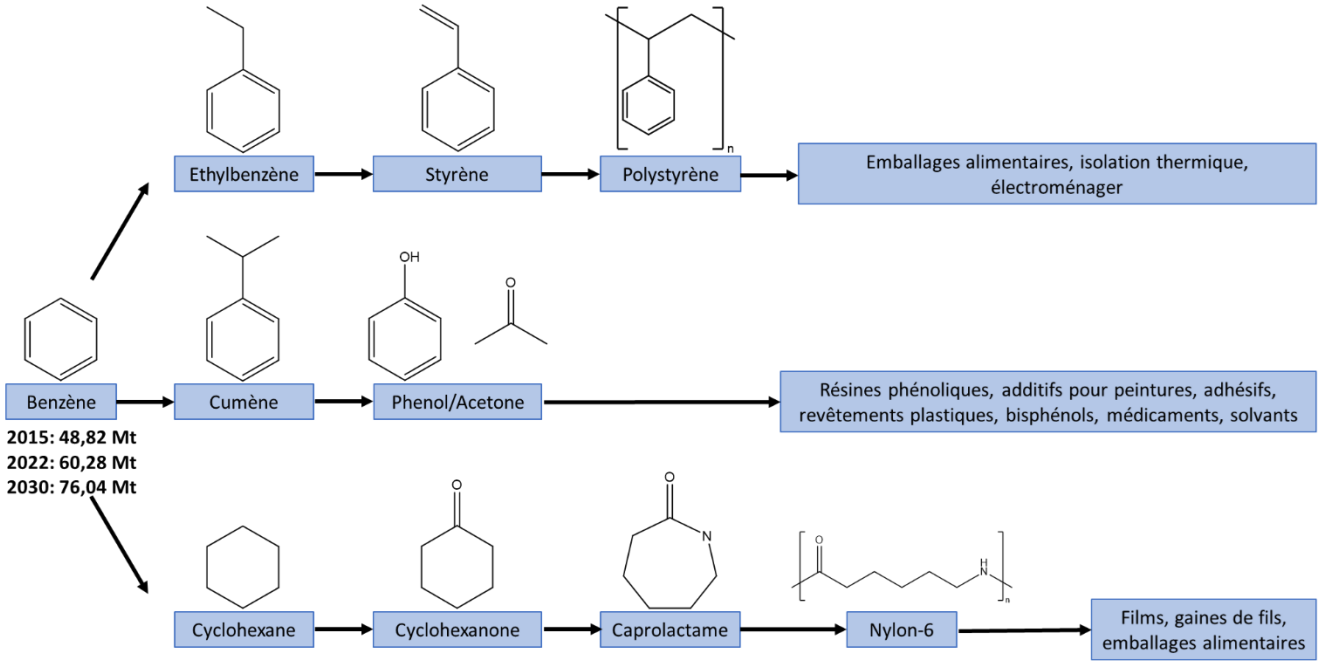

Figure I.1 : Applications et tonnages de production du benzène. Figure adaptée de [1,2]

Ainsi, le benzène peut être décliné en éthylbenzène, cumène ou cyclohexane pour produire des incontournables tels que les polystyrènes et les nylons, le toluène fournit les polyuréthanes, et les xylènes donnent les polyesters et les PET. Les productions de benzène et de toluène représentaient 48,82 Mt et 26,87 Mt en 2015, ont constamment augmenté depuis et on les prévoit à 76,04 et 40,01 Mt à l'horizon 2030[2,3]. De même, la production de xylènes a été en constante augmentation entre 2019 et 2021[4]. Ces augmentations de production répondent à une augmentation de la demande, venant des besoins grandissants de populations et de niveaux de développements croissants à l'échelle mondiale[5].

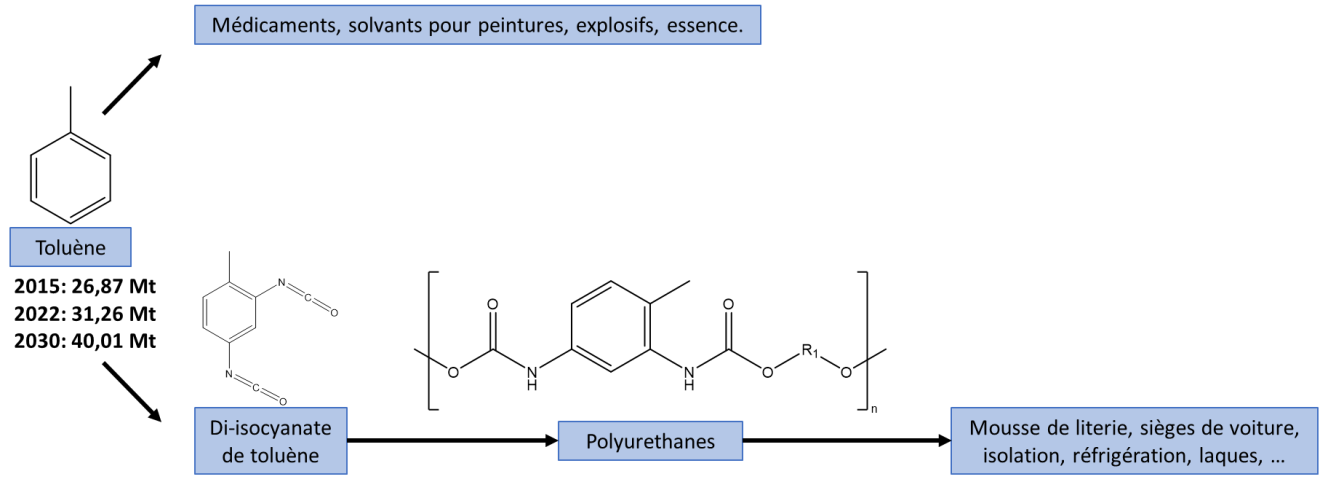

Figure I.2 : Applications et tonnages de production du toluène. Figure adaptée de [1,3]

Les problématiques d'amenuisement des ressources, pollution, effet de serre, etc. demandent une diversification des sources primaires d'hydrocarbures. En effet, la majorité de leur production provient de l'industrie pétrolière : Vapocraquage des hydrocarbures, reformage catalytique, isomérisation des aromatiques C_8 ou la distillation des goudrons de houille[5]. Une source d'hydrocarbures alternative, renouvelable, est nécessaire afin de diversifier la production de ces composés essentiels. La biomasse végétale est une manne de ces composés, et pourrait représenter une bonne alternative afin d'alléger la charge de l'industrie pétrolière sur le climat et l'environnement.

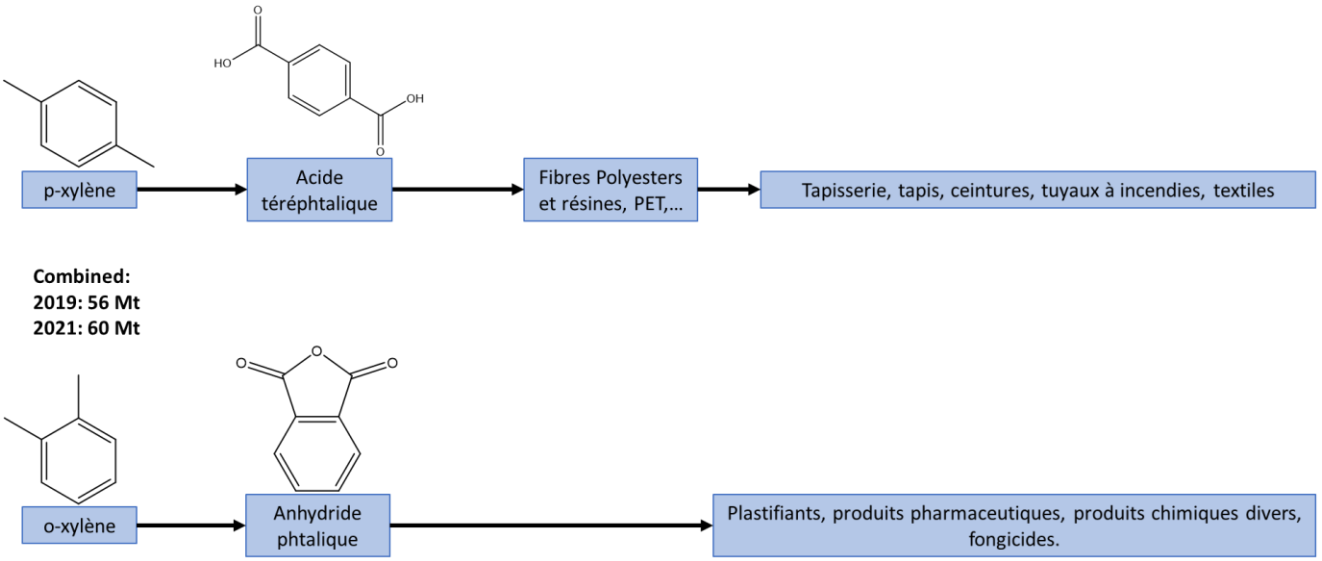

Figure I.3 : Applications et tonnages de production des xylènes. Figure adaptée de [1,4]

II – Biomasse : une source possible de BTX

La biomasse végétale est une substance composite, provenant de l'agriculture (tiges, pailles, pulpes, colza, miscanthus, etc.), la sylviculture (bois, écorce, sciures, « déchets verts », bois d'emballage, etc.) et l'aquaculture (algues et microalgues)[6], contenant cinq composants principaux, en quantités différentes selon le type de plante et son environnement de croissance : les amidons, la cellulose, les hémicelluloses, les huiles et la lignine (**Figure I.4**). Les amidons, la cellulose et les hémicelluloses sont des polysaccarides, composés de monomères d'hexose (et de pentoses, pour l'hémicellulose)[7]. Les huiles sont composées de triglycérides. Enfin, la lignine est un polymère tridimensionnel composé d'assemblages de composés phénoliques (ici représentés les alcools p-coumarylique, conifèrylique et synaptylique, parmi les plus communs[8,9]). La nature hétérogène de la biomasse rend difficile et superflue la quantification de chaque composant. Williams et al. ont cependant fourni une approximation, sur un large échantillon, des teneurs en cellulose, hémicellulose et lignine de biomasses issues d'arbres et d'herbacées. Ainsi, elles représentent respectivement 51,2%, 21% et 26,1% de la biomasse issue du bois, contre 32,1%, 18,6% et 16,3% de la biomasse issue des herbacés[10].

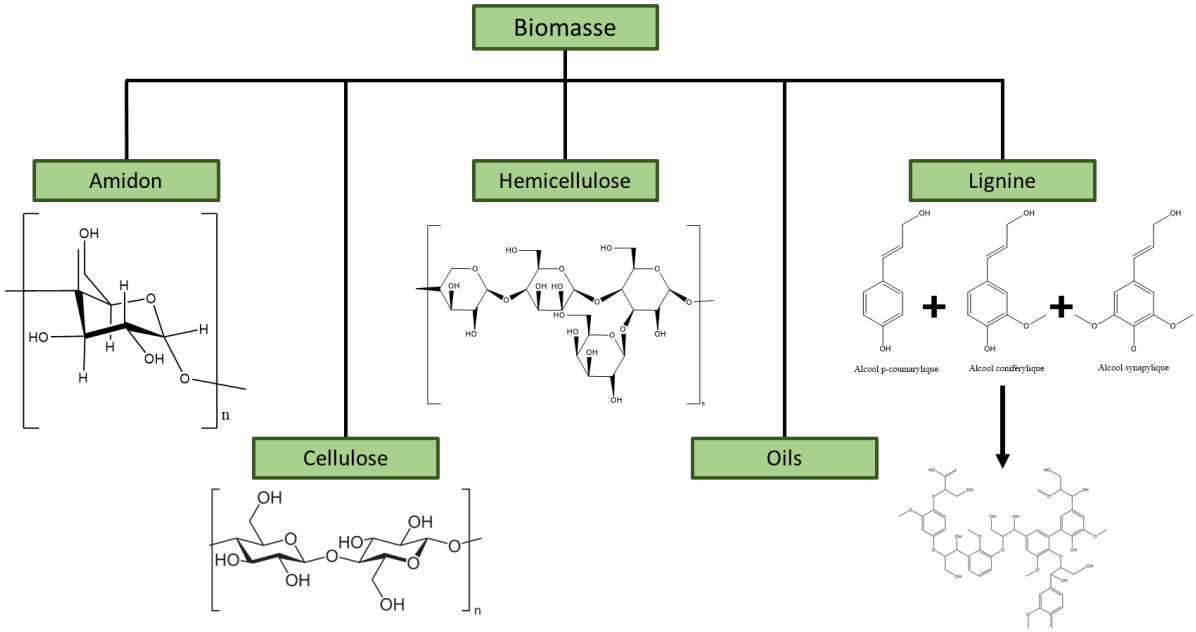

Figure I.4 : Structure moléculaire des composants communs (monomères) de la biomasse. Figure Adaptée de [7–9].

A partir de ces composants premiers, une multitude de voies s'ouvrent à la conversion de la biomasse, dépendant des applications voulues. Les huiles et les amidons, après extraction, trouvent des applications dans les industries du parfum, des additifs alimentaires (aromatiques), des biodiesels[7], ou encore pour la production de molécules plateformes telles que le furfural[11,12]. La lignine, la cellulose et l'hémicellulose ont des applications immédiates, telles que l'industrie du papier, mais représentent également une source conséquente d'hydrocarbures cycliques (et aromatiques). Une multitude de procédés permettent la valorisation de ces ressources : l'hydrolyse pour la production d'éthanol (« bio-éthanol »), la méthanisation par digestion anaérobie, la gazéification pour la production de gaz de synthèse, ou bien la liquéfaction pour la production de bio-huiles, et enfin la pyrolyse, qui selon les conditions produit un mix en quantités diverses de bio-huiles, charbon et gaz non condensables (**Figure I.5**, [13,14]).

Pour la production de BTX à partir de la biomasse lignocellulosique, il est nécessaire de dépolymériser ces hydrocarbures à longues chaines et de procéder à leur désoxygénation. En effet la présence d'oxygène dans les hydrocarbures aromatiques est problématique : d'une part, les oxygénés (esters, éthers, acides carboxyliques, etc.) peuvent réduire les indices d'octane (RON et MON) des carburants auxquels ils sont incorporés, et le pH bas (pH = 2-3)es mélanges entraînent des problèmes de durabilité pour les moteurs[8]. D'autre part, la chimie des aromatiques oxygénés diffère fortement de celle des BTX et la production des produits transformés nécessiterait en aval des modifications conséquentes pour s'adapter aux compositions différentes des mélanges de matière première.

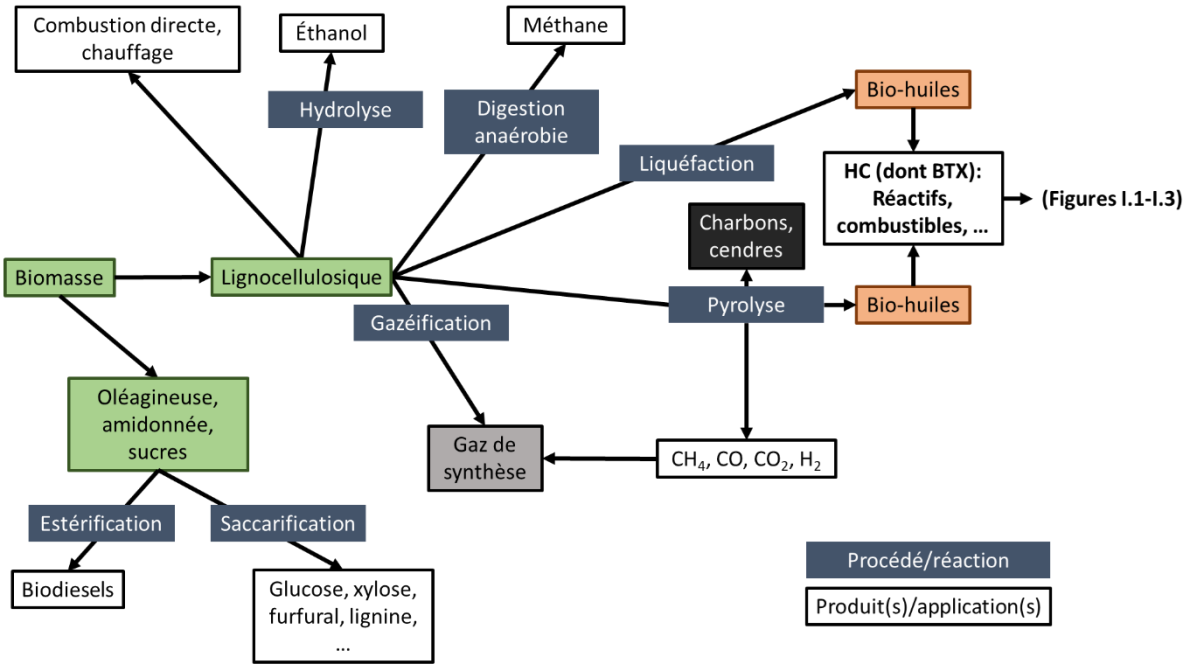

Figure I.5 : Technologies de conversion de la biomasse (traduit et adapté depuis Dickerson et Soria[13] et Huber et al. [8]).

La méthode étudiée dans ce travail pour dépolymériser et désoxygéner la biomasse lignocellulosique est la pyrolyse : elle ne demande pas de solvants, et ne demande que peu d'ajustements en fonction des charges en alimentation, et une majorité de ses produits peuvent être récupérés et revalorisé (**Figure I.5**).

II.1 – Pyrolyse de biomasse

La pyrolyse de biomasse est une décomposition thermochimique de ses composants, menée à hautes températures (400-650°C), en atmosphère non-oxydante (N_2, He, Ar, …).

II.1.a – Produits

La décomposition des polymères de la biomasse produit plusieurs familles reconnaissables (**Figure I.5**) :

Une phase solide: le biochar. Il est composé à majorité de carbone (≈ 70% [15]), fortement poreux, et possède une très grande surface spécifique. Le biochar peut être utilisé tel quel en agriculture [16], en tant que combustible[17], ou bien fonctionnalisé en charbon actif pour catalyse ou adsorption (support pour catalyse métallique, captation du CO_2, traitement d'effluents industriels, etc.[17–20]**)**.

Une autre partie de la phase solide : les cendres (fly ash). Elles se forment pendant la pyrolyse et peuvent contenir des métaux alcalins qui peuvent avoir un effet catalytique adverse ou positif sur la composition et l'homogénéité des huiles de pyrolyse, participer à la désactivation d'un éventuel catalyseur, et participer à la corrosion des installations. Les cendres peuvent être filtrées, pour récupérer ces métaux alcalins et empêcher une modification de la phase gaz [21–23].

Une partie de la phase gaz, non-condensable, est composée des gaz légers émis par les différentes réactions (déshydratation, dépolymérisation, repolymérisation, fragmentation, réarrangement, condensation) se produisant durant la pyrolyse. Pour la majorité, ces gaz sont le méthane (CH_4), les oxydes de carbone (CO_2, CO) et le dihydrogène (H_2). Ils peuvent être séparés et réutilisés dans divers procédés : H_2 et CO (gaz de synthèse) pour le procédé Fischer-Tropsch (production d'hydrocarbures), CH_4 comme combustible (chauffage, propulsion) ou comme réactif pour le vaporeformage ($CH_4 + H_2O \rightarrow CO + 3H_2$)[24] ou la déshydroaromatisation (qui produit H_2 et BTX)[25]. Cependant, bien que la production de ces gaz soit non-négligeable en pyrolyse, ils ne sont pas la cible principale de la pyrolyse (cf. procédés de gazéification[26]).

L'autre partie de la phase gaz peut être condensée en un fluide visqueux, désigné en anglais par les termes bio-oil (bio-huile), bio-crude oil, pyrolysis oil (huile de pyrolyse), liquid smoke, pyroligneous tar (goudron pyroligneux), etc. Elle est composée d'hydrocarbures majoritairement aromatiques, en grande partie oxygénés, tels que les phénols, furanes, pyranes, des acides carboxyliques et hydroxyaldéhydes divers (non exhaustif)[13]. Ce mélange hétérogène peut être traité pour en récupérer les produits utilisables et transformé (« upgradé ») pour produire les hydrocarbures à haute valeur ajoutée, cibles du procédé.

La composition des matières premières soumises à pyrolyse influe fortement sur l'équilibre final des familles de produits, ainsi que leur composition propre, mais les conditions de pyrolyse ont aussi un rôle primordial à jouer.

II.1.b – Pyrolyse lente/rapide

Les conditions de chauffage de la biomasse influent fortement sur la composition et la distribution des produits de pyrolyse. On classe deux types de pyrolyse : la pyrolyse lente, et la pyrolyse rapide. Leurs caractéristiques sont résumées dans le **Tableau I.1**.

La pyrolyse lente se caractérise par un chauffage sur plusieurs heures à faibles gradients (0,1-10°C/min), vers des températures modérées (300-700°C). Le temps de séjour des gaz de pyrolyse est également relativement long, pouvant se compter en minutes ou même en heures [20]. Elle est conduite plus généralement dans des réacteurs à lit fixe ou des réacteurs de pyrolyse Auger (alimentation et évacuation en continu de biomasse par vis dans le four de pyrolyse [27,28]). Les faibles gradients et températures minimisent la pyrolyse secondaire et le craquage thermique de la biomasse lignocellulosique, résultant en une augmentation de la quantité de biochar produite, ainsi que des gaz non-condensables[20,29]. La structure de la matière première subit un réarrangement qui la rend plus stable. Elle reste donc solide, d'où la production de plus de biochar, et de moins de bio-huiles[30].

Tableau I.1: Comparaison des caractéristiques de la pyrolyse lente vs rapide. Adapté de [20]

Caractéristiques	**Pyrolyse lente**	**Pyrolyse rapide**
Température (K)	300-700	500-
Gradient température (K/min)	0,1-10	10-12000
Temps de séjour	Minutes-heures	Secondes
Produit cible	Biochar	Bio-huiles
Réacteurs	Pyrolyseur lit fixe, réacteur Auger	Réacteur à lit fluidisé, réacteur ablatif, à cône rotatif, …
Avantages	Rendement en biochar amélioré Peu d'impact des tailles de particules	Rendement en bio-huiles amélioré
Désavantages	Haute production de CO (danger, doit être confiné)	Nécessite un contrôle de la granulométrie de la biomasse en entrée (1-2 mm) Basse teneur en eau exigée en entrée (<10%)

La pyrolyse rapide, quant à elle, met en jeu des températures plus élevées (à partir de 450-500°C [14,31]), et surtout des gradients de température extrêmement élevés (10-200°C/s), ainsi que des temps de séjour très courts (0,5-10s)[14,20,21]. Bien qu'elle puisse se tenir dans des lits fixes, la pyrolyse rapide est optimisée dans des réacteurs à lits fluidisés, et des études existent sur des réacteurs ablatifs ou à cônes rotatifs [28,32] (ces deux derniers ne nécessitant pas de gaz vecteur). Ces conditions permettent une dépolymérisation rapide, et une maximisation de la production de bio-huiles (ainsi qu'une diminution de la production de biochar). La qualité des bio-huiles (rapport O/C bas, meilleure valeur calorifique, faible teneur en eau [33]) augmente avec les temps de séjour courts, qui empêchent leur dégradation en gaz non-condensable et biochar. Durant la pyrolyse rapide, un des facteurs limitants de la qualité des huiles est le transfert de chaleur à travers la matière première, c'est pourquoi des particules

fines (1-2 mm) sont idéales, et que les lits fluidisés, qui favorisent les contacts et les échanges de chaleur, sont quasiment incontournables dans les études sur le sujet. Enfin, la matière première pour la pyrolyse rapide doit être séchée au maximum (teneur en eau <10%), car l'eau aide à la dégradation des bio-huiles [34].

Conséquemment, les procédés de pyrolyse rapide sont à privilégier afin de maximiser la production de bio-huiles de qualité [21]. Cependant, pour les applications industrielles et/ou énergétiques, la désoxygénation de ces huiles est essentielle. Les bio-huiles peuvent contenir jusqu'à 35-40% d'oxygène, possèdent toujours des valeurs calorifiques basses, comparées aux carburants issus du pétrole (≈17MJ/kg), une faible volatilité et une haute viscosité. Ainsi, afin d'être utilisables pour l'industrie chimique (dont la production des BTX), des procédés sont développés pour remédier à ces problèmes. On les qualifie « d'upgrading catalytique ».

I.1.c – Upgrading catalytique des huiles de pyrolyse

Parmi les procédés d'upgrading catalytique des bio-huiles, l'hydrotraitement (ou hydrodésoxygénation) est prometteur [35]. Les bio-huiles, sous pression d'hydrogène et grâce à un catalyseur, subissent des réactions de déshydratation, hydrolyse, hydrogénation, etc. (**Figure I.7a**), menant à des mélanges d'hydrocarbures de viscosité réduite, moins acides, et à très faibles rapports O/C (Cyclohexanes, alcools aliphatiques, benzène, …).

Cependant, deux problèmes majeurs existent avec ce procédé : d'une part, sa faisabilité et son impact environnemental sont entièrement dépendants de l'approvisionnement et de la source primaire du dihydrogène nécessaire à la réaction (cf « couleur » de l'hydrogène [36]). D'autre part, les catalyseurs les plus actifs nécessitent des charges (certes réduites) de métaux nobles, ce qui accroît le coût et l'impact environnemental du procédé. Des travaux sont menés pour remédier à ces problèmes, notamment la réduction ou substitution des métaux nobles par des analogues. Enfin, le procédé reposant sur un réactif gazeux non condensable (H_2), la conversion et les sélectivités vers les produits désirés sont hautement dépendants de la pression d'hydrogène, ajoutant une contrainte supplémentaire.

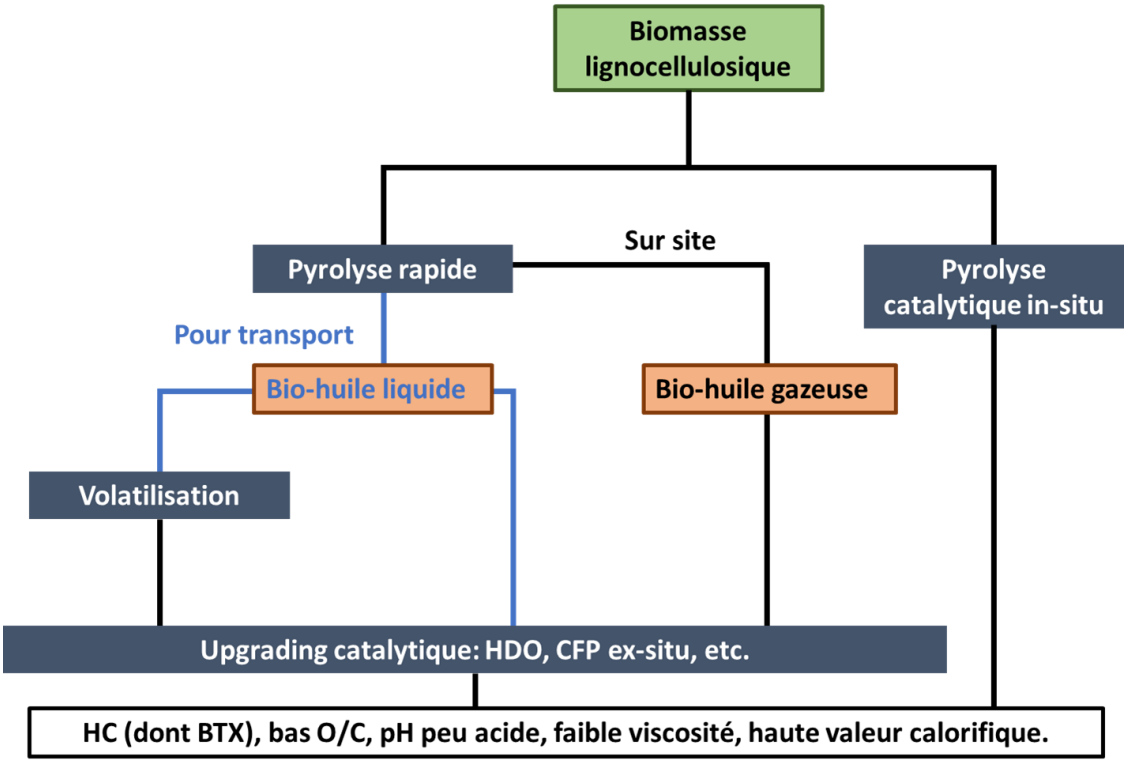

Figure I.6 : voies de traitement des bio-huiles de pyrolyse rapide (Adapté depuis Bridgwater [21]).

Une solution qui ne demande pas de changements en infrastructures est le co-feeding d'huiles de pyrolyses avec les fractions habituelles du craquage catalytique en lit fluidisé (FCC) utilisé en raffineries[37,38]. Graça et al. ont produit une série d'études sur le sujet du co-feeding de molécules modèles des bio-huiles (phénol, gaïacol, …) en FCC [39–41]. Bien que prometteur, ce procédé est limité, car les oxygénés (en particulier les phénoliques) provoquent, à partir d'une concentration minime, une accélération de la désactivation du catalyseur, et perturbent l'équilibre du procédé. Ainsi, sans étude plus poussée, cette solution n'est pas viable au long terme et ne permet pas de produire les produits cibles sans ajout de ressources fossiles.

(a) HDO

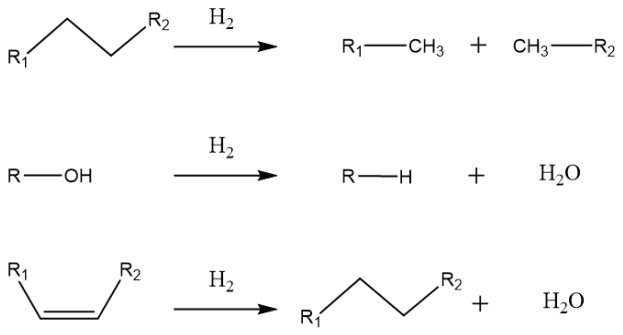

(b) CFP

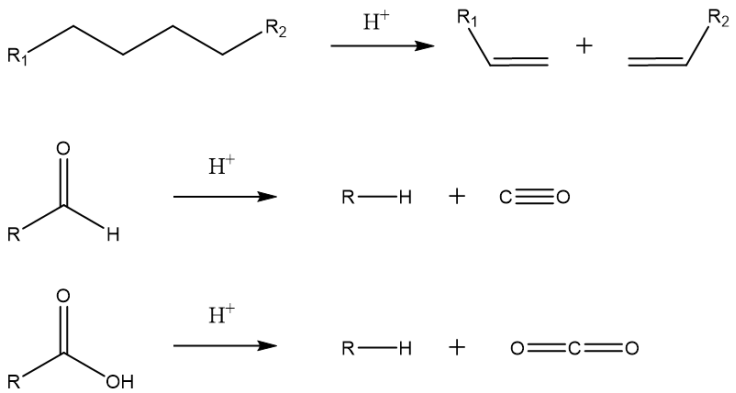

Figure I.7 : réactions communes lors de l'upgrading catalytique des huiles de pyrolyse : **(a)** en HDO ; **(b)** en CFP. (adapté depuis Dickerson et Soria[13])

Une solution alternative pour l'upgrading catalytique des huiles de pyrolyse de biomasse est le craquage des huiles de pyrolyse (CFP, i.e. catalytic fast pyrolysis), sur un catalyseur acide, dans un procédé analogue au FCC [37]. Ce procédé ne requiert ni hydrogène ni haute pression pour opérer (**Figure I.7b**) [42].

III – Pyrolyse catalytique rapide de biomasse

III.1 – Pyrolyse catalytique rapide de biomasse

III.1.a – Procédé

Comme proposé précédemment, la pyrolyse catalytique de biomasse lignocellulosique se déroule en deux étapes : d'une part, la pyrolyse rapide (forts gradients de température, hautes températures, atmosphère inerte) de la matière première est réalisée, produisant biochar, cendres, gaz non-condensables et bio-huiles sous formes vapeur, cette dernière étant favorisée par les conditions de réaction. D'autre part, un upgrading catalytique a lieu, permettant la désoxygénation des bio-huiles, et la production des composés ciblés.

Deux principales méthodes existent pour ce procédé : la CFP in-situ, et la CFP ex-situ. La différence réside dans le positionnement de l'étape d'upgrading par rapport au lit de pyrolyse. La CFP in-situ place le catalyseur en mélange intime avec la biomasse, nullifiant ainsi quasiment le temps de séjour des gaz de pyrolyse avant upgrading. La CFP ex-situ, au contraire, sépare les deux étapes. Chacune présente avantages et inconvénients, résumés dans le **Tableau I.2**.

Tableau I.2 **:** comparaison des avantages et inconvénients de la CFP in-situ vs ex-situ. Adapté de Iliopoulou et al. [43]

Caractéristique	In-Situ	Ex-Situ
Avantages	Meilleur rendement en bio-huiles et aromatiques.	Meilleur rendement en oléfines. Conditions réglables dans chaque réacteur séparément. Récupération/régénération du catalyseur simplifiées.
Inconvénients	Cokage plus rapide, plus conséquent. Transferts de chaleurs diminués car plus de matière à chauffer dans un seul réacteur. Mélange de bio-char et catalyseur coké, difficile à séparer	Cokage toujours important, même si moins rapide. Rendement en aromatiques légèrement diminué.

La cible du procédé étant les BTX, des aromatiques, il est naturel de se tourner vers la CFP in-situ pour maximiser leur production. Cependant, la flexibilité supérieure de la CFP ex-situ la rendent plus attractive pour une application en continu. En effet, bien que la CFP in situ place le catalyseur et la biomasse au contact l'un de l'autre, réduisant ainsi le temps de séjour des bio-huiles gazeuses entre émission et upgrading à essentiellement zéro, un ratio catalyseur/biomasse bien supérieur est nécessaire, afin d'assurer qu'un maximum de l'huile entre en contact avec les sites actifs pour upgrading. De plus, cet ajout de masse de catalyseur dans la zone de chauffage implique un transfert de chaleur moindre et plus lent à la biomasse elle-même, pouvant ainsi affecter les forts gradients thermiques nécessaires à la pyrolyse rapide. Ensuite, le catalyseur étant en contact avec les réactifs, il reste donc au contact des produits qui ne passent pas en phase gaz : il est mélangé au biochar et aux cendres, ce qui rend sa récupération et régénération d'autant plus difficile. Lors de la CFP ex-situ, la séparation des deux lits nécessite certes deux systèmes de chauffage indépendants, mais cet inconvénient est largement compensé par la possibilité d'affiner indépendamment les conditions de pyrolyse et de catalyse de manière optimale. Cette séparation permet également, crucialement, de procéder à la régénération du catalyseur beaucoup plus facilement, ainsi que, potentiellement, de séparer les gaz non condensables et l'eau des huiles de pyrolyse, afin d'améliorer les conditions d'upgrading et de mitiger la dégradation du catalyseur[21,43].

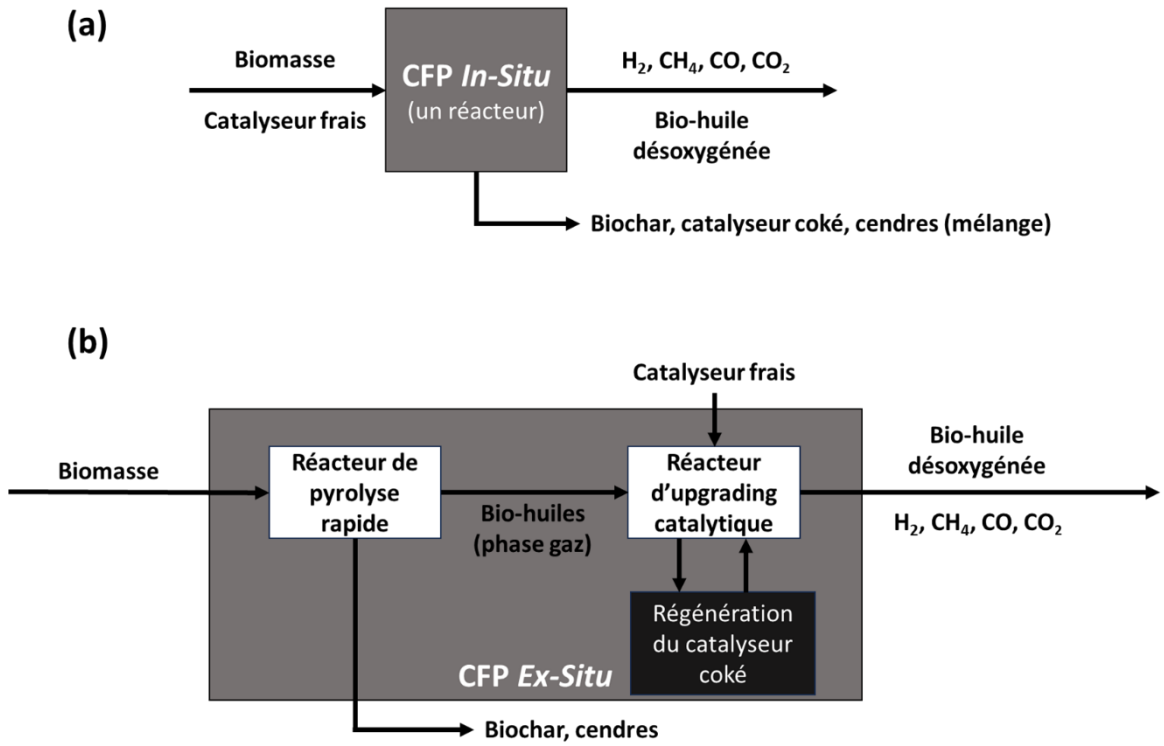

Figure I.8 : Setup de **(a)** la CFP in-situ et **(b)** la CFP ex-situ. Adapté de Iliopoulou et al. [43].

Ainsi, bien que naturellement, la sélectivité vers les aromatiques est supérieure en CFP in-situ, l'adaptabilité de la CFP ex-situ nous semble plus propice à la mise en place d'un système viable de production de BTX depuis la biomasse. Différentes techniques, abordées plus loin, permettront d'améliorer les performances générales du procédé, qui sont plus faciles à mettre en place en CFP ex-situ, du simple fait de la séparation des deux lits.

L'un des points cruciaux de la CFP est le choix du catalyseur, qui va impacter la désoxygénation et la sélectivité.

III.1.b – Catalyseurs

Afin de choisir un catalyseur adapté à la CFP ex-situ de biomasse pour la production de BTX, il est nécessaire de prendre plusieurs caractéristiques en compte : le « pouvoir de désoxygénation », la sélectivité envers les aromatiques (et plus généralement en bio-huiles), et la stabilité du catalyseur candidat.

Un grand nombre d'études ont été menées sur la question, comparant différentes structures de zéolithes avec d'autres catalyseurs (oxydes métalliques,

charbons actifs, etc.). une partie de ces études et leurs conclusions sont résumées dans le **Tableau I.3**. La plupart s'accordent sur une sélectivité en aromatique et une stabilité supérieure de la zéolithe HZSM-5 (MFI). Les performances de désoxygénation varient selon les rapports Si/Al et Catalyseur/Biomasse (C/B), néanmoins la ZSM-5 présente toujours de bonnes performances.

Norouzi et al. ont produit une étude portant sur cette question, examinant un corpus de 150 articles portant sur la pyrolyse catalytique de biomasse sur zéolithes, matériaux siliciques, charbons actifs et matériaux composites [50]. D'une manière générale, les catalyseurs produisant le plus d'aromatiques sont systématiquement ceux incorporant la HZSM-5. Des modifications (hiérarchisation, échanges de métaux, préparation de matériaux composites) permettent d'améliorer les performances et la stabilité du catalyseur (voir **III.3.c**).

C'est donc autour de ce matériau en particulier que s'articulera le travail de cette thèse.

Tableau I.3 : tests de performance pour les catalyseurs utilisés en CFP (adapté depuis Dickerson et Soria [13], Jae et al. [44]et Carlson et al.[45])

Catalyst	Temp(°C)	Feedstock	Catalyst effect	Ref
HZSM-5 (Variation du Si/Al)	500-764	Lignine « Kraft »	Bas Si/Al et hauts C/B aident à l'abattement des oxygénés et augmentent la production d'aromatiques. Températures optimales pour les aromatiques: 500-650°C.	X. Li et al. (2012) [46]
ZSM-5, Al/MCM-41, Al-MSU-F, ZnO, $Zr0_2$, CeO_2, $Cu_2Cr_2O_5$, Criterion-534, Cérine stabilisée par alumine MI-575, ardoise, biochar et cendres sourcées de biomasse	500	Rhizome de manioc	ZSM-5, Criterion-534 et Al-MSU-F produisent plus d'aromatiques et de phénoliques. ZSM-5, Criterion-534, MI-575 ont réduit le plus de carbonyles contenant des OH. ZSM-5, Criterion-534, Al/MCM-41, Al-MSU-F augmentent la fraction d'acides (acetique, formique, lactique).	A. Pattiya et al. (2010) [47]
Dolomite	500-800	Noyaux d'olives	La dolomite favorise le craquage et la production de gaz.	J.M. Encinar et al. (2009) [48]
HZSM-5n Al/MCM-41, Al-MSU-F, Cérine stabilisée par alumine MI-575.	500	Rhizome de manioc	HZSM-5 produit le plus d'aromatiques, de phénols, d'acide acétique et est le meilleur catalyseur pour la désoxygénation des dérivés de lignine. MI-575 inhibe un peu la production d'acides, et, comme HZSM-5, augmente la production de méthanol.	A. Pattiya et al. (2008)[49]
ZK-5 (2,75), SAPO-34 (0,28), FER (10), ZSM-23 (80), MCM-22 (15), SSZ-20 (45), ZSM-11 (15), ZSM-5 (15), IM-5 (20), TNU-9 (20), *BEA (19), SSZ-55 (27), Y (2,6)	600	Glucose	ZSM-5 et ZSM-11 produisent le plus d'aromatiques et le moins de coke. Les zéolithes à large pores produisent beaucoup de coke, moins d'aromatiques, mais désoxygènent mieux. La production d'aromatique est soulignée comme fonction de la taille des pores (petits pores : pas d'aromatiques, maximum pour taille moyenne).	J.Jae et al. (2011)[44]
HZSM-5 (60), Silicalite, *HBEA (50), HY (50), SiO_2/Al_2O_3 (8)	600	Glucose, xylitol, cellobiose, cellulose.	HZSM-5 produit le plus d'aromatiques, de loin.	T.R. Carlson et al. (2009)[45]

III.2 – La zéolithe MFI pour la CFP

La zéolithe MFI (**M**obil **Fi**ve, ZSM-5 : Zeolite Socony-Mobil 5) fait partie du groupe des zéolithes « big 5 » : les cinq zéolithes les plus utilisées industriellement et en recherche, concomitamment à la mordénite (MOR), la béta (*BEA), la faujasite (FAU) et la ferrierite (FER) [51]. La MFI trouve des applications comme additif aux catalyseurs de FCC [37], afin d'orienter la sélectivité des produits, dans la réduction des NOx en automobile[52,53], ainsi que dans la purification de l'air, notamment en sorption-élimination des composés organique volatiles (COV) [54–56]. La section suivante présente quelques-unes des caractéristiques essentielles de la zéolithe pour la catalyse.

III.2.a – Structure

La MFI [57,58] est une zéolithe à taille de pores intermédiaires : ses ouvertures de pores sont qualifiées de 10 MR (10 membered-rings), i.e. composées de 10 atomes T (sur les 12 distinguables) reliés entre eux par autant d'atomes d'oxygènes. Ces anneaux sont entourés et attachés ensemble par des 6 et 5 MR (**Figure I.X [010]**).

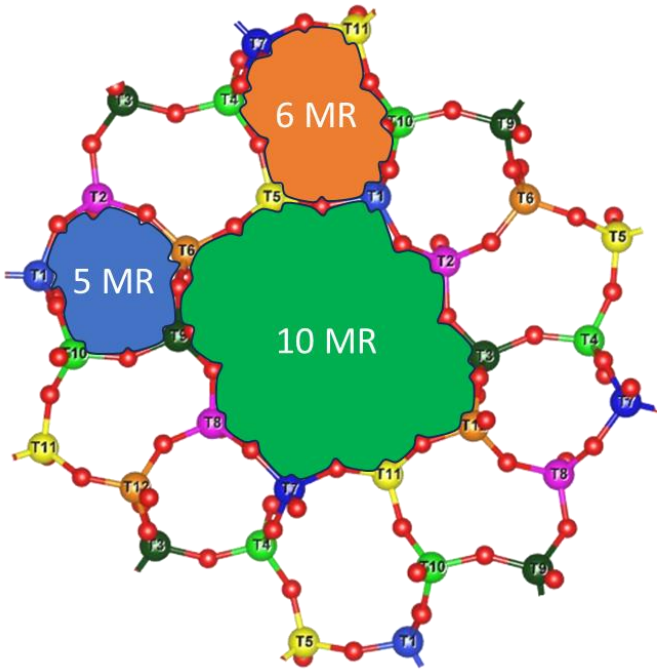

Figure I.9 : Organisation des anneaux de la zéolithe MFI selon le plan [010]. *Atomes d'oxygène en rouge. Autres couleurs : atomes T (Si, Al), équivalents si de la même couleur (en position de symétrie sur le 10 MR).*

Les 10 MR forment des canaux droits selon le plan [010], et des canaux sinusoïdaux selon le plan [100]. Ces deux systèmes de canaux sont reliés l'un à l'autre et produisent un chemin diffusionnel à 3 dimensions (**Figure I.10a et I.10b**).

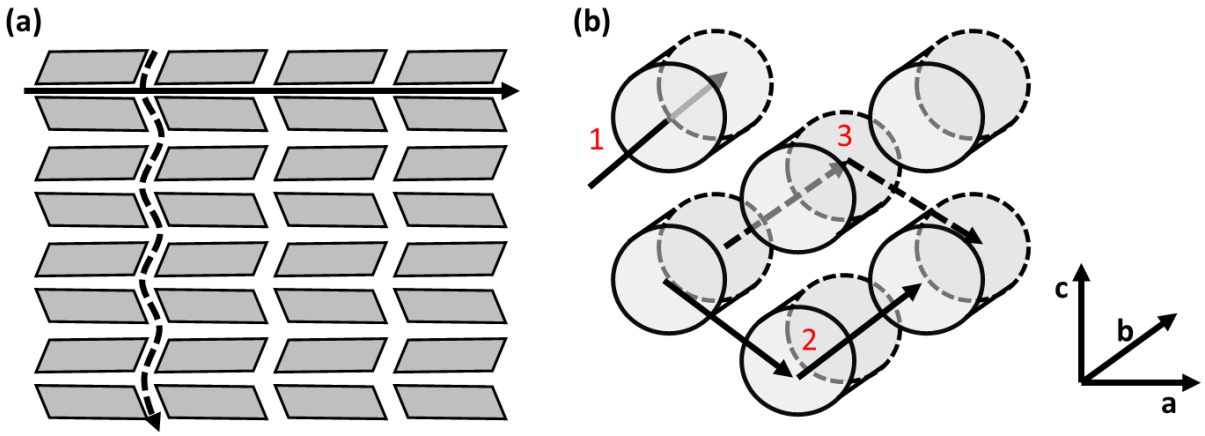

Figure I.10: **(a)** Schéma des chemins diffusionnels formés par l'intersection des canaux droits et sinusoïdaux dans la zéolithe MFI.
Flèche pleine : diffusion droite selon le plan [010]
Flèche en tirets : diffusion sinusoïdale selon le plan [100].
Reproduit depuis Figure 1.1 de [59].
(b) Schéma des chemins diffusionnels vus en perspective.
1 : Chemin selon les canaux droits du plan [010].
2 : Chemin selon les canaux sinusoïdaux du plan [100].
3 : Chemin selon les canaux sinusoïdaux du plan [100] de la cellule adjacente (flèches en tirets).

III.2.b – Acidité & atomes T

Similairement aux unités FCC, l'upgrading catalytique des huiles de pyrolyse s'opère en premier lieu par catalyse acide. La zéolithe MFI possède 12 emplacements d'atomes T (T = tétraédriques, i.e. Si, Al, Ge, Ga, … tetra-substitués par des atomes d'oxygène [60,61]) disponibles dans son motif répétable (**Figure I.9**, [57]). L'occupation de ces emplacements par un atome d'aluminium (trivalent selon la règle de l'octet) donne lieu à une charge négative, compensée par un cation, qui provient du milieu de synthèse de la zéolithe, ou bien d'échanges ioniques post-synthèse. Communément, des ions sodium (Na^+) équilibrent la

charge après synthèse (provenant de NaOH). Après échange avec l'ion ammonium (NH_4^+) puis calcination sous air ou gaz neutre (élimination de NH_3), reste un ion hydrogène. L'hydroxyle ponté [Si(OH)Al] qui en résulte présente une acidité de Brønsted. La densité, force et distribution de ces sites acides dans le catalyseur sont des facteurs majeurs qui peuvent influer sur les résultats de la réaction (Activité, Turnover Frequency, sélectivité, etc.) [62–64].

Densité des sites et appariement

Le rapport molaire Si/Al de la zéolithe est souvent utilisé pour décrire qualitativement l'acidité d'une zéolithe : plus il est bas, plus le nombre de sites potentiellement acides est élevé [59]. Ce ratio peut théoriquement tendre vers un minimum de 1 (i.e. alternance parfaite entre un atome de silicium et un atome d'aluminium dans toute la charpente du matériau – Cf Règle de Löwenstein [65]), mais la forte densité de charges négatives dans la structure apportée par les tétraèdres AlO_4^- provoque une instabilité de la zéolithe qui rend impossible certains bas rapports Si/Al. Pour la MFI, les rapports Si/Al inférieurs à 10 sont rares et souvent instables.

Plus la concentration en aluminium est élevée, plus les atomes d'Al sont susceptibles d'être incorporés dans la structure au voisinage les uns des autres (**Figure I.11a**). Cela impacte les capacités d'adsorption de la zéolithe, ainsi que la force des sites acides. En effet, la charge négative du tétraèdre $Al0_4^-$ est distribuée autour de l'aluminium. Ainsi, plus un autre Al est proche, plus la densité électronique entre les deux atomes est renforcée, ainsi que la liaison O-H des hydroxyles pontés [Si(OH)Al]. Par nature, plus cette liaison est forte, moins le proton est disponible, et donc moins « fort » est le site acide [63,64,66]. La concentration et la force des sites acides peut être mesurée via réaction modèle (craquage du n-C_6 [67]) ou bien par adsorption-désorption thermique de molécules sondes basiques (CO, Pyridine,… cf **Chapitre II** [68]).

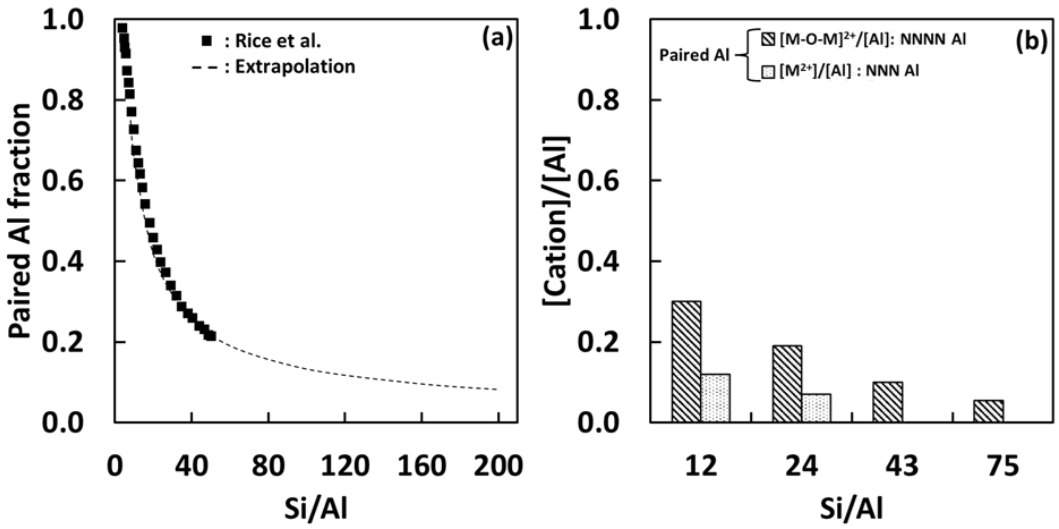

Figure I.11 : proportions théoriques des **(a)** sites Al appariés **(b)** sites Al appariés en configurations NNN et NNNN dans la charpente de MFI en fonction du rapport Si/Al.
Figures produites depuis [69].

Lors de la synthèse de la MFI, la distribution des Al est influencée notamment par le choix de l'OSDA (Organic Structure Directing Agent) et du cation neutralisant la charge de AlO_4^-[70,71]. Ainsi, le tetrapropylammonium (TPA^+), un OSDA commun dans la synthèse de la MFI, aide au placement des aluminiums au niveau des intersections des canaux [71]. Le cation sodium aide à l'incorporation d'un maximum d'aluminium dans la structure, et influe donc sur la distribution Al appariés/isolés sans interférer sur leur positionnement aux intersections. Le positionnement préférentiel des atomes Al sur des sites T particuliers ne semble pas lié à la stabilité thermodynamique de ces sites : il existe une faible différence d'énergie entre les deux extrêmes (0,38 eV entre Al en T9, le moins stable, et Al en T7, le plus stable ; la stabilité d'un Al sur un site T dépend majoritairement des angles de liaisons avec les oxygènes adjacents) [70]. De même, l'accessibilité des sites T n'est pas un facteur majeur sur le positionnement des Al : 8 des 12 sites distincts sont positionnés aux intersections entre les deux systèmes de canaux et sont donc naturellement accessibles.

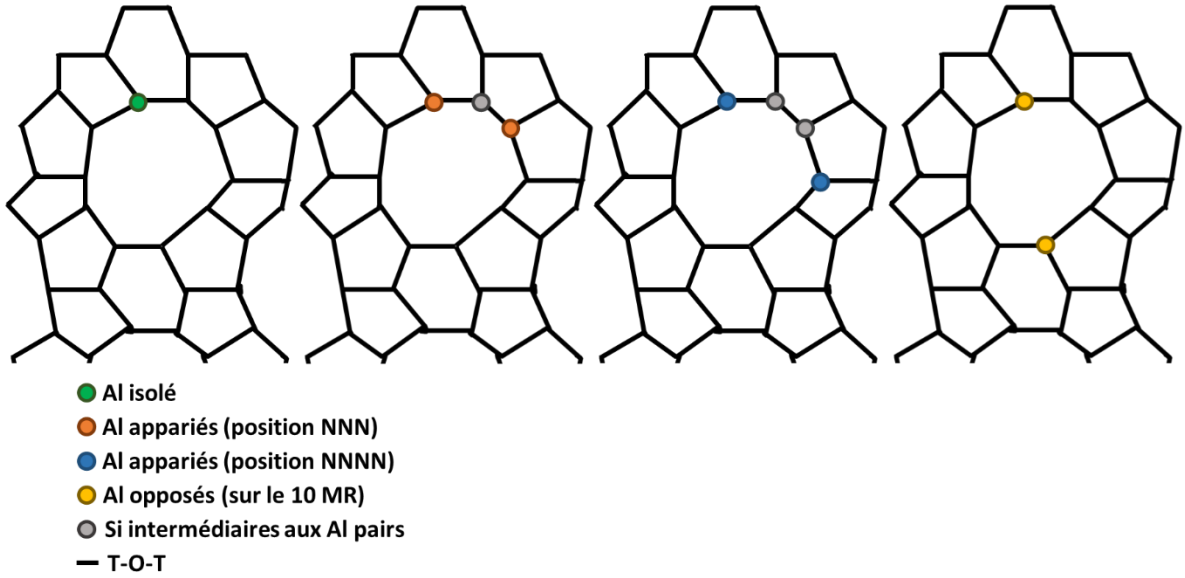

Figure I.12 : distributions et appariements différents d'Al sur le 10 MR de la MFI (adapté depuis [62],[25]).

Les aluminiums appariés sont ceux se trouvant au voisinage d'un autre aluminium, en position NNN (Next Nearest Neighbour), ou NNNN (Next Next Nearest Neighbour), représentés dans la **Figure I.12**. Une technique pour mesurer leur quantité est l'échange ionique, suivi par spectroscopie UV-visible, de cations métalliques divalents, comme le cobalt (Co^{2+})[72,73]. L'ion métallique et son complexe oxygéné permettent de quantifier les paires d'aluminium, en différenciant NNN et NNNN (**Figure I.11b**) [69].

Effet du rapport Si/Al en catalyse

Comme vu précédemment, le rapport Si/Al dans une zéolithe en définit l'acidité, tant sa force que sa concentration. Ces deux caractéristiques influent bien sûr fortement l'activité d'un catalyseur en catalyse. Derouane et al. ont montré, lors de l'acétylation catalytique de l'anisole sur zéolithe *BEA, que l'augmentation de la concentration d'aluminium depuis les hauts rapports Si/Al provoque une augmentation de l'activité catalytique, mais seulement jusqu'à une concentration limite, après quoi l'addition d'aluminium supplémentaire se fait au détriment de l'activité [74]. L'augmentation de la concentration en aluminium menant à une plus forte probabilité d'appariement des sites acides, les énergies d'adsorption des réactifs et produits augmentent (dû à la mise en jeu de deux sites pour l'adsorption des composés). Cela rend l'étape de désorption des produits limitante, produisant un effet auto-inhibant du catalyseur sur la réaction.

Lors de certaines réactions, seuls certains sites acides sont actifs. Ainsi, les réactions de craquage, du n-hexane, notamment, ou encore la dismutation du toluène, ont montré une forte dépendance sur la force des sites acides du catalyseur, ainsi que sur la position de ces derniers dans les canaux (en particulier dans les « side-pockets » de la zéolithe MOR) [67]. Donc, la diminution du rapport Si/Al, dans ces cas, n'aide pas nécessairement l'activité et peut même devenir dommageable, dans le cas où les sites acides les plus faibles ne contribuent pas à la réaction ciblée, mais peuvent participer aux réactions parasites de désactivation [75].

III.2.c – Sélectivité de forme

De manière générale, le développement des zéolithes en tant que catalyseurs industriels s'est articulé autour de leur forte acidité, mais aussi de leur sélectivité de forme, due majoritairement à la taille et la forme de leurs réseaux de canaux microporeux. Ainsi, plusieurs types de sélectivité de forme peuvent se manifester, selon la réaction et la zéolithe : premièrement, l'effet majoritaire est l'effet d'encombrement stérique, qui permet une sélection par exclusion de taille des molécules pouvant diffuser vers les sites actifs, ainsi qu'une rétention d'intermédiaires réactionnels trop volumineux pour diffuser hors des canaux, jusqu'à un réarrangement favorable à une diffusion hors des canaux.. Ensuite, peuvent exister des effets de surface, tels que des « effets de nid »[76,77], la catalyse en « bouche de pore », ou encore la sélectivité « clef-serrure » (hydroisomérisation de n-alcanes sur Pt/TON et Pt/EUO [78–80]).

Le **Tableau I.3** présente des résultats indiquant que la zéolithe MFI présente une sélectivité accrue envers les hydrocarbures aromatiques lors de la CFP. L'étude de Jae et al. [44] montre que c'est aussi le cas de la zéolithe ZSM-11 (structure MEL [81]), une autre zéolithe à canaux 10 MR tridimensionnels, là où les zéolithes à plus larges pores (*BEA, FAU, 12 MR) et d'autres à plus petits pores (ZK-5 [82], SAPO-34 [83], 8 MR) produisent bien moins d'aromatiques, voire pas du tout. D'un autre côté, la zéolithe FER (10 et 8 MR 2D) présente une sélectivité aux aromatiques 10 à 14 fois plus faible, ainsi qu'une capacité de désoxygénation bien plus réduite. Ces résultats indiquent que la sélectivité impliquée en CFP se manifeste notamment par la taille des ouvertures de pores des 10 MR, qui sont extrêmement proches des diamètres cinétiques des produits cibles, les hydrocarbures monoaromatiques, ainsi que par l'interconnectivité des canaux,

les chemins diffusionnels 3D permettant une meilleure évacuation des produits que les 2D [44].

III.3 – La désactivation, problème majeur de la CFP.

La désactivation du catalyseur est le talon d'Achille des procédés de catalyse hétérogène. En effet, de multiples facteurs, mécaniques, physiques et chimiques, entrent en jeu pour réduire l'efficacité du catalyseur, au niveau de son activité ou de sa sélectivité vers les produits cibles. Tous les procédés en phase de recherches pour applications industrielles doivent impérativement prendre en compte cet obstacle majeur, et trouver des moyens de le mitiger ou de le contourner[75]. La CFP n'y fait pas exception, et cette désactivation du catalyseur est le principal défi auquel doivent faire face les procédés en cours de développement[13,31].

III.3.a – Les différentes voies de désactivation des zéolithes en CFP

La désactivation du catalyseur en CFP est le résultat de plusieurs facteurs, dépendant du feed, du catalyseur et des conditions de réactions [75]. La **Figure I.13** en reprend les principales manifestations.

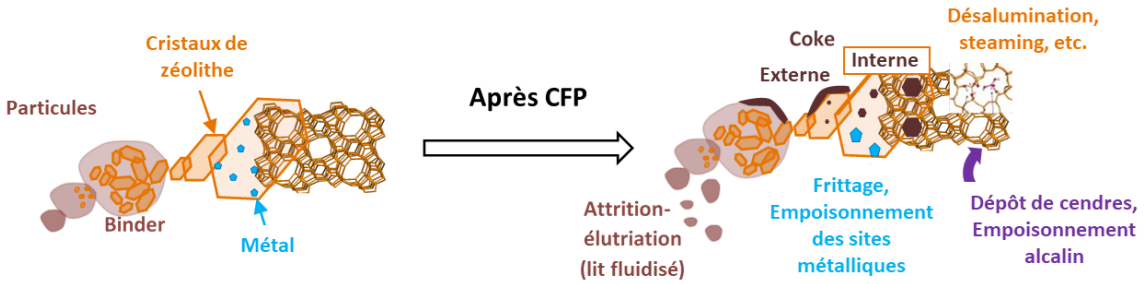

Figure I.13 : Voies de désactivation de catalyseurs zéolithiques durant la pyrolyse catalytique de biomasse.

En premier lieu, la formation de cendres lors de la pyrolyse peut mener à leur dépôt sur le catalyseur. Il a été mentionné précédemment que ces cendres peuvent contenir des métaux alcalins. Ces métaux peuvent participer à un

empoisonnement des sites acides de la zéolithe par échange ionique (K^+, Na^+, … qui peuvent remplacer les protons des sites acides de Brønsted). La diminution de l'acidité qui s'en suit peut être couplée à l'effet catalytique propre de ces métaux, ce qui peut modifier grandement l'activité et la sélectivité du catalyseur [22]. La mise en place de CFP ex-situ permet la filtration des cendres et l'élimination quasi-totale de cet aspect de la désactivation.

L'attrition et l'élutriation sont deux autres voies de désactivation du catalyseur. Elles sont principalement causées par les contraintes mécaniques imposées au catalyseur (et au binder, s'il y en a un) dans les procédés impliquant un lit catalytique agité ou fluidisé, et n'apparaissent donc pas ou peu avec des lits catalytiques fixes. Les contraintes mécaniques provoquent un « émiettage » du catalyseur, une réduction de la taille des particules (attrition), ce qui peut mener à une séparation du lit catalytique par taille de ces particules (élutriation). Ces deux phénomènes peuvent amener à des problèmes de pertes de charge et à des pertes de surface spécifique (« lissage » des surfaces externes des particules) [84].

Une autre cause de perte d'activité de la zéolithe peut être la désalumination de sa structure, causée par steaming : l'eau en phase gaz formée par la pyrolyse ou bien la combustion du coke dans une zone de régénération peut participer à une destruction partielle de la structure de la zéolithe, en ciblant particulièrement les atomes d'aluminium, responsables de l'acidité et donc de l'activité en upgrading. C'est une source de désactivation irréversible qui peut être mitigée par le contrôle de l'humidité du feed de matière première avant la pyrolyse. Invariablement, cependant, il faut renouveler le catalyseur[75].

Lorsque des métaux sont déposés à la surface de la zéolithe, les traitements thermiques ainsi que l'humidité et les conditions de réactions peuvent mener les particules métalliques bien dispersées à se regrouper, diminuant ainsi le nombre de sites métalliques disponibles pour la catalyse (frittage). Ces métaux peuvent aussi être oxydés ou réduits, certains conservant une activité en désoxygénation ou aromatisation, mais cela peut aussi équivaloir à un empoisonnement de ces sites[85,86].

Enfin, une majorité des procédés de catalyse hétérogènes appliqués à des réactifs et produits organiques subissent une désactivation due à des réactions secondaires produisent des molécules encombrantes et/ou désactivantes, communément appelées coke[75,87,88].

III.3.b – Désactivation par dépôts de coke

Comme la majorité des procédés de catalyse hétérogène, la CFP sur zéolithe provoque la formation de coke. La formation de ces molécules organiques, lourdes, difficilement désorbées, n'est pas réversible dans les conditions de réaction et mène invariablement à une perte, partielle ou totale, de l'activité de la zéolithe. C'est un processus chimique relativement complexe, qui peut impliquer une grande variété d'étapes.

Dans la littérature, le coke a été majoritairement étudié dans le contexte des réactions d'intérêt industriel, et assez peu d'études ont porté sur des cokes originaires de feeds oxygénés, tels que les huiles de pyrolyse de biomasse lignocellulosique. Indépendamment du feed, cependant, le coke est toujours retenu dans la structure de la zéolithe, selon trois principaux modes de rétention (**Figure I.14**) : il peut être faiblement volatile (ou faiblement soluble dans le milieu réactionnel, en phase liquide), ce qui l'oblige à rester condensé sur le catalyseur ; il peut être fortement adsorbé sur la surface du catalyseur, notamment sur ses sites actifs (acide/base, métal, etc.) ; enfin, il peut avoir cru tant et si bien, qu'il est incapable de diffuser hors du catalyseurs, pour raisons d'encombrement stérique. Selon les conditions réactionnelles, cela peut être un mix des trois modes.

Le coke peut se former par condensation de plusieurs intermédiaires réactionnels, ou bien par cyclisation (puis poly-cyclisation) de réactifs alkylés. La forte disponibilité et mobilité d'hydrogène est un facteur accélérant, via des transferts d'hydrogène et/ou déshydrogénations.

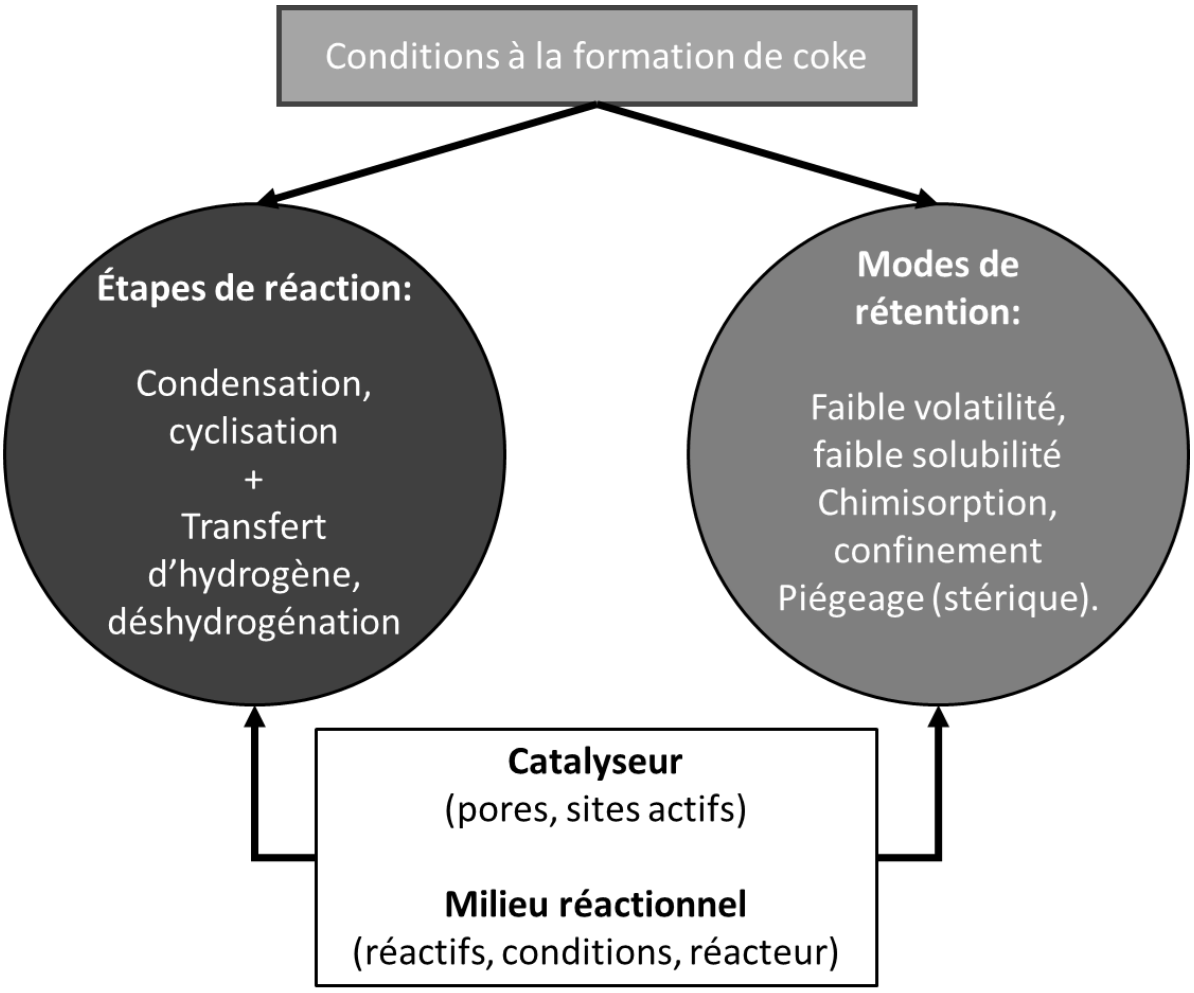

Figure I.14 : Conditions principales (physiques et chimiques) de formation catalytique de coke. *Reproduit depuis Fig 7.1 de Guisnet et Ribeiro* [75].

La composition finale du coke est aussi hautement dépendante de la température de réaction (**Tableau I.4**). Les procédés à basse température (jusqu'entre 200 à 450°C selon le procédé [75]) produisent un coke dont la composition dépend fortement du feed, qui est formé par condensation et quelques étapes de stabilisation (réarrangements, transferts d'hydrogène). Il est majoritairement retenu dans la zéolithe par sa faible volatilité (ou solubilité en phase liquide), et possiblement par piégeage stérique. Par contraste, le coke formé par les procédés à haute température (à partir d'environ 350°C), par condensation et cyclisation, avec beaucoup d'étapes de stabilisation, est plus lourd et sa composition dépend majoritairement de la forme et de la place disponible dans les pores du catalyseur (procédé à forte sélectivité de forme[89,90]). Il est alors retenu majoritairement par contraintes stériques. Ainsi, à haute température, la zéolithe MFI cokée contient majoritairement des produits comme les méthylpyrènes, alors que la FAU produit des coronènes, plus

volumineux, et la MOR, avec ses canaux linéaires produit des polyaromatiques similairement linéaires, tels que les phénanthrènes et anthracènes (**Figure I.15**) [75,89,91]. Enfin, deux mécanismes dépendant de la pression partielle de réactif existent pour la formation de coke : l'un, à haute pression (dès 1 bar), dépend du mécanisme de Sullivan (alkylations multiples, « épluchage » et contraction-expansion), tandis que l'autre, à basse pression (environ 0,1 bar), repose sur la condensation des intermédiaires réactionnels (**Figure I.15**, [89]).

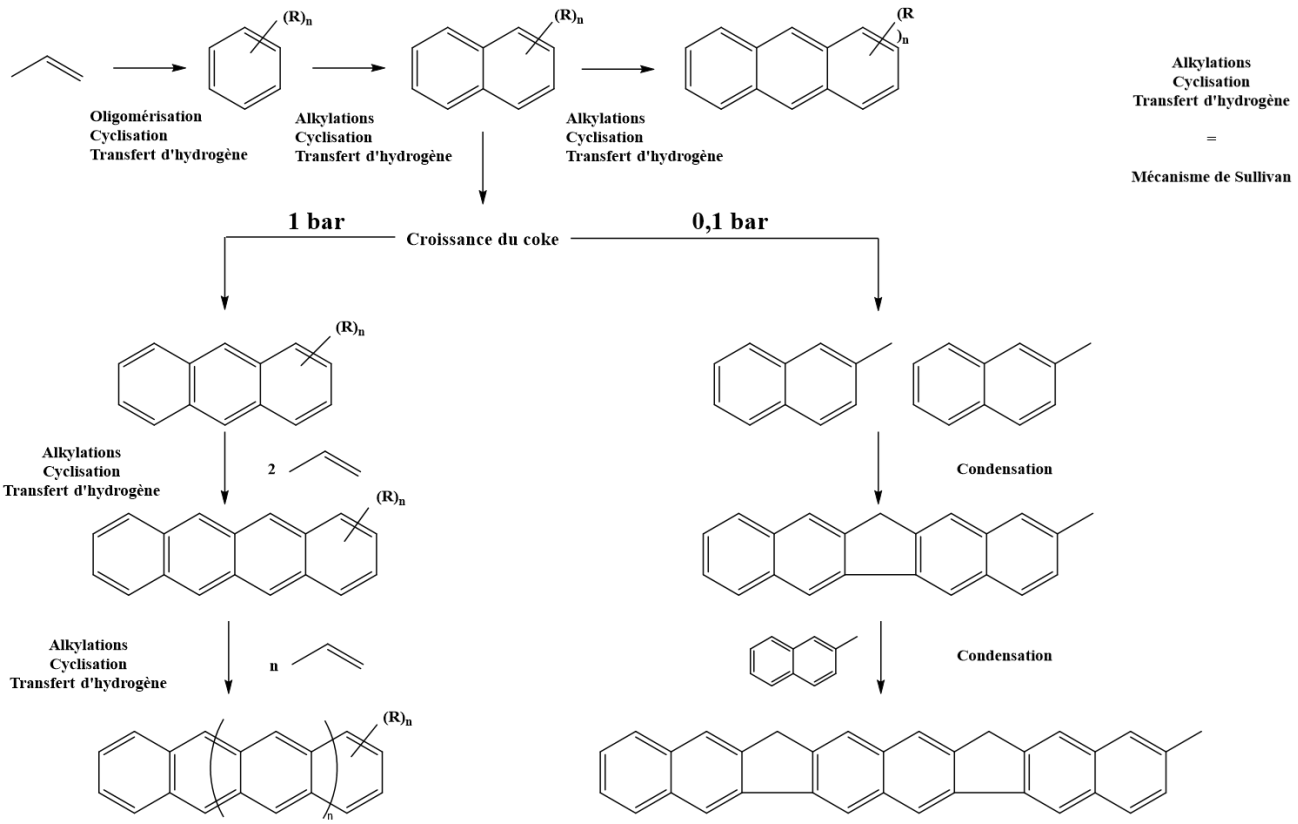

Figure I.15 : Mécanismes de formation du coke dans la zéolithe MOR selon les conditions de pression et les contraintes stériques des canaux linéaires. (adapté de Chaouati et al. [89]).

Tableau I.4 : Caractéristiques du coke selon la température du procédé catalytique. (Reproduit depuis Tableau 7.2 de Guisnet et Ribeiro[75])

Caractéristique	Coke formé à basses températures	Coke formé à hautes températures
Composition	Dépendant des réactifs	Dépendant de la structure de la zéolithe
Localisation	Micropores de la zéolithe	
Réactions de formation	Condensation, faible nombre d'étapes de stabilisation (réarrangements, transfert d'hydrogène)	Condensation, grand nombre d'étapes de stabilisation (transfert d'hydrogène, cyclisation déshydrogénante, condensation des intermédiaires de coke)
Raison de rétention	Faible volatilité/solubilité, piégeage stérique	Piégeage stérique

En ce qui concerne le coke généré par CFP sur zéolithes, il existe peu d'études explorant l'impact des conditions réactionnelles sur la formation et composition des espèces désactivantes. L'upgrading des vapeurs de pyrolyse entre dans la catégorie des hautes températures pour la formation du coke. Ainsi, la formation de coke durant l'upgrading devrait être un procédé à sélectivité de forme, influencé majoritairement par la structure de la zéolithe utilisée. Le co-feeding de molécules oxygénées avec des feeds de FCC, mentionné précédemment, a montré une forte adsorption du phénol sur les sites acides des zéolithes. Graça et al. ont montré que ce phénol accélère la désactivation du catalyseur, cependant le coke formé était principalement composé de polyaromatiques non-oxygénés [92,93]. Zhang et al., dans une étude de la CFP du furane sur zéolithe MFI, ont montré une composition classique du coke, même avec ce feed oxygéné [87], là où Liu et al. ont mis en évidence le rôle primordial des cyclopentones méthylés (intermédiaires oxygénés) dans la formation du coke polyaromatique lors du procédé de methanol-to-hydrocarbon

(MTH) [94]. Ainsi, pour la CFP d'oxygénés, bien que le résultat final semble être le même, avec une sélectivité de forme définie par la structure du catalyseur, d'autres étapes sont impliquées, dont des étapes de désoxygénation.

Pour la plupart des procédés, le coût de la désactivation du catalyseur est élevé. Maîtriser et mitiger leur désactivation devient essentiel, afin de conserver, autant que possible, l'activité et la sélectivité désirés.

III.3.b – Mitigation de désactivation par le coke

La formation de coke et la désactivation de la zéolithe qu'elle engendre sont irréversibles et inévitables pour la plupart des procédés industriels. Il existe cependant des méthodes permettant de retarder ou contourner l'inévitable. Ces méthodes s'appliquent au niveau du design du réacteur, du catalyseur ou bien des conditions opératoires.

Ainsi, le procédé de FCC, durant lequel le catalyseur zéolithique est désactivé au bout de quelques secondes seulement, dispose d'un système de renouvellement constant du lit catalytique. Le catalyseur coké est évacué vers une chambre de combustion où le coke est brûlé, fournissant la chaleur nécessaire au fonctionnement du procédé. Une fois le coke brûlé, le catalyseur est régénéré, et à nouveau acheminé dans le réacteur pour un nouveau cycle. Cette constante régénération permet un allongement de la durée de vie de la charge de catalyseur. Cependant, la combustion produit de l'eau, qui peut être dommageable pour la zéolithe, provoquant une désalumination par steaming de la charpente, et une diminution de l'acidité du catalyseur (mais en même temps renforçant la résistance du catalyseur à une désalumination prochaine)[75]. Cette désalumination peut participer à la formation d'une porosité secondaire (mésoporosité), qui est une autre méthode de mitigation de la désactivation par formation du coke.

La formation d'une porosité secondaire dans un catalyseur zéolithique peut aider à mitiger la formation de coke : par désalumination (traitement acide ou steaming) ou désilication (traitement alcalin), ou bien durant la synthèse du catalyseur, l'induction d'une porosité secondaire fournit aux réactifs un chemin diffusionnel raccourci vers les sites actifs de la zéolithe, et également un chemin raccourci pour les produits, hors de ses canaux. L'abaissement des limites diffusionnelles dans les canaux de la zéolithe réduisent le taux de formation du coke [31].

Une autre solution est de réduire la concentration des molécules « coke-makers » dans le système[75,95]. Pour les procédés d'hydro-cracking et hydroisomérisation, par exemple, une pression suffisamment élevée en hydrogène suffit à approvisionner les réactions de craquage et/ou d'isomérisation, tout en gardant la pression relative des alcènes suffisamment basse pour défavoriser les réactions de condensations qui produisent le coke[75,96].

De manière générale, la mitigation de la désactivation du catalyseur passe par une connaissance approfondie des mécanismes qui la gouverne [75]. Les bio-huiles étant un mélange complexe de nombreux composés et groupes fonctionnels, la connaissance de leur comportement individuel lors de l'upgrading catalytique est nécessaire, et des molécules modèles représentatives doivent être choisies afin de simplifier le système. Les bio-huiles contiennent une part non-négligeable de phénoliques et de groupes ether/méthoxy [35,97]**.** L'anisole est une molécule simple, comportant un cycle aromatique et un groupe méthoxy, qui produit une variété de phénoliques lors de sa dismutation sur catalyseur zéolithique, ainsi, c'est la molécule modèle choisie comme proxy pour l'étude menée durant cette thèse [98–100].

III.4 – Modélisation de l'upgrading par la transformation de l'anisole

L'anisole (methoxybenzene) est un composé aromatique que l'on retrouve dans les huiles de pyrolyse de biomasse lignocellulosique. Il est produit par alkylation sélective du phénol avec du méthanol[101–103], et est notamment un précurseur de l'anéthol, une molécule odorante (communément appelée camphre d'anis).

III.4.a – Propriétés physico-chimiques de l'anisole

L'anisole est un liquide incolore, insoluble dans l'eau et inflammable. Le **Tableau I.5** résume quelques propriétés physico-chimiques de l'anisole.

Tableau I.5: Propriétés physico-chimiques de l'anisole.

N° CAS	100-66-3
Formule brute	C_7H_80
$T_{éb}$ (°C)	154
T_{fus} (°C)	-37
M (g/mol)	108,14
ρ (g/cm³)	0,995
Dimensions (Å²)	7 x 4,3
Pictogrammes	Inflammable, Dangereux pour la santé humaine/pour la couche d'ozone.
Etude Thermochimique	Verevkin et al. [104]
Spectre et étude IR	Balfour et al. [105]

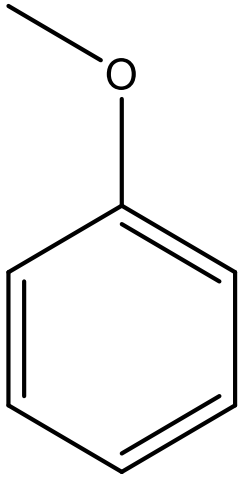

III.4.b – Etudes en littérature

Un certain nombre d'études se sont penchées sur la réactivité de l'anisole sur catalyseur zéolithiques [106], en tant que modèle pour l'upgrading catalytique de bio-huiles, en HDO [107] ou en CFP [108].

Premièrement, Zhang et al. ont établi que l'anisole ne se décompose pas thermiquement jusqu'à 350°C [109]. A 400°C, une production minime de benzène fait son apparition. A partir de 450°C, d'autres produits commencent à faire leur apparition, cette fois en quantités non-négligeables : du toluène, puis des produits de condensation, tel que le benzofurane, et d'autres de transalkylation, comme le méthylanisole et des éthylphenols. Des produits de réarrangement du benzène apparaissent après 600°C, comme le méthylcyclopentadiène. Zhang et al. proposent aussi plusieurs chemins réactionnels pour les décompositions mono- et bi-moléculaires de l'anisole. La première, après déméthylation et décarbonylation de l'anisole, a pour intermédiaire réactionnel central l'ion cyclopentènium. La seconde présente majoritairement des mécanismes de transalkylation et déméthoxylation directe (**Figure I.16**, [109]).

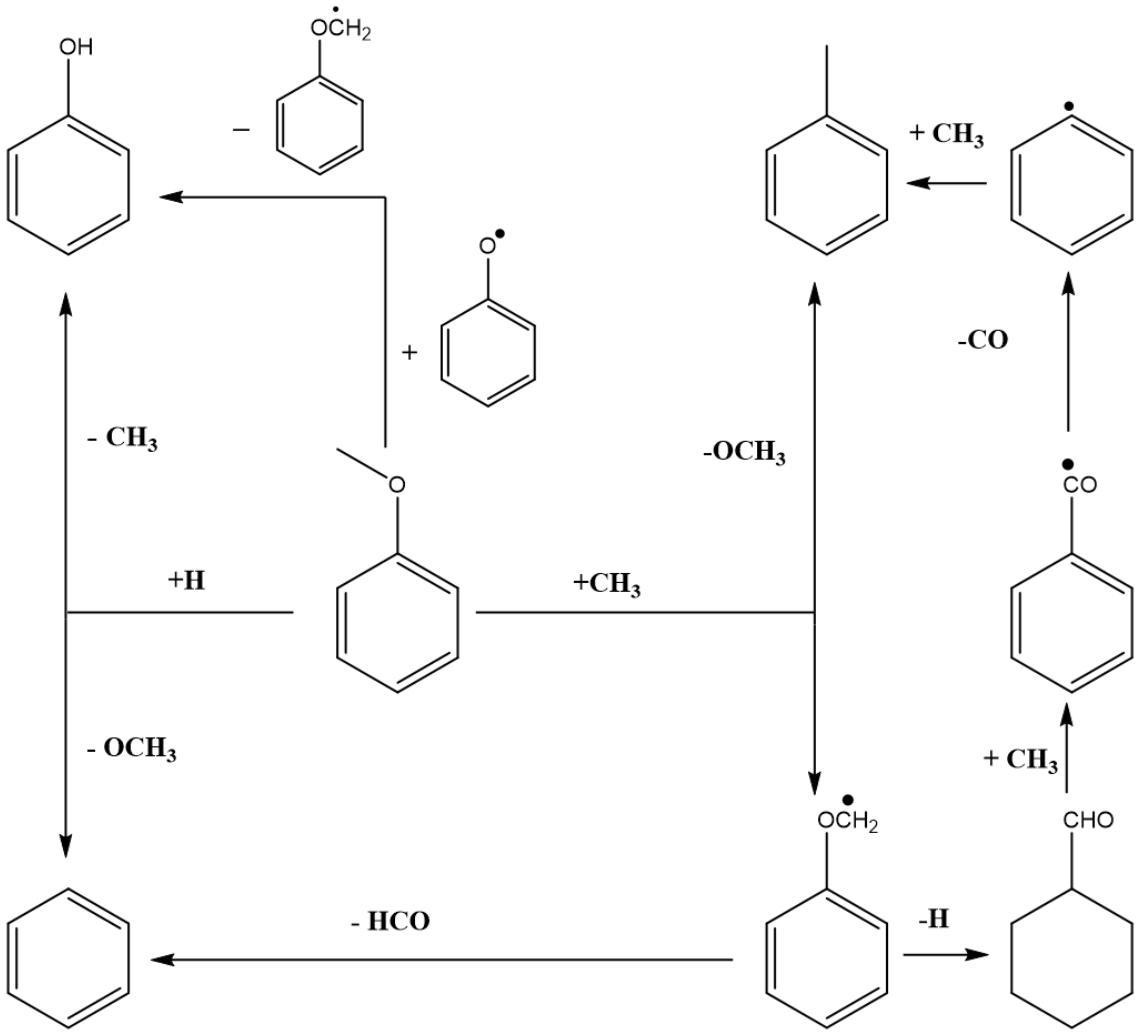

Figure I.16 : Chemins réactionnels de dégradation thermique de l'anisole (bimoléculaire avec CH_3, H et des radicaux phénoxy). (Adapté depuis Zhang et al. [109]).

L'utilisation d'un catalyseur, et particulièrement de zéolithes, semble favoriser la voie bimoléculaire et la transalkylation [98].

Xu et al. ont étudié l'hydrodésoxygénation de l'anisole à pression ambiante sur plusieurs catalyseurs zéolithiques bifonctionnels (métal-acide), et l'effet de différentes structures, métaux, temps de contact et à 250°C. Ils rapportent la production de BTX, promue par la zéolithe *BEA échangée au nickel et au fer, tandis que la ZSM-5 promeut la réaction de transalkylation.

La thèse se concentrant sur l'upgrading par craquage catalytique sur zéolithe, c'est sur ces études que nous nous concentrons. Ainsi, D.E. Resasco et coll. ont produit deux études sur la transformation de l'anisole en phase gaz sur zéolithes FAU et MFI [98,99]. Ils y ont étudié l'effet d'une multitude de facteurs sur l'activité et sélectivité du catalyseur lors de la réaction. Parmi eux, le temps de contact, la température de réaction, le gaz vecteur et le co-feeding de divers composés (eau, tétraline, hydrocarbures, etc.

Resasco et coll. ont ainsi établi la prévalence de la voie bimoléculaire lors de l'upgrading de l'anisole sur catalyseur zéolithique à faibles temps de contact[98]. Les réactions de transalkylation sont majoritaires, de la dismutation de l'anisole en phénol et méthylanisole aux réactions secondaires et ternaires produisant crésols, xylénols et autres phénoliques méthylés (**Figure I.17**). La conversion de l'anisole dans ces conditions suit un pseudo-ordre apparent de 1 [98]. L'augmentation du temps de contact favorise la conversion de l'anisole, et oriente l'équilibre des réactions vers la production des phénoliques.

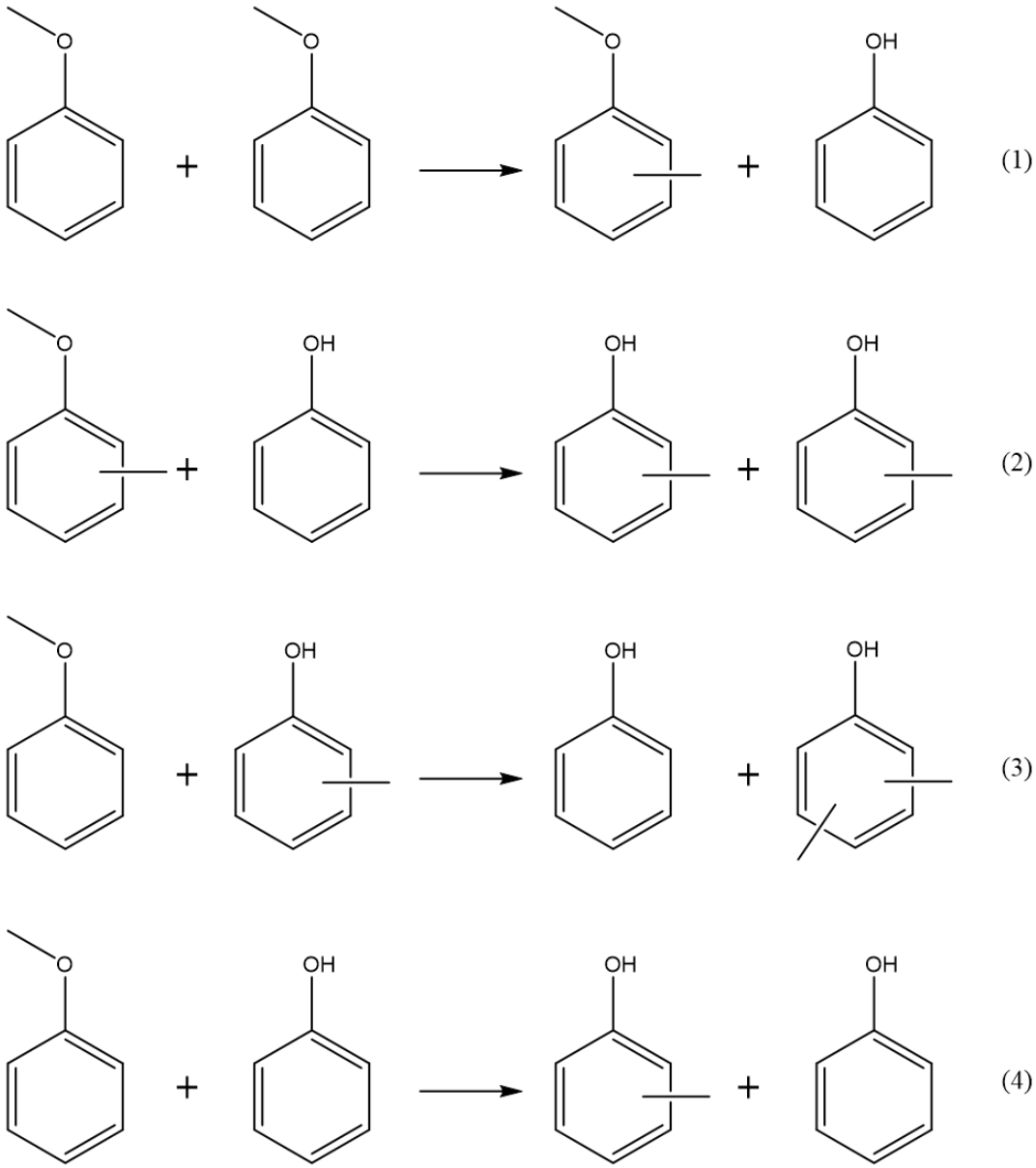

Figure I.17 : Réactions bimoléculaires majoritaires lors de la conversion d'anisole sur zéolithe en phase gaz (reproduit depuis Zhu et al. [98]).

(1) Dismutation de l'anisole en méthylanisole et phénol ;
(2) Transméthylation du méthylanisole vers le phénol, produisant deux isomères de crésol ;
(3) Transméthylation de l'anisole vers le crésol, produisant du phénol et du xylénol ;
(4) Transméthylation de l'anisole vers le phénol, produisant du crésol et du phénol.

La température influe sur la sélectivité en différents produits. Ainsi, la production de méthylanisole atteint un pic à 300°C, et décroît à températures

plus élevées, pour laisser la place aux réactions secondaires produisant crésols et xylénols.

Le gaz vecteur utilisé a un impact léger sur la désactivation : l'utilisation de dihydrogène comme gaz vecteur permet un léger ralentissement de la désactivation, ce que Zhu et al. expliquent par une possible activation de H_2 par les sites acides (moins favorisée que sur des sites métalliques), ce qui pourrait aider, comme décrit plus tôt (**III.3.b**), à la désorption des intermédiaires producteurs de coke et à empêcher la formation de coke. Cependant, l'hydrogène, sans forte pression et sans sites métalliques hydro-déshydrogénants, n'a pas d'effet visible sur le chemin réactionnel[98].

Enfin, le co-feeding d'autres réactifs avec l'anisole a plusieurs effets, selon la nature de l'additif : l'ajout d'eau, par exemple, produit une augmentation de la conversion d'anisole, et une stabilité accrue au cours du temps du catalyseur. L'eau semble également favoriser la conversion du méthylanisole au profit de la production de phénol, sans impacter les productions des produits secondaires et tertiaires. L'eau induit donc une réaction d'hydrolyse de l'anisole et du méthylanisole.

Le co-feeding d'hydrocarbures divers a également un effet important sur la conversion de l'anisole. Ainsi, la tétraline, une molécule riche en hydrogène, favorise la conversion de l'anisole, et aide à mitiger la formation de coke ainsi que l'adsorption du phénol sur les sites actifs, jouant un rôle d'adjuvant à la stabilité du catalyseur. D'autres donneur d'hydrogènes ont un effet similaire mais réduit (n-C_{10}, benzène), et le propylène, alcène léger, a un effet néfaste[99] (attendu, compte tenu de son statut de « coke-maker »[75]).

Bien que l'étude de ces facteurs et leur effet sur l'activité et la sélectivité de la MFI et la FAU lors de l'upgrading catalytique de l'anisole ait été réalisée, il existe peu d'information portant sur leur impact dans la désactivation et la formation de coke : Resasco et coll. mentionnent le rôle du phénol et l'effet du co-feeding et de certains facteurs sur la quantité de coke formée en fin de réaction [98,99], ainsi que la forte teneur en oxygène de ces espèces désactivantes, mais une identification formelle n'a pas été réalisée.

L'effet du rapport Si/Al, de haute importance en catalyse acide sur zéolithes, n'est pas mentionné par Resasco et coll. [98,99]. Zhang et al. fournissent des éléments de réponse, citant un lien entre la production du phénol et l'augmentation du rapport (densité de BAS plus faible, mais sites

individuellement plus forts), jusqu'à un certain point. De plus, la diminution du rapport Si/Al semble faciliter la conversion initiale, tout en accélérant la désactivation par formation de coke [110]. Sur le même sujet, en phase liquide, Derouane et al. ont montré l'existence d'un effet inhibiteur des faibles rapports Si/Al des zéolithes sur la conversion de l'anisole, effet qui, précédemment, n'a pas été démontré en phase gaz [74].

IV – Conclusion

Il devient de plus en plus nécessaire de réduire notre dépendance aux sources fossiles d'hydrocarbures (pétrole, gaz naturel, charbon), pour des raisons économiques, géopolitiques et climatiques. Cependant, ces hydrocarbures sont une base irremplaçable de l'industrie chimique qui a provoqué une amélioration majeure du niveau de vie mondial au cours du XX^{e} siècle. Il convient donc d'exploiter des sources alternatives d'hydrocarbures afin de diminuer notre dépendance aux ressources fossiles tout en maintenant ce niveau de vie.

Dans cette optique, la biomasse lignocellulosique issue de sylviculture, agriculture et aquaculture promet une source renouvelable et propre pour la production des molécules plateforme des industries chimiques tels que le benzène, le toluène et les xylènes (BTX).

Cet assemblage de polymères organiques oxygénés nécessite cependant d'être traitée afin de remplacer les traditionnelles sources pétrolières. Ainsi, le développement de procédés de dépolymérisation et désoxygénation est nécessaire.

La pyrolyse permet une dépolymérisation et une première désoxygénation de cette matière première en bio-huiles, qui sont composées de produits aromatiques oxygénés, tels que les phénoliques, les furanes, etc. Une étape de traitement supplémentaire est nécessaire pour arriver aux BTX depuis ces bio-huiles. Ce traitement est appelé upgrading catalytique, et peut prendre la forme d'hydrodésoxygénation ou de craquage catalytique sur zéolithes acides (CFP). La seconde option est privilégiée dans ce travail car elle ne nécessite pas l'emploi de dihydrogène ni de pressions élevées.

Une multitude de facteurs entrent en jeu lors de la CFP, dont les conditions de pyrolyse, ainsi que le choix du catalyseur. La zéolithe H-ZSM-5, de structure MFI,

est un candidat prometteur, du fait de sa sélectivité en aromatiques (dont BTX) induite par ses canaux 10 MR tridimensionnels, et par sa relative résistance à la désactivation, notamment par cokage.

Ce dernier point est un des défis majeurs pour la généralisation des procédés de CFP : en effet, l'efficacité et la viabilité d'un catalyseur dépendent en grande partie de son activité et la durabilité de celle-ci dans le temps. Ainsi, l'exploration des causes de la désactivation du catalyseur est primordiale dans le développement de catalyseurs résistants et viables commercialement.

La pyrolyse de la biomasse produisant une multitude de composés oxygénés, dont le comportement peut être individuellement très différent, et la biomasse elle-même étant de nature très diverse selon son origine, l'étude de molécules modèles, tels que les furanes ou les phénoliques, permet une simplification du système. Les aromatiques méthoxylés étant très représentés dans les bio-huiles (gaïacol, anisole, résultats de la dépolymérisation de la lignine, et qui produisent des phénoliques lors de l'upgrading), l'anisole, une molécule simple (methoxybenzène), est un bon candidat pour l'étude du comportement de cette famille lors de la CFP. L'étude de la désactivation des zéolithes lors de la réaction modèle de transformation de l'anisole sur zéolithes acides apportera des éléments de réponse quant au comportement des aromatiques méthoxylés lors de la CFP.

Le présent manuscrit apporte une pierre à l'édifice du développement de la technologie de la CFP pour la production d'hydrocarbures à haute valeur ajoutée tels que les BTX depuis la biomasse.

References

[1] Energy and environmental profile of the U.S. Chemical industry, US Department of energy, Office of industrial technologies, 2000.

[2] Benzene global market volume 2015-2030 | Statista, (n.d.). https://www.statista.com/statistics/1245172/benzene-market-volume-worldwide/ (accessed February 23, 2024).

[3] Toluene global market volume 2015-2030 | Statista, (n.d.). https://www.statista.com/statistics/1245224/toluene-market-volume-worldwide/ (accessed February 23, 2024).

[4] Xylene supply projection globally 2021 | Statista, (n.d.). https://www.statista.com/statistics/1170543/global-xylene-capacity/ (accessed February 23, 2024).

[5] M. Gayral, BTX : benzène, toluène, xylènes, (2017).

[6] C. Sourisse, Biomasse et énergie : des ressources primaires aux produits énergétiques finaux, Encyclopédie de l'énergie (2018). https://www.encyclopedie-energie.org/biomasse-et-energie-des-ressources-primaires-aux-produits-energetiques-finaux/ (accessed March 1, 2024).

[7] P.M. Donate, Green synthesis from biomass, Chem. Biol. Technol. Agric. 1 (2014) 4. https://doi.org/10.1186/s40538-014-0004-2.

[8] G.W. Huber, S. Iborra, A. Corma, Synthesis of Transportation Fuels from Biomass: Chemistry, Catalysts, and Engineering, Chem. Rev. 106 (2006) 4044–4098. https://doi.org/10.1021/cr068360d.

[9] E. Flajollet, Vers la compréhension du fonctionnement des consortia microbiens lignocellulolytiques: contribution des approches méta-omiques et biostatistiques, (n.d.).

[10] C.L. Williams, R.M. Emerson, J.S. Tumuluru, Biomass Compositional Analysis for Conversion to Renewable Fuels and Chemicals, in: J.S. Tumuluru (Ed.), Biomass Volume Estimation and Valorization for Energy, InTech, 2017. https://doi.org/10.5772/65777.

[11] H.E. Hoydonckx, W.M. Van Rhijn, W. Van Rhijn, D.E. De Vos, P.A. Jacobs, Furfural and Derivatives, in: Ullmann's Encyclopedia of Industrial Chemistry, 1st ed., Wiley, 2007. https://doi.org/10.1002/14356007.a12_119.pub2.

[12] M. Xu, S. Célérier, J.-D. Comparot, J. Rousseau, M. Corbet, F. Richard, J.-M. Clacens, Upgrading of furfural to biofuel precursors via aldol condensation with acetone over magnesium hydroxide fluorides MgF 2−x (OH) x, Catal. Sci. Technol. 9 (2019) 5793–5802. https://doi.org/10.1039/C9CY01259A.

[13] T. Dickerson, J. Soria, Catalytic Fast Pyrolysis: A Review, Energies 6 (2013) 514–538. https://doi.org/10.3390/en6010514.

[14] A. Bridgwater, Fast pyrolysis processes for biomass, Renewable and Sustainable Energy Reviews 4 (2000) 1–73. https://doi.org/10.1016/S1364-0321(99)00007-6.

[15] D. Wang, P. Jiang, H. Zhang, W. Yuan, Biochar production and applications in agro and forestry systems: A review, Science of The Total Environment 723 (2020) 137775. https://doi.org/10.1016/j.scitotenv.2020.137775.

[16] S.P. Singh Yadav, S. Bhandari, D. Bhatta, A. Poudel, S. Bhattarai, P. Yadav, N. Ghimire, P. Paudel, P. Paudel, J. Shrestha, B. Oli, Biochar application: A sustainable approach to improve soil health, Journal of Agriculture and Food Research 11 (2023) 100498. https://doi.org/10.1016/j.jafr.2023.100498.

[17] J.F. Peters, D. Iribarren, J. Dufour, Biomass Pyrolysis for Biochar or Energy Applications? A Life Cycle Assessment, Environ. Sci. Technol. 49 (2015) 5195–5202. https://doi.org/10.1021/es5060786.

[18] M. Guilmont, R. Gadiou, Y.L. Brech, M.-O. Simonnot, A. Dufour, J. Raya, C. Courson, CHARACTERIZATION AND CATALYTIC PERFORMANCES OF BIOCHARS SYNTHESIZED FROM A HYPERACCUMULATOR PLANT: ALYSSUM MURALE, (2023).

[19] R. Demol, A. Dufour, Y. Rogaume, G. Mauviel, Production of Purified H 2 , Heat, and Biochar from Wood: Comparison between Gasification and Autothermal Pyrolysis Based on Advanced Process Modeling, Energy Fuels 36 (2022) 488–501. https://doi.org/10.1021/acs.energyfuels.1c03528.

[20] H. Tan, C.T. Lee, P.Y. Ong, K.Y. Wong, C.P.C. Bong, C. Li, Y. Gao, A Review On The Comparison Between Slow Pyrolysis And Fast Pyrolysis On The Quality Of Lignocellulosic And Lignin-Based Biochar, IOP Conf. Ser.: Mater. Sci. Eng. 1051 (2021) 012075. https://doi.org/10.1088/1757-899X/1051/1/012075.
[21] A.V. Bridgwater, Review of fast pyrolysis of biomass and product upgrading, Biomass and Bioenergy 38 (2012) 68–94. https://doi.org/10.1016/j.biombioe.2011.01.048.
[22] G. Yildiz, F. Ronsse, R. Venderbosch, R. van Duren, S.R.A. Kersten, W. Prins, Effect of biomass ash in catalytic fast pyrolysis of pine wood, Applied Catalysis B: Environmental 168–169 (2015) 203–211. https://doi.org/10.1016/j.apcatb.2014.12.044.
[23] A.J. Soria, A.G. McDonald, S.R. Shook, Wood solubilization and depolymerization using supercritical methanol. Part 1: Process optimization and analysis of methanol insoluble components (bio-char), Hfsg 62 (2008) 402–408. https://doi.org/10.1515/HF.2008.067.
[24] L. Chen, Z. Qi, S. Zhang, J. Su, G.A. Somorjai, Catalytic Hydrogen Production from Methane: A Review on Recent Progress and Prospect, Catalysts 10 (2020) 858. https://doi.org/10.3390/catal10080858.
[25] A. Beuque, Unravelling the active site(s) in Methane dehydroaromatization over Mo/HZSM-5 catalysts: From cradle to grave, (n.d.).
[26] Hydrogen Production: Biomass Gasification, Energy.Gov (n.d.). https://www.energy.gov/eere/fuelcells/hydrogen-production-biomass-gasification (accessed February 29, 2024).
[27] F. Campuzano, R.C. Brown, J.D. Martínez, Auger reactors for pyrolysis of biomass and wastes, Renewable and Sustainable Energy Reviews 102 (2019) 372–409. https://doi.org/10.1016/j.rser.2018.12.014.
[28] A. Saravanan, R.V. Hemavathy, T.R. Sundararaman, S. Jeevanantham, P.S. Kumar, P.R. Yaashikaa, Solid waste biorefineries, in: Refining Biomass Residues for Sustainable Energy and Bioproducts, Elsevier, 2020: pp. 3–17. https://doi.org/10.1016/B978-0-12-818996-2.00001-6.
[29] S. Al Arni, Comparison of slow and fast pyrolysis for converting biomass into fuel, Renewable Energy 124 (2018) 197–201. https://doi.org/10.1016/j.renene.2017.04.060.
[30] Rangabhashiyam. S, Balasubramanian. P, The potential of lignocellulosic biomass precursors for biochar production: Performance, mechanism and wastewater application—A review, Industrial Crops and Products 128 (2019) 405–423. https://doi.org/10.1016/j.indcrop.2018.11.041.
[31] L.Y. Jia, M. Raad, S. Hamieh, J. Toufaily, T. Hamieh, M. Bettahar, G. Mauviel, M. Tarrighi, L. Pinard, A. Dufour, Catalytic fast pyrolysis of biomass : superior selectivity of hierarchical zeolite to aromatics, Green Chem. 19 (2017) 5442–5459. https://doi.org/10.1039/C7GC02309J.
[32] B.M. Wagenaar, J.A.M. Kuipers, W. Prins, W.P.M. Van Swaaij, The Rotating Cone Flash Pyrolysis Reactor, in: A.V. Bridgwater (Ed.), Advances in Thermochemical Biomass Conversion, Springer Netherlands, Dordrecht, 1993: pp. 1122–1133. https://doi.org/10.1007/978-94-011-1336-6_87.
[33] S. Xiu, A. Shahbazi, Bio-oil production and upgrading research: A review, Renewable and Sustainable Energy Reviews 16 (2012) 4406–4414. https://doi.org/10.1016/j.rser.2012.04.028.
[34] J. Eke, J.A. Onwudili, A.V. Bridgwater, Influence of Moisture Contents on the Fast Pyrolysis of Trommel Fines in a Bubbling Fluidized Bed Reactor, Waste Biomass Valor 11 (2020) 3711–3722. https://doi.org/10.1007/s12649-018-00560-2.
[35] H. Wang, J. Male, Y. Wang, Recent Advances in Hydrotreating of Pyrolysis Bio-Oil and Its Oxygen-Containing Model Compounds, ACS Catal. 3 (2013) 1047–1070. https://doi.org/10.1021/cs400069z.
[36] J.M.M. Arcos, D.M.F. Santos, The Hydrogen Color Spectrum: Techno-Economic Analysis of the Available Technologies for Hydrogen Production, Gases 3 (2023) 25–46. https://doi.org/10.3390/gases3010002.
[37] M. Guisnet, F. Ramôa, Chapitre 7 : Le craquage catalytique (FCC), unité clé des raffineries, in: Chapitre 7 : Le craquage catalytique (FCC), unité clé des raffineries, EDP Sciences, 2006: pp. 109–128. https://doi.org/10.1051/978-2-7598-0249-4.c009.
[38] G. Fogassy, N. Thegarid, Y. Schuurman, C. Mirodatos, From biomass to bio-gasoline by FCC co-processing: effect of feed composition and catalyst structure on product quality, Energy Environ. Sci. 4 (2011) 5068. https://doi.org/10.1039/c1ee02012a.
[39] I. Graça, A.M. Carmo, J.M. Lopes, M.F. Ribeiro, Improving HZSM-5 resistance to phenolic compounds for the bio-oils/FCC feedstocks co-processing, Fuel 140 (2015) 484–494. https://doi.org/10.1016/j.fuel.2014.10.002.

[40] I. Graça, J.M. Lopes, M.F. Ribeiro, F. Ramôa Ribeiro, H.S. Cerqueira, M.B.B. de Almeida, Catalytic cracking in the presence of guaiacol, Applied Catalysis B: Environmental 101 (2011) 613–621. https://doi.org/10.1016/j.apcatb.2010.11.002.
[41] I. Graça, F.R. Ribeiro, H.S. Cerqueira, Y.L. Lam, M.B.B. de Almeida, Catalytic cracking of mixtures of model bio-oil compounds and gasoil, Applied Catalysis B: Environmental 90 (2009) 556–563. https://doi.org/10.1016/j.apcatb.2009.04.010.
[42] R.H. Venderbosch, A Critical View on Catalytic Pyrolysis of Biomass, ChemSusChem 8 (2015) 1306–1316. https://doi.org/10.1002/cssc.201500115.
[43] E.F. Iliopoulou, K.S. Triantafyllidis, A.A. Lappas, Overview of catalytic upgrading of biomass pyrolysis vapors toward the production of fuels and high-value chemicals, WIREs Energy Environ 8 (2019) e322. https://doi.org/10.1002/wene.322.
[44] J. Jae, G.A. Tompsett, A.J. Foster, K.D. Hammond, S.M. Auerbach, R.F. Lobo, G.W. Huber, Investigation into the shape selectivity of zeolite catalysts for biomass conversion, Journal of Catalysis 279 (2011) 257–268. https://doi.org/10.1016/j.jcat.2011.01.019.
[45] T.R. Carlson, G.A. Tompsett, W.C. Conner, G.W. Huber, Aromatic Production from Catalytic Fast Pyrolysis of Biomass-Derived Feedstocks, Top Catal 52 (2009) 241–252. https://doi.org/10.1007/s11244-008-9160-6.
[46] X. Li, L. Su, Y. Wang, Y. Yu, C. Wang, X. Li, Z. Wang, Catalytic fast pyrolysis of Kraft lignin with HZSM-5 zeolite for producing aromatic hydrocarbons, Front. Environ. Sci. Eng. 6 (2012) 295–303. https://doi.org/10.1007/s11783-012-0410-2.
[47] A. Pattiya, J.O. Titiloye, A.V. Bridgwater, Evaluation of catalytic pyrolysis of cassava rhizome by principal component analysis, Fuel 89 (2010) 244–253. https://doi.org/10.1016/j.fuel.2009.07.003.
[48] J.M. Encinar, J.F. González, G. Martínez, S. Román, Catalytic pyrolysis of exhausted olive oil waste, Journal of Analytical and Applied Pyrolysis 85 (2009) 197–203. https://doi.org/10.1016/j.jaap.2008.11.018.
[49] A. Pattiya, J.O. Titiloye, A.V. Bridgwater, Fast pyrolysis of cassava rhizome in the presence of catalysts, Journal of Analytical and Applied Pyrolysis 81 (2008) 72–79. https://doi.org/10.1016/j.jaap.2007.09.002.
[50] O. Norouzi, S. Taghavi, P. Arku, S. Jafarian, M. Signoretto, A. Dutta, What is the best catalyst for biomass pyrolysis?, Journal of Analytical and Applied Pyrolysis 158 (2021) 105280. https://doi.org/10.1016/j.jaap.2021.105280.
[51] B. Louis, C.C. Rocha, A. Balanqueux, M. Boltz, P. Losch, C. Bernardon, V. Bénéteau, P. Pale, M.M. Pereira, Unraveling the importance of zeolite crystal morphology, (n.d.).
[52] E.-M. El-Malki, R.A. Van Santen, W.M.H. Sachtler, Active Sites in Fe/MFI Catalysts for NOx Reduction and Oscillating N2O Decomposition, Journal of Catalysis 196 (2000) 212–223. https://doi.org/10.1006/jcat.2000.3034.
[53] X. Wang, H.-Y. Chen, W.M.H. Sachtler, Mechanism of the Selective Reduction of NOx over Co/MFI: Comparison with Fe/MFI, Journal of Catalysis 197 (2001) 281–291. https://doi.org/10.1006/jcat.2000.3097.
[54] M. Drobek, A. Figoli, S. Santoro, N. Navascués, J. Motuzas, S. Simone, C. Algieri, N. Gaeta, L. Querze, A. Trotta, G. Barbieri, R. Mallada, A. Julbe, E. Drioli, PVDF-MFI mixed matrix membranes as VOCs adsorbers, Microporous and Mesoporous Materials 207 (2015) 126–133. https://doi.org/10.1016/j.micromeso.2015.01.005.
[55] B. Grahovski, R. Velinova, P. Shestakova, A. Naydenov, H. Kolev, I. Yordanova, G. Ivanov, K. Tenchev, S. Todorova, Catalytic Oxidation of VOC over Cobalt-Loaded Hierarchical MFI Zeolite, Catalysts 13 (2023) 834. https://doi.org/10.3390/catal13050834.
[56] X. Wang, D. Chen, Y. Jia, Z. Jiang, K. Li, S. Chaianansutcharit, P. Reubroycharoen, L. Guo, Preparation of nano-MFI zeolites doped with Al/Ti and their performance in VOC sorption, Dalton Trans. (2024) 10.1039.D3DT04314B. https://doi.org/10.1039/D3DT04314B.
[57] MFI: Framework Type, (n.d.). https://europe.iza-structure.org/IZA-SC/framework.php?STC=MFI (accessed February 6, 2024).
[58] G.T. Kokotailo, S.L. Lawton, D.H. Olson, W.M. Meier, Structure of synthetic zeolite ZSM-5, Nature 272 (1978) 437–438. https://doi.org/10.1038/272437a0.
[59] F.R. Ribeiro, M. Guisnet, Les zéolithes, un nanomonde au service de la catalyse: un nanomonde au service de la catalyse, EDP Sciences, 2012.
[60] J. Weitkamp, Zeolites and catalysis, Solid State Ionics 131 (2000) 175–188. https://doi.org/10.1016/S0167-2738(00)00632-9.

[61] T. Derbe, S. Temesgen, M. Bitew, A Short Review on Synthesis, Characterization, and Applications of Zeolites, Advances in Materials Science and Engineering 2021 (2021) 1–17. https://doi.org/10.1155/2021/6637898.
[62] B.C. Knott, C.T. Nimlos, D.J. Robichaud, M.R. Nimlos, S. Kim, R. Gounder, Consideration of the Aluminum Distribution in Zeolites in Theoretical and Experimental Catalysis Research, ACS Catal. 8 (2018) 770–784. https://doi.org/10.1021/acscatal.7b03676.
[63] A.J. Jones, R.T. Carr, S.I. Zones, E. Iglesia, Acid strength and solvation in catalysis by MFI zeolites and effects of the identity, concentration and location of framework heteroatoms, Journal of Catalysis 312 (2014) 58–68. https://doi.org/10.1016/j.jcat.2014.01.007.
[64] J. Dědeček, E. Tabor, S. Sklenak, Tuning the Aluminum Distribution in Zeolites to Increase their Performance in Acid-Catalyzed Reactions, ChemSusChem 12 (2019) 556–576. https://doi.org/10.1002/cssc.201801959.
[65] W. Loewenstein, The distribution of aluminum in the tetrahedra of silicates and aluminates, American Mineralogist 39 (1954) 92–96.
[66] P. Losch, H.R. Joshi, O. Vozniuk, A. Grünert, C. Ochoa-Hernández, H. Jabraoui, M. Badawi, W. Schmidt, Proton Mobility, Intrinsic Acid Strength, and Acid Site Location in Zeolites Revealed by Varying Temperature Infrared Spectroscopy and Density Functional Theory Studies, J. Am. Chem. Soc. 140 (2018) 17790–17799. https://doi.org/10.1021/jacs.8b11588.
[67] H. Issa, J. Toufaily, T. Hamieh, J.D. Comparot, A. Sachse, L. Pinard, Mordenite etching in pyridine: Textural and chemical properties rationalized by toluene disproportionation and n-hexane cracking, Journal of Catalysis 374 (2019) 409–421. https://doi.org/10.1016/j.jcat.2019.05.004.
[68] S. Bordiga, C. Lamberti, F. Bonino, A. Travert, F. Thibault-Starzyk, Probing zeolites by vibrational spectroscopies, Chemical Society Reviews 44 (2015) 7262–7341. https://doi.org/10.1039/C5CS00396B.
[69] M.J. Rice, A.K. Chakraborty, A.T. Bell, Al Next Nearest Neighbor, Ring Occupation, and Proximity Statistics in ZSM-5, Journal of Catalysis 186 (1999) 222–227. https://doi.org/10.1006/jcat.1999.2544.
[70] A. Ghorbanpour, J.D. Rimer, L.C. Grabow, Periodic, vdW-corrected density functional theory investigation of the effect of Al siting in H-ZSM-5 on chemisorption properties and site-specific acidity, Catalysis Communications 52 (2014) 98–102. https://doi.org/10.1016/j.catcom.2014.04.005.
[71] V. Pashkova, S. Sklenak, P. Klein, M. Urbanova, J. Dědeček, Location of Framework Al Atoms in the Channels of ZSM-5: Effect of the (Hydrothermal) Synthesis, Chemistry A European J 22 (2016) 3937–3941. https://doi.org/10.1002/chem.201503758.
[72] J. Dědeček, Z. Sobalík, B. Wichterlová, Siting and Distribution of Framework Aluminium Atoms in Silicon-Rich Zeolites and Impact on Catalysis, Catalysis Reviews 54 (2012) 135–223. https://doi.org/10.1080/01614940.2012.632662.
[73] J. Dědeček, D. Kaucký, B. Wichterlová, O. Gonsiorová, Co 2+ ions as probes of Al distribution in the framework of zeolites . ZSM-5 study, Physical Chemistry Chemical Physics 4 (2002) 5406–5413. https://doi.org/10.1039/B203966B.
[74] E.G. Derouane, G. Crehan, C.J. Dillon, D. Bethell, H. He, S.B. Derouane-Abd Hamid, Zeolite Catalysts as Solid Solvents in Fine Chemicals Synthesis, Journal of Catalysis 194 (2000) 410–423. https://doi.org/10.1006/jcat.2000.2933.
[75] M. Guisnet, F.R. Ribeiro, eds., Deactivation and regeneration of zeolite catalysts, Imperial College Press ; Distributed by World Scientific, London : Singapore, 2011.
[76] E. Derouane, Shape selectivity in catalysis by zeolites: The nest effect, Journal of Catalysis 100 (1986) 541–544. https://doi.org/10.1016/0021-9517(86)90127-2.
[77] C.A. Fyfe, Gordon.J. Kennedy, C.T. De Schutter, G.T. Kokotailo, Sorbate-induced structural changes in ZSM-5 (silicalite), J. Chem. Soc., Chem. Commun. (1984) 541. https://doi.org/10.1039/c39840000541.
[78] M. Guisnet, “Ideal” bifunctional catalysis over Pt-acid zeolites, Catalysis Today 218–219 (2013) 123–134. https://doi.org/10.1016/j.cattod.2013.04.028.
[79] J.A. Martens, D. Verboekend, K. Thomas, G. Vanbutsele, J. Pérez-Ramírez, J.-P. Gilson, Hydroisomerization and hydrocracking of linear and multibranched long model alkanes on hierarchical Pt/ZSM-22 zeolite, Catalysis Today 218–219 (2013) 135–142. https://doi.org/10.1016/j.cattod.2013.03.041.
[80] J.A. Martens, G. Vanbutsele, P.A. Jacobs, J. Denayer, R. Ocakoglu, G. Baron, J.A. Muñoz Arroyo, J. Thybaut, G.B. Marin, Evidences for pore mouth and key–lock catalysis in hydroisomerization of long n-alkanes

over 10-ring tubular pore bifunctional zeolites, Catalysis Today 65 (2001) 111–116. https://doi.org/10.1016/S0920-5861(00)00577-0.
[81] MEL: Framework Type, (n.d.). https://america.iza-structure.org/IZA-SC/framework.php?STC=MEL (accessed March 7, 2024).
[82] KFI: Framework Type, (n.d.). https://america.iza-structure.org/IZA-SC/framework.php?STC=KFI (accessed March 7, 2024).
[83] S. Wilson, P. Barger, The characteristics of SAPO-34 which influence the conversion of methanol to light olefins, Microporous and Mesoporous Materials 29 (1999) 117–126. https://doi.org/10.1016/S1387-1811(98)00325-4.
[84] C.H. Bartholomew, Mechanisms of catalyst deactivation, Applied Catalysis A: General 212 (2001) 17–60. https://doi.org/10.1016/S0926-860X(00)00843-7.
[85] E.F. Iliopoulou, S. Stefanidis, K. Kalogiannis, A.C. Psarras, A. Delimitis, K.S. Triantafyllidis, A.A. Lappas, Pilot-scale validation of Co-ZSM-5 catalyst performance in the catalytic upgrading of biomass pyrolysis vapours, Green Chem. 16 (2014) 662–674. https://doi.org/10.1039/C3GC41575A.
[86] C.A. Mullen, P.C. Tarves, L.M. Raymundo, E.L. Schultz, A.A. Boateng, J.O. Trierweiler, Fluidized Bed Catalytic Pyrolysis of Eucalyptus over HZSM-5: Effect of Acid Density and Gallium Modification on Catalyst Deactivation, Energy Fuels 32 (2018) 1771–1778. https://doi.org/10.1021/acs.energyfuels.7b02786.
[87] H. Zhang, S. Shao, R. Xiao, D. Shen, J. Zeng, Characterization of Coke Deposition in the Catalytic Fast Pyrolysis of Biomass Derivates, Energy Fuels 28 (2014) 52–57. https://doi.org/10.1021/ef401458y.
[88] S. Du, D.P. Gamliel, M.V. Giotto, J.A. Valla, G.M. Bollas, Coke formation of model compounds relevant to pyrolysis bio-oil over ZSM-5, Applied Catalysis A: General 513 (2016) 67–81. https://doi.org/10.1016/j.apcata.2015.12.022.
[89] N. Chaouati, A. Soualah, M. Chater, M. Tarighi, L. Pinard, Mechanisms of coke growth on mordenite zeolite, Journal of Catalysis 344 (2016) 354–364. https://doi.org/10.1016/j.jcat.2016.10.011.
[90] L. Rollmann, Shape selectivity and carbon formation in zeolites, Journal of Catalysis 56 (1979) 139–140. https://doi.org/10.1016/0021-9517(79)90099-X.
[91] M. Guisnet, P. Magnoux, U. Cnrs, R. Pineau, P. Ceder, Coking and Deactivation of Zeolites Influence of the Pore Structure, (n.d.) 27.
[92] I. Graça, J.-D. Comparot, S. Laforge, P. Magnoux, J.M. Lopes, M.F. Ribeiro, F.R. Ribeiro, Effect of phenol addition on the performances of H–Y zeolite during methylcyclohexane transformation, Applied Catalysis A: General 353 (2009) 123–129. https://doi.org/10.1016/j.apcata.2008.10.032.
[93] I. Graça, A. Fernandes, J.M. Lopes, M.F. Ribeiro, S. Laforge, P. Magnoux, F. Ramôa Ribeiro, Effect of phenol adsorption on HY zeolite for n-heptane cracking: Comparison with methylcyclohexane, Applied Catalysis A: General 385 (2010) 178–189. https://doi.org/10.1016/j.apcata.2010.07.011.
[94] Z. Liu, X. Dong, X. Liu, Y. Han, Oxygen-containing coke species in zeolite-catalyzed conversion of methanol to hydrocarbons, Catal. Sci. Technol. 6 (2016) 8157–8165. https://doi.org/10.1039/C6CY01463A.
[95] M. Guisnet, F. Alvarez, G. Giannetto, G. Perot, Hydroisomerization and hydrocracking of n-heptane on Pth zeolites. Effect of the porosity and of the distribution of metallic and acid sites., Catalysis Today 1 (1987) 415–433. https://doi.org/10.1016/0920-5861(87)80007-X.
[96] M. Guisnet, G. Perot, Zeolite Bifunctional Catalysis, in: F.R. Ribeiro, A.E. Rodrigues, L.D. Rollmann, C. Naccache (Eds.), Zeolites: Science and Technology, Springer Netherlands, Dordrecht, 1984: pp. 397–420. https://doi.org/10.1007/978-94-009-6128-9_15.
[97] X. Jiang, J. Zhou, J. Zhao, D. Shen, Catalytic conversion of guaiacol as a model compound for aromatic hydrocarbon production, Biomass and Bioenergy 111 (2018) 343–351. https://doi.org/10.1016/j.biombioe.2017.06.026.
[98] X. Zhu, R.G. Mallinson, D.E. Resasco, Role of transalkylation reactions in the conversion of anisole over HZSM-5, Applied Catalysis A: General 379 (2010) 172–181. https://doi.org/10.1016/j.apcata.2010.03.018.
[99] T. Prasomsri, A.T. To, S. Crossley, W.E. Alvarez, D.E. Resasco, Catalytic conversion of anisole over HY and HZSM-5 zeolites in the presence of different hydrocarbon mixtures, Applied Catalysis B: Environmental (2011) S0926337311002347. https://doi.org/10.1016/j.apcatb.2011.05.026.
[100] JuliaM. Jacobs, RudyF. Parton, AnnaM. Boden, PeterA. Jacobs, Self-Alkylation of Anisole Over Acid Medium-Pore Zeolites, in: Studies in Surface Science and Catalysis, Elsevier, 1988: pp. 221–230. https://doi.org/10.1016/S0167-2991(09)60818-1.

[101] M. Marczewski, J.-P. Bodibo, G. Perot, M. Guisnet, ALKYLATION OF AROMATICS PART I. REACTION NETWORK OF THE ALKYLATION OF PHENOL BY METHANOL ON USHY ZEOLITE, (n.d.) 8.
[102] M. Marczewski, G. Perot, M. Guisnet, Alkylation of Aromatics II. Alkylation of Phenol with Methanol on Various Zeolites, Studies in Surface Science and Catalysis 41 (1988) 273–282. https://doi.org/10.1016/S0167-2991(09)60824-7.
[103] S. Balsama', P. Beltrame, P.L. Beltrame, P. Carniti, L. Forni, G. Zuretti, Alkylation of phenol with methanol over zeolites, Applied Catalysis 13 (1984) 161–170. https://doi.org/10.1016/S0166-9834(00)83334-5.
[104] S.P. Verevkin, Weaving a web of reliable thermochemistry around lignin building blocks: phenol, benzaldehyde, and anisole, J Therm Anal Calorim (2021). https://doi.org/10.1007/s10973-021-10924-x.
[105] W.J. Balfour, The vibrational spectrum of anisole, Spectrochimica Acta Part A: Molecular Spectroscopy 39 (1983) 795–800. https://doi.org/10.1016/0584-8539(83)80019-1.
[106] P.D. Chantal, S. Kaliaguine, J.L. Grandmaison, Reactions of phenolic compounds over HZSM-5, Applied Catalysis 18 (1985) 133–145. https://doi.org/10.1016/S0166-9834(00)80304-8.
[107] J. Zhang, B. Fidalgo, A. Kolios, D. Shen, S. Gu, Mechanism of deoxygenation in anisole decomposition over single-metal loaded HZSM-5: Experimental study, Chemical Engineering Journal 336 (2018) 211–222. https://doi.org/10.1016/j.cej.2017.11.128.
[108] R. Thilakaratne, J.-P. Tessonnier, R.C. Brown, Conversion of methoxy and hydroxyl functionalities of phenolic monomers over zeolites, Green Chem. 18 (2016) 2231–2239. https://doi.org/10.1039/C5GC02548F.
[109] T. Zhang, C. Bhattarai, Y. Son, V. Samburova, A. Khlystov, S.A. Varganov, Reaction Mechanisms of Anisole Pyrolysis at Different Temperatures: Experimental and Theoretical Studies, Energy Fuels 35 (2021) 9994–10008. https://doi.org/10.1021/acs.energyfuels.1c00858.
[110] J. Zhang, B. Fidalgo, D. Shen, R. Xiao, S. Gu, Mechanism of transmethylation in anisole decomposition over HZSM-5: Experimental study, Journal of Analytical and Applied Pyrolysis 122 (2016) 323–331. https://doi.org/10.1016/j.jaap.2016.09.009.

Chapitre II

Partie Expérimentale

Introduction

This work focuses on catalysis performance, as well as catalyst deactivation during anisole transformation and catalytic fast pyrolysis of biomass. Therefore, experiments are divided into three main parts: first, catalyst preparation (if non-commercial) and characterisation; second, catalytic test (anisole transformation, catalytic fast pyrolysis of biomass); finally, characterisation of the spent catalyst.

The author's publications being included in the manuscript, their respective experimental sections are shortened to retain only the parts that receive further attention and development in said publication.

I – Catalysts preparation and characterisation (prior to testing)

I.1 – Preparation

I.1.a – Supplier

Zeolite catalysts are used throughout this study. Most are commercial materials, from companies Zeolyst, Tosoh, Misuzawa, Alsi-Penta, UOP and Süd Chemie. Their IZA denominations are MFI, FAU *BEA and MOR. A zeolite of JZO structure was synthesized.

IDs and details of the materials are presented in **Table II.1**.

Table II.1: "Parent" catalysts ID, Si/Al and suppliers.

Structure	ID	Si/Al	Supplier
MFI	T9	9	Tosoh
	T12	12	
	A12	12	Alsi-Penta
	A24	24	
	Z29	29	Zeolyst
	Z43	43	
	M50	50	Misuzawa
	Z75	75	Zeolyst
	Z201	201	
*BEA	BEA(12.5)	12.5	Zeolyst
	BEA(13.7)	13.7	
FAU	FAU(6)	6	
	FAU(15)	15	
	FAU(30)	30	
MOR	MOR(10)	10	Süd Chemie
	MOR(80)	80	/

I.1.b – Calcination under air

All materials were originally in either NH_4^+ or H^+ forms. All were treated under air and the following conditions:

From ambient to 373K, with a 1 $K.min^{-1}$ gradient; plateau for 1 h.

From 373 K to 723 K (100°C to 450°C), with a heating ramp of 10 $K.min^{-1}$; plateau for 6 h.

For tests, all catalysts were compacted (under less than 1 t), crushed and sieved to $0.2 < Ø < 0.4$ mm.

They were stored in a desiccator until use to prevent water adsorption.

I.2 – Characterisation

I.2.a – Inductively-Coupled Plasma – Optical Emission Spectroscopy : ICP-OES

Inductively-Coupled Plasma – Optical Emission Spectroscopy is a destructive technique that provides the chemical composition of a sample. The material is broken down in a (generally strongly acidic) solution, and is then pulverized into a high-energy plasma (Ar). This atomises/ionises the sample, and the resulting elements are placed in an excited state, emitting characteristic light rays when electron deexcitation occurs. This light allows for identification of the elemental make-up of the sample, while the characteristic emission rays' intensity is directly related to the element's concentration in the medium.

Quantification of most elements of the periodic table with this technique is possible (with fewer and fewer exceptions), and highly accurate.

In the present work, ICP-OES was used to assess Si/Al ratios of most zeolites. Samples were dissolved in an acid solution (4 mL HNO_3 >68%, 3 mL HCl 34-37%, 1 mL HF 47-51% and 42 mL Ultra-pure water), with microwave assistance (Anton-Paar Multiwave Pro), and analysed with ICP-OES – 5110 Agilent VDV.

I.2.b – ^{29}Si Nuclear Magnetic Resonance (NMR)

Nuclear Magnetic Resonance is a non-destructive technique which exploits the response of an atom's nucleus to an induced magnetic field, which changes depending on its environment (neighbouring atoms). ^{29}Si MAS NMR spectrum have been performed at ENSICaen on MFI zeolites, to assess the aluminium distribution in relation to Si atoms in the zeolite framework.

Solid-state ^{29}Si MAS NMR spectra were performed on a Bruker Avance 400 III HD spectrometer at resonance frequency of 79.53 MHz, with a 7 mm NMR probe. The spectra were obtained using a 6µs single pulse at a spinning speed of 6 kHz, with a recycle delay of 20s. The ^{29}Si chemical shifts were referenced to tetramethylsilane (TMS) at 0 ppm.

I.2.c – X-Rays Diffraction (XRD)

X-ray diffraction is a non-destructive technique with which the study of crystallinity within a sample is possible. A monochromatic source emits X-ray light, which is diffracted by the sample, and collected on a screen. Different crystalline structures as well as different elements produce different diffraction angles; thus, each crystalline structure possesses its own characteristic peaks on a diffractogram. Debye and Scherrer's equations allow for more in depth analysis: lattice parameters, grain size, phase(s) identification, crystallinity or amorphization, etc.

For this study, X-ray diffraction was performed with a PANalytical X'Pert Pro diffractometer with a copper (Cu) radiation source (λ = 1.5418 Å, 45 kV, 40 mA), and was mainly performed to assess the degree of amorphization of the commercial samples.

I.2.d – Scanning Electron Microscopy (SEM)

Scanning Electron Microscopy is a technique that provides surface-level information on a sample. It is bombarded by an electron beam (generated by a heated tungsten source); these primary electrons interact with the sample's surface, producing (by inelastic interactions) secondary electrons, which are collected by a detector, and in turn, the map provided by secondary electrons (via their scattering and release energy) is transcribed into a black-and-white image. These image provide information such as morphology (crystallisation patterns, surface topology, etc.) and an estimate of the general particle size.

Measurements were performed at IC2MP using a Scanning Electron Microscope JEOL 7900F.

I.2.e – N_2-physisorption

N_2-physisorption is a non-destructive technique which consists of subsequent adsorption and desorption of nitrogen at 77K onto available surfaces of a solid, essentially coating it in a layer of N_2 molecules.

This allows for the assessment of several textural properties of the material, namely porous volume (meso and micropores), pore sizes and size distribution, as well as specific surface area. For the purposes of this study, micro and

mesoporous volumes are systematically measured, using sorption isotherms, t-plot method, and the Harkins-Jura calculation model (monolayer thickness between 4.5 and 5.5 Å). Total pore volume was measured at $P/P^0 = 0.98$.

Several isotherm profiles result from different types of materials (strong/weak adsorptions, pore sizes – macro/meso/micro pores – and shapes - "ink bottle", slit-shaped, …). Zeolites (except those used as molecular sieves and adsorption applications – CHA, GIS, …), and those used in the present work, display mostly type I sorption isotherms, with hysteresis loop types H3 and H4 [1].

For the measurements, 50 to 150 mg of zeolite were weighed. Samples were degassed under advanced vacuum, at 623 K (350°C) for 15h, then the sample flasks were plugged on the 3Flex (Micromeritics) apparatus.

I.2.f – Pyridine adsorption-desorption followed by Fourier Transformed Infra-Red Spectroscopy (Pyr-FTIR)

The acidic properties of zeolites are of paramount importance in their catalytic activity. Knowledge of their quantity and nature is therefore essential. Pyridine adsorption-desorption followed by Fourier Transformed Infra-Red Spectroscopy is a technique that allows for the quantification and differentiation of Brønsted and Lewis, as well as strong and weaker acid sites.

Circular wafers of 10 to 25 mg of the proton-form catalysts are prepared (compression under < 1 t). These are then dried under air at 393 K (120°C) for 1 h, then under high vacuum at 473 K (200°C) for 1 h. The wafer is then cooled to 423 K (150°C), and a first "blank" spectrum is recorded. Pyridine is then introduced in the cell at a pressure of 1.5×10^{-3} bar for 5 min. The cell is then put under advanced vacuum again, for 1h, after which a second spectrum is taken. The temperature is then increased by increments of 100 K, plateaued for 1h, with a spectrum being taken after each, until 723 K (450°C).

The technique relies on the absorption of IR light by the wafer. Chemisorption of a probe molecule (CO, CO_2, H_2, or in this case pyridine) generates new bands on the IR spectra, characteristic of the probe and its interaction with the catalyst. Pyridine thus interacts with Brønsted and Lewis acid sites (**Scheme II.1**). Following the evolution of the OH characteristic bands in the

3800-3200 cm^{-1} region also gives information about the accessibility of pyridine to these hydroxyls, as well as the nature of these hydroxyls (Si-OH, Si-OH-Al).

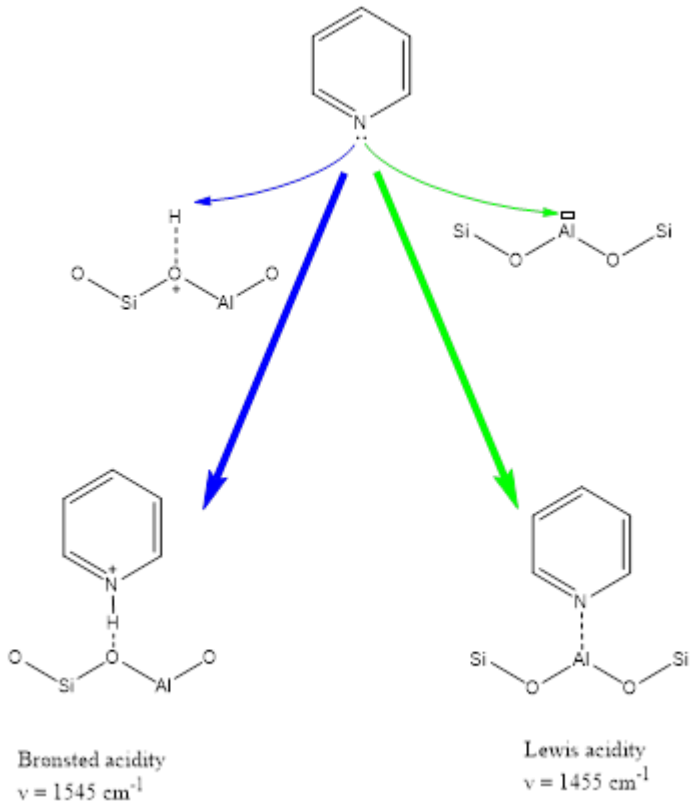

Scheme II.1: Pyridine coordination on BAS and LAS.

Interaction between Pyridine and BAS produces the pyridinium ion, giving rise to bands at 1490, 1545 and 1640 cm^{-1}, while interaction with LAS produces bands at 1455, 1490 and 1600 to 1630 cm^{-1}. To determine the concentration of each type of site (or $[PyH^+]$ and [PyL], in $\mu mol.g^{-1}$), only the bands at 1545 and 1455 cm^{-1} can be used reliably, as the others overlap. Beer-Lambert-Bouguer's law (**Eq. II.1**), and each band's molar attenuation coefficient (ε_{1545} = 1.13 $cm^2.mol^{-1}$ for $[PyH^+]$, and ε_{1455} = 1.28 $cm^2.mol^{-1}$ for the band at 1455 cm^{-1} for [PyL]) are used to obtain the concentrations[2,3].

$$A = \varepsilon * l * [C] \qquad \textbf{(Eq. II.1)}$$

Where A is the absorption value on the spectrum, l the length of the cell and [C] the species concentration (here, either [PyL] or $[PyH^+]$).

I.3 – Characterisation example: H-ZSM5 Si/Al = 43 (Z43, a.k.a. CBV8014)

A brief example of some of the previously described techniques is presented here, with commercial catalyst, designated CBV 8014, and supplied by Zeolyst. It is an MFI structure zeolite, and Zeolyst lists it as having a SiO_2/Al_2O_3 ratio of 80, therefor an Si/Al ratio of 40.

After ICP analysis, providing Si and Al wt.%, the ratio can be calculated again, with the equation:

$$\frac{Si}{Al} = \frac{Si\ wt.\%}{Al\ wt.\%} * \frac{M_{Al}}{M_{Si}} \qquad \textbf{(Eq. II.2)}$$

In this case, it gives a ratio of 43. These ratios are used in the catalysts nomenclature (here, Z43).

^{29}Si MAS NMR spectroscopy was performed on the catalyst, resulting in

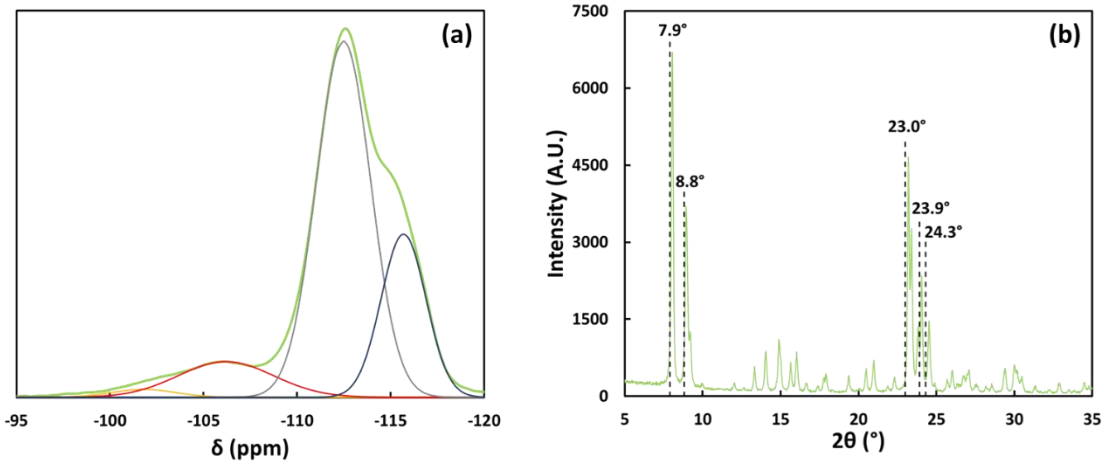

Figure II.1: (a)NMR spectrum and **(b)** X-ray diffractogram of the commercial Z43 catalyst.
(a): —Si(3SI,1Al): ≈ 1.8% ; —Si(3Si,1Al): ≈ 11.2% ; — Si(4Si,0Al): ≈ 63.1% — Si(4Si,0Al): ≈ 23.9%.

the spectrum shown in **Figure II.1a**. It shows the distribution of Al T atoms around Si in the zeolite structure.

In **Figure II.1a**, the NMR spectrum was decomposed with the Origin software, to produce the contribution of each separate peak to the spectrum in the -95 to -120 ppm chemical shift. Thus, peaks from -110 ppm show Si atoms

with no Al atoms in their immediate vicinity. Differences can arise due to geometry between the -112 and -117 ppm peaks. A large band at -105 ppm, and a smaller one at -102 ppm show Si atoms with one Al atom in their immediate vicinity. Literature also predicts the existence of terminal silanol groups participating to the former, although we could not differentiate the two. [4,5]

Notably absent are Si atoms with two Al in neighbouring position; thus, for this particular catalyst, Al atoms in the NNN position are absent. [6]

Figure II.1-b shows the X-Ray diffractogram of the Z43 catalyst. The diffractogram was obtained in a scan range from 4.99 to 35.00° (2θ), with a step size of 0.0167113°, and 700 s per step. Here, MFI exhibits characteristic peaks at $2\theta = 7.9°, 8.8°, 23.0°, 23.9°, 24.3°$. These are clearly present, although a consistent shift of around 0.15° can be observed. This might be due to a slight inclination of the surface of the sample during the measurements. Peaks are sharp, showing no sign of significant amorphization [7].

Previous work on this catalyst produced the following SEM micrographs:

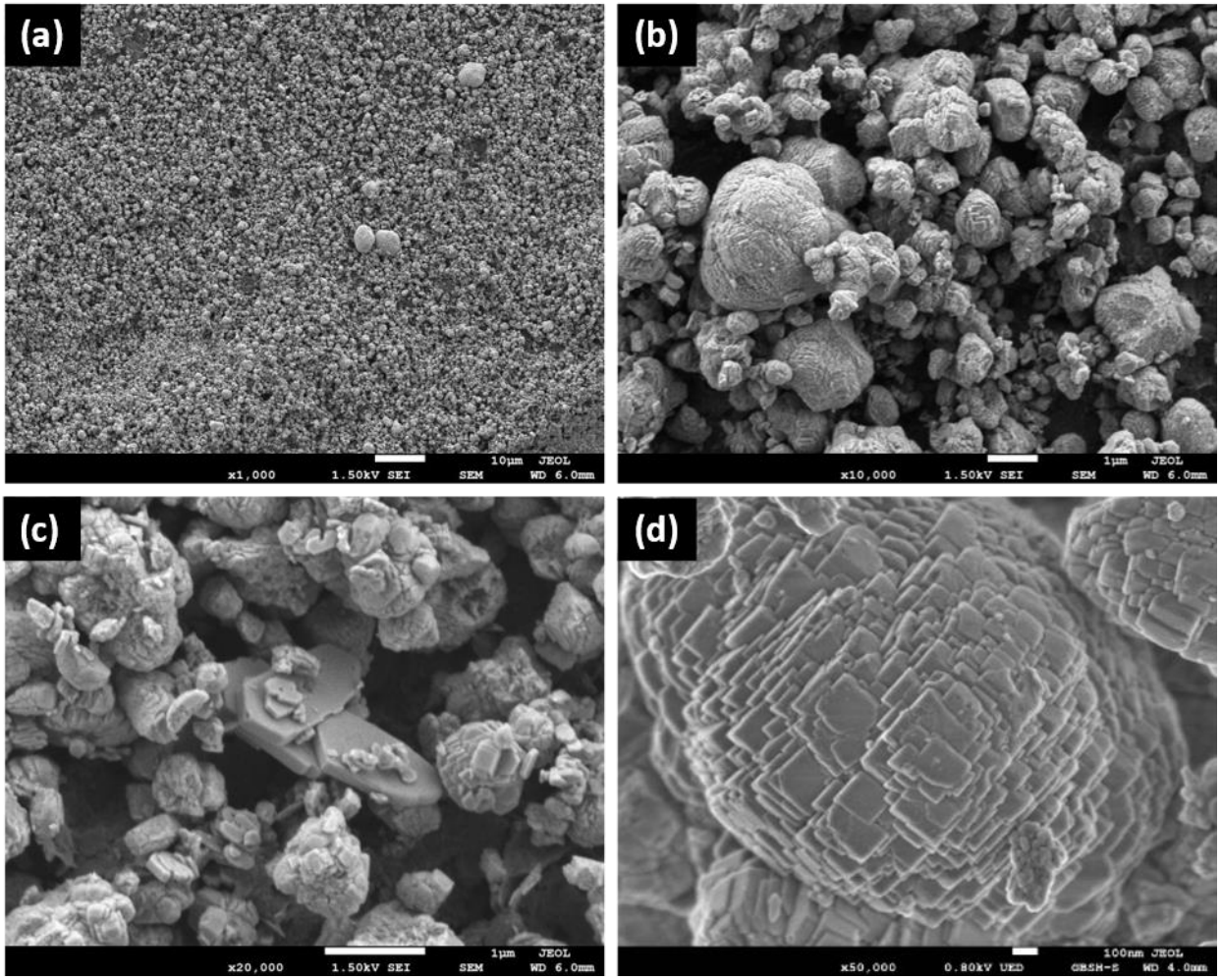

Figure II.2: SEM imagery of Z43 catalyst at enhancements x1000 (a), 10 000 (b), 20 000 (c) and 50 000 (d).

This confirms the micrometric nature of the commercial catalyst (**Figure II.2a and b**). Indeed, a range of particle diameters between about 1 and 10 µm can be observed. This also shows the heterogeneous morphological distribution of the catalyst, with some well-defined typical hexagonal crystals displayed, but the majority appearing to be the result of crystal intergrowth (**Figure II.2b, c and d**). This results in long diffusion paths for reactants, and very low activity for the sites inside the particles, with potentially an easier deactivation than with nano-sized materials.[8]

The textural properties of Z43 are shown in **Figure II.3**.

Figure II.3a shows the adsorption and desorption isotherms of nitrogen physisorption at 77 K. As mentioned in **I.2.e**, the sorption isotherm is of type I,

with an H3 hysteresis. This highlights the microporosity of the sample, reminiscent of zeolites, while a small mesoporosity is present, generated by aggregates of particles, such as seen in the previous SEM images. The microporous volume of the sample, calculated using t-plot and the Harkins-Jura method, is approximately 0.16 $cm^3.g^{-1}$.

Figures II.3b and **3c** show the FTIR spectra of the Z43 catalysts, the former highlighting the bonding of pyridine to acid sites (subtracted spectra) and the latter the hydroxyl region. in **Figure II.3b**, peaks at 1495 cm^{-1} indiscriminately show pyridine bonding to Brønsted and Lewis acid sites, while those at 1545 and 1455 cm^{-1} show Brønsted and Lewis bonding separately. In the higher temperature spectra, at 1462 cm^{-1}, a shoulder to the Lewis peak can be seen, corresponding to the formation of iminium ions, by degradation of pyridine. In **Figure II.3c**, the black spectrum, corresponding to the fresh sample, shows three main features: an intense band at 3610 cm^{-1}, corresponding to bridged hydroxyl groups (Si-O(H)-Al), a shouldered band at 3740 cm^{-1}, for the terminal Si-OH on the outer surface, and a broad, faint band, centred around 3470cm^{-1}, assigned to hydroxyl nests in the structure. The shoulder (at 3725 cm^{-1}) of the 3740 cm^{-1} band can be attributed to silanol groups located in the intraparticular defects (of which Z43 has many, due to the aggregates shown in **Figure II.2**). The absence of a band at 3665 cm^{-1} indicates the absence of hydroxyl groups associated to extra-framework aluminium (EFAl). [9]

Using **Eq.II.1**, the sites concentrations are $[PyH^+]$ = 281 $\mu mol.g^{-1}$ and [PyL] = 45 $\mu mol.g^{-1}$.

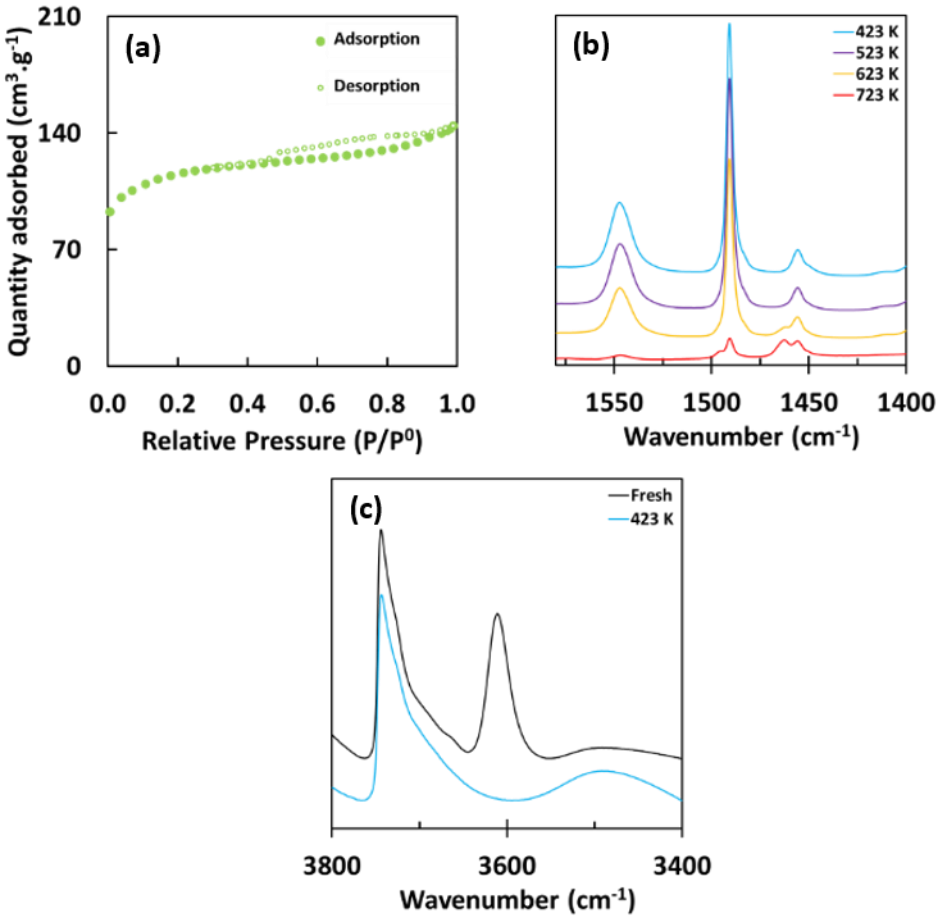

Figure II.3: Textural characterisation of Z43: **(a)** N_2-physisorption, adsorption-desorption; Pyridine sorption and evacuation on Z43 **(b)** Brønsted and Lewis acid sites characteristic peaks (1400 – 1580 cm^{-1}) and **(c)** OH zone (3400 - 3800 cm^{-1}).

II – Catalytic tests

II.1 – Anisole conversion (IC2MPoitiers, ENSICaen)

II.1.a – Experimental setup for anisole transformation Experimental setup

Anisole transformation experiments were carried out at laboratory scale in the setup described in **Scheme II.2**. This in-house unit consists of a fixed bed reactor, an oven, GC-FID, and PID controller. An on-line condenser, cooled to 273 K (0°C), is placed at the end of the setup. Non-condensable gases are evacuated to the lab exhaust system. From the oven to the cooler, all connecting pipes and lines are heated to 623 K (350°C).

The tubular fixed-bed reactor was first designed and built by the glass-blower technicians (J-J. Colin, C. Rouvier) in IC2MP. It was redesigned in ENSICaen (A. Lanel, N. Pichot), for practical and efficiency reasons. Performances were unaffected by this redesign.

Constant feeds of reactant and carrier gas are respectively delivered by a Metrohm Dosimat and a Bronkhorst mass flow controller. Pressure in the setup is assessed by an on-line gauge (and does not exceed 1.4 bar). Temperature and gas flows are controlled by the PID (control software by B. Leroux, IC2MP).

Chromatograms are processed on the PID with the CompassCDS software.

Before tests, catalysts are sieved to particles of $0.2 < ø < 0.4$ mm diameter (pellets formed under 500 kg then crushed in a mortar). Catalyst pre-treatment is as follows: heating to 373 K (1 $K.min^{-1}$ from ambient), with a 1 h plateau, to avoid any steaming damage from adsorbed water. Further heating (1 $K.min^{-1}$) to 673 K followed with a 1 h plateau at the final temperature. Liquid anisole is then injected (0.01 $mL.min^{-1}$) with a *Metrohm 725 Dosimat* and vaporized at the reactor inlet. The operating conditions are: $P_{anisole}$ = 0.048 atm, N_2 flowrate (STP)= 100 $mL.min^{-1}$, T = 673 K, $0.016 < W/F° < 0.17$ $g_{cata}.h.g_{feed}^{-1}$.

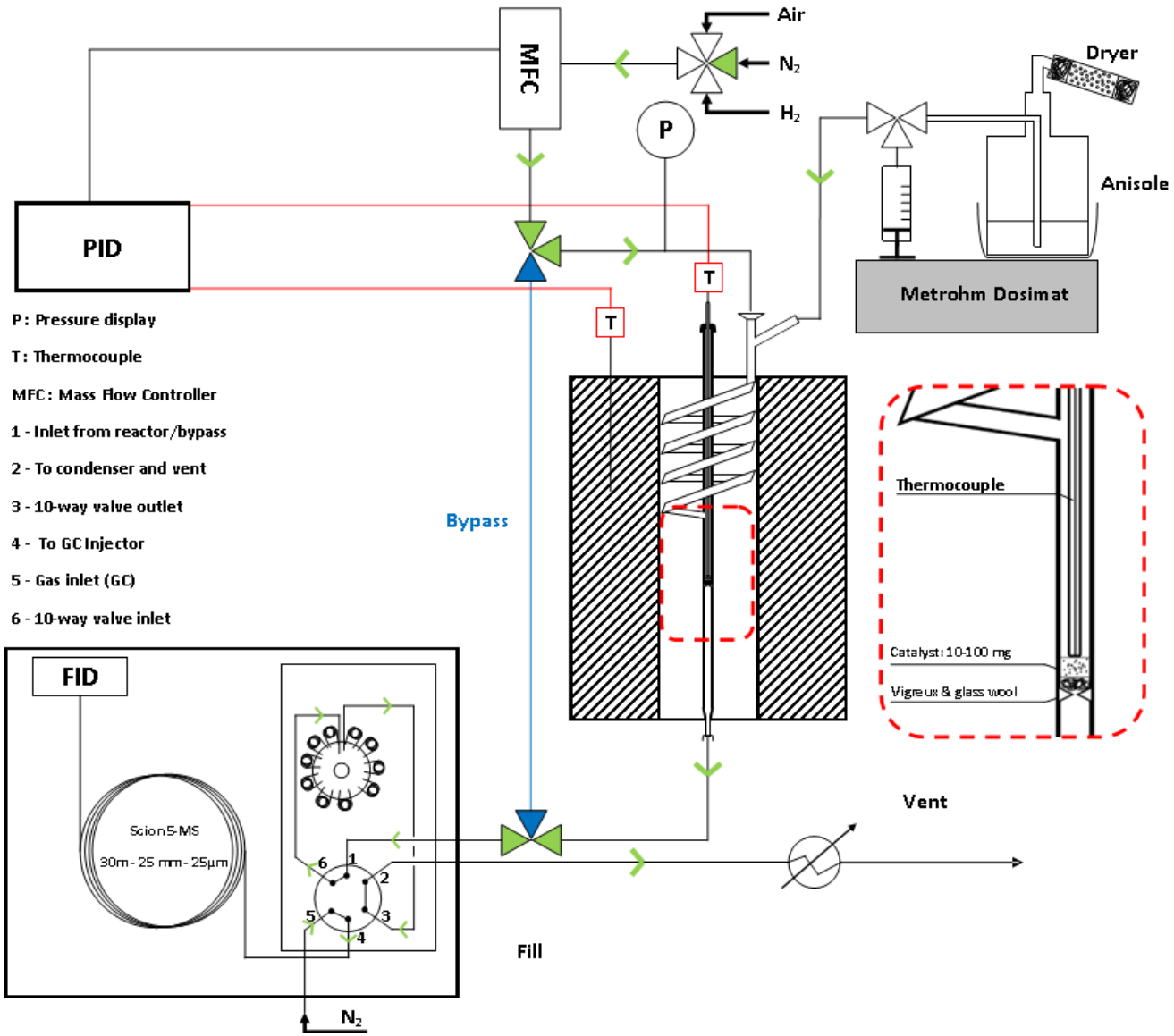

Scheme II.2: Experimental setup for anisole transformation on zeolite catalysts.

II.1.b – Parameters of the catalytic tests

This setup allows for the variation of temperature, reactant, and carrier gas flow, but not total pressure. The reaction parameters were chosen to reproduce results of Resasco and coll. on anisole transformation over HZSM[10,11].

As such, one important variable is the contact time of the reactant on the catalyst, which is given by the following equation:

$$\mathrm{W/F}\ (=\ \tau)\ = \frac{W_{cata}}{F_{feed}} \qquad \textbf{(Eq. II.3)}$$

Here, it is expressed in the unit : gcata.h.gfeed-1. It leads to the calculation of α (catalyst activity, gfeed.h-1.gcata-1), which is the slope of the curve drawn by **Eq II.4**:

$$|-\ln(1 - X_i)| = \mathrm{f(W/F)} \qquad \textbf{(Eq. II.4)}$$

Where Xi is the fractional conversion at ti (Time on Stream -TOS-, h).

Reaction temperature is fixed at 673 K (400°C) and is constant. There is no thermal (non-catalytic) conversion of anisole at this temperature.

The pressure in the reactor does not exceed 0.4 MPa over atmospheric pressure.

II.1.c – Reaction products identification

After reaction, products are separated, and a small fraction is injected in GC-FID. The majority is recovered in a condenser, cooled to 273 K (0°C).

This mixture was injected into GC-MS (GC-QTOF, Agilent). Quantification (**Chapter** I) was performed by GC-FID (Agilent technologies 7820A, HP-5 column). **Figure II.4** shows the chromatogram of the reaction mixture. There are more than 30 products, mostly (methyl)phenols and (methyl)anisole isomers. While the method runs for 45 minutes, nothing of interest is significantly detected after 25 minutes. Products are separated by families, detailed more thoroughly in **Figure II.5a to 5f**.

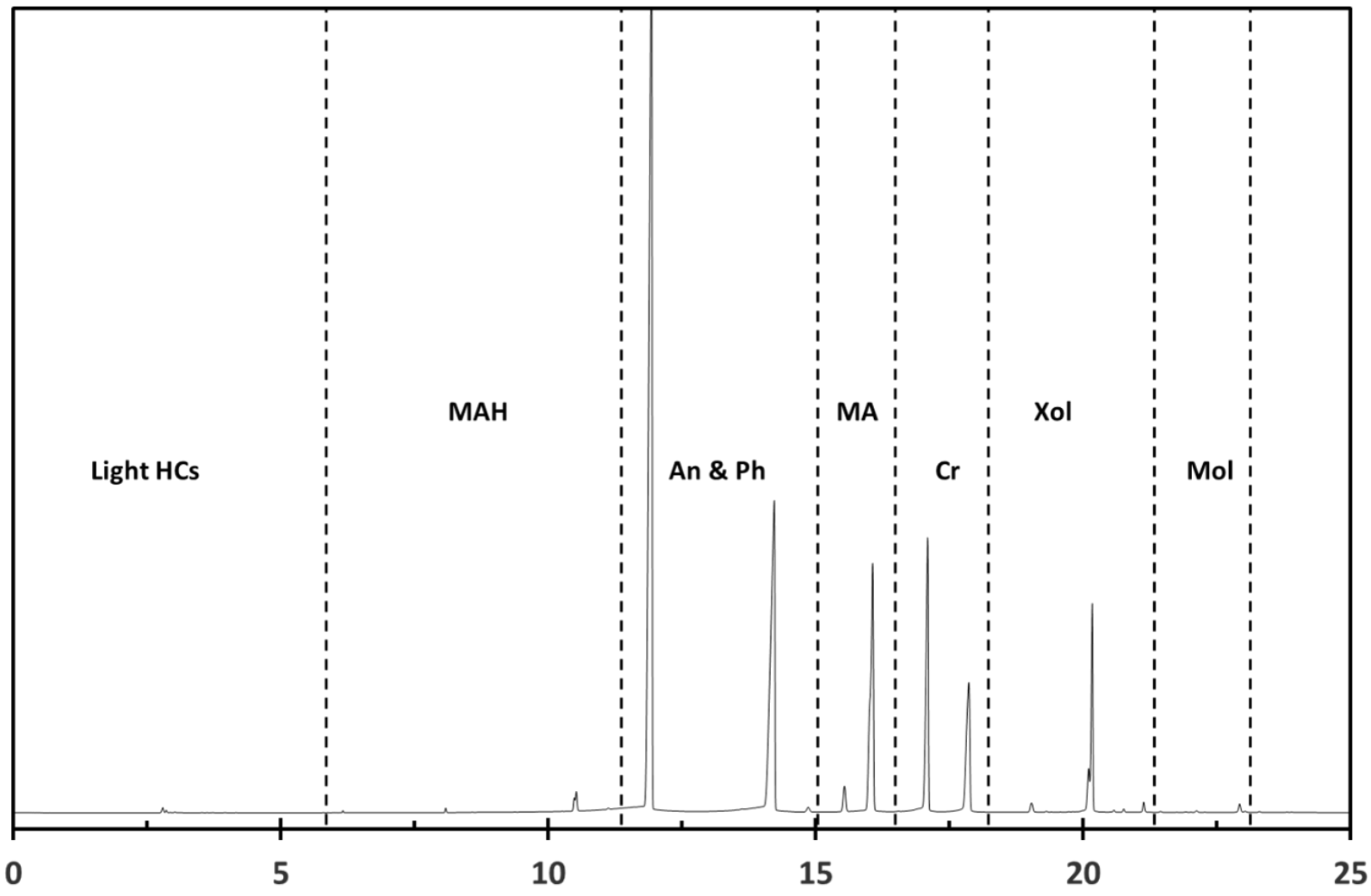

Figure II.4: Full chromatogram of the identified products in the reaction mixture

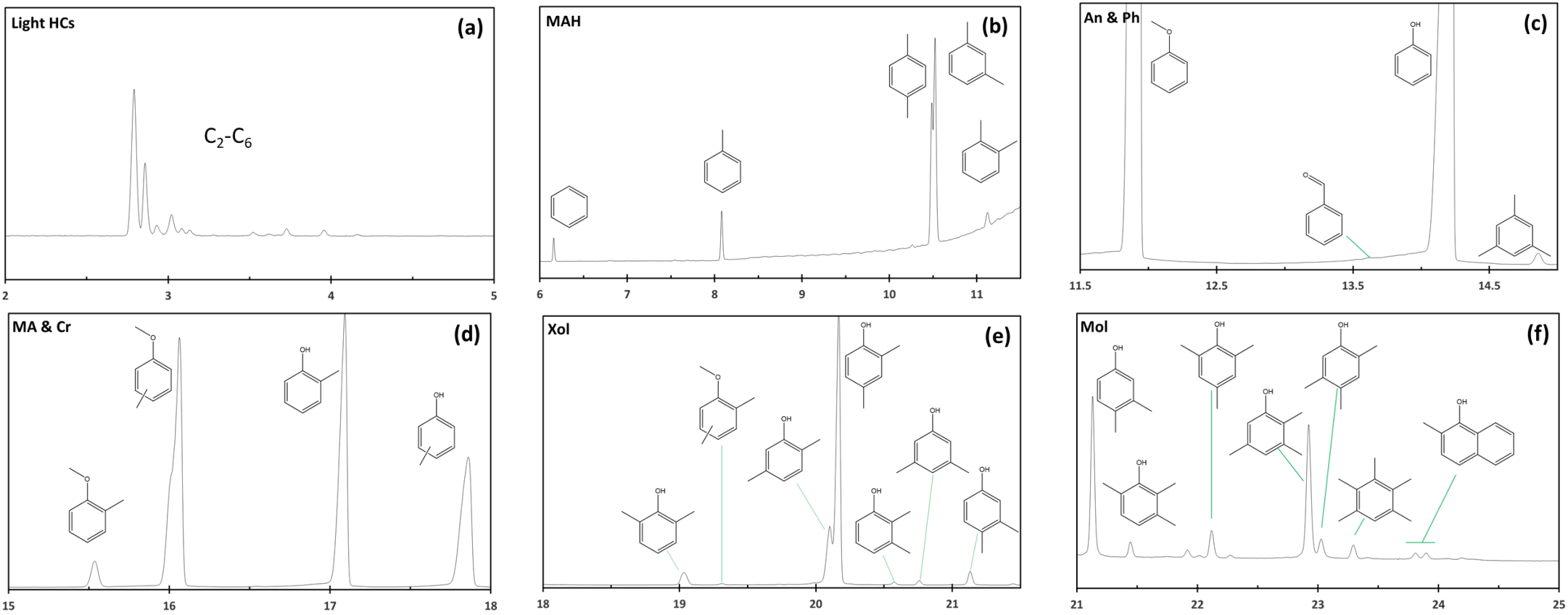

Figure II.4: Chromatograms for the reaction mixture of anisole transformation, separated by retention times. **(a)** Light Hydrocarbons, **(b)** Monoaromatic Hydrocarbons, **(c)** Anisole, Benzaldehyde, Phenol and Trimethylbenzene (mesitylene), **(d)** Methyl-anisoles and Cresols, **(e)** Xylenols and dimethyl-anisole, **(f)** Mesitols and heavies.

Isomers are distinguished (whenever possible) one from another according to their respective boiling points (**Table II.3**), and their differences in retention times are assessed thanks to them.

Table II.3: reaction products isomers and their respective boiling points (for separation in GC)

Isomer	Boiling Point (K)	Isomer	Boiling Point (K)
p-Xylene	411	2,6-Xylenol	476
m-Xylene	412	2,5-Xylenol	485
o-Xylene	417	2,4-Xylenol	485
2-Methylanisole	444	2,3-Xylenol	490
3-Methylanisole	448.5	3,5-Xylenol	495
4-Methylanisole	448.5	3,4-Xylenol	500
o-Cresol	464	2,3,6-Mesitol	499
p-Cresol	475.1	2,4,6-Mesitol	493
m-Cresol	475.2	2,3,5-Mesitol	504
		2,4,5-Mesitol	505

II.1.d – On-line products analysis

As shown in **Scheme II.2**, the setup includes ten 500 µL heated injection loops, capable of storing the products. These are filled during the reaction (every ½, 2, 5, 10 or 20 minutes, during the first hour of reaction, as it was observed this is when most of the deactivation takes place), and injected into the GC-FID apparatus, allowing for a kinetic study of the catalyst activity and subsequent deactivation (**Chapter III**).

II.2 – Catalytic Fast Pyrolysis (LRGP, Nancy)

II.2.a – Experimental setup

Catalytic fast pyrolysis experiments were carried out on the setup represented in **Scheme II.3**. This is an ex-situ CFP setup, meaning that pyrolysis and catalytic upgrading take place in two separate reactors. Both are heated to 773 K (500°C); N_2 is used as carrier gas. Pressure in the setup is monitored and kept at a constant 0.2 MPa above atmospheric pressure, by way of a control valve downstream from both reactors and condensers. Pyrolysis is carried out in R1, then the gas-phase products are carried to R2, where upgrading takes place. After upgrading, condensation occurs in methanol, cooled down by a mixture of propanol and liquid nitrogen (around the melting point of propanol, i.e., 184 K, or -89°C). Non-condensable gases are evacuated to a vent.

Oak wood pellets are introduced in the feed tube and flushed with N_2 for an hour, then pushed, one by one into R1 using magnets in and outside the feed tube.

The upper N_2 inlet prevents the pyrolysis gases from remaining in the upper part of R1. The lower inlet is the main one, allowing for circulation towards R2. The upper right inlet is shut off after flushing of the biomass pellets.

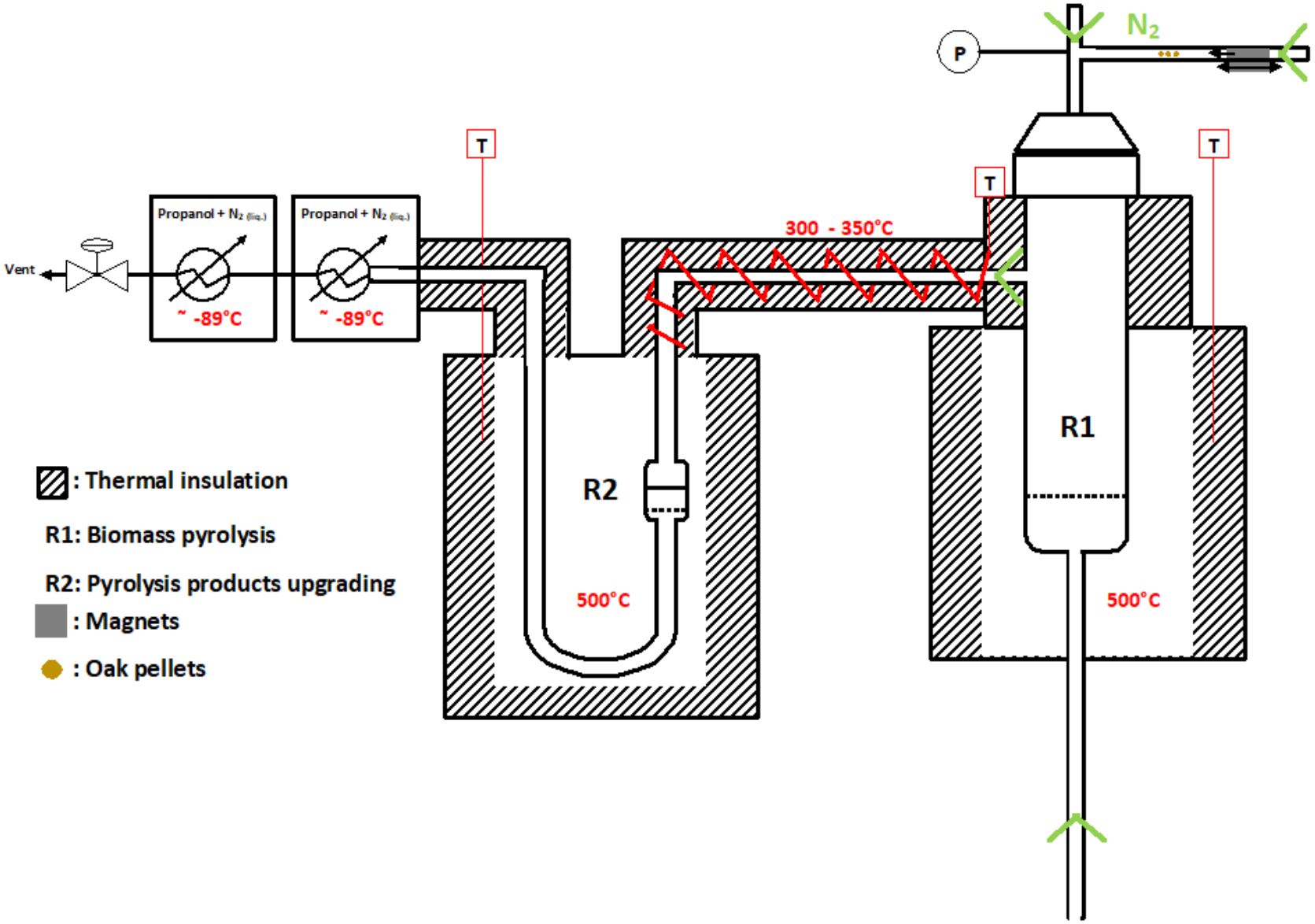

Scheme II.3: Experimental setup for *ex-situ* catalytic fast pyrolysis of oak wood on zeolite catalysts

II.2.b – Parameters of the catalytic tests

During these experiments, several factors are monitored: the mass of biomass (oak pellets) and residence time of pyrolysis gas in R1, the mass of catalyst in R2 and the temperatures of both R1 and R2 (pyrolysis and upgrading temperatures). The masses of biomass and catalyst are of paramount importance and their ratio is crucial in the determination of the process's efficacy[12].

Table II.4 gives these parameters, while **Eq. II.5** gives the calculation of the pyrolysis gases' residence time inside the pyrolysis reactor:

$$t_i = \frac{V_{R1}}{F_{N_2}^{upwards}} \qquad \textbf{(Eq. II.5)}$$

With V_{R1} the volume of R1 (pyrolysis reactor) and $F_{N_2}^{upwards}$ the volumetric flow of nitrogen vector gas coming from the lower inlet in R1.

Table II.4: experimental parameters of the CFP experiments

T (K)		m_{cata} (g)	$m_{biomass}$ (g)	$Biomass/Catalyst$	t_i (s)
R1	R2				
773	773	0.5	0.425	0.85	2.38

II.2.c – Products analysis

After reaction, products are stored at 269 K (-4°C) in closed flasks, and analysed by injection in GC-MS/FID for identification and quantification.

III – Characterisation of deactivated catalysts and deactivating species

III.1 – Spent catalyst characterisation

A very important aspect of catalytic studies is the catalyst deactivation.

Whenever hydrocarbons are involved with heterogeneous catalysts, unwanted hydrocarbon deposition can occur, contributing to this deactivation. Studying these "coke" deposits can shed some light on the deactivation mechanisms, by their composition, location within the catalyst, mode of deposition, bonding to the active sites, etc. [13].

After reaction, each and every catalyst loading was kept and stored in glass vials at ambient temperature, for later study.

Study of a catalyst's residual active sites and porosity can also provide information on the matter.

Methods for the aforementioned study of the spent catalysts' textural and physico-chemical properties are the same as those presented in **I-2.a** and **I-2.b**, with the exception of the degassing step for N_2-physisorption (instead of heating, it is performed at ambient temperature, to prevent oxidation of the coke species under air, and/or thermal desorption) and the pretreatment for pyr-FTIR analysis (293-423 K under air instead of 293-723 K, for the reasons cited previously).

III.2 – Characterisation of deactivating coke species

The term "coke" refers to hydrocarbon deposition during the reaction of organic compounds on solid catalysts. These hydrocarbons, mostly polyaromatic compounds, such as pyrene, phenanthrene, anthracene, etc., can be formed through various mechanisms (polycyclisation, generally at the expense of the target reaction[14]. They may be retained in the zeolite by steric hindrance (too large to diffuse out of the porosity), sorption to an active site, or low volatility (and solubility, in the case of liquid phase processes).

Techniques for the characterisation of said coke are destructive: hydrocarbons oxidation or zeolite structure “digestion” by hydrofluoric acid.

III.2.a – Coke content through thermogravimetric analysis (TGA)

This technique consists in the constant registering of a sample’s mass as it is heated under controlled atmosphere (oxidising or not). Thermal changes of the sample lead to a change in mass (carbon oxidation, crystalline structure change, etc.).

Since zeolites are stable at high temperatures, this study focuses on the oxidation of hydrocarbons under air flow. This allows for the measurement of the catalyst’s coke amount.

Coke quantification was carried out on a SDT Q600 TD/TG unit. Approximately 20 mg of the sample was placed in a platinum crucible on one of the scales (another, empty crucible, serves as a blank on the second scale). It was heated under air flow (100mL.min^{-1}), from ambient temperature to 1173 K (900°C). A plateau was maintained at 303 K (30°C), then with a gradient of 10 K.min^{-1} until 1173 K. This temperature was maintained for 10 minutes before cooldown.

The effluent gas flow was monitored via mass spectrometry (QG Hidden Analytical), measuring H_2O (m/z = 18) and CO_2 (m/z = 44) emissions from the combustion.

III.2.b – Elemental Analysis/atomic absorption spectroscopy (C,H,O)

This technique gives the elemental composition (H, C, O) of the coke deposited on the catalyst.

The sample is placed in a highly oxidative environment, burning off all the coke molecules. Calibration curves for each element are used to assess the sample’s atomic composition, by analysis of the oxidation gases absorption spectra.

In Poitiers, Elemental analysis is carried out with a Flash EA 1112/ Flash 2000 Thermo analyser.

III.2.c – "Coke" extraction and analysis

Coke extraction is carried out by dissolving the zeolite structure and the carbon deposits in an HF solution (aqueous hydrofluoric acid, 40%). The trapped hydrocarbon can then be extracted and analysed.

Boric acid is used to capture the excess fluor ions, and sodium bicarbonate is used to neutralise acids in the resulting mixture. Carbonated compounds are extracted using CH_2Cl_2 (liquid-liquid extraction). Some insoluble hydrocarbons may remain in suspension (typically, heavy polyaromatics); Büchner filtration allows for their recovery (black aggregates). None were found in this study.

The organic liquid phase is then injected into GC-MS (GC-QTOF, Agilent) and GC-FID (Agilent Technologies 7820 A, Agilent technologies HP-5 columns) for identification and quantification.

A blank test for the coke extraction conditions is carried out. Anisole, phenol and o-cresol are injected in GC-MS alone and after having undergone the coke extraction process described above. Then, a mixture of anisole and phenol is injected, alone and after the extraction process. Cresol is a product of the reaction of anisole and phenol in the reaction conditions. If HF triggered the transalkylation reaction described in previous work, or any other, between anisole and phenol, the test would show it. No reaction is found to take place: no fluorination, hydrolysis, etc. took place during the test, and thus the dissolution of the zeolite framework and coke molecules adsorbed therein in HF does not affect the nature of the coke species during extraction (**Annexes**, **Figure V.S1**).

III.3 – Coke characterisation example: Z43 after anisole transformation

Anisole transformation was carried out on Z43 on the experimental setup in **Scheme II.2**., with the experimental conditions in **Table II.5**.

Table II.5: Experimental conditions for zeolite coking & analysis.

m_{Z43} (g)	50
$D_{Anisole}$ (mL.min^{-1})	0.01

D_{N_2} (mL.min^{-1})	100
$W/_F$ (g_{cata}.h.$g_{anisole}^{-1}$)	0.09
T (K)	673
TOS (h)	1

TGA was performed on the blackened spent catalyst, yielding the graph in **Figure II.5**, showing the weight loss of the catalyst, first as water is desorbed, then as coke is burned off. It also shows (blue and black dots) the emission of water and carbon dioxide, detected by the mass spectrometer. After analysis, the powder is white again.

Maxima in water and CO_2 emission correspond to the weight loss previously mentioned. For the second weight loss (combustion, starting at around 523 K, or 250°C), there is no sign of a shoulder, or of a change in the weight loss rate, indicating that the coke is burning uniformly. This indicates that there are no hard and soft coke, but rather the same kind of coke in the catalyst.[7]

During the combustion phase, there is a weight loss, therefore a mass of coke, of 7.7%.

Elemental analysis for this sample reveals a 6.58 wt.% carbon loading, and a 0.85wt.% hydrogen loading. The gap with the coke mass of the TGA is explained by the oxygen content (not accurately measured with Elemental analysis, due to the water content), and the water content seen in **Figure II.5**, (around 2 wt.% in the spent catalyst).

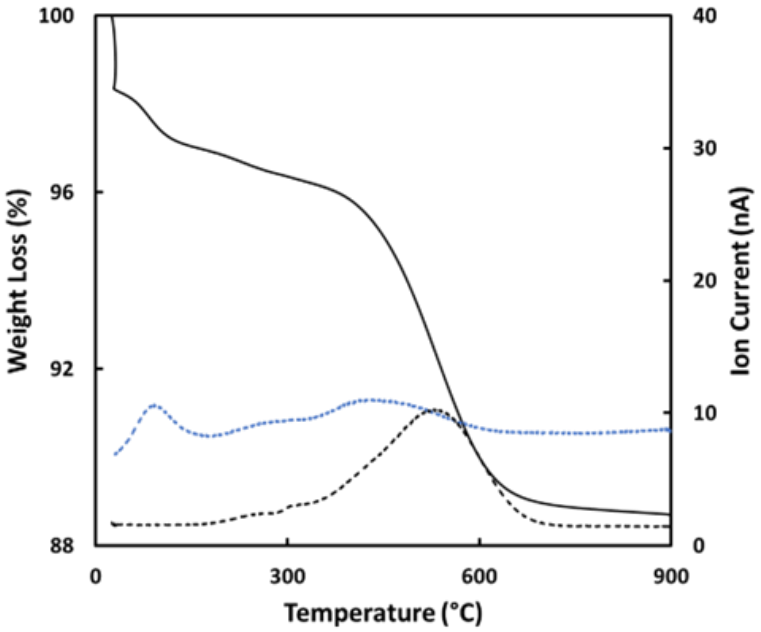

Figure II.5: —TGA analysis of the coked Z43 after 1h of anisole transformation.

- - H_2O and CO_2 emission (from drying and combustion).

After extraction (protocol in **III.2.c**), the soluble coke is injected in GC-MS, resulting in the chromatogram shown in **Figure II.6**. Before 4minutes, nothing can be distinguished from the dichloromethane peak, the solvent used for the liquid-liquid extraction.

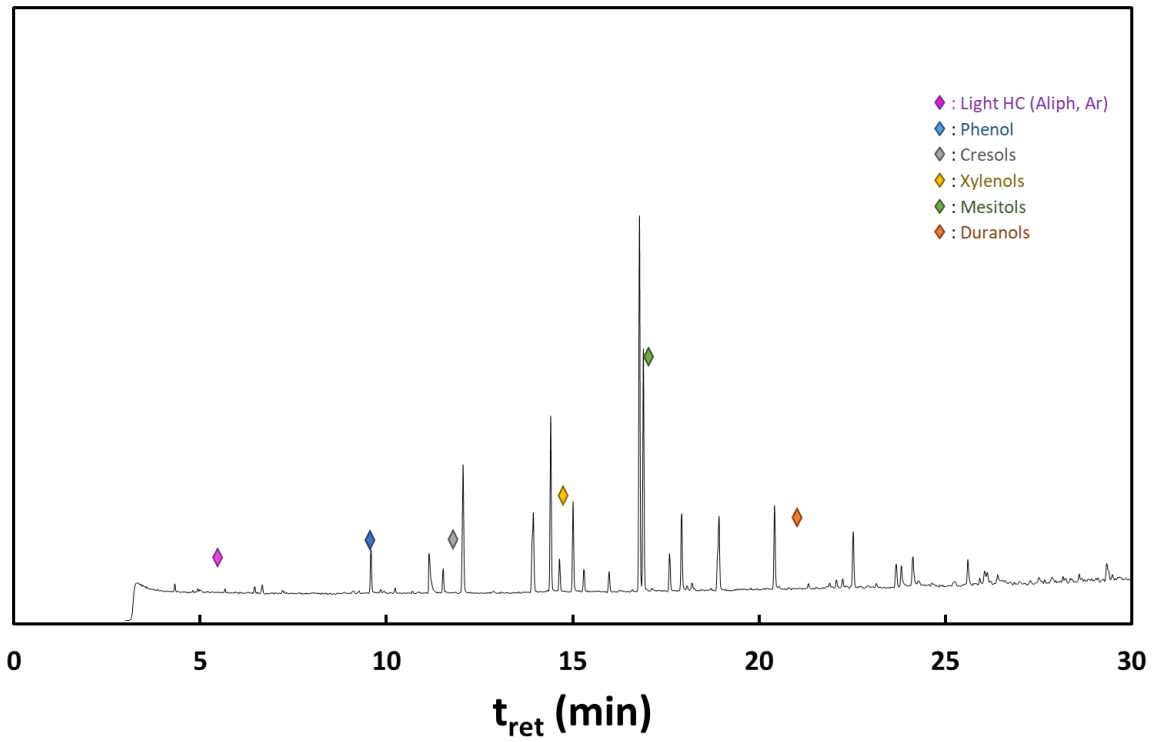

Figure II.6: Chromatogram (GC-MS) of the soluble coke extracted from the spent Z43 after 1h of anisole transformation.

This chromatogram shows the main compounds found in the coke fraction, namely, phenol and its methylated derivatives (up to tetramethyl phenol - Duranol), as well as some lighter and/or monoaromatic compounds. Very few polycyclic compounds were found. (Further exploitation can be found in **Chapters III and V**).

IV – Conclusion

The present work aims to shed light on the activity and stability of zeolite catalysts during anisole conversion and, ultimately, CFP. As such, this chapter has provided the techniques used to assess said activity and stability, from the catalyst's intrinsic (physico-chemical, textural, structural) properties to its state after said reactions. Here were also provided the experimental setups and conditions of both reactions, and a rough example of data exploitation for one of the catalysts in the study (Z43).

Based on these considerations, the next chapter highlights activity, stability and coke and products shape selectivity during anisole transformation for Z43. It explores the reaction mechanism of anisole disproportionation, the reaction's yields in products and coke, as well as the deactivation mode and kinetics of the catalyst.

References:

[1] K.S.W. Sing, Reporting physisorption data for gas/solid systems with special reference to the determination of surface area and porosity (Recommendations 1984), Pure and Applied Chemistry 57 (1985) 603–619. https://doi.org/10.1351/pac198557040603.

[2] E. Selli, L. Forni, Comparison between the surface acidity of solid catalysts determined by TPD and FTIR analysis of pre-adsorbed pyridine, Microporous and Mesoporous Materials 31 (1999) 129–140. https://doi.org/10.1016/S1387-1811(99)00063-3.

[3] M. Guisnet, P. Ayrault, C. Coutanceau, M. Fernanda Alvarez, J. Datka, Acid properties of dealuminated beta zeolites studied by IR spectroscopy, Faraday Trans. 93 (1997) 1661–1665. https://doi.org/10.1039/a607609b.

[4] C.J.H. Jacobsen, C. Madsen, T.V.W. Janssens, H.J. Jakobsen, J. Skibsted, Zeolites by con®ned space synthesis ± characterization of the acid sites in nanosized ZSM-5 by ammonia desorption and 27Al/29Si-MAS NMR spectroscopy, Microporous and Mesoporous Materials (2000).

[5] D.S.A. Silva, W.N. Castelblanco, D.H. Piva, V. De Macedo, K.T.G. Carvalho, E.A. Urquieta-González, Tuning the Brønsted and Lewis acid nature in HZSM-5 zeolites by the generation of intracrystalline mesoporosity—Catalytic behavior for the acylation of anisole, Molecular Catalysis 492 (2020) 111026. https://doi.org/10.1016/j.mcat.2020.111026.

[6] M.J. Rice, A.K. Chakraborty, A.T. Bell, Al Next Nearest Neighbor, Ring Occupation, and Proximity Statistics in ZSM-5, Journal of Catalysis 186 (1999) 222–227. https://doi.org/10.1006/jcat.1999.2544.

[7] A. Beuque, H. Hao, E. Berrier, N. Batalha, A. Sachse, J.-F. Paul, L. Pinard, How do the products in methane dehydroaromatization impact the distinct stages of the reaction?, (2022).

[8] V. Valtchev, J.-P. Gilson, J.D. Rimer, J.W. Steed, Zeolite Crystal Engineering, Crystal Growth & Design (2023). https://doi.org/10.1021/acs.cgd.3c01015.

[9] A. Bonnin, J.-D. Comparot, Y. Pouilloux, V. Coupard, D. Uzio, L. Pinard, Mechanisms of aromatization of dilute ethylene on HZSM-5 and on Zn/HZSM-5 catalysts, Applied Catalysis A: General 611 (2021) 117974. https://doi.org/10.1016/j.apcata.2020.117974.

[10] T. Prasomsri, A.T. To, S. Crossley, W.E. Alvarez, D.E. Resasco, Catalytic conversion of anisole over HY and HZSM-5 zeolites in the presence of different hydrocarbon mixtures, Applied Catalysis B: Environmental (2011) S0926337311002347. https://doi.org/10.1016/j.apcatb.2011.05.026.

[11] X. Zhu, R.G. Mallinson, D.E. Resasco, Role of transalkylation reactions in the conversion of anisole over HZSM-5, Applied Catalysis A: General 379 (2010) 172–181. https://doi.org/10.1016/j.apcata.2010.03.018.

[12] L.Y. Jia, M. Raad, S. Hamieh, J. Toufaily, T. Hamieh, M. Bettahar, G. Mauviel, M. Tarrighi, L. Pinard, A. Dufour, Catalytic fast pyrolysis of biomass : superior selectivity of hierarchical zeolite to aromatics, Green Chem. 19 (2017) 5442–5459. https://doi.org/10.1039/C7GC02309J.

[13] M. Guisnet, P. Magnoux, U. Cnrs, R. Pineau, P. Ceder, Coking and Deactivation of Zeolites Influence of the Pore Structure, (n.d.) 27.

[14] M. Guisnet, P. Magnoux, Organic chemistry of coke formation, Applied Catalysis A: General 212 (2001) 83–96. https://doi.org/10.1016/S0926-860X(00)00845-0.

Chapitre III

Sélectivité de forme envers les produits et le coke lors de la dismutation de l'anisole sur zéolithe H-ZSM-5

Le chapitre suivant est publié dans la revue ***Applied Catalysis A : General*** sous la référence suivante :

N. Pichot, J.W. Hounfodji, M. Badawi, V. Valtchev, S. Mintova, J.-P. Gilson, A. Dufour, L. Pinard, Products and coke shape-selectivity during anisole disproportionation over HZSM-5, Applied Catalysis A: General. 665 (2023) 119352. https://doi.org/10.1016/j.apcata.2023.119352

Abstract

La conversion de l'anisole sur zéolithe MFI (Si/Al = 43) à pression atmosphérique et 673 K est une réaction modèle pour l'upgrading des bio-huiles de pyrolyse catalytique de biomass (CFP – Catalytic Fast Pyrolysis). L'activité catalytique et la sélectivité sont évaluées expérimentalement, tandis que la désactivation est évaluée expérimentalement et par calculs théoriques en DFT. La dismutation de l'anisole est une réaction de type alkylation de Friedel-Crafts entre deux molécules d'anisole. Les réactions consécutives produisent du phénol, des crésols et des xylénols comme produits primaire, secondaires et tertiaires respectivement. Les effets mésomères des groupes méthoxy et hydroxyle, additionnés à la sélectivité de forme de la zéolithe, résultent en une forte sélectivité pour le p-méthylanisole, le o-crésol et le 2,4-xylénol. La formation de coke consiste exclusivement de méthylphénols contenant 0 à 4 groupements méthyl. Leur rétention dans la zéolithe est due aux effets stériques pour les plus gros, et à une forte adsorption sur les sites acides pour les autres, ce qui est confirmé par les calculs en DFT. La désactivation de la MFI est provoquée par un « fouling » des micropores, plutôt que par l'empoisonnement des sites actifs.

Mots clés : Anisole, désactivation, sélectivité de forme, zéoltihe.

I – Introduction

Petrochemicals are pervasive in our daily lives as plastics, packaging, clothing, digital devices, medical equipment, tires… and provide substantial benefits to society, including a growing number of applications in various cutting-edge, clean technologies critical to sustainable energy systems. They are set to account for more than a third of the growth in oil demand by 2030 and nearly half by 2050. At the same time, transportation fuels demand should decrease, due to the combined effects of better fuel economy, increasing use of public transport, alternative fuels, and electrification. Hence, the landscape for petrochemical, oil, and gas industries is evolving to develop more "high-value chemicals" (HVCs), such as aromatics. [1–5]

The majority of BTX (Benzene, Toluene, Xylene, etc.) is currently provided by catalytic reforming of desulfurized naphtha and non-catalytic steam cracking of various oil cuts. The catalytic fast pyrolysis (CFP) of biomass represents an interesting route to green aromatics and olefins by mimicking the fluid catalytic cracking of crude oil. [6–8] The pyrolysis is conducted in a dual fluidized bed on a zeolite catalyst; the latter shifts the chemical composition of bio-oils to petroleum-compatible products. The volatile oxygenates formed by biomass pyrolysis diffuse within the catalyst particles and contact the catalytic acid sites to form the targeted products (aromatics, olefins) but also coke and gas (mainly CO, CO_2)[9]. Despite the growing interest in biomass CFP, this process is still in its infancy compared with other thermochemical technologies (gasification or combustion). Some technologies are close to commercialization (Anellotech/Axens, BioBTX, RTI International [10], …), but require the development of more stable catalysts with increased BTX selectivity. [11,12]

Indeed, the most important economic and technical problem of this emerging process remains the deactivation of the zeolite catalyst. [13-16] This deactivation mostly occurs by coke deposition, i.e. polyaromatic hydrocarbons (PAH). Jia et al. studied the molecular composition of coke deposited after oak CFP. [6] After mineralization of the zeolitic framework with hydrofluoric acid, and recovery of the molecules released by a liquid-liquid extraction with dichloromethane, two fractions are obtained: soluble and insoluble. They showed that the soluble portion consisted mainly of mono and bicyclic aromatics (alkylbenzenes and alkylnaphtalenes). In contrast, the insoluble portion

contained mostly polyaromatics, some oxygenated compounds and molar masses up to 1000 $g.mol^{-1}$. Coke is either found in the micropores and mesopores (internal coke) or in a less confined environment (external coke). The latter two have a less detrimental effect than the first one. [6] Therefore, mastering catalyst stability is essential to control selectivity and activity. Therefore, there is a strong incentive to understand the mechanisms leading to any loss in activity and/or selectivity, as well as find preventive measures and regenerative solutions to develop cheaper and cleaner processes. [13–15] The catalyst regeneration has been partially studied by Prasomsri et *al.*, who found a recovery of activity for an HY zeolite flushed with tetralin: the H-donor solvent, when flushed alone, would help to regenerate some of the active site; when anisole is co-fed tetralin, the initial conversion is fully recovered. [16]

Biomass CFP is modelled like the well-established FCC (Fluidized Catalytic Cracking) process, to upgrade otherwise unusable heavy oil fractions. [17–19] CFP aims to produce a similar slate, by breaking down lignocellulosic compounds. Some differences exist between the two processes, the first and main being that CFP feedstock contains lots of oxygen, which affects, of course, the reactions involved in the upgrading, but also could affect the deactivation of the catalyst, notably the nature of coke deposition in the channels. Graça et *al.* showed that co-feeding phenol to FCC feedstock further hindered the activity of MFI zeolite, by phenol adsorption on active sites; other effects occur, such as an increase in coke amount, as well as composition (aromaticity, size). [13,20]

Among all the studied catalysts, H-ZSM-5 zeolite has shown interesting selectivity in deoxygenated aromatics due to its moderate pore openings, internal pore space and steric hindrance [11,12,21–24] but a lot of coke is produced. It can poison the active sites (“poisoning”) or block their access. Pore blocking is more harmful than poisoning, since one coke molecule can block access to several acid sites. Tri-dimensional zeolites (such as the H-ZSM-5 type MFI) are more resistant to coking than mono-dimensional zeolite (e.g., MOR or ERI), because more options to enter and exit the porosity are offered to reactants and products, respectively. [25]

Lignocellulosic biomass, when pyrolyzed, releases abundant oxygenates in methoxy functional groups (guaiacol, syringol, and derivatives). [9,22] Since the methoxy group is its only functional group, anisole (or methoxybenzene) is a logical model compound to investigate the reactivity of methoxy-substituted compounds present in the gas phase during the fast pyrolysis of lignin. [26,27]

The present work aims to answer the following questions:

How do hydroxyl and methoxy groups affect the catalyst's activity, selectivity, and deactivation?

How does catalyst deactivation proceed during anisole conversion (pore blocking, active site poisoning, ...)?

An experimental approach coupled with DFT calculations is used to probe the three features of a catalyst, namely activity, selectivity, and stability. In particular, the effect of time on stream (reaction time, ToS, h) and contact time (W/F, $g_{cata}.h.g_{feed}^{-1}$) on catalyst activity and product selectivity are assessed as well as deactivation by coke deposition. For the latter, coke composition, its kinetics of formation and affinity for the active sites will receive a particular attention.

II – Experimental

II.1 – Catalyst and reagent

The ZSM-5 (Si/Al = 43) zeolite is provided by Zeolyst, originally in NH_4^+ form. Calcination is performed to obtain the protonic form under N_2 (P_{atm}, 100 $mL.min^{-1}$) at 373 K for an hour (5 $K.min^{-1}$ from ambient) for water removal, then under air (P_{atm}, 100 $mL.min^{-1}$) at 823 K for 6 hours (10 $K.min^{-1}$). The micropore volume measured by N_2-physisorption at 77 K and the concentration of Brønsted acid sites probed by pyridine thermodesorption at 423 K are 0.164 $cm^3.g^{-1}$ and 281 $\mu mol.g^{-1}$, respectively. Anisole (>99%) from Sigma Aldrich is used as reagent.

II.2 – Catalytic tests

(Full protocol in **Chapter II** part **II.1**)

Conversion and molar yields are calculated with **(Eq. III.1)** and **(Eq. III.2)**.

$$\text{X (mol\%)} = \left(1 - \frac{\frac{A_{Anisole}}{7}}{\frac{A_{tot}}{\bar{n}_{Ctot}}}\right) * 100 \qquad \textbf{(Eq. III.1)}$$

where $A_{Anisole}$ the area of the anisole peak (GC-FID); 7 the number of carbon atoms in anisole; A_{tot} the sum of all peak area in the chromatogram; $\bar{n}_C$ the mean number of carbon atoms per molecule in the product fraction.

$$Y_i \text{ (mol\%)} = \left(\frac{\frac{A_i}{n_{Ci}}}{\sum_i\left(\frac{A_i}{n_{Ci}}\right)}\right) * 100 \qquad \textbf{(Eq. III.2)}$$

where A_i the area of the target product's peak; n_{Ci} the number of carbon atoms in the target product.

For all experiments, the molar yield of methane and light alkanes (cracking products) is negligible (< 0.5%). The carbon balance is higher than 95%.

Once the anisole injection is finished, the catalyst undergoes stripping under N_2 for 15 minutes at 673 K. The reactor is removed immediately from the oven and quenched under air flow.

II.3 – Spent catalyst characterization

Nitrogen physisorption (TriFlex, **Chapter II** part **I.2.e**).

Pyridine adsorption followed by infrared (IR) spectroscopy (Nicolet Magna FTIR iS50 spectrometer, **Chapter II** part **I.2.f**) [28,29].

Molar extinction coefficients are previously determined to be respectively 1.13 cm.µmol^{-1} and 1.28 cm.µmol^{-1} for Brønsted and Lewis acidities. [29]

Coke content by TDA-TGA (SDT Q600, **Chapter II** part **III.2.a**)

Carbon, hydrogen, and oxygen contents in coke are assessed using elemental analysis by atomic absorption spectroscopy (Flash EA 1112/Flash 2000 Thermo, **Chapter II** part **III.2.b**)

Coke extraction, identification and quantification (**Chapter II** part **III.2.c**) [30].

II.4 – Atomistic simulations

DFT calculations are performed using the Vienna Ab initio Simulation Package (VASP) [31]. The semi-local exchange-correlation functional of Perdew-Burke-Ernzrhof (PBE) in the general gradient approximation (GGA) is used. [32] The electron-ion interactions are described using the Projected Augmented Wave (PAW) method, with a cut-off energy set to 450 eV. [33] Kohn-Sham equations are solved self-consistently with a convergence criterion of 10^{-6} eV. The ionic relaxation is systematically conducted until the forces applied on each atom are smaller than 0.02 eV.A^{-1}. Considering the large cell size, the Brillouin zone integration large is performed using the Γ-point only. Furthermore, to predict accurately the adsorption energies of the different molecules considered, dispersion interactions are accounted using the D2 correction. [34,35]

The adsorption energies of the different molecules in the zeolite, ΔE_{ads}, are computed using the total energies of the bare zeolite $E_{zeolite}$, of the single molecule in the gas phase E_X, and of the molecule adsorbed in the zeolite $E_{zeolite-X}$, as follows **(Eq. III.3)**:

$$\Delta E_{ads} = E_{(zeolite-X)} - E_{(zeolite)} - E_{(X)} \quad \textbf{(Eq. III.3)}$$

In order to understand the mechanisms that govern adsorption, knowledge of the interactions involved in the adsorption process is very important. They are classified into two categories: van der Waals (more precisely London, or so-called dispersion related to the polarizability of the molecules) forces and electrostatic forces.

The contribution of London dispersion interactions, ΔE_{disp}, to the total interaction energy, is calculated as follows **(Eq. III.4)**:

$$\Delta E_{disp} = E_{disp\ (zeolite-X)} - E_{disp\ (zeolite)} - E_{disp\ (X)} \quad \textbf{(Eq. III.4)}$$

where the energies considered are, for each term, the contribution of dispersive interaction to the total energy.

III – Results and Discussion

III.1 – Activity and selectivity of H-ZSM-5 (43) catalyst

The transformation of anisole (methoxybenzene) takes place at 673 K on the H-ZSM-5(43) catalyst. **Figure III.1a** shows the evolution of anisole conversion as a function of time-on-stream (ToS), at three contact times ranging from 0.04 to 0.17 $g_{cata}.h.g_{feed}^{-1}$. As expected, the longer the contact time, the higher the deactivation rate. **Figure III.1b** displays the test of the first-order rate equation (i.e. $|-\ln(1-X_t)|$ vs W/F) at different ToS. Straight lines through the origin are obtained regardless of ToS, indicating that the bimolecular transformation of anisole follows an apparent first order reaction. The time evolution of the kinetic rate ($k_{anisole}$) is shown in **Figure III.1c**. $k_{anisole}$ ($g_{feed}.h^{-1}.g_{cata}^{-1}$) evolves according to an exponential decay function with a horizontal asymptote emerging after only a few minutes of operation (**Eq. III.5**).

$$k_{anisole} = 11.2\ e^{-11.1t} + 3.23 \quad \textbf{(Eq. III.5)}$$

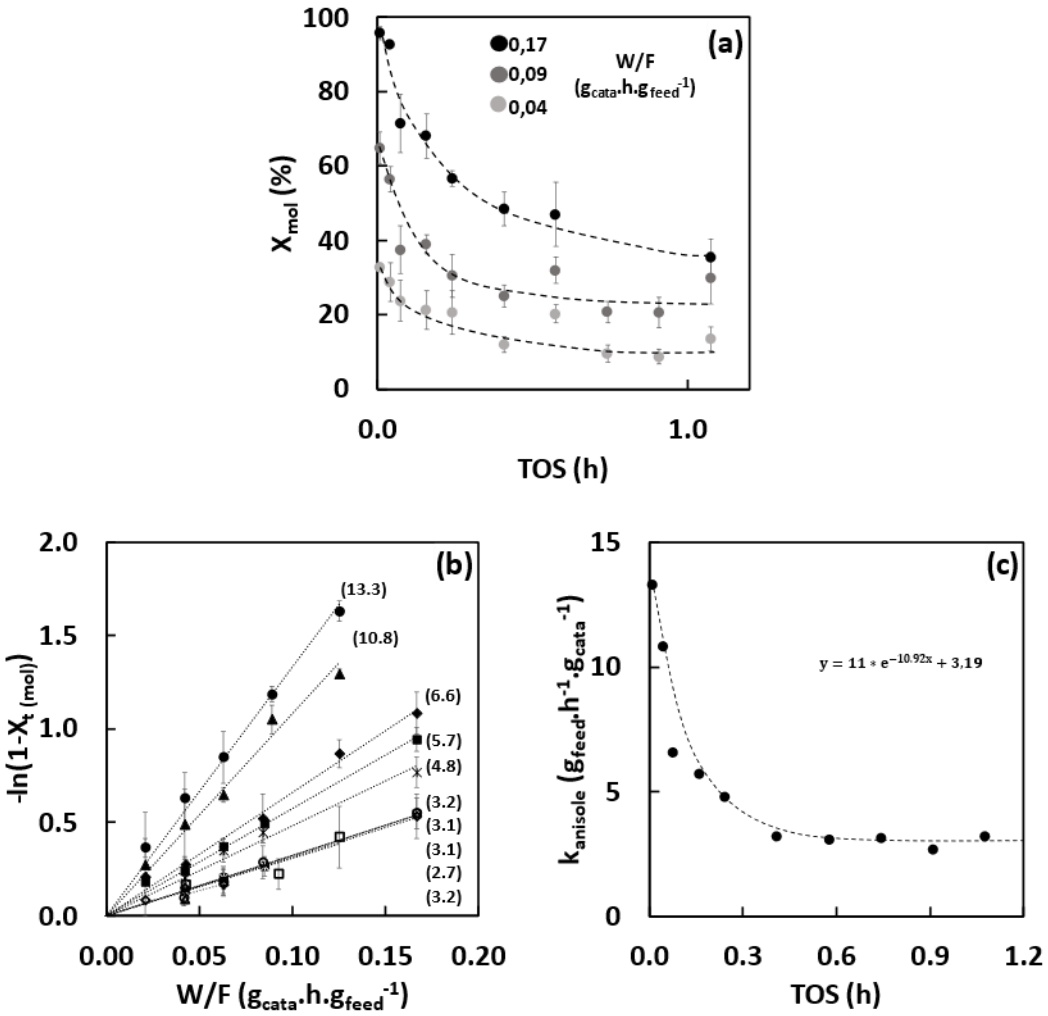

Figure III.1*:* **(a)**: Anisole conversion as a function of time-on-stream obtained at different W/F and at 673 K **(b)**: Test for the first-order rate equation at various ToS (h) **(c)**: Time evolution of $k_{anisole}$.
Each data point corresponds to 2 to 3 experiments.

Two distinct regimes occur: a fast deactivation followed by a steady state, suggesting that the catalyst no longer undergoes any change, at least with respect to the rate of anisole conversion. Notably, the deactivation remains relatively low compared to the FCC catalyst (order of magnitude of a few seconds [36,37]).

Anisole transformation leads to phenol (**Ph**), methylanisoles (**MA**), cresols (**Cr**), xylenols (**Xol**), and aromatics (**Ar**), such as benzene, toluene, xylene. **Figure III.2** shows the evolution of the formation of these products for different ToS and various contact times. The quasi-absence of methane in the products means that the cleavage of alkyl aryl ethers does not occur, as mentioned by Guisnet and coll. [38,39]

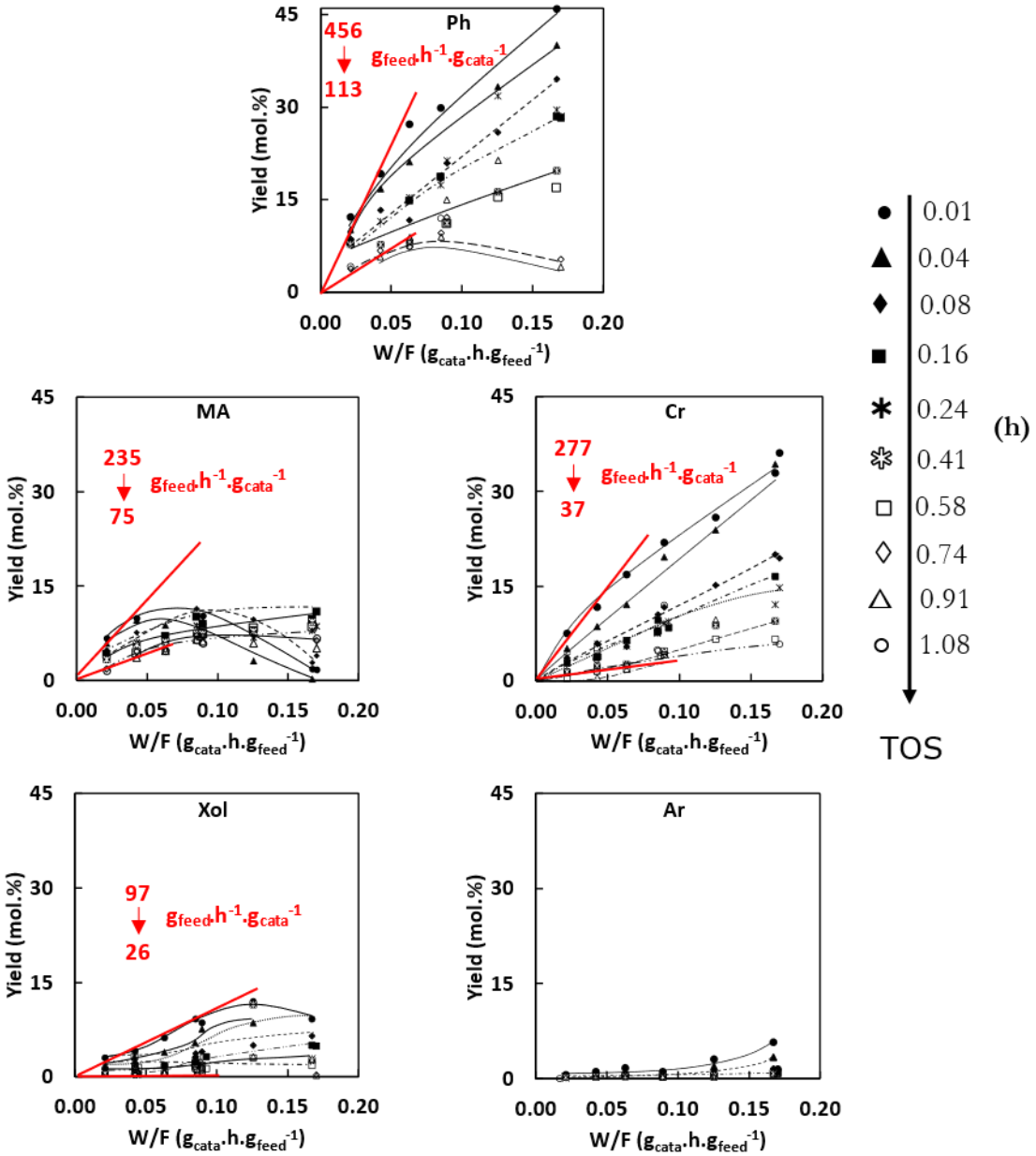

Figure III.2: Mass yields for phenol (Ph), methylanisoles (MA), cresols (Cr), xylenols (Xol) and aromatics (Ar) as a function of contact time and at different time-on-stream. *(Lines are only drawn to guide the eye).*

On the fresh catalyst, phenol and cresol are the main products and their mass yields are proportional to contact time. Upon catalyst deactivation, the cresols yield decreases but remains proportional to W/F, whereas phenol yields go through a maximum. On the fresh catalyst and at low contact time, the yield of methylanisoles is also proportional to contact time and is in the same proportions as those of phenol and cresols. Indeed, the initial formation rates of phenol, cresols, and methylanisoles are in the same range of 456, 235, and 277 $g_{feed}.h^{-1}.\ g_{cata}^{-1}$, respectively. The successive transformations of methylanisole

appear only at high contact time on the fresh or slightly deactivated catalyst. As for the other oxygenated products, the yield of xylenols is also proportional to contact time, but with a kinetic rate cut threefold (97 $g_{feed}.h^{-1}.g_{cata}^{-1}$). Deactivation is detrimental to this formation. The yield of aromatics is low even at high contact time, and almost zero on the deactivated catalyst. All these evolutions agree with earlier observation by Zhu et al. [40]

These variations in selectivity could result from a conversion effect, rather than from deactivation with ToS. **Figure III.3** illustrates this assertion by plotting product yields as a function of anisole conversion over both fresh and deactivated catalysts.

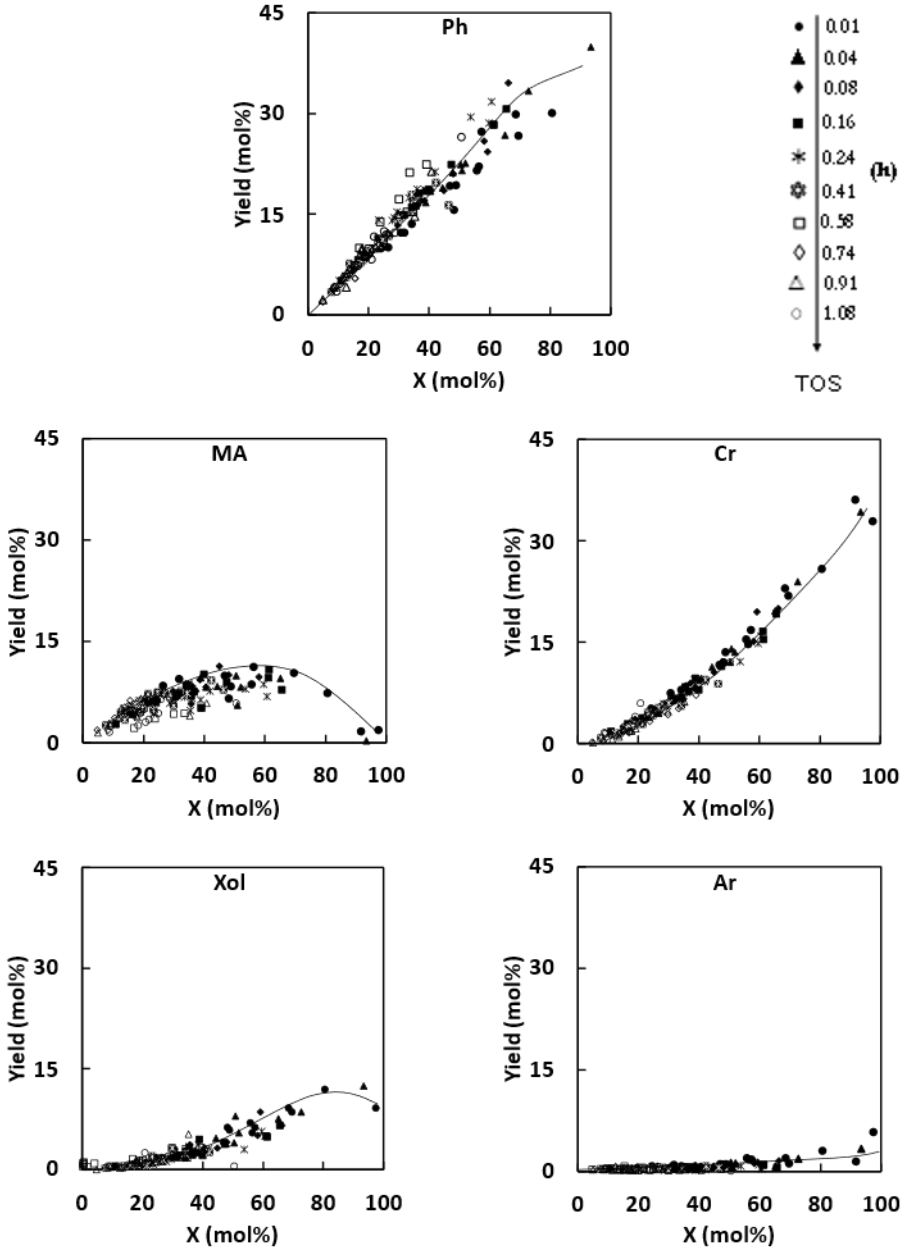

Figure III.3: Mass yields into phenol (Ph), methylanisoles (MA), cresols (Cr), xylenols (Xol) and aromatics (Ar) as a function of anisole conversion (%). (*Lines are only drawn to guide the eye*).

Product yields depend more on anisole conversion than on the degree of catalyst deactivation. Phenol and methylanisoles are the primary products of the reaction. Cresols are secondary product that is formed just after a low conversion of anisole (< 5 %) and xylenols are tertiary products that appears when the conversion is higher (> 20 %). As for aromatics, they are minor products formed at high conversion (> 40%).

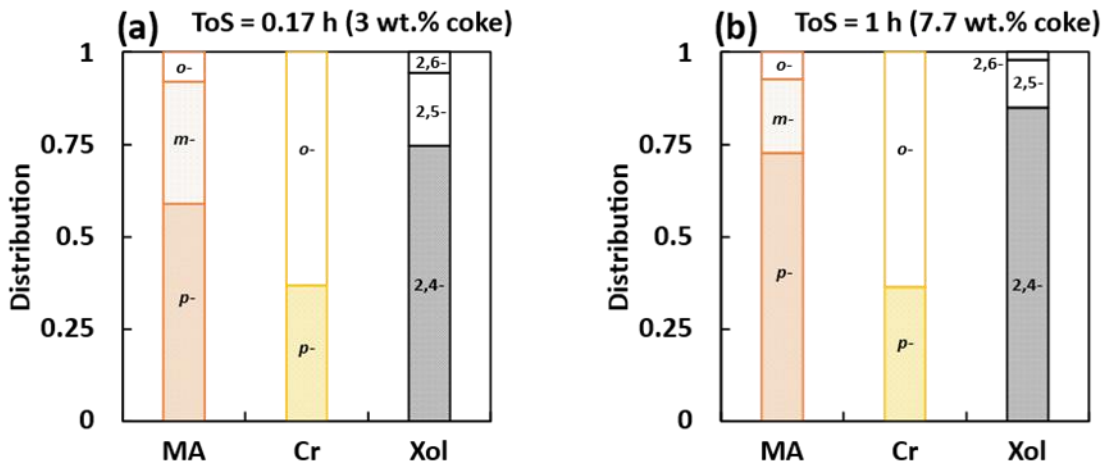

Figure III.4: Distribution of the desorbed isomers of methylanisoles (MA), cresols (Cr), and xylenols (Xol) at different ToS.

Figure III.4 compares the distribution of MA, Cr, and Xol isomers at different stages of catalyst deactivation. Their distribution changes slightly as a function of coke deposit and is noticeably different from the thermodynamic equilibrium. [39,40] For methylanisoles, while the meta position should be favoured, the main isomer is the *p*-MA. The methoxy function acts as an ortho/para directing group on the aromatic cycle (due to its +M mesomeric effect). [41] Among the 6 possible xylenol isomers, 2,4-xylenol with one methyl in ortho position, and another on in para of the hydroxyl group, is the most abundant. The additional shape selectivity of the MFI framework promotes the formation of para isomers. The higher the coke content, the higher the para selectivity, due to the neutralization of the non-selective outer acid sites, as already observed for xylenes[42].

The hydroxyl group has a stronger electron donation effect (+M) than the methoxy group, leading to higher selectivities for cresol's para and ortho isomers. Moreover, the impact of product shape selectivity on methylphenols is lesser than with methylanisoles, because they are smaller and therefore diffuse more rapidly.

Xylenol has six isomers, but the resonance effect of the hydroxyl function combined with the "product shape selectivity" of the zeolite results in high 2,4-xylenol (o,p-) selectivity (> 85%), mainly on the deactivated catalyst.

The disproportionation of anisole is a Friedel-Crafts-like alkylation between two anisole molecules. The reaction begins with the formation of an

oxonium ion by protonation of an anisole molecule on the BAS (step ①). This oxonium ion, with its strong attractor inductive effect, allows a π electron pair on another anisole (in the gas phase) aromatic ring to reach the carbon of the methoxy group, leading to the O-C bond cleavage (step ②). This produces phenol, as well as an arenium ion. The latter is converted to methylanisole by regeneration of the BAS (step ③). The methoxy group is an ortho/para-directing group, thus the formation of meta-methylanisole is greatly limited (para>ortho for steric hindrance reasons).

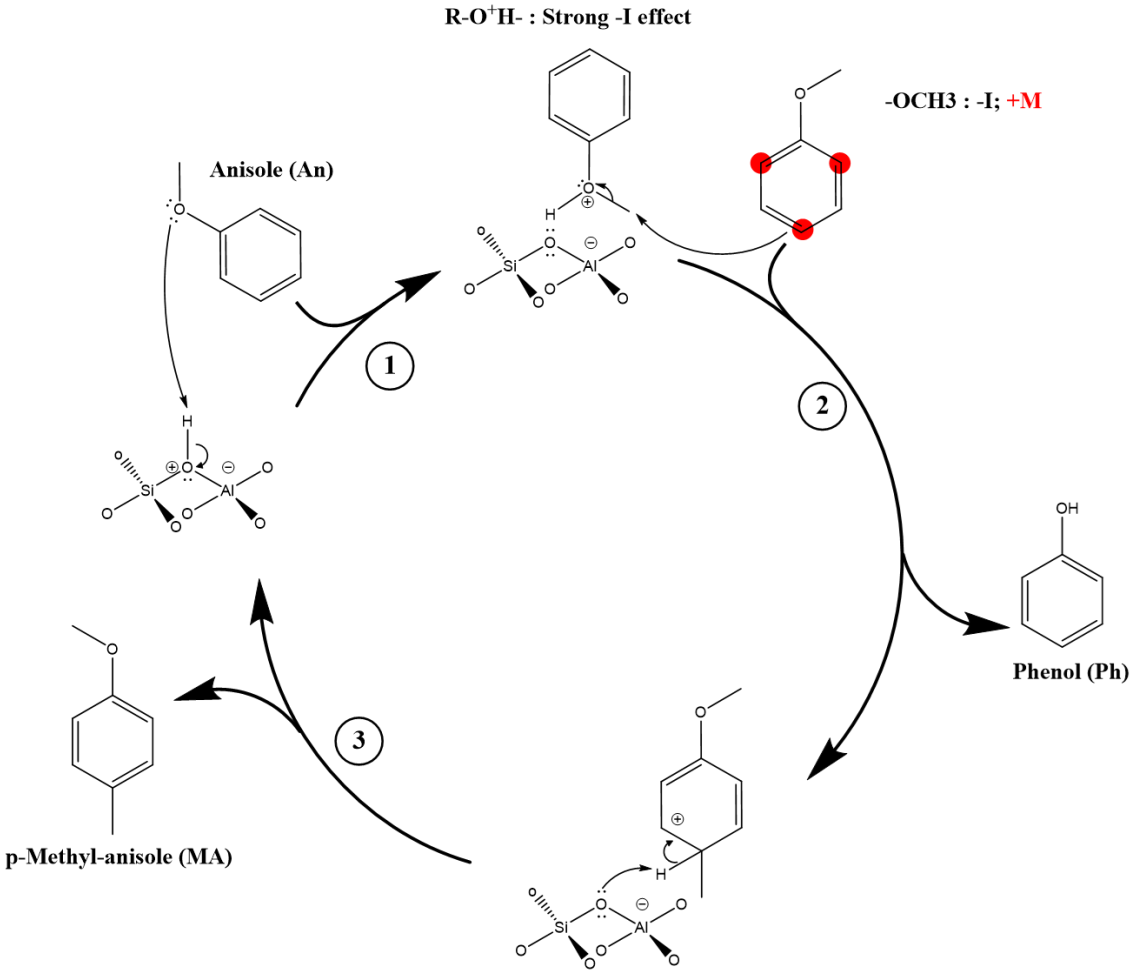

Scheme III.1: Anisole disproportionation on zeolite: a Friedel-Crafts-like reaction mechanism.

Anisole disproportionation leads to the formation of *p*-methylanisole and phenol (primary products) which can comproportionate to *p*- and *o*- cresols (secondary product). The latter can also result from a transalkylation reaction between anisole and phenol. A transalkylation reaction is also possible between anisole and the secondary product, yielding mainly 2,4-xylenol (o-,p-).

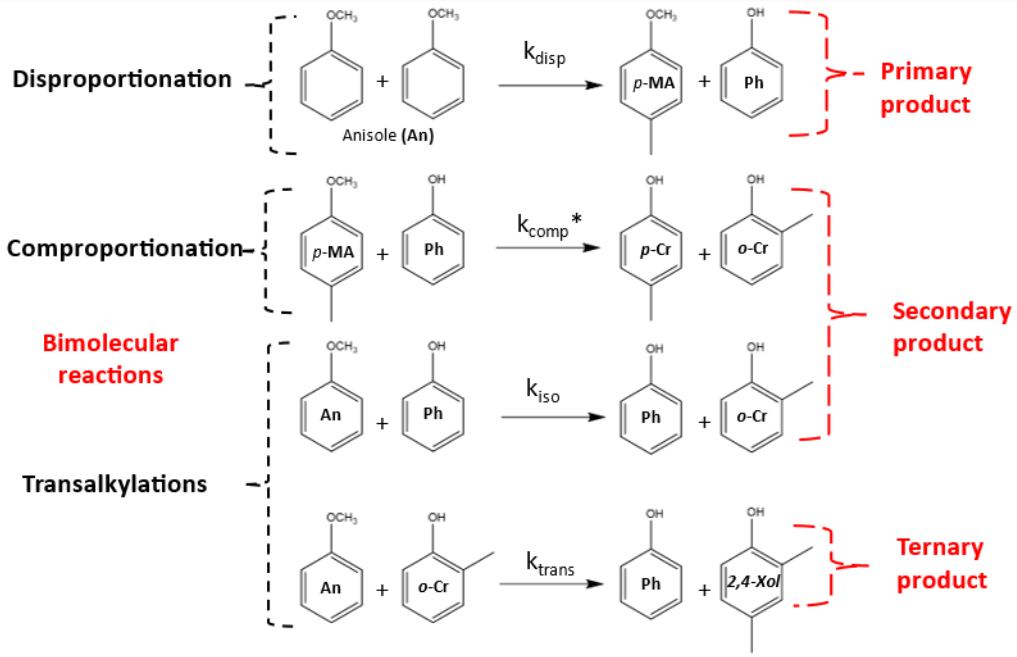

Scheme III.2: Bimolecular reactions involved in anisole transformation.

III.2 – Coke composition

The main issue for anisole transformation, as for CFP and in general FCC, is catalyst deactivation by coke formation in zeolite micropores and/or its deposition on external surface. Prior to coke analysis, loosely adsorbed reaction products are first removed by nitrogen stripping for 15 min.

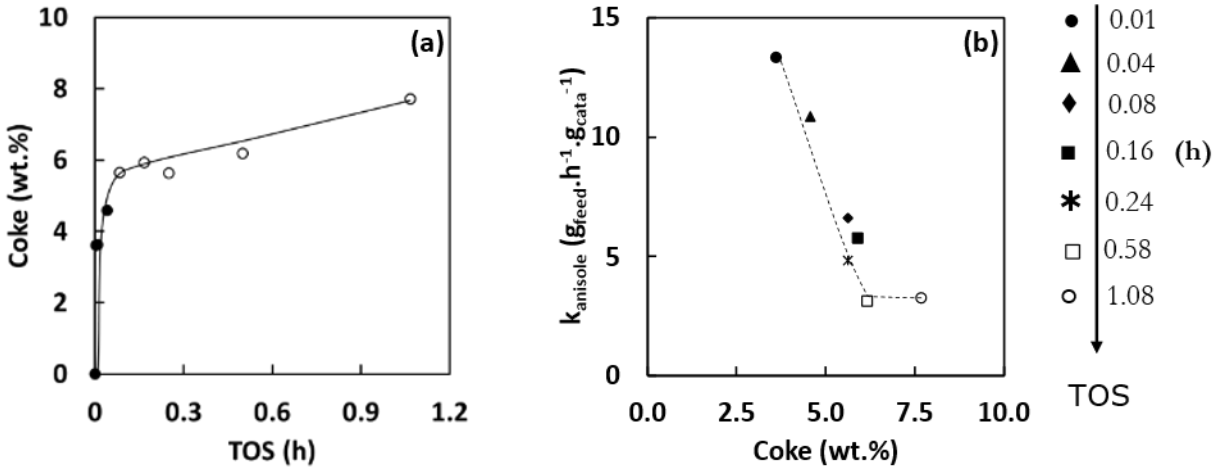

Figure III.5: **(a)**: Coke content (wt.%) as a function of time-on-stream **(b)**: Kinetic rate of anisole transformation as a function of coke content.

Figure III.5a shows the time evolution of coke content with a W/F of 0.13 $g_{cata}.h\ .\ g_{feed}^{-1}$. A fast coke build-up (6 wt.% within 3 minutes) is followed by a slower step. The kinetic rate constant of anisole transformation is first inversely proportional to coke content (**Figure III.5b**) and then reaches a plateau at a higher amount (> 7 wt.%). The mode of deactivation is thus directly related to the amount of coke.

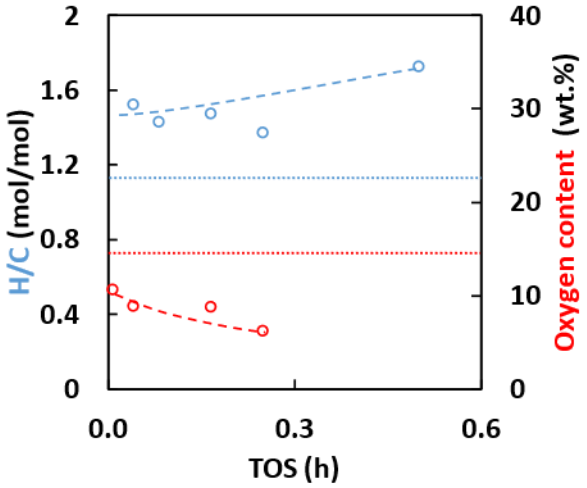

Figure III.6: Time evolution of the elemental composition of the coke: hydrogen to carbon molar ratio and oxygen weight content. (Parallel dotted lines: H/C ratio and oxygen content of anisole).

Figure III.6 shows the hydrogen/carbon ratio and oxygen content of coke as a function of ToS. The first coke molecules trapped in the zeolite micropores have higher H/C ratios than the reactant, it then increases with ToS, while concurrently, the oxygen content is lower than on the reactant and decreases with ToS. As olefins, xylene, benzene, have H/C molar ratios of 2, 1.25 and 1, respectively, this suggests that the coke molecules trapped in the zeolite micropores are composed of a single-ring aromatic with one hydroxyl group and/or methyl groups. These coke molecules originate from the successive transalkylation of anisole and their resulting products.

The chemical composition of coke is obtained after mineralization of the zeolite framework with concentrated hydrofluoric acid, followed by liquid-liquid extraction with dichloromethane. All coke molecules recovered are soluble in CH_2Cl_2, even at high coke content. The hydrofluoric acid used for the dissolution of the zeolite framework is a weak acid, used mainly in organic chemistry for the

fluorination of organic molecules [43–45]. The reactivity of HF on oxygenated molecules is low, both for fluorination and alcohol dehydration. In addition, the extraction is performed at room temperature and for a short period of time [47], thus avoiding any side reactions.

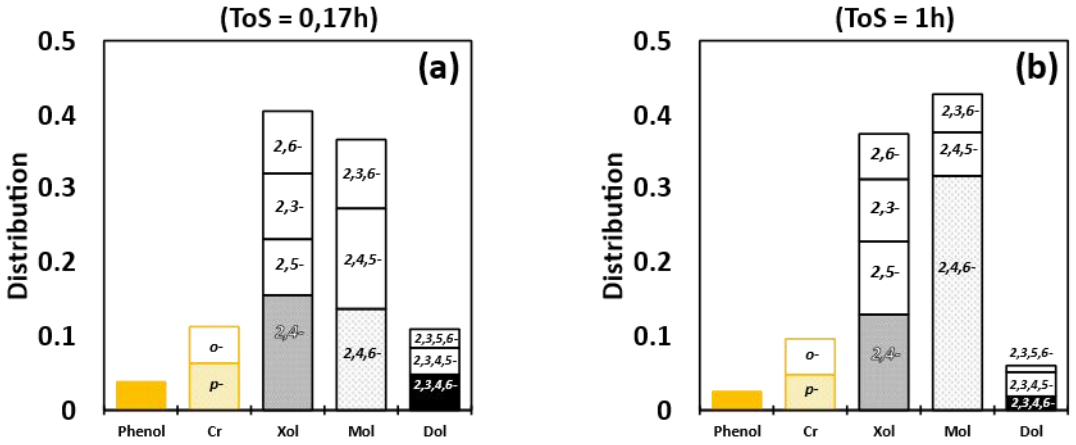

***Figure III.7**:* Distribution of the coke components (isomers and families) at ToS of 0.17 h **(a)** and 1 h **(b)**.

Figure III.7 compares the composition of the coke extracted after short and longer ToS. Regardless of ToS, the coke consists almost exclusively of phenolic rings substituted with 0 to 4 methyl groups. There are no ethers or polyaromatics, even after 1 h. The phenolic compounds appear to hinder the growth mechanisms of "traditional" coke. As coking is a shape-selective process [46], the size and shape of the H-ZSM-5 channel intersections determine the shape and maximum size of the coke molecules trapped in its microporosity. Irrespective of the reactant, (alkanes [47], olefins [48], aromatics, and alcohols [49]), the coke trapped at the channels intersection is composed of methylpyrenes [50]. Coke formation progresses by successive expansions and contractions of the methylated aromatic ring with the growth of a side carbon chain (Sullivan mechanism). When the side carbon chain contains 5 carbon atoms, an auto-alkylation occurs and, after hydride transfer, produces a new aromatic ring. However, with anisole dismutation, coke consists only of phenolic compounds. The absence of polyaromatic compounds suggests that the hydroxyl group hinders the expansion/contraction mechanism, caused by a mesomeric effect. Only successive transalkylation reactions take place and lead mainly to the formation of mesitol (Mol: trimethylphenol) and to a lesser extent durenol (Dol:

tetramethylphenol) (**Figure III.7**). Their retention is obviously due to steric constraints.

Among the coke molecules, some reaction products such as phenol, cresols, and xylenols are found, despite N_2 stripping. However, the isomer distribution differs between desorbed and trapped molecules. While the desorbed xylenol is mainly the 2,4- isomer (**Figure III.4**), the trapped molecules are composed of 4 of the six possible isomers: 2,3-, 2,4-, 2,5- and 2,6-. 2,4-xylenol remains the main isomer but in a lower proportion. The presence of reaction products among the coke molecules means that their retention is not due to steric constraints but to chemical retention. Desorption and retention of the same molecule demonstrate heterogeneity in the strength of the adsorption sites, *i.e.,* the Brønsted acid sites (BAS). Strong BAS would retain a reactant while weaker ones are active in the Friedel-Craft reaction.

III.3 – Computed adsorption energies of phenolic compounds

Among the 12 distinguishable T sites in H-ZSM-5 zeolite, T11 (equivalent to T5) and T12 (equivalent to T6) were selected as the most representative T sites**.** [34,35] **Table III.1** compares the adsorption energies, ΔE_{ads}, and the contribution of London dispersion interactions, $\Delta E_{disp,}$ on T11 and T12 aluminium atoms of some selected molecules. All the adsorption energies are negative, implying their exothermic nature.

Table III.1: Comparison of adsorption energies and the contribution of London dispersion interaction of selected molecules on T11 and T12 atoms.

	ΔE_{ads} (kJ.mol^{-1})		ΔE_{disp} (kJ.mol^{-1})		Length	Width	σ	pK_A[a]
Compound	T11	T12	T11	T12		(Å)	(Å²)	
An	**-110.0**	**-133.7**	**-118.4**	**-106.2**	**7**	**4.3**	**30.1**	
o-MA	-108.8	-104.1	-146.1	-151.2	7	5.5	38.5	
m-MA	-137.0	-145.1	-112.4	-132.7	7.4	4.9	36.3	
p-MA	-139.1	-129.0	-131.5	-132.9	8.0	4.3	34.4	
Ph	-82.1	-100.6	-100.0	-109.4	5.7	4.3	24.5	9.95
o-Cr	-103.0	-114.6	-113.2	-118.5	5.9	4.6	27.1	10.28
m-Cr	-90.2	-116.1	-124.4	-109.0	6.2	4.9	30.4	10.09
p-Cr	-110.5	-124.9	-108.0	-113.2	6.7	4.3	28.8	10.26
2,4-Xol	-96.0	-123.7	-130.5	-169.6	6.7	5.5	36.9	10.45
2,5-Xol	-110.9	-123.0	-127.4	-120.6	6.9	5.0	34.5	10.22
2,4,6-Mol	-11.8	-11.0	-187.2	-181.6	6.7	6.7	44.9	10.88
2,3,5,6-Dol	-4.6	-7.4	-197.3	-207.8	6.9	6.7	46.2	10.88
benzene	-71.4	-28.0	-100.7	-94.6	5.0	4.3	21.5	
toluene	-74.6	-67.8	-103.5	-108.0	5.9	4.3	25.4	

[a]: values from CRC Handbook of Tables for Organic Compound identification, third edition, 1984, ISBN 0-8493-0303-6. For Mesitol: https://www.chemicalbook.com/ProductMSDSDetailCB3682841_EN.htm (consulted 09/05/2023). For Durenol: https://www.guidechem.com/encyclopedia/2-3-5-6-tetramethyl-phenol-dic370230.html (consulted 09/05/2023).

Figure III.8 displays the final geometries of ether and phenolic molecules on Al12 acid site. Ethers, anisole and *m*-methyl anisole, lead to the formation of a hydrogen bond between the oxygen of the adsorbates and the hydrogen of the BAS. On phenolic compounds, regardless of the number of methyl group, a second hydrogen bond appears between the hydrogen of the hydroxyl group and an oxygen atom of zeolite. The adsorption energies of oxygenated molecules are higher than that of aromatics owing to the presence of hydrogen bond. But, despite additional hydrogen bonds, the adsorption energy stays higher (in absolute value) on ether molecules than on phenolic molecules.

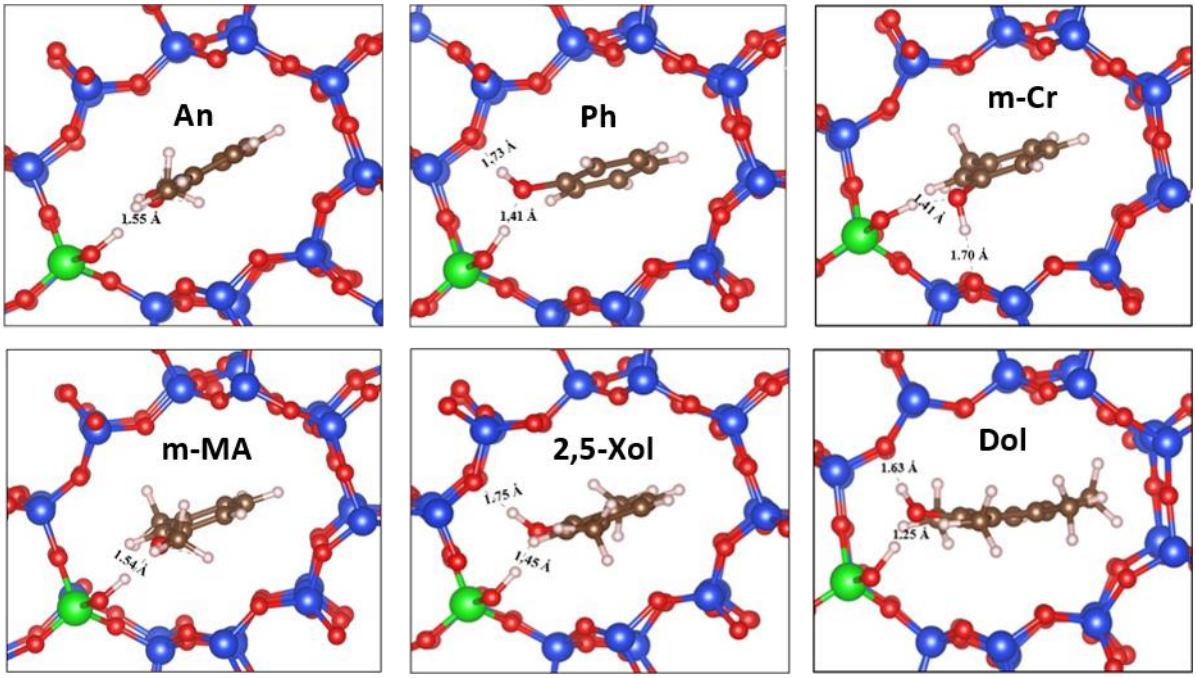

Figure III.8: Final geometries of anisole, m-methylanisole and phenolic compounds adsorbed on Al12 acid site. Dashed lines represent hydrogen bonds.

On phenol, cresols and xylenols molecules, ΔE_{ads} depends on their pk_A value; the higher the basic strength (higher pK_A), the higher the adsorption energies (in absolute value) (**Figure III.9a**). Moreover, ΔE_{ads} is always 15-20 $kJ.mol^{-1}$ higher on Al12 than on Al11, demonstrating the heterogeneity of the acid sites strength. For the larger molecules, mesitol and durenol, ΔE_{ads} become very small due to a higher contribution of London dispersion interactions (in absolute value). ΔE_{disp} depends on the size of the molecule, which may be described by a simple descriptor: the parameter σ (σ = L.W ≡ $Å^2$, with L the molecule "length" and W the molecule "width" -both in Å- displayed in Table III.1). $\ln|\Delta E_{disp}|$ is directly proportional to σ. (**Figure III.9b**).

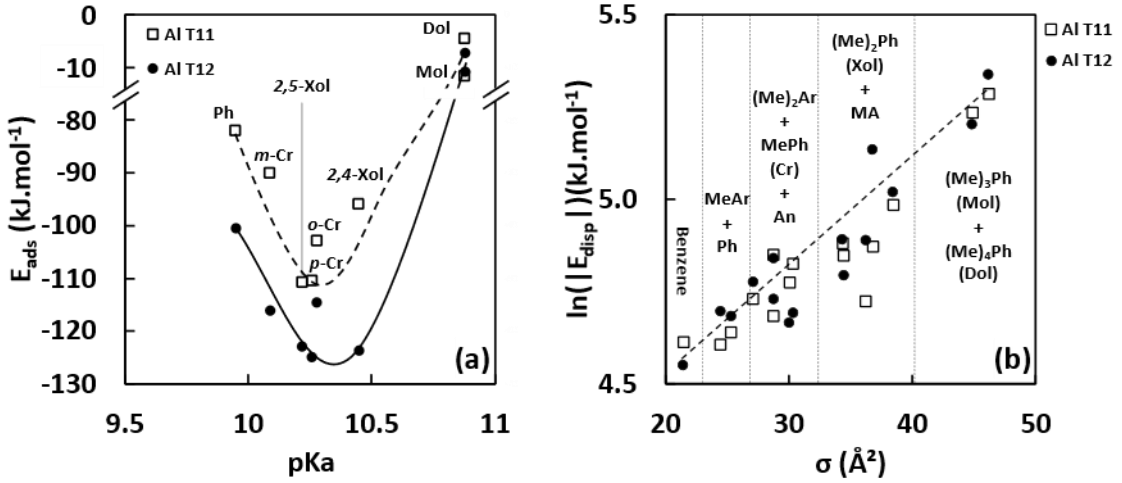

Figure III.9: Evolution of **(a)** adsorption energies with pKa for phenolic molecules and **(b)** natural logarithm of dispersion energies with the σ steric parameter for each molecule, on sites T11 and T12

GC-MS and FID show no anisole or derivatives in the coke, while DFT indicates they are more easily adsorbed on BAS than phenol. Even when these "coke" molecules completely occupy any and all available sites, anisole should competitively adsorb against phenol and other weakly adsorbed compounds. This is not the case, and indicates that anisole, when adsorbed onto an acid site, is automatically transformed by transalkylation, participating to the steady-state conversion, and also the further methylation of phenolics in coke, while producing the "base" phenol. Moreover, while phenol has been shown to inhibit anisole disproportionation[51], the stronger adsorption energies of anisole, when compared to phenolics, explains the steady-state previously discussed: Anisole competitively adsorbs on BAS against these phenolics, allowing for its continued transformation.

III.4 – Toxicity of the oxygenated coke molecules

The coke formed during anisole transformation is composed mostly of methylated phenols, the main products of successive transalkylations. The fundamental difference between the carbon deposition observed here and the one in FCC begs the following question: How does carbon deposition affects the textural properties, and deactivation mode of the HZSM-5 during the transformation of anisole?

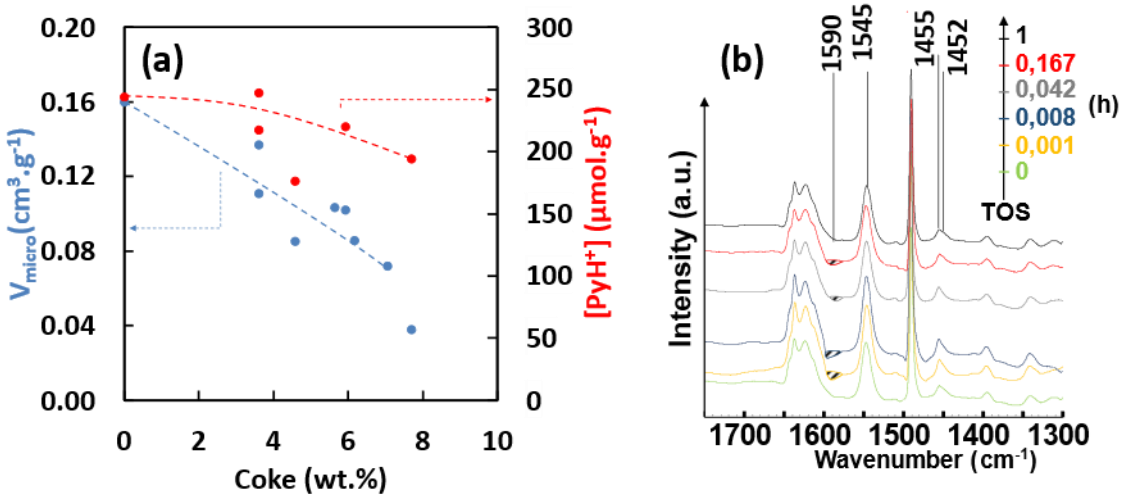

Figure III.10: **(a)** Concentration of Brønsted acid sites and micropore volume as a function of coke content **(b)** IR signature of coke displacement by pyridine in MFI.

Figure III.10a shows the residual concentration of BAS and micropore volume as a function of coke content. The microporosity loss is proportional to coke content, while the BAS concentration is less affected. The discrepancy could be explained in part by an overestimation of the concentration of the acidic sites actually accessible [52]. Indeed, basic pyridine could displace less basic molecules (phenolics) adsorbed on BAS; however, such competition appears limited (negative peak at 1590 cm-1, **Figure III.10b**).

This does not fully explain the above discrepancy, as a loss of access to micropore volume should mean an equal loss of access to the sites contained within that volume. The computed average molecular mass of coke (114 $g.mol^{-1}$, GC-FID of the soluble coke) is a way to estimate the number of coke molecules per BAS. This mass is relatively low, when compared to those obtained in other hydrocarbon conversion processes [53,54], or even biomass conversion [16,55], >130-220 and 340 $g.mol^{-1}$ respectively. [6,56] **Figure III.11a** shows that the number of coke molecules in the zeolite very rapidly reaches twice the number of accessible BAS, meaning that coke deposition leads to progressive fouling rather than acid site poisoning. [57]

The average coke density can be derived from GC-FID of soluble coke (0.930 $g.cm^{-3}$) to assess the actual volume occupied by coke in the zeolite. As shown by **Figure III.11b**, it is roughly equal to the one given by N_2-physisorption, except at later TOS, and higher coke contents. It implies that coke obstructs more

volume than it physically occupies. This confirms the fouling proposed by Prasomsri et al. [16], with pore plugging starting at higher coke contents.

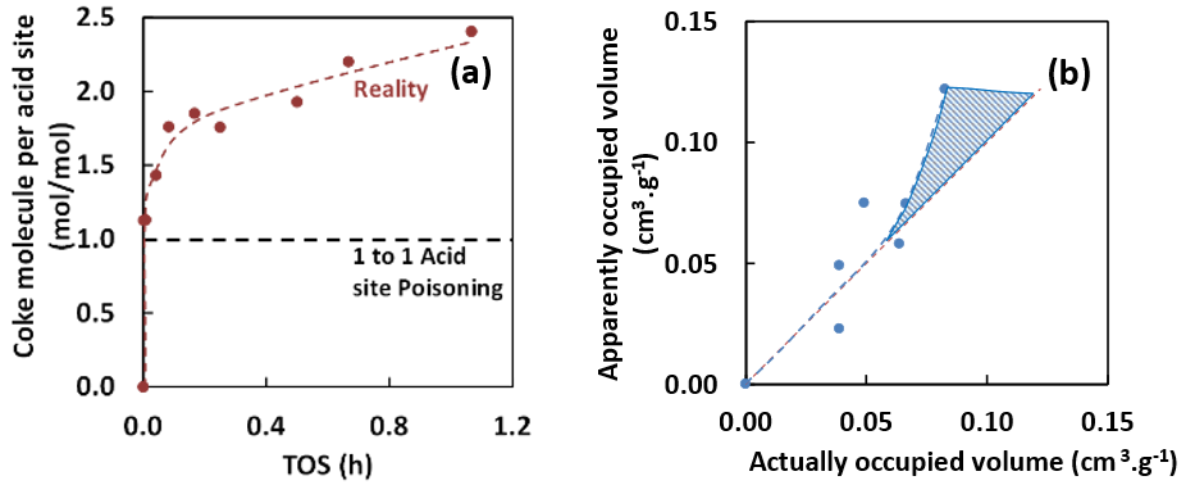

Figure III.11: **(a)** Assessment of the number of "coke" molecules per available acid sites on the fresh catalyst; **(b)** Comparison between the measurable microporous volume inaccessible to N_2-Physisorption (i.e., the apparently occupied volume) and the calculated volume, actually occupied by the "coke" molecules.

IV – Conclusion

The transformation of anisole on HZSM-5 (Si/Al = 43) at 673 K under atmospheric pressure, a proxy for lignocellulosic biomass catalytic fast pyrolysis, is followed with particular attention to product selectivity, reaction kinetics and catalyst deactivation. An apparent first-order reaction rate is evidenced. A strong shape selectivity is evidenced, due to electronic (mesomeric and inductive) as well as steric (zeolite shape selectivity and molecule size) effects. The catalyst deactivates by a strong retention of (methyl)phenols (reaction products), rather than the more usual coking (production and deposition of polyaromatics). Phenol and its methylated products are strongly adsorbed on the catalyst, as expected from their size and pKa, leading to catalyst fouling, rather than the often observed active (acid) sites poisoning. As the zeolite Si/Al ratio is 43, its aluminium (Brønsted acid) sites are mostly isolated. Further studies could focus on the effect of Si/Al ratio (and aluminium density) as well as on silanols nature and quantity to help design more resilient catalysts. While the CFP process is often compared to FCC, its operating conditions, mainly temperature (673 K vs 823 K for typical FCC), are considerably milder and explain the absence of polycyclic " hard coke". Such a feature is likely to facilitate catalyst regeneration.

Catalyst regeneration could be either combustion, as in FCC, or with (partially or not) oxidative plasma, or even by extracting the "coke" molecules, with an appropriate hydrogen-donor solvent. Optimization of this important step could significantly affect the overall process productivity and heat balance. Hierarchization of the zeolite either by top-down (decreasing the size of crystalline domains of µm size crystals with unbiased leaching with for instance NH_4F) or bottom-up (synthesis of nanosized zeolites) processes have already demonstrated their efficiency in providing easier regeneration steps as more coke is present on the external/mesoporous surfaces. When coke is located on these surfaces, its removal by combustion is facilitated as oxygen diffusion becomes less limiting.

V – References

[1] E.J. Cho, L.T.P. Trinh, Y. Song, Y.G. Lee, H.-J. Bae, Bioconversion of biomass waste into high value chemicals, Bioresource Technology 298 (2020) 122386. https://doi.org/10.1016/j.biortech.2019.122386.

[2] J.S.M. Samec, Holistic Approach for Converting Biomass to Fuels, Chem 4 (2018) 1199–1200. https://doi.org/10.1016/j.chempr.2018.05.010.

[3] E.F. Iliopoulou, K.S. Triantafyllidis, A.A. Lappas, Overview of catalytic upgrading of biomass pyrolysis vapors toward the production of fuels and high-value chemicals, WIREs Energy Environ. 8 (2019). https://doi.org/10.1002/wene.322.

[4] O. Ezekoye, H. Lavandier, C. Lorbeer, W. Rehm, J. Wallach, Chemicals and capital markets: Growing sustainably, (2022). https://www.mckinsey.com/industries/chemicals/our-insights/chemicals-and-capital-markets-growing-sustainably#/ (accessed March 7, 2023).

[5] S. Alfano, F. Berruti, N. Denis, A. Santagostino, The future of second-generation biomass, (n.d.).

[6] L.Y. Jia, M. Raad, S. Hamieh, J. Toufaily, T. Hamieh, M. Bettahar, G. Mauviel, M. Tarrighi, L. Pinard, A. Dufour, Catalytic fast pyrolysis of biomass : superior selectivity of hierarchical zeolite to aromatics, Green Chem. 19 (2017) 5442–5459. https://doi.org/10.1039/C7GC02309J.

[7] T.R. Carlson, G.A. Tompsett, W.C. Conner, G.W. Huber, Aromatic Production from Catalytic Fast Pyrolysis of Biomass-Derived Feedstocks, Top Catal 52 (2009) 241–252. https://doi.org/10.1007/s11244-008-9160-6.

[8] T.R. Carlson, Y.-T. Cheng, J. Jae, G.W. Huber, Production of green aromatics and olefins by catalytic fast pyrolysis of wood sawdust, Energy Environ. Sci. 4 (2011) 145–161. https://doi.org/10.1039/C0EE00341G.

[9] V.B.F. Custodis, S.A. Karakoulia, K.S. Triantafyllidis, J.A. van Bokhoven, Catalytic Fast Pyrolysis of Lignin over High-Surface-Area Mesoporous Aluminosilicates: Effect of Porosity and Acidity, ChemSusChem 9 (2016) 1134–1145. https://doi.org/10.1002/cssc.201600105.

[10] D.C. Dayton, J.R. Carpenter, A. Kataria, J.E. Peters, D. Barbee, O.D. Mante, R. Gupta, Design and operation of a pilot-scale catalytic biomass pyrolysis unit, Green Chem. 17 (2015) 4680–4689. https://doi.org/10.1039/C5GC01023C.

[11] J. Jae, G.A. Tompsett, A.J. Foster, K.D. Hammond, S.M. Auerbach, R.F. Lobo, G.W. Huber, Investigation into the shape selectivity of zeolite catalysts for biomass conversion, Journal of Catalysis 279 (2011) 257–268. https://doi.org/10.1016/j.jcat.2011.01.019.

[12] T.R. Carlson, T.P. Vispute, G.W. Huber, Green Gasoline by Catalytic Fast Pyrolysis of Solid Biomass Derived Compounds, ChemSusChem 1 (2008) 397–400. https://doi.org/10.1002/cssc.200800018.

[13] J.M. Silva, M.F. Ribeiro, I. Graça, A. Fernandes, Bio-oils/FCC co-processing: Insights into the adsorption of guaiacol on Y zeolites with distinct acidity and textural properties, Microporous and Mesoporous Materials 323 (2021) 111170. https://doi.org/10.1016/j.micromeso.2021.111170.

[14] I. Graça, J.M. Lopes, H.S. Cerqueira, M.F. Ribeiro, Bio-oils Upgrading for Second Generation Biofuels, Ind. Eng. Chem. Res. 52 (2013) 275–287. https://doi.org/10.1021/ie301714x.

[15] A. Aho, N. Kumar, K. Eränen, T. Salmi, M. Hupa, D.Y. Murzin, Catalytic Pyrolysis of Biomass in a Fluidized Bed Reactor, Process Safety and Environmental Protection 85 (2007) 473–480. https://doi.org/10.1205/psep07012.

[16] T. Prasomsri, A.T. To, S. Crossley, W.E. Alvarez, D.E. Resasco, Catalytic conversion of anisole over HY and HZSM-5 zeolites in the presence of different hydrocarbon mixtures, Applied Catalysis B: Environmental (2011) S0926337311002347. https://doi.org/10.1016/j.apcatb.2011.05.026.

[17] I.A. Vasalos, A.A. Lappas, E.P. Kopalidou, K.G. Kalogiannis, Biomass catalytic pyrolysis: process design and economic analysis, WIREs Energy Environ 5 (2016) 370–383. https://doi.org/10.1002/wene.192.

[18] G. Yildiz, F. Ronsse, R. van Duren, W. Prins, Challenges in the design and operation of processes for catalytic fast pyrolysis of woody biomass, Renewable and Sustainable Energy Reviews 57 (2016) 1596–1610. https://doi.org/10.1016/j.rser.2015.12.202.

[19] F.L. Mendes, V.L. Ximenes, M.B.B. de Almeida, D.A. Azevedo, N.S. Tessarolo, A. de Rezende Pinho, Catalytic pyrolysis of sugarcane bagasse and pinewood in a pilot scale unit, Journal of Analytical and Applied Pyrolysis 122 (2016) 395–404. https://doi.org/10.1016/j.jaap.2016.08.001.

[20] I. Graça, A. Fernandes, J.M. Lopes, M.F. Ribeiro, S. Laforge, P. Magnoux, F. Ramôa Ribeiro, Bio-oils and FCC feedstocks co-processing: Impact of phenolic molecules on FCC hydrocarbons transformation over MFI, Fuel 90 (2011) 467–476. https://doi.org/10.1016/j.fuel.2010.09.028.

[21] J.D. Adjaye, N.N. Bakhshi, Production of hydrocarbons by catalytic upgrading of a fast pyrolysis bio-oil. Part I: Conversion over various catalysts, (1995) 23.
[22] E.J. Soltes, T.A. Milne, eds., Pyrolysis Oils from Biomass: Producing, Analyzing, and Upgrading, American Chemical Society, Washington, DC, 1988. https://doi.org/10.1021/bk-1988-0376.
[23] E.F. Iliopoulou, S.D. Stefanidis, K.G. Kalogiannis, A. Delimitis, A.A. Lappas, K.S. Triantafyllidis, Catalytic upgrading of biomass pyrolysis vapors using transition metal-modified ZSM-5 zeolite, Applied Catalysis B: Environmental 127 (2012) 281–290. https://doi.org/10.1016/j.apcatb.2012.08.030.
[24] T.C. Hoff, D.W. Gardner, R. Thilakaratne, K. Wang, T.W. Hansen, R.C. Brown, J.-P. Tessonnier, Tailoring ZSM-5 Zeolites for the Fast Pyrolysis of Biomass to Aromatic Hydrocarbons, ChemSusChem 9 (2016) 1473–1482. https://doi.org/10.1002/cssc.201600186.
[25] M. Guisnet, P. Magnoux, D. Martin, Roles of acidity and pore structure in the deactivation of zeolites by carbonaceous deposits, in: C.H. Bartholomew, G.A. Fuentes (Eds.), Studies in Surface Science and Catalysis, Elsevier, 1997: pp. 1–19. https://doi.org/10.1016/S0167-2991(97)80138-3.
[26] L. Jia, F. Buendia-Kandia, S. Dumarcay, H. Poirot, G. Mauviel, P. Gérardin, A. Dufour, Fast Pyrolysis of Heartwood, Sapwood, and Bark: A Complementary Application of Online Photoionization Mass Spectrometry and Conventional Pyrolysis Gas Chromatography/Mass Spectrometry, Energy Fuels 31 (2017) 4078–4089. https://doi.org/10.1021/acs.energyfuels.7b00110.
[27] Y. Le Brech, L. Jia, S. Cissé, G. Mauviel, N. Brosse, A. Dufour, Mechanisms of biomass pyrolysis studied by combining a fixed bed reactor with advanced gas analysis, Journal of Analytical and Applied Pyrolysis 117 (2016) 334–346. https://doi.org/10.1016/j.jaap.2015.10.013.
[28] J. Ward, The nature of active sites on zeolites IX. Sodium hydrogen zeolite, Journal of Catalysis 13 (1969) 364–372. https://doi.org/10.1016/0021-9517(69)90445-X.
[29] C. Miranda, J. Urresta, H. Cruchade, A. Tran, M. Benghalem, A. Astafan, P. Gaudin, T.J. Daou, A. Ramírez, Y. Pouilloux, A. Sachse, L. Pinard, Exploring the impact of zeolite porous voids in liquid phase reactions: The case of glycerol etherification by tert-butyl alcohol, Journal of Catalysis 365 (2018) 249–260. https://doi.org/10.1016/j.jcat.2018.07.009.
[30] P. Magnoux, P. Roger, C. Canaff, V. Fouche, N.S. Gnep, M. Guisnet, New Technique for the Characterization of Carbonaceous Compounds Responsible for Zeolite Deactivation, (n.d.) 14.
[31] G. Kresse, J. Hafner, *Ab initio* molecular dynamics for liquid metals, Phys. Rev. B 47 (1993) 558–561. https://doi.org/10.1103/PhysRevB.47.558.
[32] Perdew, J.P., Burke, K., and Ernzerhof, M., Generalized gradient approximation made simple., Physical Review Letters, 77 (1996) 3865-3868.
[33] G. Kresse, D. Joubert, From ultrasoft pseudopotentials to the projector augmented-wave method, Physical Review B 59 (1999) 1758–1775. https://doi.org/10.1103/PhysRevB.59.1758.
[34] S. Grimme, Semiempirical GGA-type density functional constructed with a long-range dispersion correction, Journal of Computational Chemistry 27 (2006) 1787–1799. https://doi.org/10.1002/jcc.20495.
[35] S. Grimme, Accurate description of van der Waals complexes by density functional theory including empirical corrections, Journal of Computational Chemistry 25 (2004) 1463–1473. https://doi.org/10.1002/jcc.20078.
[36] F.R. Ribeiro, M. Guisnet, Les zéolithes, un nanomonde au service de la catalyse, EDP Sciences, 2012.
[37] J.S. Magee, M.M. Mitchell, Fluid Catalytic Cracking: Science and Technology, Elsevier, 1993.
[38] M. Marczewski, J.-P. Bodibo, G. Perot, M. Guisnet, ALKYLATION OF AROMATICS PART I. REACTION NETWORK OF THE ALKYLATION OF PHENOL BY METHANOL ON USHY ZEOLITE, (n.d.) 8.
[39] M. Marczewski, G. Perot, M. Guisnet, Alkylation of Aromatics II. Alkylation of Phenol with Methanol on Various Zeolites, Studies in Surface Science and Catalysis 41 (1988) 273–282. https://doi.org/10.1016/S0167-2991(09)60824-7.
[40] X. Zhu, R.G. Mallinson, D.E. Resasco, Role of transalkylation reactions in the conversion of anisole over HZSM-5, Applied Catalysis A: General 379 (2010) 172–181. https://doi.org/10.1016/j.apcata.2010.03.018.
[41] T.W.G. Solomons, C.B. Fryhle, S.A. Snyder, Organic chemistry, 11e ed., Wiley, Hoboken, NJ, 2014.
[42] N.Y. Chen, Personal Perspective of the Development of Para Selective ZSM-5 Catalysts, Ind. Eng. Chem. Res. 40 (2001) 4157–4161. https://doi.org/10.1021/ie000870p.
[43] A.K. Kuriakose, J.L. Margrave, Kinetics of the Reactions of Elemental Fluorine. IV. Fluorination of Graphite, J. Phys. Chem. 69 (1965) 2772–2775. https://doi.org/10.1021/j100892a049.
[44] Y. Liu, L. Jiang, H. Wang, H. Wang, W. Jiao, G. Chen, P. Zhang, D. Hui, X. Jian, A brief review for fluorinated carbon: synthesis, properties and applications, Nanotechnology Reviews 8 (2019) 573–586. https://doi.org/10.1515/ntrev-2019-0051.

[45] M. Dubois, N. Batisse, K. Guérin, P. Thomas, Fluorine: Characteristics, Chemistry and Applications Controlled fluorination using atomic fluorine, (n.d.).
[46] M. Guisnet, J.-P. Gilson, Zeolites for Cleaner Technologies, Imperial College Press, 2005. https://doi.org/10.13140/2.1.3317.8401.
[47] M. Raad, A. Astafan, S. Hamieh, J. Toufaily, T. Hamieh, J.D. Comparot, C. Canaff, T.J. Daou, J. Patarin, L. Pinard, Catalytic properties of Ga-containing MFI-type zeolite in cyclohexane dehydrogenation and propane aromatization, Journal of Catalysis 365 (2018) 376–390. https://doi.org/10.1016/j.jcat.2018.06.029.
[48] A. Bonnin, Y. Pouilloux, V. Coupard, D. Uzio, L. Pinard, Deactivation mechanism and regeneration study of Zn/HZSM-5 catalyst in ethylene transformation, Applied Catalysis A: General 611 (2021) 117976. https://doi.org/10.1016/j.apcata.2020.117976.
[49] F. Ferreira Madeira, K. Ben Tayeb, L. Pinard, H. Vezin, S. Maury, N. Cadran, Ethanol transformation into hydrocarbons on ZSM-5 zeolites: Influence of Si/Al ratio on catalytic performances and deactivation rate. Study of the radical species role, Applied Catalysis A: General 443–444 (2012) 171–180. https://doi.org/10.1016/j.apcata.2012.07.037.
[50] M. Guisnet, F.R. Ribeiro, eds., Deactivation and regeneration of zeolite catalysts, Imperial College Press ; Distributed by World Scientific, London : Singapore, 2011.
[51] I. Graça, J.-D. Comparot, S. Laforge, P. Magnoux, J.M. Lopes, M.F. Ribeiro, F.R. Ribeiro, Effect of phenol addition on the performances of H–Y zeolite during methylcyclohexane transformation, Applied Catalysis A: General 353 (2009) 123–129. https://doi.org/10.1016/j.apcata.2008.10.032.
[52] I. Graça, J.-D. Comparot, S. Laforge, P. Magnoux, J.M. Lopes, M.F. Ribeiro, F. Ramôa Ribeiro, Influence of Phenol Addition on the H-ZSM-5 Zeolite Catalytic Properties during Methylcyclohexane Transformation, Energy Fuels 23 (2009) 4224–4230. https://doi.org/10.1021/ef9003472.
[53] K. Qian, D.C. Tomczak, E.F. Rakiewicz, R.H. Harding, G. Yaluris, W.-C. Cheng, X. Zhao, A.W. Peters, Coke Formation in the Fluid Catalytic Cracking Process by Combined Analytical Techniques, (n.d.).
[54] N. Chaouati, A. Soualah, M. Chater, M. Tarighi, L. Pinard, Mechanisms of coke growth on mordenite zeolite, Journal of Catalysis 344 (2016) 354–364. https://doi.org/10.1016/j.jcat.2016.10.011.
[55] S. Du, D.P. Gamliel, M.V. Giotto, J.A. Valla, G.M. Bollas, Coke formation of model compounds relevant to pyrolysis bio-oil over ZSM-5, Applied Catalysis A: General 513 (2016) 67–81. https://doi.org/10.1016/j.apcata.2015.12.022.
[56] A. Beuque, M. Barreau, E. Berrier, J.-F. Paul, N. Batalha, A. Sachse, L. Pinard, Transformation of Dilute Ethylene at High Temperature on Micro- and Nano-Sized H-ZSM-5 Zeolites, Catalysts 11 (2021) 282. https://doi.org/10.3390/catal11020282.
[57] J.W. Beeckman, G.F. Froment, Catalyst Deactivation by Active Site Coverage and Pore Blockage, Ind. Eng. Chem. Fund. 18 (1979) 245–256. https://doi.org/10.1021/i160071a009.

Chapitre IV

Dismutation de l'anisole sur H-ZSM-5 : le rôle-clé du rapport Si/Al sur l'effet auto-inhibiteur

Le chapitre suivant est publié dans la revue ***Applied Catalysis A : General*** sous la référence suivante :

N. Pichot, J.W. Hounfodji, H. El Siblani,M. Badawi, V. Valtchev, S. Mintova, J.-P. Gilson, A. Dufour, L. Pinard, Anisole disproportionation on HZSM-5: the key role of Si/Al ratio on auto-inhibition effect, Applied Catalysis A: General. 671 (2024) 119565. https://doi.org/10.1016/j.apcata.2024.119565

Abstract

La conversion de l'anisole a été étudiée à 673 K sur des zéolithes H-ZSM-5 avec des rapports Si/Al allant de 9 à 201. L'influence de la distribution des sites acides de Brønsted sur l'activité catalytique et la sélectivité envers les produits de réaction a été étudiée expérimentalement. Les énergies d'adsorption des réactif et produits sur les aluminium appariés et isolés sont calculées par DFT. Le rapport Si/Al n'affecte pas les sélectivités. De Si/Al = 201 à Si/Al = 29, l'augmentation de la concentration des sites acides augmente l'activité. Cependant, le changement de distribution des sites de « majoritairement isolés » à de plus en plus d'appariement inhibe fortement la conversion et l'activité initiales. Ce comportement est attribué à l'étape de désorption des produits de réaction, qui devient l'étape limitante du principe de Sabatier. Ceci est en accord avec l'augmentation significative des énergies d'adsorption entre les sites acides appariés et isolés. Quand l'énergie d'adsorption de l'anisole en phase gaz devient similaire à celle des produits, un effet auto-inhibiteur se manifeste, déjà connu pour des procédés en phase liquide.

Mots clés : ZSM-5, DFT, Energies d'adsorption, Position de l'aluminium.

I – Introduction

Catalytic conversion of hydrocarbons on zeolites takes place in major oil refining processes. Heavy products, often referred to as coke, are often formed and their retention leads to deactivation by poisoning acid sites and/or blocking pores [1–6].

The catalytic conversion of biomass-derived oxygenated molecules is becoming an important route to produce green aromatics [7–10]. With these polar reactants, the deactivation can also result from the poisoning of acid sites by reaction products (auto-inhibition) [11–13]. For example, in the Friedel-Craft acetylation of anisole, the formation of small (and even minimal) amounts of polyacylated species inhibits the catalyst activity due to the strong adsorption of these products on acid sites [12,13]. Such inhibition from polar molecules is not exclusive to liquid phase reactions, but can also occur in the gas phase. Hydrocarbon cracking on HY zeolite at 623 K has shown that the addition of phenol increases the deactivation of the catalyst, due to its strong adsorption (even at high temperatures) on acidic sites [14–16]. Hence, adsorption competition between hydrocarbons and phenol governs catalyst activity. Recently, for the disproportionation of anisole on HZSM-5 at 673 K, we have shown that catalyst deactivation results in part from the inhibitory effect of the reaction products [17]. The molecules trapped in the zeolite micropores are polymethyl-phenols, and their retention is due to strong adsorption on the acid sites, as confirmed by DFT calculations.

The effects of competitive adsorption between reactants and products depend on the polarity and polarizability of the zeolite, as suggested by Derouane et al. [13]. Indeed, it was shown that during acetylation of anisole on BEA zeolite with low Al content, the initial reaction rate is proportional to the Al content, whereas the rate decreases at high Al content. This suggests that the Si/Al ratio plays a key role in the competitive adsorption effects between reactants and products, and that the inhibitory effect is mitigated on zeolite with low aluminium content [13]. The key role of the Si/Al ratio on the auto-inhibition effect seems well established for liquid phase reactions. For gas phase, DFT investigations have shown that the adsorption selectivity can be strongly tuned upon variation of the Si/Al ratio [18,19]. Does this auto-inhibition effect apply for gas-phase anisole disproportionation? Anisole is an interesting surrogate

molecule to understand the catalytic conversion of methoxy-phenols produced by lignin pyrolysis [20].

The aim of this study is to investigate the impact of ZSM-5 zeolite acidity on gas-phase anisole transformation using nine commercial zeolites with Si/Al ratios ranging from 9 to 201, with particular interest on activity, product selectivity in the initial stage of the reaction, *i.e.,* on coke-free catalysts, as well as describing the interactions between oxygenates and Brønsted acid sites.

II – Experimental

II.1 – Catalysts

ZSM-5 zeolites were sourced from Alsi-Penta (Si/Al = 12 & 24 - SM-27, SM-55), Mizusawa (Si/Al = 50 – SILTON^{TM} series), Tosoh (Si/Al = 9 & 12 – HSZ-822HOA & HSZ-820NHA), and Zeolyst (Si/Al = 29, 43, 75 & 201 – CBV5524G, CBV8014, CBV1502 & CBV28014). Some were in NH_4^+ form, therefore calcination was performed to convert to the protonic form: under N_2 (P_{atm}, 100 mL/min) at 373 K for an hour (5 K/min from room temperature) for drying, then under air (P_{atm}, 100 mL/min) at 823 K for 6 hours (10 K/min). The catalysts are referred to as follows: the capital letters A, M, T and Z for the supplier (respectively Alsi-penta, Mizusawa, Tosoh and Zeolyst), and the number for the Si/Al ratio. An asterisk is added when the catalyst contains a large amount of extra-framework aluminium species.

II.2 – Characterisations

Nitrogen physisorption (**Chapter II** part **I.2.e**)

Solid state ^{29}Si MAS (Magic Angle Spinning) NMR spectra were performed on a Bruker Avance 400 III HD spectrometer at resonance frequency of 79.53 MHz, with a 7 mm NMR probe. The spectra were obtained using a 6µs single pulse at a spinning speed of 6 kHz, with a recycle delay of 20s. The ^{29}Si

chemical shifts were referenced to tetramethylsilane (TMS) at 0 ppm (**Chapter II** part **I.2.c**)

^{27}Al MAS NMR experiments were carried out on a Bruker AVII 500 spectrometer (v27Al = 130.3 MHz). A 3.2 mm MAS NMR probe (Bruker) was used, and the MAS frequency was 5 kHz. The ^{27}Al chemical shifts were referenced to $Al(NO_3)_3$ at 0 ppm.

Catalysts Crystal particle sizes were assessed by laser diffraction (Particle size analyser – MT3000II).

Pyr-FTIR (*Nicolet Magna FTIR iS50* spectrometer, **Chapter II** part **I.2.f**) [21,22]. Molar extinction coefficients were previously determined to be respectively 1.13 cm.µmol^{-1} and 1.28 cm.µmol^{-1} for Brønsted and Lewis acid sites [22].

II.3 – Catalytic test

(Chapter II part **II.1**)

II.4 – Atomistic simulations

Periodic DFT calculations were performed using the VASP code [23]. PAW pseudopotentials have been used [24] with the PBE+D2 level of theory [25,26]. The plane-wave cut-off energy was set to 450 eV, following a series of convergence test. The equations of Kohn-Sham [27,28] were solved by self-consistent field (SCF) iteration until total energies were converged to within 1 x 10^{-6} eV as convergence criterion. The ionic relaxation of all the structures was carried out systematically until the force of each atom was less than 0.02 eV/A.. The integration zone of the Brillouin zone was sampled using only the (1 x 1 x 1) k-point grid.

The adsorption energies ΔE_{ads} of guest molecules in the porous matrix have been computed as follows (**Eq. IV.1**):

$$\Delta E_{ads} = E_{(zeol-X)} - E_{(zeol)} - E_{(X)} \qquad \textbf{(Eq. IV.1)}$$

With $E_{zeolite}$ the energy of the empty zeolite, E_X the energy of the isolated molecule, and $E_{zeolite\text{-}X}$, the energy of the relaxed zeolite with the molecule inside.

III – Results and discussions

III.1 – Characterization of commercial zeolites

Table IV.1 summarizes the textural and acidic properties of the commercial H-ZSM-5 zeolites: Alsi Penta (A), Misuzawa (M), Tosoh (T) and Zeolyst (Z). On all materials, micropore volumes correspond to an MFI structure, i.e. around 0.16 $cm^3.g^{-1}$ [29,30], and mesopore volumes are relatively low, below 0.10 $cm^3.g^{-1}$ (**Figure IV.1a**). Particles are around 8 µm in diameter.

Nitrogen Physisorption isotherms are provided as **Figure IV.S1**. They show type I isotherms for all catalysts but Z29, T9* and T12. These show an H3 or H4 type hysteresis; they are nanoparticle agglomerates, as opposed to others, which are micron sized catalysts[31]. This is corroborated in **Figure IV.S2** by the SEM analysis of T9*, T12, Z43 and M50. T9* and T12 clearly show the micron-sized agglomerates of nano-sized crystals, while Z43 shows micron-sized crystal intergrowths and M50 shows very well-defined micron-sized crystals. This results in shorter diffusion pathways for reactants and products in T9* and T12, compared to Z43 and M50.

Table IV.1: Selected acid and textural properties of commercial H-ZSM-5 zeolites.

Catalyst¤	**Supplier**	**Si/Al[a]**	**[PyH$^+$][b]**	**[PyL][b]**	**V_{micro}[c]**	**V_{meso}[d]**	**Particle size[e]**
		mol/mol	µmol.g^{-1}	µmol .g^{-1}	cm^3.g^{-1}	cm^3.g^{-1}	µm
T9*	T	9	1038	139	0.15	0.07	9.00
A12	A	12	980	41	0.18	0.02	
T12*	T	12	641	183	0.16	0.08	7.59
A24	A	24	463	7	0.14	0.04	
Z29*	Z	29	338	53	0.16	0.10	
Z43	Z	43	281	49	0.16	0.05	
M50*	M	50	164	50	0.14	0.07	7.66
Z75	Z	75	148	21	0.13	0.12	
Z201	Z	201	67	38	0.16	0.07	

¤Catalysts are labelled with a letter (supplier) and a number (Si/Al ratio)

[a] ICP analysis, [b] concentration of pyridine adsorbed on Brønsted (PyH^+) and Lewis (PyL) acid sites, respectively, after evacuation at 423 K; [c] microporous volume calculated using the t-plot method ; [d] mesoporous volume =V_{total}-V_{micro} (V_{total} : volume adsorbed at P/P_0=0.98); [e] particle sizes obtained with particle size analyser - SYNC[32]; *Presence of large amount of EFAl species, seen either with IR or (^{27}Al) MAS NMR spectrometry

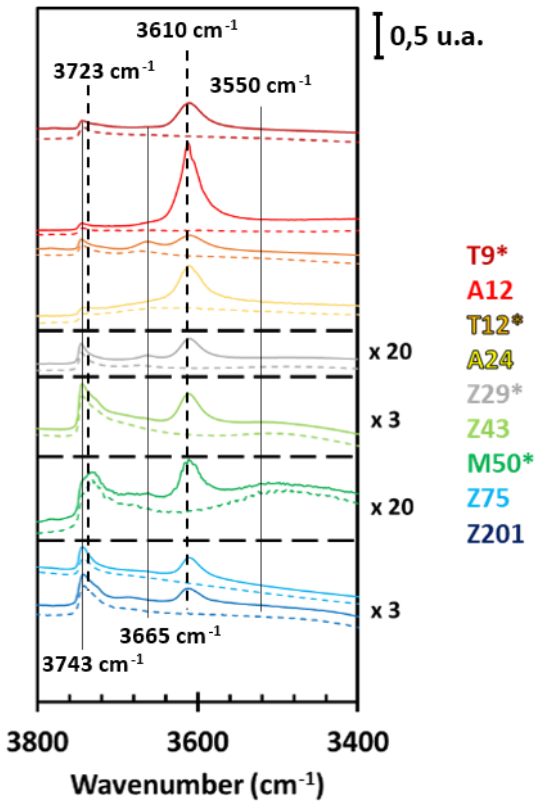

Figure IV.2: FTIR spectra in the hydroxyl group stretching region before (full line) and after (dotted lines) pyridine adsorption at 423 K.

The concentration of Brønsted acid sites (BAS) probed by IR monitoring of adsorbed pyridine ranges from 67 to 1038 µmol.g^{-1} and, except for Tosoh zeolites, is proportional to the aluminium content measured by ICP (**Figure IV.1b**), suggesting that most aluminium atoms are in the zeolite framework. As a result, the concentration of Lewis acid sites (LAS) is low, below 50 µmol.g^{-1} for most of the catalysts. In contrast, on T9* and T12*, LAS concentrations are high, 139 and 183 µmol.g^{-1}, respectively, suggesting that these materials may be partially dealuminated during the 673 K calcination.

Figure IV.2 compares the hydroxyl band intensities of the different zeolites. The bands at 3743 cm^{-1} with a shoulder at 3723 cm^{-1} are attributed to external and internal silanol, respectively. A large amount of internal silanol on M50* results in the appearance of a broad band at 3550 cm^{-1} ascribed to hydroxyl nests [33]. The silanol groups present on high aluminium content zeolites retain pyridine at 423 K, whilst on zeolites with a lower Al content, the silanol groups are not acidic enough to retain pyridine at 423 K.

The band at 3610 cm^{-1} corresponds to bridged hydroxyls (BAS) and increases with decreasing Si/Al ratio. The band at 3665 cm^{-1} is assigned to extra-

framework aluminium species (EFAl). The presence of hydroxylated EFAl species is limited on all commercial zeolites, except T12*; they can limit pyridine accessibility to BAS. On T9*, all the BAS are accessible to pyridine despite a large amount of non-hydroxylated EFAl species, suggesting that the latter are located outside the zeolite crystal.

Aluminium speciation in H-ZSM-5 catalysts is investigated by single pulse 27Al MAS NMR experiments on hydrated samples. The relative amounts of tetrahedrally coordinated framework Al at bridging acid sites (BASs) versus non-framework, octahedrally coordinated Al (Al(VI)) are obtained from the integrated areas of the ~55 and 0 ppm peaks, respectively (**Figure IV.3**).

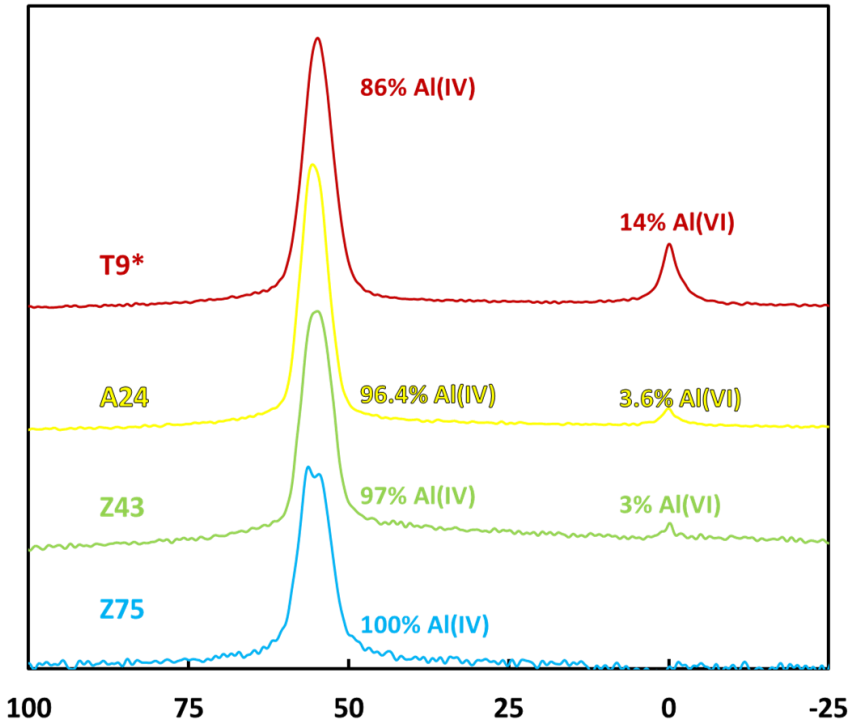

Figure IV.3: 27Al MAS NMR spectra of **T9***, **A24**, **Z43** and **Z75** samples

Only the T9* catalyst presents a high amount of extra framework Al (14%), while A24, Z43 and Z75 present 3.6, 3 and 0% of those species, respectively. These values are in accordance with the IR spectra in **Figure IV.2**.

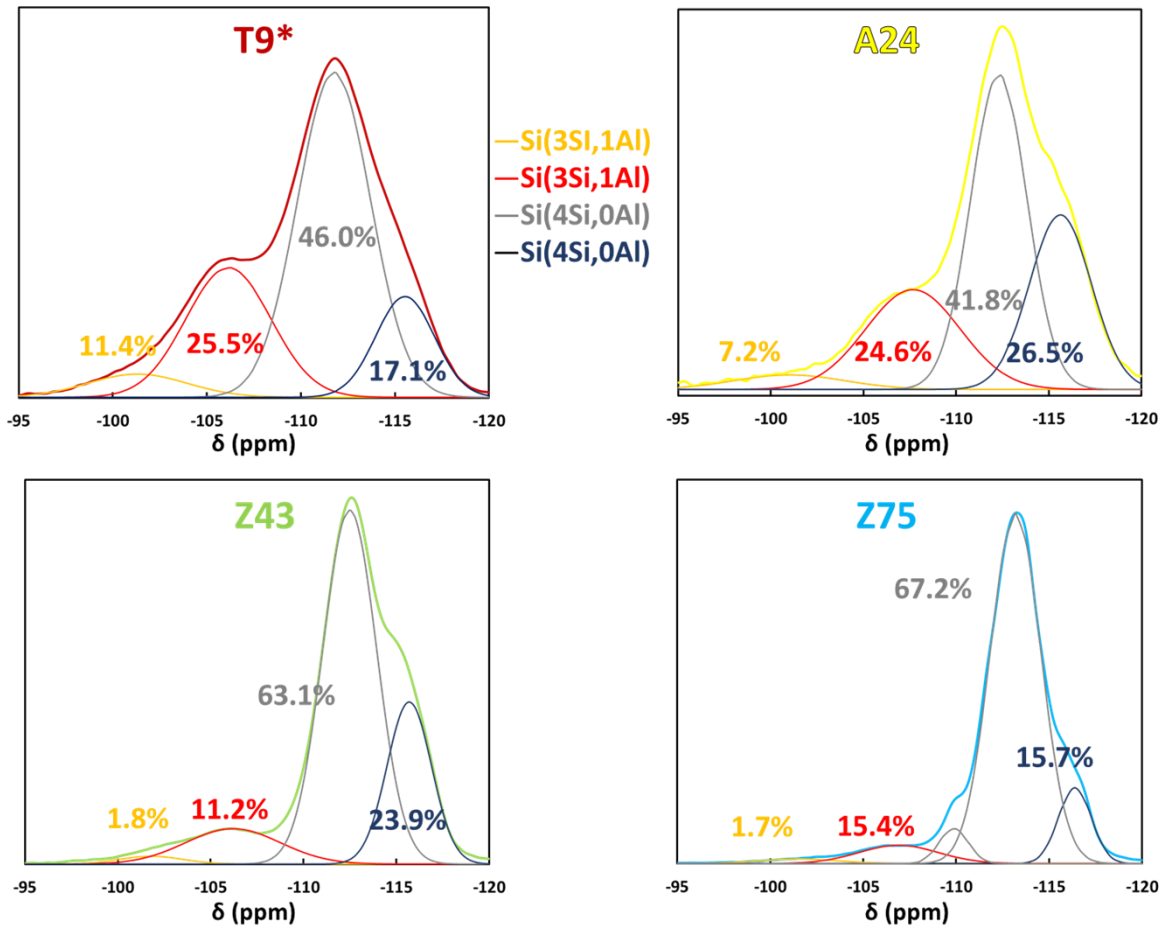

Figure IV.4: ^{29}Si NMR spectra for catalysts **T9***, **A24**, **Z43** and **Z75** in the Al substitution region[34,35].

Figure IV.4 compares the ^{29}Si NMR spectra of catalysts T9*, A24, Z43 and Z75 showing the distribution of Al species around Si atoms in the MFI structure. Peaks from 110 ppm (grey and dark blue) show Si atoms with only other Si atoms in neighbouring positions (Si(-O-Si)4). Red bands around 105 to 107 ppm show either Si atoms with an adjacent Al or a terminal silanol. Finally, yellow bands around 100 ppm show Si atoms with an Al in a neighbouring position. In all four spectra there is no noticeable peak around 95 ppm, indicating the absence of two Al atoms in an NNN (Next Nearest Neighbour, i.e. separated by one Si atom) position: the closest Al atoms could be to each other is in the NNNN (Next Next Nearest Neighbour, i.e. separated by two Si atoms) position, within the same 10 Membered-Ring (**10 MR**) [36]. This observation underlines the structural limitations of Al clustering within the zeolite framework. As expected, the lower the Si/Al ratio, the higher the density of Si with Al in a neighbouring position. Conversely, the higher the Si/Al ratio, the higher the number of "isolated" Si

atoms. Pairing of aluminium atoms was verified by Co2+ exchange followed by IR in another work on T9* (Sold by Tosoh as an HZSM-5 Si/Al = 12.5), and produced 68% of “paired” Al [37].

III.2 Initial activity and selectivity

The conversion of anisole was studied at 673 K on the nine commercial catalysts. **Figure IV.5a** shows the natural logarithm of initial conversion as a function of contact time (W/F). A straight line through the origin is obtained, regardless of the Si/Al ratio. Although the anisole transformation is a bimolecular reaction, it follows an apparent first-order kinetic rate [17].

Figure IV.5b plots the initial catalyst activity as a function of the BAS concentration. From a Si/Al ratio of 29 upwards, the initial activity is proportional to BAS concentration, except on M50* due to EFAl blocking their access. The turnover frequency of Brønsted acid sites (**Figure IV.5c**) is high, on the order of 400-500 h^{-1}, but unexpectedly, increasing aluminium content is detrimental to anisole disproportionation. This is not due to pore blocking by EFAl species, as initial activity is very low on low Si/Al, EFAl-free catalysts, such as A12 (**Figure IV.2**). The length of the diffusion path also is not a major factor here, with T9* and T12 being nanosized crystals, with shorter diffusion paths, that should help with outward diffusion of the reactant and products, and overall, with activity.

Catalysts with higher Brønsted acidities (T9*, T12*,A12, A24*) show very low activities (**Figure IV.5b**). Among them, T9* and T12* exhibit somewhat higher activities than the other two. They also differentiate by their higher LAS count (**Table IV.1**). Assuming that, with these lower Si/Al ratios, BAS have no activity (seen for A12 and A24*, **Figure IV.5c**), a TOF_0 for T9* and T12*’s Lewis acid sites can be calculated, giving 61.4 h^{-1} and 100.1 h^{-1} respectively. This indicates that, for these low Si/Al ratios catalysts, LAS display some activity, albeit 8 to 10 times inferior to the one shown by higher Si/Al ratios BAS. Lewis acidity has already been shown to help guaiacol adsorption [38] on Y zeolites, and also improve catalyst stability in the context of pyrolysis vapor catalytic upgrading on HZSM-5 [39].

Terminal silanol groups have recently been shown to have some acid strength, positively correlated with Al concentration [40], and that could provide

additional activity to neighbouring BAS. While this effect could be present here, **Figure IV.2** shows the very low acidity of silanol groups in higher Si/Al zeolites, and also their very low concentration for lower Si/Al zeolites, thus rendering their effect negligible at best in this study.

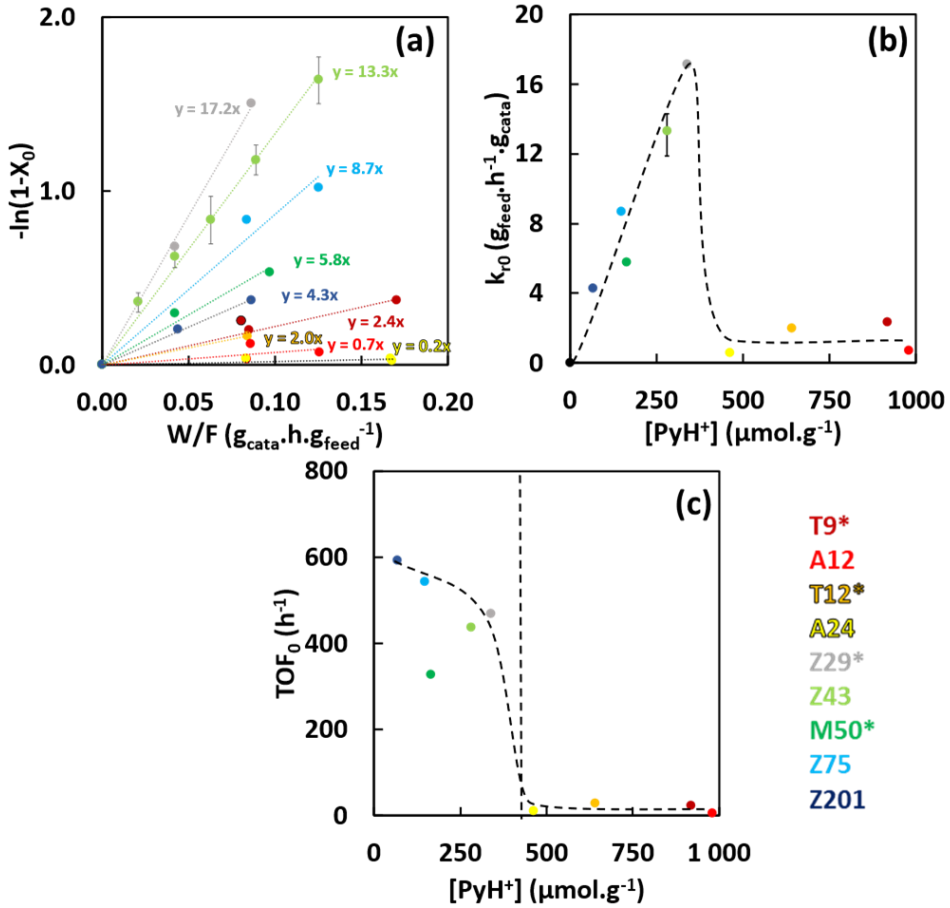

Figure IV.5: **(a)** Test for the first order rate equation for anisole transformation at 673 K on MFI zeolites with different Si/Al ratio **($-\ln(1-X_0) = k_{r_0} . \frac{W}{F}$)**; **(b)** Initial rates (k_{r0}, $g_{feed}.h^{-1}.g_{cata}^{-1}$) as a function of catalyst initial acidity; **(c)** Initial Turnover Frequency (h^{-1}) as a function of initial acidity.

Anisole (An) transformation produces phenol (Ph), *o-, m-, p*-methylanisols (MA), *o-, m-, p*-cresols (Cr), 2,4-, 2,5-xylenols (Xol). The deoxygenated aromatics yield is low, and the quasi absence of methane production suggests that the cleavage of aryl ethers does not occur. **Figure IV.6** shows the yields of initial products as a function of initial anisole conversion. Phenol and methylanisoles are primary products, cresol a secondary product appearing at low conversion (< 5%) and xylenols are tertiary products appearing at conversion above 20% [17].

Si/Al molar ratio has no impact on product selectivity, but only on the initial activity.

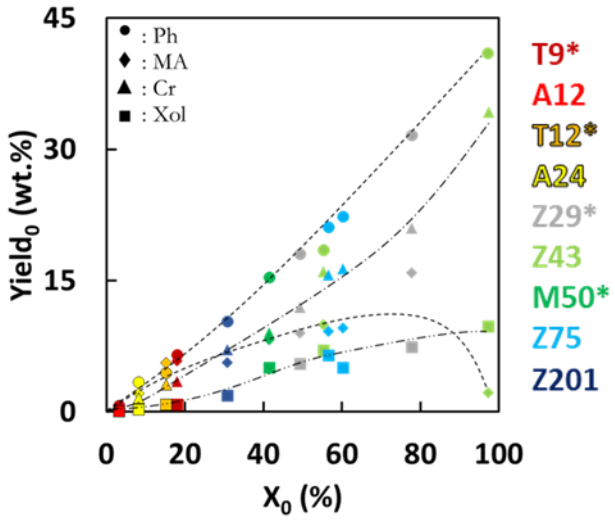

Figure IV.6: Initial yields for phenol, methylanisoles, cresols and xylenols *vs* initial conversion.

The low activity of the Al-rich zeolites (Si/Al ≤ 24) could be related to Al distribution in the framework. Indeed, the ^{29}Si NMR results showed that on the aluminium-poor zeolite, Al atoms are isolated, while on the aluminium-rich zeolite, in addition to the isolated Al, two Al in the NNNN (Next Next Nearest Neighbour) position are possible. To investigate the effect of aluminium distribution on catalyst activity, the adsorption energies of anisole and disproportionation products on isolated Al and on two Al in NNNN, NNN and opposite positions were modelled.

III.3 – Computed adsorption energies of phenolic compounds

Among the 12 distinct T sites in H-ZSM-5 zeolite, Al11 (equivalent to Al5) and Al12 (equivalent to Al6) are identified as the most representative isolated sites [41]. When associated with a next nearest neighbour (NNN configuration), Al3 (equivalent to Al9) is selected for Al11 and Al7 (equivalent to Al1) for Al12 [42,43]. For the NNNN and opposite configurations, the pairs Al8 & Al5 and Al8 & Al2 have been selected. **Table IV.2** compares the adsorption energies, ΔE_{ads} on these Al atoms for selected molecules (reactant and products). All the adsorption energies are negative, indicating their exothermic nature. Moreover, a consistent difference of approximately 50 kJ.mol^{-1} is observed between the isolated and paired sites.

Table IV.2: Adsorption energies for oxygenated compounds on paired and unpaired Al sites on 10 MR MFI zeolites

	ΔE_{ads} (kJ.mol^{-1})					
	Al11	Al12	Al8 & Al2 (opposite)	Al3 & Al11 (NNN)	Al7 & Al12 (NNN)	Al8 & Al5 (NNNN)
Anisole	**-110.0**	**-133.7**	**-141.9**	**-155.3**	**-170.2**	**-179.1**
o-Methylanisole	-108.8	-104.1	-143.3	-155.2	-146.0	-161.2
m-Methylanisole	-137.0	-145.1	-150.9	-166.1	-153.3	-183.5
p-Methylanisole	-139.1	-129.0	-164.0	-174.8	-160.5	-173.0
Phenol	-82.1	-100.6	-130.2	-152.3	-128.5	-168.0
o-Cresol	-103.0	-114.6	-134.8	-131.7	-138.3	-150.0
m-Cresol	-90.2	-116.1	-132.3	-124.4	-130.2	-153.9
p-Cresol	-110.5	-124.9	-152.4	-179.2	-153.3	-177.1
2,4-Xylenol	-96.0	-123.7	-156.2	-144.7	-161.3	-180.2
2,5-Xylenol	-110.9	-123.0	-160.5	-178.5	-143.5	-186.7

Figure IV.7 compares the final geometry of the anisole and phenol molecules on isolated Al12, Al8 & Al2 in opposite position and Al8 & Al5 in NNNN

positions. Figures showing the final geometries of multiple molecules (reactant and products) are also given in the Supporting Information. (**Figures IV.S3 to S12**).

Anisole adsorbs by forming a hydrogen bond between its oxygen and the Brønsted acid site on isolated Al12 and one between its oxygen and each BAS for Al in the NNNN position. In the case of phenol (and by extension cresol and xylenol), in addition to the oxygen bond of the molecule, a second bond appears on the isolated Al12. The alcohol proton has formed a hydrogen bond with an oxygen atom in the zeolite. For the NNNN sites, phenol (and by extension Cr and Xol) adsorbs only with its oxygen, which forms a hydrogen bond with each BAS. For isolated Al, the adsorption energies of ethers (anisole, MA) were higher than those of phenols, even with the second H-bond (**Table IV.2**). This is still the case for paired (NNN, NNNN, and opposite) sites, although the energy difference is much smaller. For the opposite configuration, due to the distance between the two aluminium atoms, it is not possible to form hydrogen bonds with both BAS simultaneously, reducing the adsorption energies by about 20 to 30 kJ.mol^{-1} (**Table IV.2**).

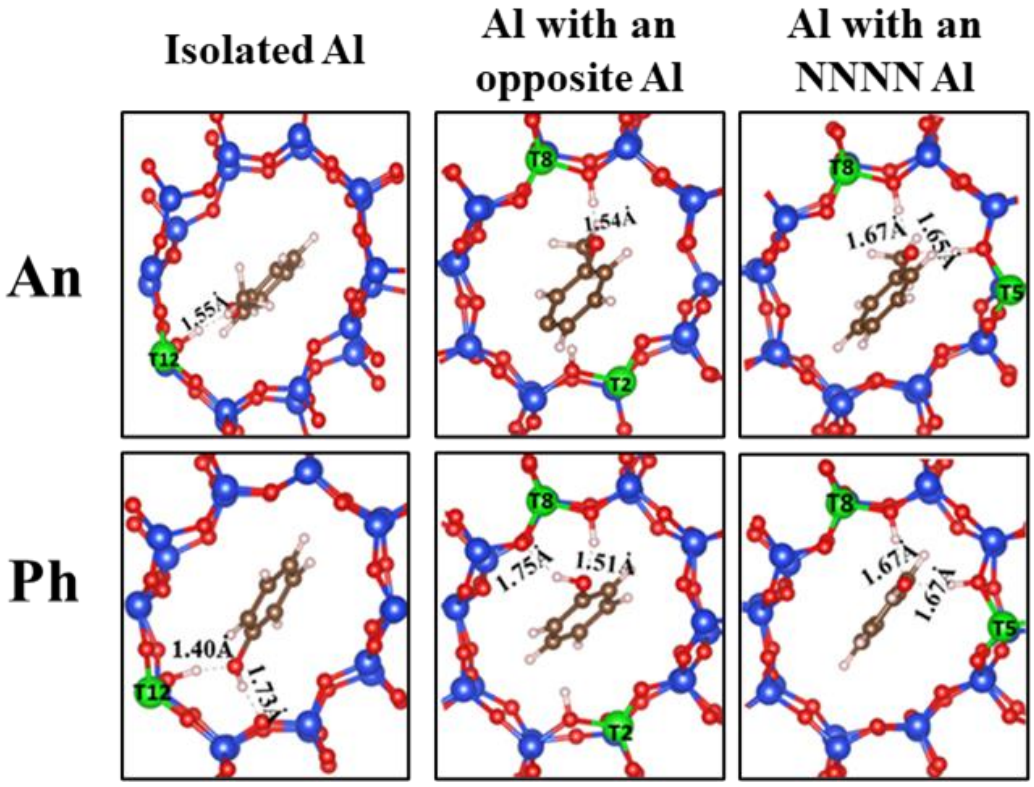

Figure IV.7: Final geometries of anisole and phenol adsorbed on isolated aluminium, as well as aluminium with another (NNNN and opposite) aluminium in the 10 MR.

The adsorption energy (E_{ads}) is always lower when the aluminium is isolated, regardless of the oxygenated molecules (**Table IV.2**). If a second aluminium atom is present on the 10 MR, E_{ads} increases significantly, even if it is in the opposite position. Irrespective of the oxygenated molecules, Eads decreases by 30-40 kJ.mol^{-1} when a second aluminium atom is in the NNN position in the 10-MR, and by a further 20-30 kJ.mol^{-1} when it is in the NNNN position. Therefore, the stronger adsorption site for oxygenated compounds is two aluminium atoms in the Next Next Nearest Neighbour position. According to the Sabatier principle, the high adsorption energy of the oxygenated molecules could create an auto-inhibitory effect where the desorption of phenolic molecules is the rate-limiting step for anisole conversion. The key role of the Si/Al ratio on the auto-inhibition effect seems well established for gas-phase reactions involving oxygenated compounds. The present results also pave the way for potential advances in the design of more efficient and selective catalysts for gas-phase conversion processes of phenolic compounds.

IV – Conclusion

The conversion of anisole at 673 K under atmospheric pressure and on nine HZSM-5 with Si/Al ratios ranging from 9 to 201 has been carried out. Catalyst initial activity and product selectivity were the main experimental focus, and product adsorption energies computed by DFT.

Si/Al ratio, while greatly affecting initial conversion, does not affect product selectivity, which is only correlated to conversion and zeolite structure (confinement effect). This influence on conversion, therefore activity, is explained in large part by differences in anisole adsorption energies between isolated and paired active sites, and the reduced gap between adsorption energies of anisole and phenolics on paired sites ($27.9 < \Delta_{\mathrm{An-Ph}}^{Isolated\ Al} < 33.1$ kJ.mol^{-1} vs $11.1 < \Delta_{\mathrm{An-Ph}}^{Paired\ Al} < 11.7$ kJ.mol^{-1}). This smaller gap on paired sites prevents anisole from displacing other adsorbates. This is a typical illustration of the Sabatier principle, where a decrease in Si/Al ratio leads to an auto-inhibition effect by making phenolics desorption the rate-limiting step of the process. Even the shorter diffusion pathways of the nano-sized zeolites in the study do not prevent or mitigate it. This auto-inhibition effect, previously evidenced for liquid-phase (Derouane et al.), is highlighted here for gas-phase anisole disproportionation.

Further studies could focus on the effect of Al distribution and density on deactivation, as well as coke composition and retention in the zeolite. Moreover, well-engineered (identical crystal size, well-controlled “defect” nature and quantity, …) ZSM-5 with varying Si/Al ratios could lead to the design of even more optimal catalysts fitted for regeneration.

References

[1] M. Guisnet, F.R. Ribeiro, eds., Deactivation and regeneration of zeolite catalysts, Imperial College Press ; Distributed by World Scientific, London : Singapore, 2011.
[2] M. Guisnet, P. Magnoux, Organic chemistry of coke formation, Applied Catalysis A: General 212 (2001) 83–96. https://doi.org/10.1016/S0926-860X(00)00845-0.
[3] M. Guisnet, L. Costa, F.R. Ribeiro, Prevention of zeolite deactivation by coking, Journal of Molecular Catalysis A: Chemical 305 (2009) 69–83. https://doi.org/10.1016/j.molcata.2008.11.012.
[4] J.R. Rostrup-Nielsen, Industrial relevance of coking, Catalysis Today 37 (1997) 225–232. https://doi.org/10.1016/S0920-5861(97)00016-3.
[5] G.A. Fuentes, C.H. Bartholomew, Catalyst Deactivation 1997, Elsevier, 1997.
[6] M. Argyle, C. Bartholomew, Heterogeneous Catalyst Deactivation and Regeneration: A Review, Catalysts 5 (2015) 145–269. https://doi.org/10.3390/catal5010145.
[7] L.Y. Jia, M. Raad, S. Hamieh, J. Toufaily, T. Hamieh, M. Bettahar, G. Mauviel, M. Tarrighi, L. Pinard, A. Dufour, Catalytic fast pyrolysis of biomass : superior selectivity of hierarchical zeolite to aromatics, Green Chem. 19 (2017) 5442–5459. https://doi.org/10.1039/C7GC02309J.
[8] J. Liang, G. Shan, Y. Sun, Catalytic fast pyrolysis of lignocellulosic biomass: Critical role of zeolite catalysts, Renewable and Sustainable Energy Reviews 139 (2021) 110707. https://doi.org/10.1016/j.rser.2021.110707.
[9] S. Wan, Y. Wang, A review on ex situ catalytic fast pyrolysis of biomass, Front. Chem. Sci. Eng. 8 (2014) 280–294. https://doi.org/10.1007/s11705-014-1436-8.
[10] A.J. Foster, J. Jae, Y.-T. Cheng, G.W. Huber, R.F. Lobo, Optimizing the aromatic yield and distribution from catalytic fast pyrolysis of biomass over ZSM-5, Applied Catalysis A: General 423–424 (2012) 154–161. https://doi.org/10.1016/j.apcata.2012.02.030.
[11] D. Rohan, C. Canaff, E. Fromentin, M. Guisnet, Acetylation of anisole by acetic anhydride over a HBEA zeolite—Origin of deactivation of the catalyst, Journal of Catalysis 177 (1998) 296–305. https://doi.org/10.1006/jcat.1998.2108.
[12] E.G. Derouane, C.J. Dillon, D. Bethell, S.B. Derouane-Abd Hamid, Zeolite Catalysts as Solid Solvents in Fine Chemicals Synthesis 1. Catalyst Deactivation in the Friedel–Crafts Acetylation of Anisole, (n.d.).
[13] E.G. Derouane, G. Crehan, C.J. Dillon, D. Bethell, H. He, S.B. Derouane-Abd Hamid, Zeolite Catalysts as Solid Solvents in Fine Chemicals Synthesis, Journal of Catalysis 194 (2000) 410–423. https://doi.org/10.1006/jcat.2000.2933.
[14] I. Graça, J.-D. Comparot, S. Laforge, P. Magnoux, J.M. Lopes, M.F. Ribeiro, F.R. Ribeiro, Effect of phenol addition on the performances of H–Y zeolite during methylcyclohexane transformation, Applied Catalysis A: General 353 (2009) 123–129. https://doi.org/10.1016/j.apcata.2008.10.032.
[15] I. Graça, A. Fernandes, J.M. Lopes, M.F. Ribeiro, S. Laforge, P. Magnoux, F. Ramôa Ribeiro, Effect of phenol adsorption on HY zeolite for n-heptane cracking: Comparison with methylcyclohexane, Applied Catalysis A: General 385 (2010) 178–189. https://doi.org/10.1016/j.apcata.2010.07.011.
[16] I. Graça, A.M. Carmo, J.M. Lopes, M.F. Ribeiro, Improving HZSM-5 resistance to phenolic compounds for the bio-oils/FCC feedstocks co-processing, Fuel 140 (2015) 484–494. https://doi.org/10.1016/j.fuel.2014.10.002.
[17] N. Pichot, J.W. Hounfodji, M. Badawi, V. Valtchev, S. Mintova, J.-P. Gilson, A. Dufour, L. Pinard, Products and coke shape-selectivity during anisole disproportionation over HZSM-5, Applied Catalysis A: General 665 (2023) 119352. https://doi.org/10.1016/j.apcata.2023.119352.
[18] S. Chibani, M. Chebbi, S. Lebègue, L. Cantrel, M. Badawi, Impact of the Si/Al ratio on the selective capture of iodine compounds in silver-mordenite: a periodic DFT study, Physical Chemistry Chemical Physics 18 (2016) 25574–25581. https://doi.org/10.1039/C6CP05015H.
[19] T. Ayadi, M. Badawi, L. Cantrel, S. Lebègue, Rational approach for an optimized formulation of silver-exchanged zeolites for iodine capture from first-principles calculations, Molecular Systems Design & Engineering 7 (2022) 422–433. https://doi.org/10.1039/D1ME00149C.
[20] X. Zhu, R.G. Mallinson, D.E. Resasco, Role of transalkylation reactions in the conversion of anisole over HZSM-5, Applied Catalysis A: General 379 (2010) 172–181. https://doi.org/10.1016/j.apcata.2010.03.018.

[21] J. Ward, The nature of active sites on zeolites IX. Sodium hydrogen zeolite, Journal of Catalysis 13 (1969) 364–372. https://doi.org/10.1016/0021-9517(69)90445-X.
[22] C. Miranda, J. Urresta, H. Cruchade, A. Tran, M. Benghalem, A. Astafan, P. Gaudin, T.J. Daou, A. Ramírez, Y. Pouilloux, A. Sachse, L. Pinard, Exploring the impact of zeolite porous voids in liquid phase reactions: The case of glycerol etherification by tert-butyl alcohol, Journal of Catalysis 365 (2018) 249–260. https://doi.org/10.1016/j.jcat.2018.07.009.
[23] G. Kresse, J. Hafner, *Ab initio* molecular dynamics for liquid metals, Phys. Rev. B 47 (1993) 558–561. https://doi.org/10.1103/PhysRevB.47.558.
[24] G. Kresse, D. Joubert, From ultrasoft pseudopotentials to the projector augmented-wave method, Physical Review B 59 (1999) 1758–1775. https://doi.org/10.1103/PhysRevB.59.1758.
[25] J.P. Perdew, K. Burke, M. Ernzerhof, Generalized Gradient Approximation Made Simple, Phys. Rev. Lett. 77 (1996) 3865–3868. https://doi.org/10.1103/PhysRevLett.77.3865.
[26] S. Grimme, Semiempirical GGA-type density functional constructed with a long-range dispersion correction, J. Comput. Chem. 27 (2006) 1787–1799. https://doi.org/10.1002/jcc.20495.
[27] P. Hohenberg, W. Kohn, Inhomogeneous Electron Gas, Phys. Rev. 136 (1964) B864–B871. https://doi.org/10.1103/PhysRev.136.B864.
[28] W. Kohn, L.J. Sham, Self-Consistent Equations Including Exchange and Correlation Effects, Phys. Rev. 140 (1965) A1133–A1138. https://doi.org/10.1103/PhysRev.140.A1133.
[29] F.R. Ribeiro, M. Guisnet, Les zéolithes, un nanomonde au service de la catalyse, EDP Sciences, 2012.
[30] I. Batonneau-Gener, A. Sachse, Determination of the Exact Microporous Volume and BET Surface Area in Hierarchical ZSM-5, J. Phys. Chem. C 123 (2019) 4235–4242. https://doi.org/10.1021/acs.jpcc.8b11524.
[31] K.S.W. Sing, Reporting physisorption data for gas/solid systems with special reference to the determination of surface area and porosity (Recommendations 1984), Pure and Applied Chemistry 57 (1985) 603–619. https://doi.org/10.1351/pac198557040603.
[32] Laser Diffraction (LD): Particle Size Analyzers :: Microtrac, (n.d.). https://www.microtrac.com/products/particle-size-shape-analysis/laser-diffraction/ (accessed August 31, 2023).
[33] L. Lin, X. Zhang, N. He, J. Liu, Q. Xin, H. Guo, Operando Dual Beam FTIR Study of Hydroxyl Groups and Zn Species over Defective HZSM-5 Zeolite Supported Zinc Catalysts, Catalysts 9 (2019) 100. https://doi.org/10.3390/catal9010100.
[34] C.J.H. Jacobsen, C. Madsen, T.V.W. Janssens, H.J. Jakobsen, J. Skibsted, Zeolites by con®ned space synthesis ± characterization of the acid sites in nanosized ZSM-5 by ammonia desorption and 27Al/29Si-MAS NMR spectroscopy, Microporous and Mesoporous Materials (2000).
[35] D.S.A. Silva, W.N. Castelblanco, D.H. Piva, V. De Macedo, K.T.G. Carvalho, E.A. Urquieta-González, Tuning the Brønsted and Lewis acid nature in HZSM-5 zeolites by the generation of intracrystalline mesoporosity—Catalytic behavior for the acylation of anisole, Molecular Catalysis 492 (2020) 111026. https://doi.org/10.1016/j.mcat.2020.111026.
[36] M.J. Rice, A.K. Chakraborty, A.T. Bell, Al Next Nearest Neighbor, Ring Occupation, and Proximity Statistics in ZSM-5, Journal of Catalysis 186 (1999) 222–227. https://doi.org/10.1006/jcat.1999.2544.
[37] J. Dědeček, D. Kaucký, B. Wichterlová, O. Gonsiorová, Co 2+ ions as probes of Al distribution in the framework of zeolites . ZSM-5 study, Physical Chemistry Chemical Physics 4 (2002) 5406–5413. https://doi.org/10.1039/B203966B.
[38] J.M. Silva, M.F. Ribeiro, I. Graça, A. Fernandes, Bio-oils/FCC co-processing: Insights into the adsorption of guaiacol on Y zeolites with distinct acidity and textural properties, Microporous and Mesoporous Materials 323 (2021) 111170. https://doi.org/10.1016/j.micromeso.2021.111170.
[39] X. Li, X. Zhang, S. Shao, L. Dong, J. Zhang, C. Hu, Y. Cai, Catalytic upgrading of pyrolysis vapor from rape straw in a vacuum pyrolysis system over La/HZSM-5 with hierarchical structure, Bioresource Technology 259 (2018) 191–197. https://doi.org/10.1016/j.biortech.2018.03.046.
[40] P. Bräuer, O. Situmorang, P.L. Ng, C. D'Agostino, Effect of Al content on the strength of terminal silanol species in ZSM-5 zeolite catalysts: a quantitative DRIFTS study without the use of molar extinction coefficients, Phys. Chem. Chem. Phys. 20 (2018) 4250–4262. https://doi.org/10.1039/C7CP07826A.
[41] A.J. Jones, E. Iglesia, The Strength of Brønsted Acid Sites in Microporous Aluminosilicates, ACS Catal. 5 (2015) 5741–5755. https://doi.org/10.1021/acscatal.5b01133.

[42] P. Losch, H.R. Joshi, O. Vozniuk, A. Grünert, C. Ochoa-Hernández, H. Jabraoui, M. Badawi, W. Schmidt, Proton Mobility, Intrinsic Acid Strength, and Acid Site Location in Zeolites Revealed by Varying Temperature Infrared Spectroscopy and Density Functional Theory Studies, J. Am. Chem. Soc. 140 (2018) 17790–17799. https://doi.org/10.1021/jacs.8b11588.
[43] R. E. Fletcher, S. Ling, B. Slater, Violations of Löwenstein's rule in zeolites, Chemical Science 8 (2017) 7483–7491. https://doi.org/10.1039/C7SC02531A.

Chapitre V

Unconventional coke composition during high temperature anisole disproportionation on zeolites

Le chapitre suivant a été soumis à la revue ***Applied Catalysis A : General*** avec les auteurs et le titre suivant : N. Pichot, N. Chaouati, M. Fahda, V. Valtchev, J-P Gilson, A. Dufour, L. Pinard, Unconventional coke composition during high temperature anisole disproportionation on zeolites, Applied Catalysis A: General.

Abstract

La désactivation et la sélectivité de forme envers les produits de réaction et le coke sont étudiées sur des zéolithes à tailles de pores moyenne, large et extra-large avec différents rapports Si/Al, pour la dismutation de l'anisole à 673 K. La modélisation de la désactivation comme fonction du temps de réaction souligne le rôle clé du volume microporeux des zéolithes dans l'activité. Les variations de sélectivité envers le méthylanisole (produit primaire) et le crésol (produit secondaire) sont dues à la prévalence d'un chemin réactionnel sur un autre pour la production du crésol. La nature des produits (méthylphénols) inhibe la formation des polyaromatiques non-oxygénés « classiques », formés habituellement via le mécanisme de Sullivan, ce qui laisse uniquement des monoaromatiques, adsorbés sur la zéolithe, et disponibles pour les réactions de transalkylation avec l'alimentation d'anisole, car ayant pollué la majeure partie de la surface dans les canaux du catalyseur.

Mots clés : ZSM-5, DFT, Energies d'adsorption, Position de l'aluminium

I – Introduction

Catalytic Fast Pyrolysis (CFP) on zeolites is a promising route to produce high value hydrocarbons from biomass-derived feedstocks [1–4] as it avoids a costly hydrodeoxygenation (highly exothermic reaction at high pressure with H_2 consumption) [5,6]. However, during CFP a fast catalyst deactivation occurs due to coke formation [7,8]. Overcoming this obstacle is a necessary step to scale-up and commercialise the process [9]. To better understand the fundamentals of such deactivation, focusing on the conversion of single model molecules is a first step to apprehend the behaviour of the oxygenated hydrocarbons present in pyrolytic bio-oils.

Consequently, two options are available: co-feeding these model molecules with well-known feeds, or pure model molecules (hydroxy-, methoxy-functions, aldehydes, ketones, furans…). Among these options, co-feeding phenol with a classical FCC charge has been explored extensively by Graça et al. [10–15]. Model molecules such as furans, guaiacol and other phenolics, and anisole conversion under CFP operating conditions have already been reported [7,16–23]. Among these model compounds, anisole is a good proxy for the methoxy-substituted aromatics in biomass pyrolysis (present in bio-oils derived from lignin pyrolysis), as it consists of a C_6 aromatic ring and a CH_3O- group.

Anisole transformation on acidic zeolites is a bimolecular reaction (disproportionation) and produces mainly methylated phenolics, and very few non-oxygenated compounds [17–19,24]. Previous work showed a fast deactivation due to the formation and subsequent strong adsorption of phenolics, the primary reaction products[17,19]. The main reaction mechanism is a series of transalkylations producing the so- called “coke” retained on the catalyst surface and/or porosity [19], and causing its deactivation [25–31].

The formation and nature of deactivating species, are usually highly dependent on temperature: i) low temperatures (up until around 723 K) [32,33] lead to the formation, by condensation and rearrangement, of alkenes (aliphatic of cyclical), dienes, naphteno-aromatics, strongly adsorbed on the active sites, ii) higher temperatures (from around 723 K) [32,33] yield polyaromatic hydrocarbons (PAH), such as pyrene, indene…, by hydrogen transfers and dehydrogenating coupling [33]. Steric hindrance on these heavy polyaromatics traps them in the zeolite microporosity [33].

High temperature coke formation is also a highly shape-selective and complex process [33,34]. Zeolite structure determines the size and shape of the molecules retained in the channels (methylpyrenes are formed on **MFI**, coronene-like coke forms on **FAU**, and the monodimensional channels of **MOR** produce linear molecules, such as phenanthrenes and anthracenes [25,33,35]). One of the most common mechanism includes constant alkylation of aromatic cycles, with paring reactions leading to autocyclisation of the precursors (**Scheme V.S1** *in supplementary material*) [36–38]. Another path necessitates low reactant partial pressure, and consists in dehydrogenating coupling of adsorbed coke precursors [35].

As of oxygenated molecules processing on acidic zeolites, far less details are available on the "coke" composition and effect of porosity on its formation than on conventional PAH coke. Co-feeding phenol with oil-derived FCC feedstocks showed that phenol was strongly adsorbed on Brønsted acid sites in the zeolite porosity: Graça et al. reported that phenol affected the coke formation rate and quantity, and identified mostly polyaromatics and adsorbed phenol in the coke [10,11]. Zhang et al. studied furan CFP on **MFI** and reported no oxygenates in the coke although no component identification was performed [7]. Ma et al. studied Lignin CFP on multiple catalysts (**FAU**, **MFI**, ***BEA** and amorphous silica-alumina), but reported only the amount of coke produced [39]. Other studies focusing on the minimization of coke formation do not discuss coke composition [40]. Liu et al. found some oxygenates (methylated cyclopentenones) in the coke on methanol to hydrocarbon spent zeolite catalysts, identified as coke precursors in the formation of conventional polyaromatic coke [41].

In the case of anisole disproportionation on zeolites, the usual PAH were not found in MFI, and instead, deactivation was due to monoaromatic phenolic products strongly adsorbed on active sites in the zeolite channels [19], indicative of low-temperature coke [19,33]. Previous work showed a strong impact of Si/Al ratio on the catalytic activity [42], and of catalyst structure [18]. They could impact deactivation and coke formation mechanism and make-up, given the aforementioned coke shape selectivity effects at high temperatures.

This contribution studies anisole disproportionation with 10 (**MFI**) and 12 Membered-Ring (MR) (***BEA**, **MOR**, **FAU**) zeolites as well as a newly discovered 16 MR (**JZO**) zeolite; the latter possesses a 3D channel network, and supercages [43,44]. We will first focus on the effects of structure and acidity on catalytic

activity, product yield, and isomer selectivity. Second, we study the coke deposits and the effect of zeolite structure and acidity on its composition, formation mechanism, finally its effect on the zeolite deactivation mode.

Does anisole disproportionation produce the same coke species previously reported for **MFI** with the other structures ? Is it, yet again, a shape-selective process, with larger pores allowing for the growth of polyaromatic hydrocarbons?

II – Experimental section

II.1 – Catalysts

One **MFI** zeolite is provided by Tosoh (Si/Al = 12), HSZ-820NHA). Another **MFI**, as well as the three **FAU** and one ***BEA** are sourced from Zeolyst (respectively **MFI** Si/Al = 43 – CBV8014 –, **FAU** Si/Al = 6, 15, 30 – CBV712, CBV720, CBV730 –, and ***BEA** Si/Al = 12.5 – CP814e). The second ***BEA** zeolite is provided by UOP (***BEA** Si/Al = 13.7 – Sample ID 75085-2042003829). One **MOR** zeolite is provided by ZEOCAT (**MOR** Si/Al = 10 – ZM-510-Z3464). Another mordenite catalyst with higher Si/Al ratio is also used (**MOR** Si/Al = 80). Finally, the **JZO** zeolite is synthesised with the method described by **Fahda et al.** (**JZO** Si/Al = 23.4 – ZEO-1)[44]. **MFI**, ***BEA** and **MOR** zeolites are in NH_4^+ form, therefore calcination is performed to convert to the protonic form: under N_2 (P_{atm}, 100 mL.min^{-1}) at 373 K for an hour (5 K.min^{-1} from room temperature) for drying, then under air (P_{atm}, 100 mL.min^{-1}) at 823 K for 6 hours (10 K.min^{-1}).

Catalysts are named with their structure followed by their Si/Al ratio in parentheses. Example: **MFI**(43).

II.2 – Characterizations

Si/Al ratio measured by ICP-OES (**Chapter II** part **I.2.a**).

Pyridine adsorption (423 K) monitored by Pyr-FTIR (**Chapter II** part **I.2.f**)

Beer-Lambert-Bouguer's law:

$$C = \frac{A}{\varepsilon} * \frac{S}{m} * 1000 \quad \textbf{(Eq. V.1)}$$

where C is the acid sites concentration (µmol.g^{-1}), A the band's area (absorption.cm^{-1}), S the wafer's surface (2 cm²), m the mass of the wafer (mg), and ε the molar extinction coefficient (cm.µmol^{-1}).

Molar extinction coefficients were previously determined to be respectively 1.13 cm.µmol^{-1} and 1.28 cm.µmol^{-1} for Brønsted and Lewis acid sites [46].

Nitrogen physisorption (**Chapter II** part **I.2.e**)

Crystal sizes are assessed with SEM imagery (values from previous works [44,47], **Chapter II** part **I.2.d**).

Coke content assessed via thermogravimetric analysis (**Chapter II** part **III.2.a**).

Coke extraction, identification and quantification (**Chapter II** part **III.2.c**) [26].

Blank test for the effect of HF on the oxygenated aromatics (**Chapter II** part **III.2.a)** (**Figure V.S1**).

II.3 – Catalytic tests

Catalytic tests (**Chapter II** part **II.1**)

Conversion (X_t, wt.%), yields ($Y_{i,t}$, wt.%) and selectivities ($S_{i,t}$, %) were calculated as follows:

$$X_t(wt.\%) = \left(1 - \frac{A_{Anisole,t}}{A_{total,t}}\right) * 100 \quad \textbf{(Eq. V.2)}$$

$$Y_{i,t}(wt.\%) = \left(\frac{A_{i,t}}{A_{total,t}}\right) * 100 \quad \textbf{(Eq. V.3)}$$

$$S_{i,t}(\%) = \left(\frac{Y_{i,t}}{X_t}\right) * 100 \quad \textbf{(Eq. V.4)}$$

Where $A_{Anisole,t}$, $A_{total,t}$ and $A_{i,t}$ represent the areas of the anisole, the sum of all the peaks and the peak of the product ***i***, at any given ***t*** time, respectively.

III – Results and discussion

III.1 – Characterisation

The aim of the present work is to assess the effects of different zeolite structures and acidity on anisole disproportionation (catalyst activity and deactivation, main product selectivities, coke formation). Thus, five structures were chosen: **MFI** (10 MR, interconnected straight and sinusoidal channels)[48], ***BEA** (12 MR, 3D interconnected straight channels)[49], **MOR** (12 and 8 MR, 2D straight channels, side pockets)[50], **FAU** (12 MR, 3D, supercages)[51] and **JZO** (16 and 12 MR, 3D interconnected straight channels, supercages)[52]. At least two Si/Al ratios (i.e. BAS concentrations) were selected for each commercial catalyst, in order to distinguish the structural effects from those originating from acidity. **Table V.1** summarizes all characterisations of these catalysts.

Brønsted acid site concentrations range from 88 to 641 µmol.g^{-1} and micropore volumes are as expected: **MFI**: ≈ 0.17 $cm^3.g^{-1}$, **MOR**: ≈ 0.20$cm^3.g^{-1}$, **FAU**: ≈ 0.30 $cm^3.g^{-1}$ [46]. The lower value for ***BEA** could be explained by a partial collapse of the catalyst structure (0.16 $cm^3.g^{-1}$ *vs* 0.22 $cm^3.g^{-1}$).

Table V.1: Structural, chemical and textural properties of the commercial and synthesized zeolites

Structure	Pore network (Å)	Si/Al[a]	[PyH$^+$][b] (µmol.g^{-1})	[PyL][b] (µmol.g^{-1})	V_{micro}[c] (cm^3.g^{-1})	V_{meso}[c] (cm^3.g^{-1})	External Surface[c] (m^2.g^{-1})	BET Surface[d] (m^2.g^{-1})	Crystal size (nm)
MFI	{[100] **10** 5.1 x 5.5 ↔ [010] **10** 5.3 x 5.6}***	12	641	183	0.16	0.08		415	
		43	281	42	0.16	0.05	82	452	500[e]
***BEA**	**12** 6.6 x 6.7* ↔ **12** 5.6 x 5.6*	12.5	315	316	0.16	0.86	201	535	30[f]
		13.7	641	93	0.16	0.27	192	496	980
MOR	[001] **12** 6.5 x 7.0* ↔ [001] **8** 2.6 x 5.7**	10	360	281	0.20	0.05	50	445	
		80	97	37	0.20	0.10	102	485	
FAU	[111] **12** 7.4 x 7.4***	6	481	186	0.27	0.15	147	722	
		15	270	101	0.31	0.21	155	873	370[f]
		30	88	18	0.34	0.20	166	742	
JZO	[100] **16** 10.6 x 9.4 / 10.5 x 9.6 *** ↔ [100] **12** 6.6 x 6.8	23.4	513	155	0.26	0.14	140	666	470[f]

[a] Calculated from the mass ratios measured by ICP-OES. [b] Pyridine adsorption-desorption (423 K) monitored by FTIR. [c] N_2-physisorption at 77 K, calculated with the t-plot curve of the Harkins-Jura method.[d] N_2-Physisorption at 77 K, BET method. SEM values given by previous works on the catalysts [e] [47], [f] [44]

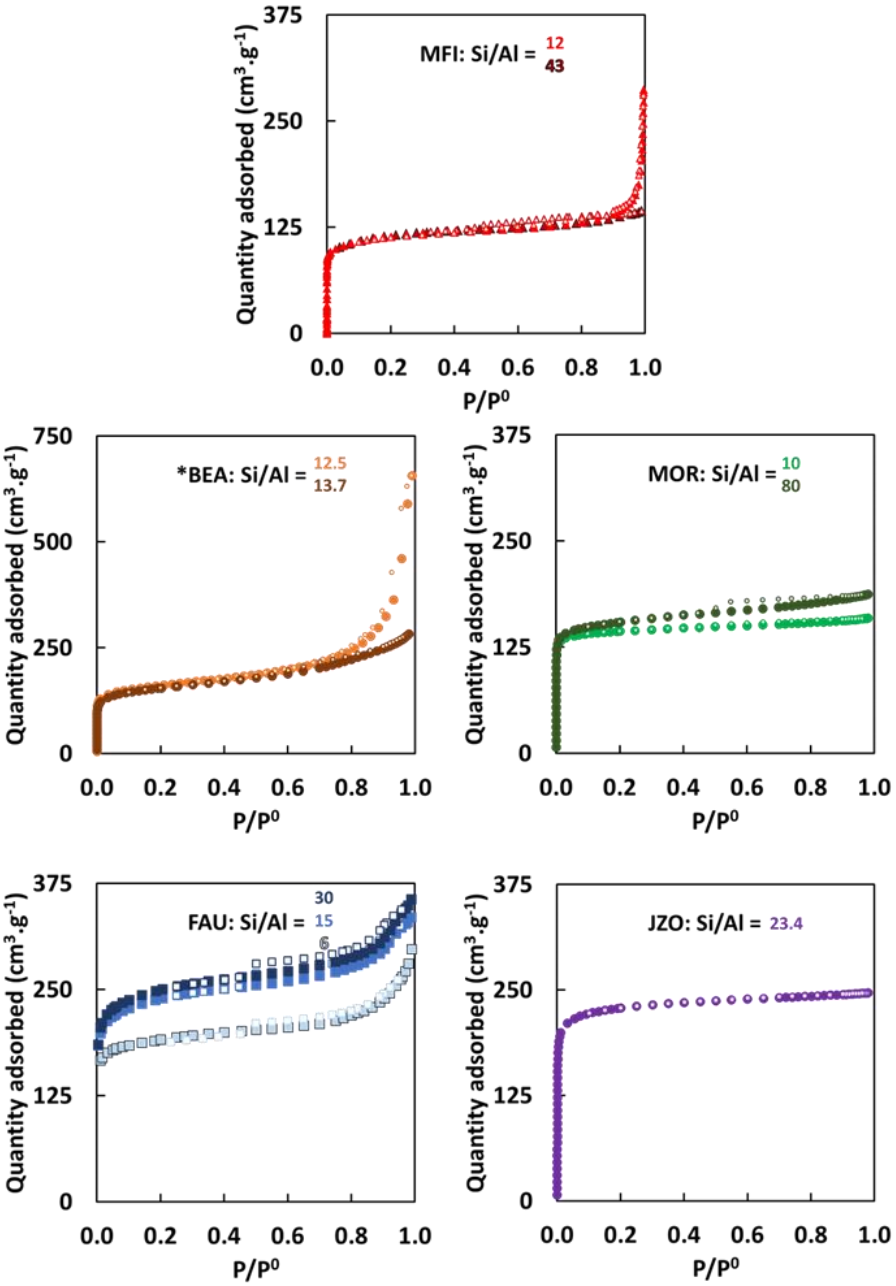

Figure V.1: N_2-Physisorption isotherms (77 K) of the zeolite catalysts. Full symbols: adsorption; open symbols: desorption.

Figure V.1 shows the different N_2-physisorption isotherms for each catalyst. Pore volumes (micro- and meso-pores), external surface and BET specific areas, are presented in **Table V.1**. Zeolites are highly porous materials, with type I isotherms. **MFI** (43) and **MOR** (80) present H4 type hysteresis loops (microporous slit-like pores) [53,54] while **MFI** (12) and ***BEA**(12.5) present high H3 type hysteresis loops. **FAU** (15) and **FAU** (30) both present relatively lower but larger H3 type hysteresis loops. **MFI** (12) and ***BEA** (12.5) both exhibit higher N_2 intake at high P/P^0 than **MFI** (43) and ***BEA** (13.7). This is indicative of

intraparticular mesoporosity induced by the agglomeration of nanosized crystals [53,54].

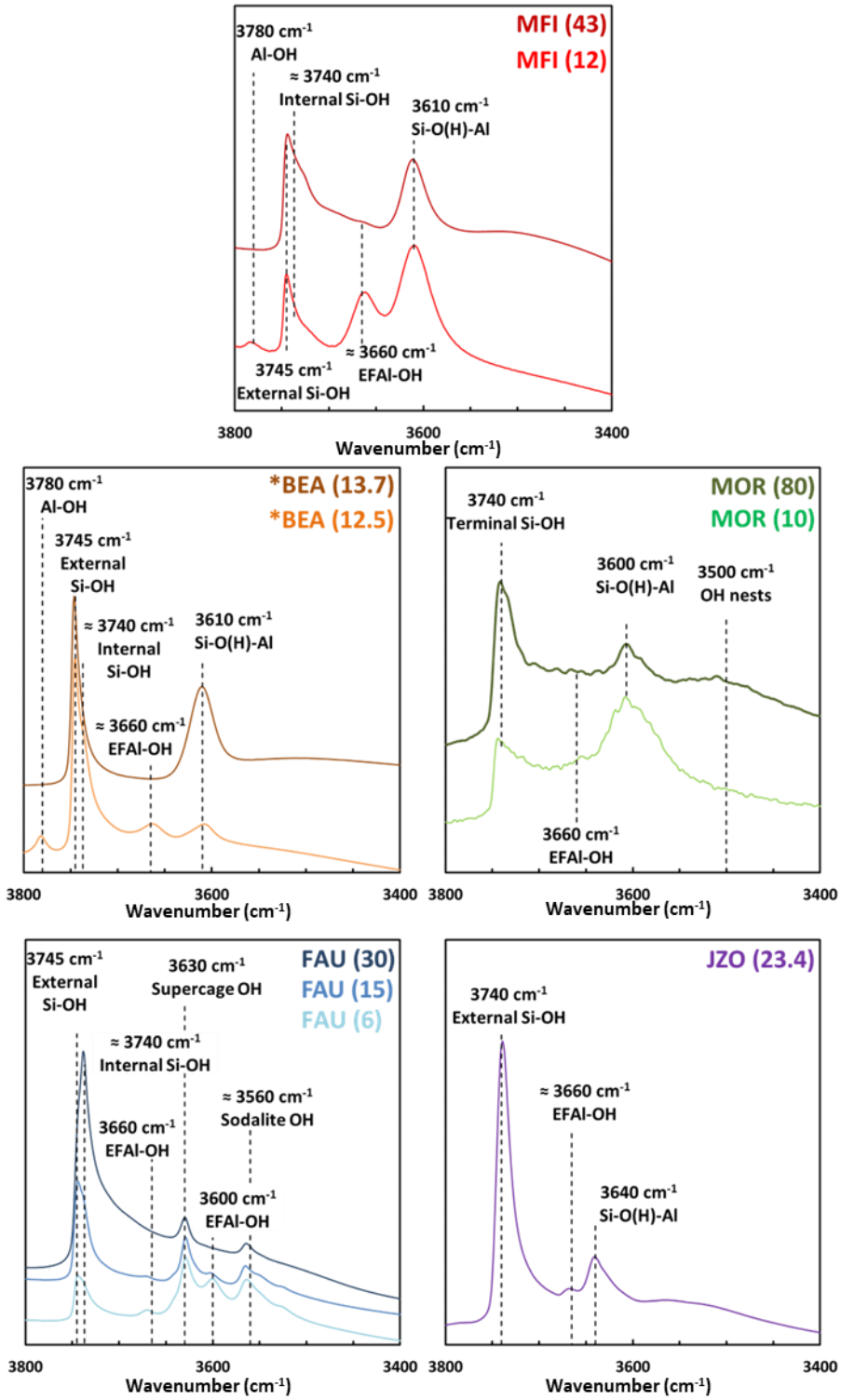

Figure V.2 FTIR spectra of the hydroxyl region (3800 – 3400 cm^{-1}) of the fresh catalysts.
Intensities (a.u.) are normalised to 20 mg samples for each structure.

Figure V.2 shows the OH stretching vibration region of the different zeolite catalysts. Each exhibit their respective characteristic bands:

MFI, ***BEA**, and **MOR** exhibit peaks indicative of bridged hydroxyls (Si-O(H)-Al), between 3600 and 3610 cm^{-1}, and **JZO** at 3640 cm^{-1} [44,55]. These bridged hydroxyls correspond to the Brønsted acid sites. Faujasites show unique bands around 3630 and 3560 cm^{-1}, corresponding respectively to bridged hydroxyls in supercages and sodalite cages. On ***BEA**(12.5) and **MFI**(12), a small band at 3780 cm^{-1}, belongs to Al-bonded OH groups [55].

JZO displays a broad peak at 3740 cm^{-1}, associated with external silanols [44,55]. These peaks are supplemented by shoulders around 3740 cm^{-1}, belonging to internal Si-OH [55].

MFI (12), ***BEA** (12.5), **MOR** (10), **FAU** (6) and **JZO** (23.4) display a broad band around 3660 cm^{-1} indicative of extra-framework-Al-bonded hydroxyl groups (EFAl-OH) [55,56]. **FAU**(6) and **FAU**(15), albeit to a lower extent, exhibit a small band at 3600 cm^{-1} (EFAl-OH). [55].

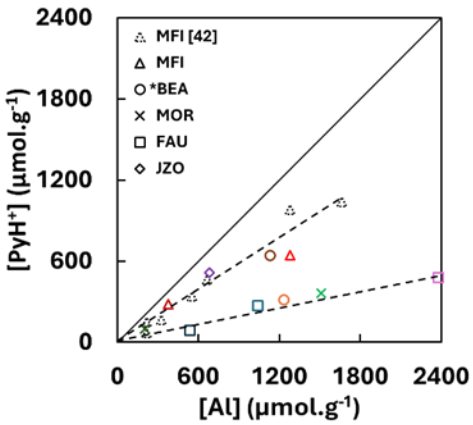

Figure V.3: Evolution of Bronsted acid site concentration (BAS) with Al content (µmol.g^{-1}) of the various zeolites.
Black full line: [PyH^+] = [Al]. **MFI**: dotted symbols are from previous work [42].

Figure V.3 shows the Brønsted acid sites (BAS) concentrations of the various zeolites probed by Py-FTIR as a function of their aluminium content. BAS concentrations range from 67 to 1038 µmol.g^{-1} (**MFI** Si/Al = 201 and **MFI** Si/Al = 9). They are proportional to aluminium content, and this suggests that most

aluminium atoms are in the framework. ***BEA**(12.5), having EFAl-OH (**Figure V.2**) has a lower BAS concentration, despite a higher aluminium content than ***BEA** (13.7) [57]. The values of [PyH^+] of the **FAU** are relatively low due to the presence of BAS in sodalite cages, less accessible to pyridine. Acidity could be underestimated slightly for these catalysts [55].

III.2 – Catalytic tests

Anisole disproportionation at 673 K under N_2 flow (0.048 atm partial pressure of anisole) is performed on each catalyst at different contact times (0.02 $g_{cata}.h.g_{anisole}^{-1}$ < W/F° < 0.17 $g_{cata}.h.g_{anisole}^{-1}$).

III.2.a Effects of structure, BAS concentration on TOF and deactivation modelling

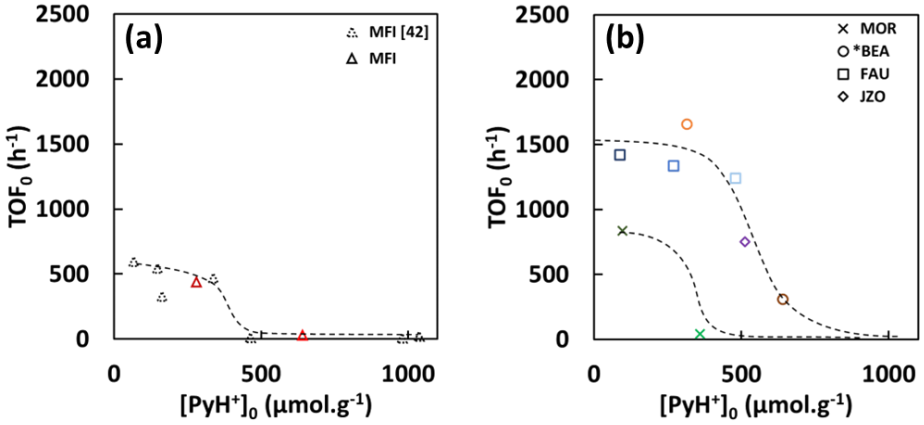

Figure V.4: TOF_0 evolution as a function of their BAS concentration **(a) MFI** and **(b)** the 12 and 16 MR catalyst.
MFI: dotted symbols are results from previous work [42].
All dotted lines are only to guide the eye.

Figure V.4a and **4b** show the initial Turnover Frequencies (TOF_0) evolution of the catalysts, as a function of their initial Bronsted acidities. TOF_0 is calculated as follows:

$$TOF_0 = \frac{\alpha_0}{[PyH^+]_0} \qquad \textbf{(Eq. V.5)}$$

With α_0 the initial activity obtained from the slope of the line drawn with $|\ln(1-X_0)| = f(W/F)$.

In **MFI**, the highest TOF_0 are three times lower than in **FAU** and ***BEA**, while the curves retain the same shape. This indicates that the larger pores **FAU** and ***BEA** promote the bimolecular reactions involved in anisole conversion.

The drop in TOF_0, previously reported for **MFI**, also occurs with the 12 and 16 MR catalysts. Higher acidity **MFI,** with very low activity, have negligible TOF_0. The larger pores of **FAU**, ***BEA** and **JZO** mitigate the drop, and the interconnectivity of the channels plays a role as well: the three-dimensional **FAU**, BEA and **JZO** provide higher TOF_0, even at higher acidities, while the two-dimensional **MOR** behaves more like an **MFI**.

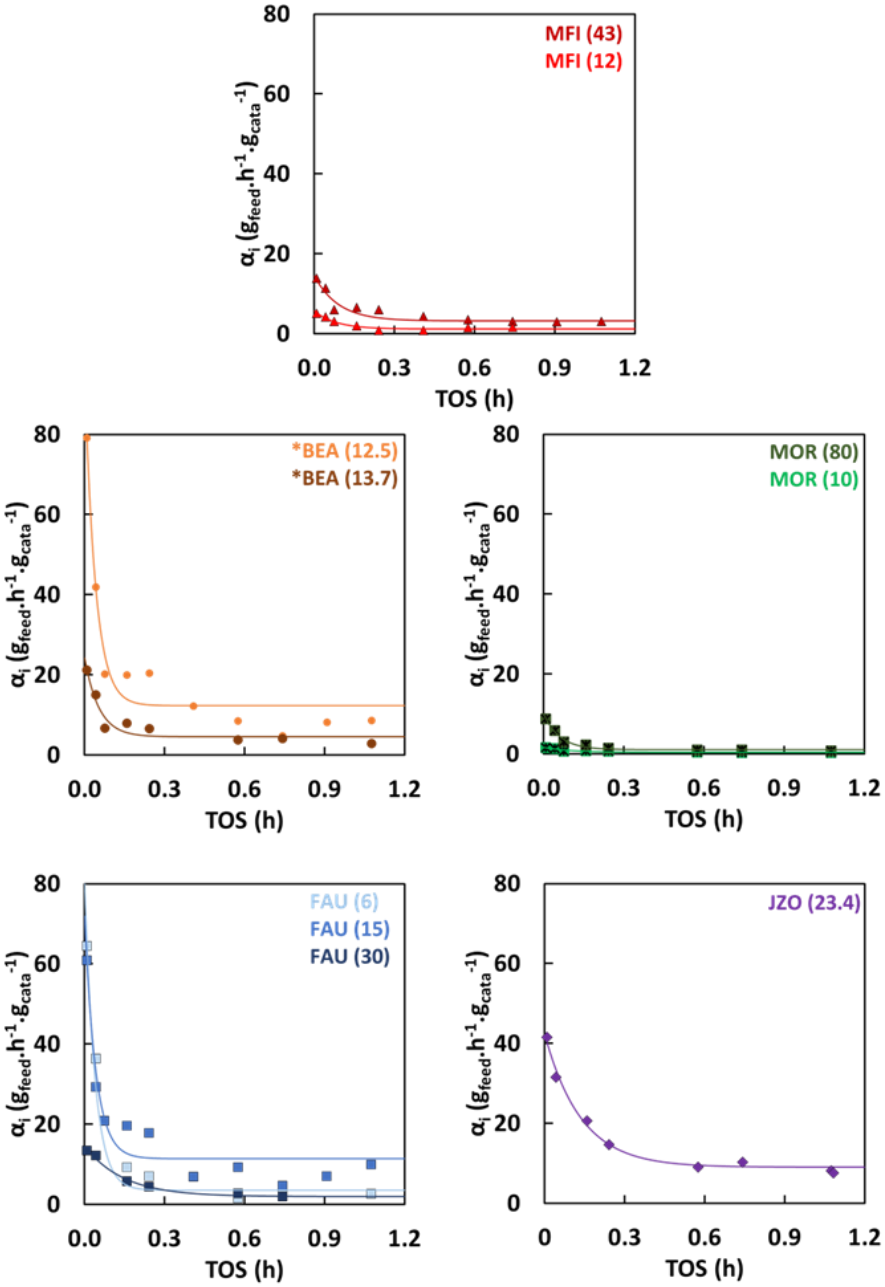

Figure V.5: Evolution of activity with time on stream for anisole disproportionation on zeolites.

Figure V.5 shows the catalyst deactivation over 1h of reaction. Independently of the zeolite structure and acidity, deactivation is fast and important and levels after 0.3 h.

***BEA** and **MOR** catalysts behave as **MFI(43),** the highest acidity leading to the lowest residual activity; **MOR**(10) is almost inactive irrespective of TOS.

In the case of the **FAU** catalysts, a higher acidity promotes a higher initial activity, but also faster deactivation rates and lower final activities: **FAU**(6) has a

final activity 30 times lower than at the start of the run, 6 times for **FAU**(15) and 7 times for **FAU**(30).

While **JZO**(23.4) possesses 16 and 12 MR, its BAS are located only in 12 MR channels, and its activity is in the range of ***BEA** and **FAU**. It also deactivates, albeit somewhat slower than the other zeolites, and its final activity is similar to ***BEA**(12.5) and **FAU**(15). Earlier, **Fahda et al.** poised that the 16 MR channels provide an efficient diffusion of the reaction products, allowing for slower deactivation of the catalyst[44].

All activity curves follow an inverse exponential law :

$$\alpha_i = \alpha_1 * e^{-k_D * TOS} + \alpha_2 \qquad \textbf{(Eq. V.6)}$$

$\boldsymbol{\alpha_0}$ (*i.e.* $\boldsymbol{\alpha_1 + \alpha_2}$) is the initial catalyst activity, and k_D is the deactivation constant for each catalyst. **Table V.2** shows these values for each catalyst, as well as coke content and coefficient of determination, the latter showing its applicability to all our zeolite catalysts.

The higher k_D, the faster and higher the catalyst deactivation. It is highest for **FAU**(6), **FAU**(15), and ***BEA**(12.5). $\boldsymbol{\alpha_1}$ represents the active species that will cease participating to the reaction, while $\boldsymbol{\alpha_2}$ represents the active species responsible for the (low) residual, steady-state activity.

Eq. V.6 is reminiscent of the deactivation function previously used by Guisnet and Ribeiro[33]:

$$\phi_i = \frac{\alpha_i}{\alpha_0} = \frac{\alpha_1}{\alpha_0} e^{-k_D * TOS} + \frac{\alpha_2}{\alpha_0} \qquad \textbf{(Eq. V.7)}$$

Where the dimensionless number ϕ_i is the deactivation of the catalyst at any TOS_i (h) and the added factors ($\frac{\alpha_1}{\alpha_0}$, $\frac{\alpha_2}{\alpha_0}$) indicate that deactivation is not solely a factor of coke deposition.

Table V.2: activities (α), deactivation constants (k_D), determination coefficient (R^2) and coke content for each catalyst

Grey row: ***MFI*** *reference from* [19].

Structure	Si/Al	$\alpha_i = \alpha_1 * e^{-k_D * TOS} + \alpha_2$				
		α_1 ($g_{feed}.h^{-1}.g_{cata}^{-1}$)	α_2	k_D (h^{-1})	R^2	Coke content (wt.%)
MFI	12	4.5	1.2	12.2	0.92	7.3
	43	11.2	3.2	11.1	0.96	7.6
***BEA**	12.5	83.3	12.4	24.9	0.95	11.2
	13.7	19.7	4.6	18.6	0.92	14.9
MOR	10	1.2	0.4	9.6	0.89	1.9
	80	8.8	1.1	16.6	0.99	3.4
FAU	6	77.4	3.6	26.2	0.95	11.1
	15	60.5	11.4	24.2	0.93	10.3
	30	12.6	2.0	6.8	0.99	6.7
JZO	23.4	33.2	9.1	7.3	0.99	11.2

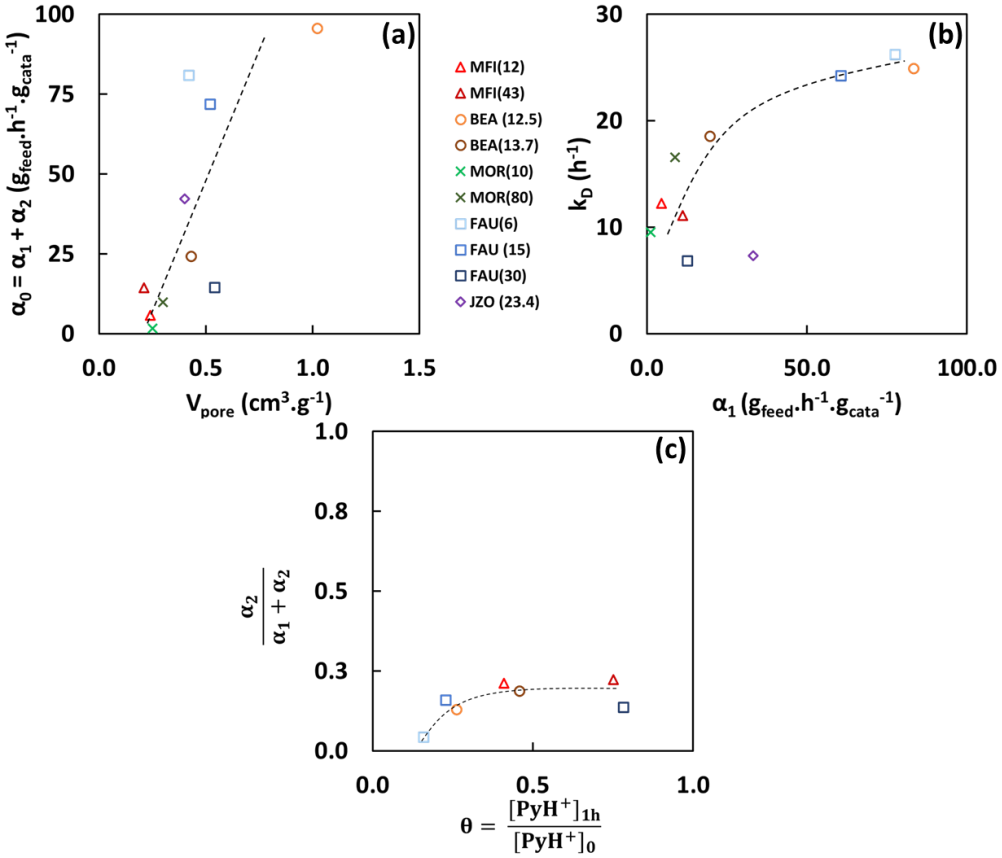

Figure V.6: Dependence of the deactivation law on the textural and physico-chemical properties of the catalyst : **(a)** initial activity *vs.* porous volume; **(b)** deactivation constant *vs.* pre-exponential factor (α_1); **(c)** residual activity contribution *vs.* remaining Brønsted acidity after 1h (θ).

α_0 increases with zeolite porosity (**Figure V.6a**). As **Figure V.1** shows that ***BEA**(12.5) is nano-sized, while ***BEA**(13.7) is micron-sized, this highlights the benefits of crystal size reduction. **Figure V.6b** shows that k_D and α_1 are also positively correlated, *i.e.* more active species will lead to a faster deactivation. This trend, however, seems to be somewhat mitigated on **JZO**, probably due to the secondary 16 MR porosity. While Brønsted acidity is intimately linked to initial activity and TOF (**Figure V.4**), the ratio steady state activity/initial activity ($\frac{\alpha_2}{\alpha_1+\alpha_2} = \frac{\alpha_2}{\alpha_0}$) does not depend on the initial acidity (**Figure V.S2**), and remains in the range of 15 to 20% (only **FAU** (6) falls under 10%). Other factors considered as the degree of hierarchisation, BET surface area and acid sites density in the catalyst have no significant impact on this ratio (**Figure V.S2**). In addition, **Figure V.6c** shows that $\frac{\alpha_2}{\alpha_0}$ does not significantly depend on the availability of the acid sites, *i.e.* that some occupied acid sites still participate to the reaction, either by competitive adsorption of the reactants, or by activation of the adsorbed

"deactivating" species. This behaviour was reported, for instance, in liquid and gas phase isomerisation and alkylation reactions of hydrocarbons [58].

Figure V.4 and **Figure V.5** indicate the presence of an auto-inhibition effect of the Al sites proximity for ***BEA** and **MOR**, as previously reported for **MFI** [42]. This inhibition is somewhat attenuated for ***BEA** due to the interconnectivity (3D) of its channels, lacking on **MOR** (2D), where acid sites in the 8 MR side-pockets would play an additional role.

Zeolite structure and acidity do not therefore change the general deactivation pathways. For all catalysts, activity decreases to around 20% of its initial value before reaching steady state. The main factor influencing activity is the catalyst total pore volume. The residual activity is not directly linked to the remaining accessible acid sites and thus "coke" participates to the anisole transformation. Initial TOF's are highly dependent on acidity, with additional influences of both pore size (10, 12, 16 MR) and channel interconnectivity (2D – **MOR** – vs 3D – FAU, ***BEA**, **JZO**). As a result, higher BAS concentrations tend to rapidly decrease initial activity and TOF_0, due to the auto-inhibition effect produced by higher adsorption energies induced by "paired" acid sites. This effect is enhanced by the low interconnectivity of the 2D zeolites (**MOR**) and mitigated with larger pore sizes in 3D, 12^+ MR zeolites (***BEA**, FAU, **JZO**). These larger pore openings and channels promote bimolecular reactions by largely mitigating (or eliminating) the steric hindrance of the channels.

III.2.b Products selectivities, structural and acidity effects.

Anisole disproportionation on **MFI** zeolites mainly leads to transalkylation as the primary products (methylanisole and phenol), react further and methylated phenolates, such as cresols (secondary products), xylenols (tertiary products) and mesitols (further methylation of xylenols) appear in the product slate [17,19,42]. It is still the case for other zeolite structures, but some changes are noticeable, due either to acidity or structure.

Figure V.7 shows the evolution of conversion (X, wt.%) and main products selectivities (S_i, %) against time on stream for some of the catalysts (see **Figure V.S3** for all catalysts).

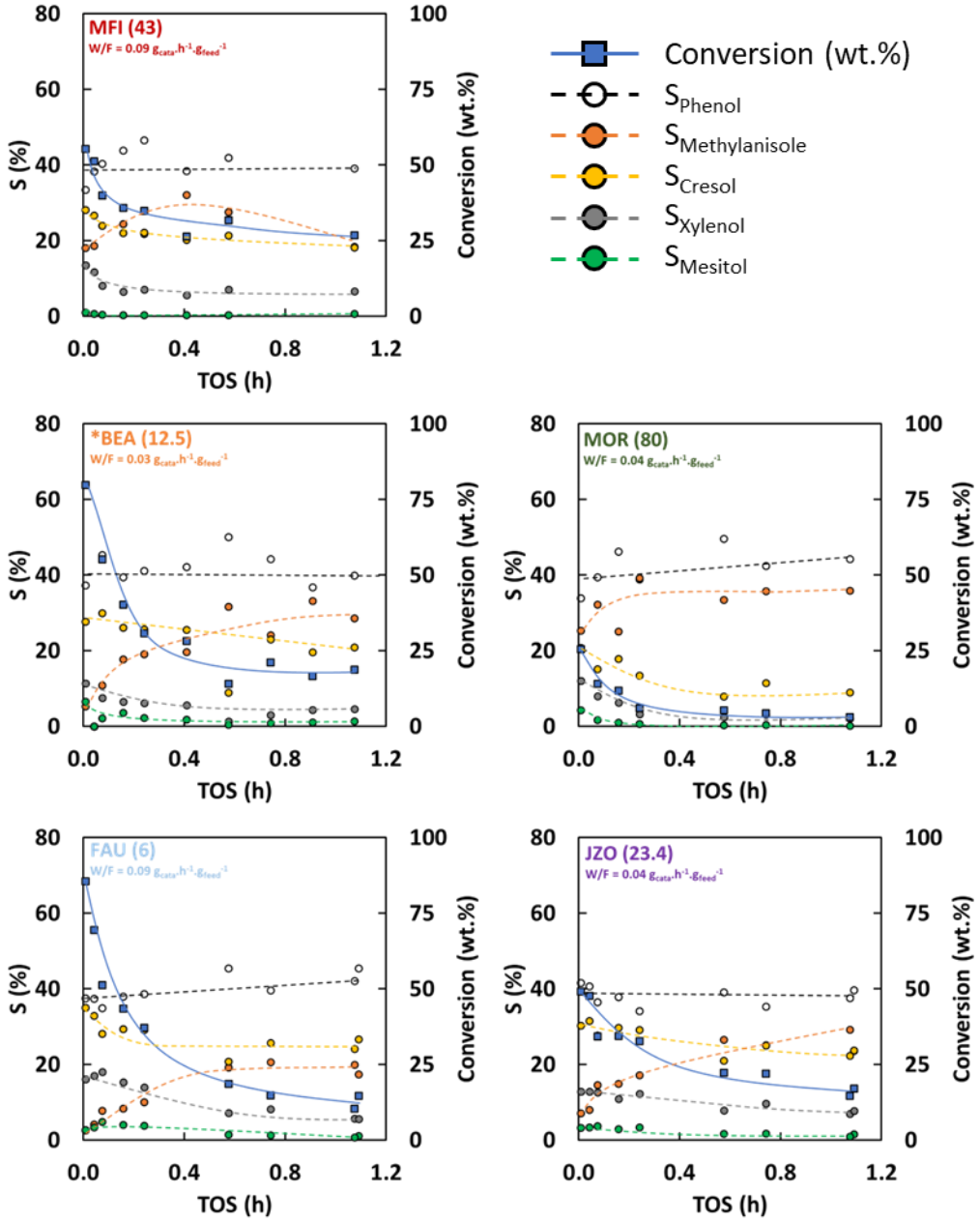

Figure V.7: Anisole conversion and products selectivity for selected catalysts with time on stream.
T = 673 K; P_{An} = 0.048 atm; P_{tot} = 1 atm.

Phenol selectivity, around 40 %, is mostly independently of the zeolite structure or acidity as most reactions involving anisole are producing phenol, compensating for its consumption in secondary reactions[19]. This confirms that the overall reaction pathway is not and remains the same as previously reported for **MFI**.

Methylanisole selectivity follows the same pattern: it increases as conversion decreases and reaches a plateau at steady-state. The latter depends

only on contact time, as was shown previously for **MFI** (43) [19]. Cresol selectivity evolves inversely to that of methylanisole, but again independently of structure and acidity. For most structures, when cresol and methylanisole selectivities cross before reaching their respective plateaus, the cause is the equilibrium between the two main paths to cresol production is shifted. It evolves from mainly **Reaction(1)** to mainly **Reaction(2)**:

$MA_{(ads)} + Ph_{(g)} \rightarrow Cr_{(ads)} + Cr_{(g)}$ **Reaction(1)**

$An_{(g)} + Ph_{(ads)} \rightarrow Ph_{(g)} + Cr_{(ads)}$ **Reaction(2)**

Such an overtaking of **Reaction(1)** (hereafter called **Path I**) by **Reaction(2)** (hereafter called **Path II**) was visible in the coke composition on **MFI** from previous work, where more methylated products were present at higher TOS [19]. It is indicative of catalyst fouling by phenol adsorption followed by its methylation and these new active species participate to the steady-state conversion of anisole, and further methylation of the coke species. The continued presence of **Path I** even after its decrease as **Path II** dominates comes from the competitive adsorption of anisole and methylanisole on BAS, due to higher adsorption energies than $(Me)_x$Phenols (-110 to -145 $kJ.mol^{-1}$ on single sites versus -82 to -124 $kJ.mol^{-1}$ for phenolics [19]).

Xylenol production follows the same pattern as cresol, leading to Mesitol production.

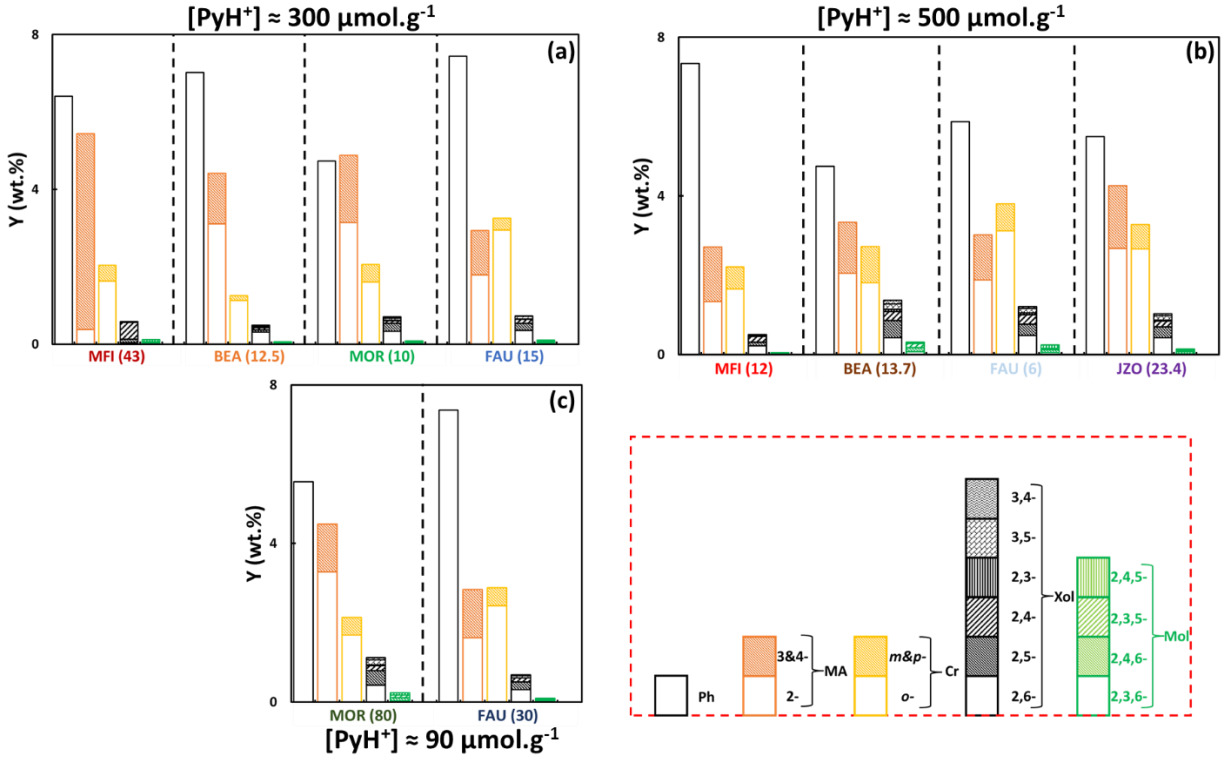

Figure V.8: Isomers yields and distribution at identical conversion (X = 13.6 ± 0.75 wt.%) and acidity: catalysts at [PyH$^+$] ≈ 300 µmol.g^{-1}, **(b)** 500 µmol.g^{-1} and **(c)** 90 µmol.g^{-1}.
Ph: Phenol (White); MA: Methylanisole (Orange); Cr: Cresol (Yellow); Xol : Xylenol (Black); Mol : Mesitol (Green).

Figure V.8 displays the yields for the main products and their position isomers at isoconversion (≈13.5 wt.%) for each catalysts, and at isoacidity (**Figure V.8a**: 300 µmol.g^{-1}, **Figure V.8b**: 500 µmol.g^{-1} and **Figure V.8c** 90 µmol.g^{-1}).

Previous work on **MFI** showed that the yields for the main products were not affected by acidity, but rather a function of conversion [42]. **MFI** (43) also showed a strong shape selectivity for the para of methylanisole, not found in the cresols (mainly the ortho- isomer). It was, however, found in the xylenol isomers in the coke: the combination of high shape selectivity towards p-MA, and high availability of the o-Cr increased the quantity of the 2,4-Xol in the product fraction as well as in the coke content (followed by a high proportion of 2,4,6-Mol when coke "aged", after more reaction time)[19]. The m-MA isomer is almost absent due to the o- and p- directing effect of the methoxy group, while the o-MA isomer is less produced, due to its steric hindrance.

In **MFI**(12), the higher shape selectivity for p-MA is absent due to the stronger retention of products on its BAS, in agreement with previous DFT

calculations (with the increase of the concentration of acid sites, the para- and meta- isomers of MA are more strongly retained by the BAS, thus diffuse less easily out of the zeolite channels, and are therefore more likely to react with other molecules in the gas phase) [42]. This re-establishes the selectivity induced by the electronic effects for the ortho- and para- isomers. It also impacts the production of 2,4-Xol, no longer favoured compared to other Xol isomers.

For **FAU** and ***BEA**, the higher acidity promotes transalkylations, and the production of Xol and Mol. It does not, however, promote significant changes in the isomer selectivity, with o-cresol staying the main Cr isomer. This is echoed by the higher selectivity for the 2,X- isomers of Xol (mainly X = 4, 5, 6 for steric reasons). ***BEA**(13.7) and **FAU**(6) show much higher Xol and Mol yields than their less acidic counterparts. This is likely due to the faster fouling mentioned in **Figure V.7** (and **Figure V.S3**) induced by their higher acidity and higher adsorption energies of the products. For ***BEA**, the differences are amplified by the nanosized crystals of ***BEA**(12.5) favouring faster MA diffusion, without further transalkylation. **FAU** also shows the inverse effect of other structures, with higher acidity delaying and even preventing the prevalence of **Path II** (**Figure V.S3**).

As for the **MOR** catalysts, higher acidity produces the inverse effect of other structures: further methylation is no longer promoted by higher acidity, and it behaves as an **MFI**. **MOR**(10) is also the only catalyst with a higher MA than Ph selectivity. There is a slight decrease in Xol and Mol, but not in Cr. This implies an almost immediate fouling of the catalyst, similar to **MFI**(12), ***BEA**(13.7) and **FAU**(6), and thus **Path II** is immediately favoured for the production of phenolics. This alone, however, does not entirely explain why MA is produced at a higher rate than Ph on **MOR**(10).

Mordenites possess 8 MR side pockets, accessible to molecules the size of toluene (here, Ph), where they can react [59]. MA, larger than Ph (H_3C-O- > HO-, plus methyl substituent), cannot access these side pockets and their BAS. This size-exclusion effect is not noticeable with **MOR**(80), most likely due to its weaker acidity and thus adsorption of the products, which allows for already easier diffusion out of the channels.

Thus, zeolite structure has a clear effect on anisole disproportionation and isomer selectivity, but acidity also plays a role: the shape selectivity of **MFI** for p-MA is hindered by a higher BAS concentration, while the larger channels of ***BEA**, **FAU** and **JZO** (and supercages of the latter two) promote bimolecular reactions and faster diffusion. Higher acidity in **FAU** shifts the Cr production equilibrium

between **Paths I and II** towards the former. Finally, 2D zeolite **MOR** provides a unique product selectivity when paired with high acidity, due to the size exclusion effect of its side-pockets.

III.3 – Coke formation and composition

The initial deactivation step of **MFI** during anisole disproportionation was attributed to the fast filling of the porous volume (and adsorption on the BAS) by the reaction products, so-called “oxygenated coke species”, and none of the habitual polyaromatic species were found in hydrocarbon transformation processes [19,42]. The next part provides information on the effect of zeolite structure on the composition of this unconventional “coke”.

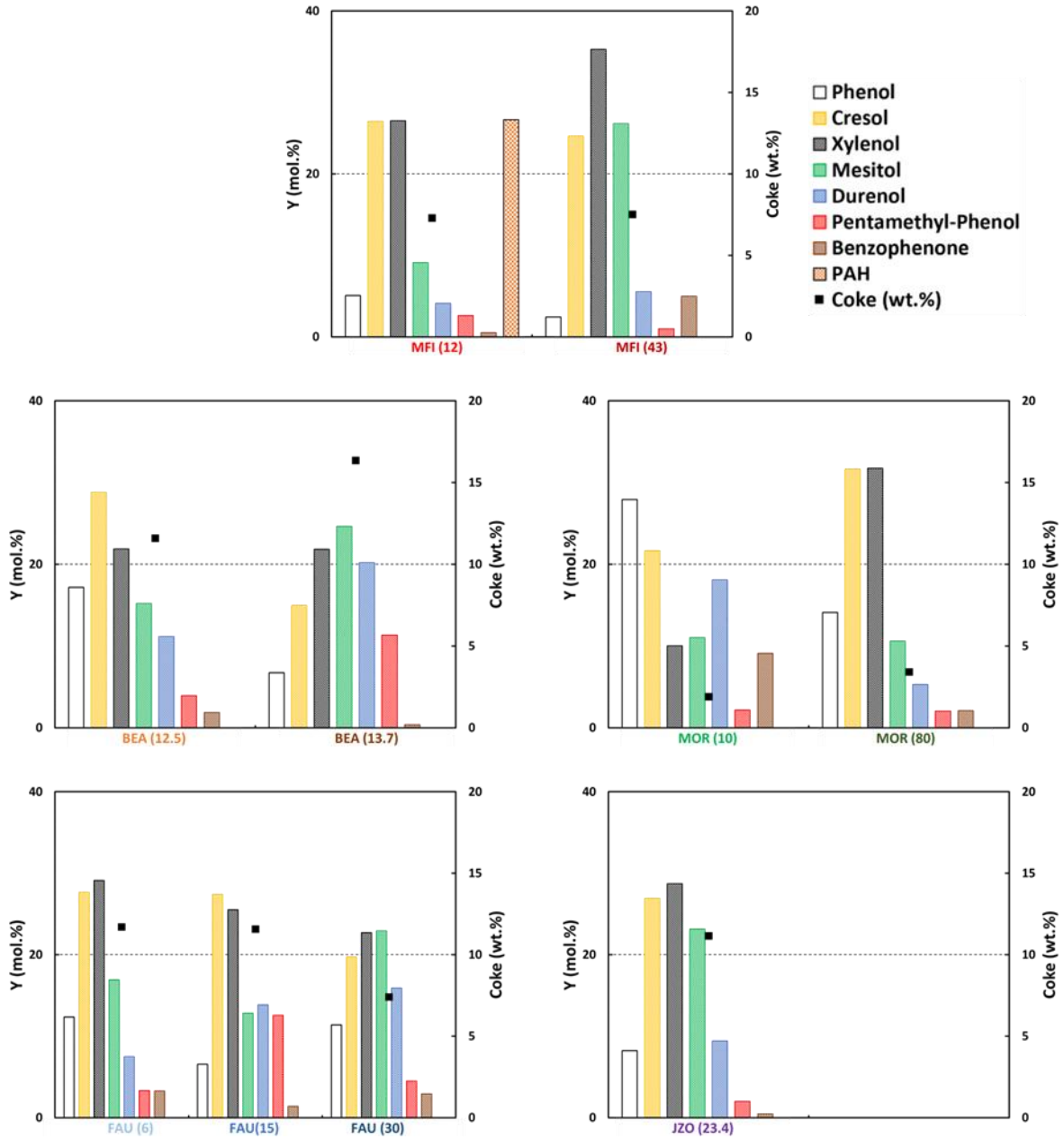

Figure V.9: Quantification of the main coke components after 1h of reaction for each catalyst. (Y: fraction of the components in the soluble coke extract).

Figure V.9 displays the distribution of the main coke components for each catalyst. These include the reaction products: phenol, cresol (methyl-phenol), xylenol (dimethyl-phenol), mesitol (trimethyl-phenol), as well as more methylated phenolics: durenol (tetramethyl-phenol) and pentamethyl-phenol. No anisole or methylanisole are detected. A notable addition is benzophenone, previously not identified due to background noise and impurities on the GC-MS chromatogram. Pentamethyl-phenol, previously not seen for similar reasons, is also found on each spent catalyst. Thus, structure and acidity do not significantly change the coke composition as it was reported previously on **MFI**(43) [19].

The quantification of the main species leads to the average molar mass and density presented in **Table V.3**. While the coke quantity on the catalyst and its exact composition varies with zeolite structure and acidity, its average molar mass and density show fairly low variation: from 121 to 132 g.mol^{-1} and 0.99 to 1.03 g.cm^{-3} respectively.

Table V.3: Average coke content, molar mass and density for each catalyst.

Structure	Si/Al	Coke (wt.%)	$\overline{M}_{coke}$ (g.mol^{-1})	$\overline{\rho}_{coke}$ (g.cm^{-3})
MFI	12	7.3	173.5	1.27
	43	7.6	123.1	1.02
***BEA**	12.5	11.2	121.3	1.02
	13.7	14.9	132.3	1.00
MOR	10	1.9	124.3	1.03
	80	3.4	115.7	0.99
FAU	6	11.1	122.7	1.01
	15	10.3	128.3	1.00
	30	6.7	127.5	1.01
JZO	23.4	11.2	121.6	1.00

The average coke contents are function of the available pore volume for each structure: the larger pores of the 3D ***BEA**, **FAU** and **JZO** accommodate more coke (pore filling), while the 2D channels of **MOR** are easily obstructed, and thus allow for lower coke content (pore blocking, **Figure V.S4**) [60]. Higher anisole conversion also produces more coke.

As observed above for product shape selectivity, zeolite structure and acidity affect the distribution of the coke components: higher acidity in ***BEA** shifts the composition towards more methylated products (mesitol, durenol, pentamethylphenol), while the weaker sites of FAU produce the inverse effect, primarily emphasizing the retention of cresol and xylenol [61].

Notable exception, **MFI** (12) produces and retains conventional polyaromatic hydrocarbons (oxygenated and not, see **Table V.S1**), in addition to the retention of the reaction products. This implies that the combination of high acidity (641 $\mu mol.g^{-1}$) and smaller pore openings (10 MR) promotes the formation of polyaromatic coke, at low conversion, while it is inhibited on the other catalysts. The coke content between **MFI** (12) and **MFI** (43) does not vary significantly (7.3 wt.% ad 7.6% respectively). However, since **MFI** (12) promotes the formation of PAH, the average coke molecular mass and density increase by 50 $g.mol^{-1}$ and 0.25 $g.cm^{-3}$ respectively.

Literature provides two conditions for coking through the Sullivan mechanism [36,37]. First, a steady source of alkylation on the aromatic cycles for the paring mechanism. In the present case, it occurs by multiple transalkylation reactions on the phenolics. Second, the ring contraction-expansion of the C_6 aromatic cycle after carbon transfer via propylcarbenium cycle formation and opening should take place. The absence of alkyl groups bigger than methyl on the phenolics shows that this second condition is not fulfilled. Therefore, no polyaromatics are detected on the spent catalysts, except **MFI**(12) (**Figure V.9**), therefore the Sullivan mechanism (**Scheme V.S1**) does not occur. It was previously proposed that the hydroxyl function found in the extracted coke was responsible for inhibiting the Sullivan mechanism [19]. **Scheme V.1** proposes an explanation for this inhibition:

The electronic effect of the hydroxyl group increases the electron density on the aromatic cycle(①), irrespective of its degree of methylation. The resulting mesomeric forms (②) all show a positive charge on the oxygen, and adsorption on the zeolite BAS stabilises this configuration(③), preventing the formation of carbenium species susceptible to induce the paring reaction in **Scheme V.S1**[36]. Similarly, this mesomeric effect and the resulting enhanced adsorption energies prevent bimolecular condensation reactions that would result in bulkier coke content[35].

The presence of some hydroxyl-substituted polyaromatic species on **MFI**(12) (**Figure V.9**) shows that, either high acidity or the resulting high adsorption energies for the reaction products, help overcome the less-than favourable conditions for conventional coke formation. Chaouati et al. showed that, with low reactant partial pressure, another coke growth mechanism occurs by condensation (dehydrogenating coupling) of adsorbed species [35]. It is

normally limited by high adsorption energies and higher reactant partial pressure.

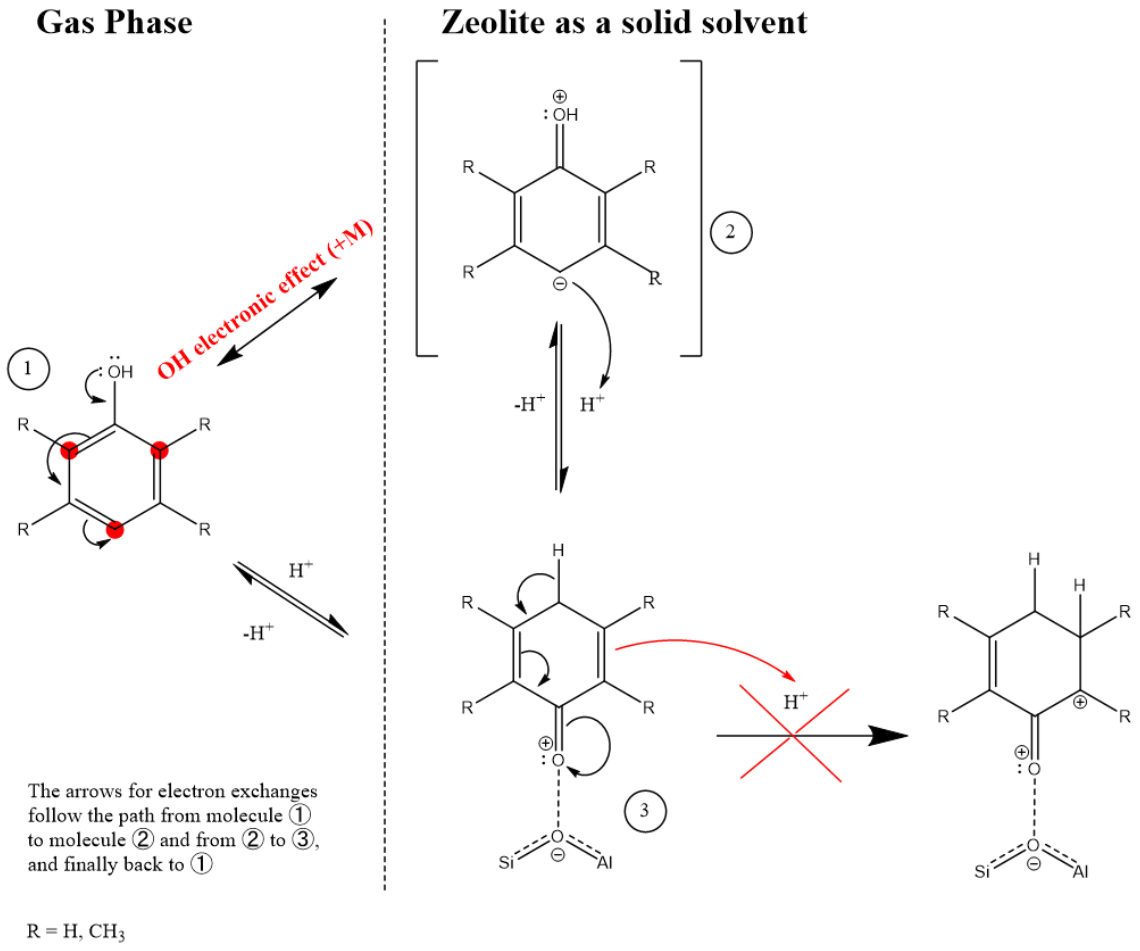

Scheme V.1: Proposed mechanism adsorption of $(Me)_x$ phenols on zeolite acid sites

In a nutshell, previous work on **MFI** showed that deactivation occurs by adsorption of reaction products on the active sites and fouling of the zeolite channels. It is extended here for other zeolitic materials. The nature of those deactivating species is not influenced by structure nor acidity, and only their distribution changes. The multiple methylations of the phenolic species could be likened to “aging” of the coke species. Those methyl-phenolics are present in the samples, even with the larger openings, in higher amount than their respective acid sites, thus they are most likely strongly adsorbed everywhere in the zeolite channels, and not only on Brønsted acid sites (fouling of the catalyst).

III.4 – Deactivation modes and “coke” toxicity

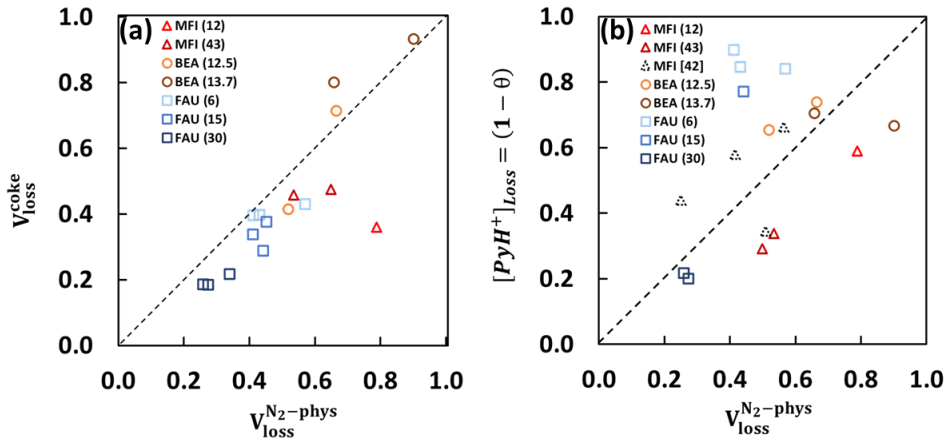

Figure V.10: ***(a)*** Comparison between relative porous volume losses, measured by N_2-physisorption (**Eq. V.8**) and calculated with the $\bar{\rho}_{coke}$ at ToS = 1h (**Eq. V.9**).
(b) Measured relative acidity loss (**Eq. V.10**) relative to apparent loss in microporous volume for **MFI**, ***BEA** and FAU at ToS = 1h.

Figure V.10 shows the degradation of physico-chemical properties (Brønsted acidity and micropore volume) of the catalysts after 1h on stream. **Figure V.10a** compares the relative micropore volume loss measured by N_2-physisorption (**Eq. V.8**) and the one calculated with $\bar{\rho}_{coke}$ (**Eq. 9**). These values are similar for most catalysts, indicating that N_2 can access the whole porosity of the zeolites, even with the presence of high amounts of coke. Thus, there is no blockage (or plugging) of the channels by the “coke” species, as opposed to n-heptane cracking over **HFAU** (723 K, high coke content) [27]. This is explained by the relatively small size of these molecules, compared to the pore openings. They could diffuse in the channels without steric hindrance, especially for the larger pore openings if other factors were not involved [25].

$$V_{loss}^{N_2-phys} = \left(1 - \frac{V_{spent}}{V_0}\right)_{N_2-phys} \quad \textbf{(Eq. V.8)}$$

$$V_{loss}^{coke} = \left(\frac{\%coke}{100.\rho_{coke}.V_0}\right) \quad \textbf{(Eq. V.9)}$$

Figure V.10b relates the relative acidity loss (**Eq. 10**) with the micropore volume loss (**Eq. V.8**). Most of the data points are above or on the x = y dotted

line, indicating that the acidity loss occurs at the same rate as the loss in micropore volume. Thus, there is no difference in accessibility between N_2 and pyridine in the zeolite channels (for ***BEA**, **FAU** and **MFI**), and no partial or total pore blocking/plugging for the catalysts. The phenomenon of coke displacement by pyridine during Pyr-FTIR, previously mentioned for **MFI** [12,19], is responsible for an underestimation of the loss of acidity. It is observed for **MFI** as well as **FAU** and ***BEA** (**Figure V.S5**), thus explaining the position of the data points under the dotted line. There is no major loss of acidity without loss of porous volume, therefore an active site poisoning is unlikely.

$$[PyH^+]_{Loss} = (1 - \theta) = \left(1 - \frac{[PyH^+]_{1h}}{[PyH^+]_0}\right) \quad \textbf{(Eq. V.10)}$$

Finally, **Figure V.11** shows the relationship between the coke content and textural properties of the zeolites: **Figure V.11a** plots the average number of coke molecules per available acid site against the initial acidity of the catalysts ($[PyH^+]_0$). It shows that, with the exception of **MFI**(12) and **MOR**(10), every other zeolite holds multiple coke molecules per available acid site. While this number decreases with higher initial acidity, it shows that a majority of the coke molecules cannot adsorb onto BAS. It is therefore most likely adsorbed on silanols.

Figure V.11b shows that coke content first increases with acid BAS density, to then level around 2 mmol.cm^{-3} being then only function of the zeolite pore size and channel connectivity. The coke content therefore only depends on the surface available for adsorption, and, just as with **MFI**, the deactivation mode for anisole disproportionation is by fouling of the zeolite channels by adsorption of the phenolic compounds. Overall, although Phenol and its methyl derivatives are easily adsorbed and cover most of the zeolite, the coke toxicity to the acid sites is quite low, according to the steady-state observed for most catalysts.

MFI(12) holds less than 1 coke molecule per available acid site, while still holding the same coke weight as **MFI**(43). It is indicative of the growth of the conventional PAH species. As for **MOR**(10), the very low amount of coke in the spent catalyst explains the lower coke to BAS ratio.

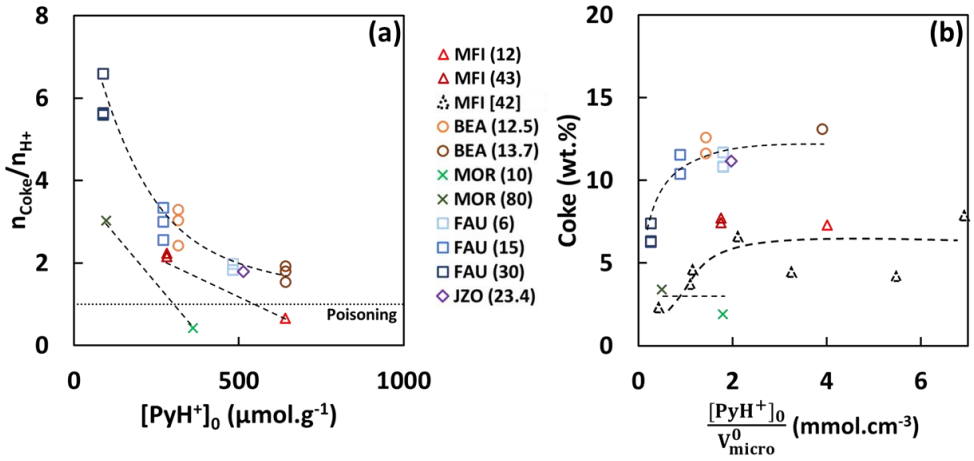

Figure V.11: (a) Number of coke molecules per initial acid site relative to the catalyst acidity and **(b)** coke content relative to acid sites density in the microporous volume.

Although phenol adsorption is strong on BAS, and is a deactivating factor in most cases, anisole disproportionation is an exception: the results in **Figures V.5, V.6** and **V.7**, with the low amount of phenol in the coke (**Figure V.9**), lead to the conclusion that the steady-state is in part produced by the activation of phenol ,by its very adsorption, for the transalkylation reactions with anisole in the gas phase. Similarly, any anisole or methylanisole adsorbed on BAS are rapidly transformed into phenolics, thus explaining their absence from the coke make-up. Consequently, **Scheme V.2** shows the proposed reaction "arborescence" for anisole disproportionation in acid zeolites. Whichever reaction path is followed, anisole stays the main reagent, and phenol the main product directly in the gas phase, as is the case no matter the conversion, contact time or catalyst.

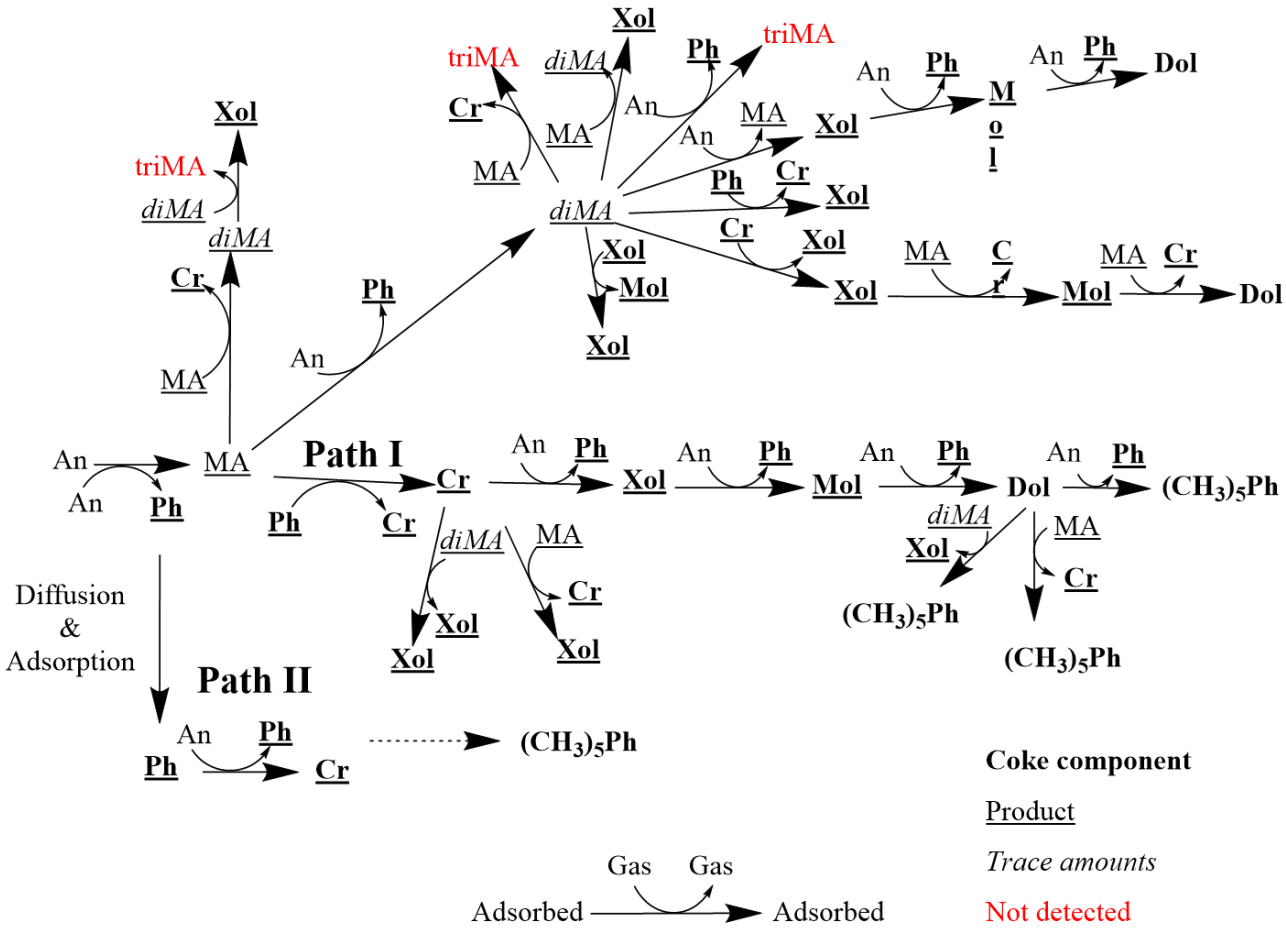

Scheme V.2: Proposed bimolecular reactions paths for anisole and its reaction products.

(An – Anisole; Ph – Phenol; MA – Methylanisole; Cr – Cresol; Xol – Xylenol; Mol – Mesitol; Dol – Durenol; diMA – Dimethylanisole; triMA – Trimethylanisole)

IV – Conclusion

Zeolitic catalysts (10, 12 and 16 MR) with varying acidities, channel interconnectivity and crystal sizes were tested in anisole disproportionation, a model reaction to assess the behaviour of methoxy-aromatics during catalytic upgrading of primary pyrolysis products. Different zeolite structures produced the same light, oxygenated “coke” molecules (methyl-phenolics), independently of their pore sizes, channel geometry, etc. Acidity affects only the coke composition in **MFI**, probably in relation to the auto-inhibition effect of lower Si/Al ratios . these produced oxygenated derivatives of conventional PAH species (alcohols, methoxy, aldehyde, etc. substituted species). These are uncommon in literature, and their formation by the Sullivan mechanism is inhibited by the electronic effects of the oxygen groups. Here they are formed, probably via condensation of the adsorbed species (another coke formation mechanism referenced to in literature, allowed by the low partial pressure of reactant).

In conclusion, anisole is representative of the methoxy function behaviour in the biomass pyrolysis oils catalytic upgrading conditions. However, the numerous remarkable phenomena that are reported here (steady-state activity, unconventional oxygenated coke species, inhibition of the polyaromatic coke formation) are not found in the conditions of biomass catalytic fast pyrolysis. Thus, more complex feeds should be studied (anisole combined with olefins, guaiacol, …) to provide more accurate descriptions of the biomass components. Some of this co-feeding work was proposed, notably with tetraline and propylene, the latter being detrimental to the overall activity and promoting coke formation.

V – References

[1] J.D. Adjaye, N.N. Bakhshi, Production of hydrocarbons by catalytic upgrading of a fast pyrolysis bio-oil. Part I: Conversion over various catalysts, (1995) 23.

[2] T.R. Carlson, G.A. Tompsett, W.C. Conner, G.W. Huber, Aromatic Production from Catalytic Fast Pyrolysis of Biomass-Derived Feedstocks, Top Catal 52 (2009) 241–252. https://doi.org/10.1007/s11244-008-9160-6.

[3] T.R. Carlson, Y.-T. Cheng, J. Jae, G.W. Huber, Production of green aromatics and olefins by catalytic fast pyrolysis of wood sawdust, Energy Environ. Sci. 4 (2011) 145–161. https://doi.org/10.1039/C0EE00341G.

[4] T. Dickerson, J. Soria, Catalytic Fast Pyrolysis: A Review, Energies 6 (2013) 514–538. https://doi.org/10.3390/en6010514.

[5] M. Hellinger, H.W.P. Carvalho, S. Baier, D. Wang, W. Kleist, J.-D. Grunwaldt, Catalytic hydrodeoxygenation of guaiacol over platinum supported on metal oxides and zeolites, Applied Catalysis A: General 490 (2015) 181–192. https://doi.org/10.1016/j.apcata.2014.10.043.

[6] X. Xu, E. Jiang, Z. Li, Y. Sun, BTX from anisole by hydrodeoxygenation and transalkylation at ambient pressure with zeolite catalysts, Fuel 221 (2018) 440–446. https://doi.org/10.1016/j.fuel.2018.01.033.

[7] H. Zhang, S. Shao, R. Xiao, D. Shen, J. Zeng, Characterization of Coke Deposition in the Catalytic Fast Pyrolysis of Biomass Derivates, Energy Fuels 28 (2014) 52–57. https://doi.org/10.1021/ef401458y.

[8] S. Du, J.A. Valla, G.M. Bollas, Characteristics and origin of char and coke from fast and slow, catalytic and thermal pyrolysis of biomass and relevant model compounds, Green Chem. 15 (2013) 3214. https://doi.org/10.1039/c3gc41581c.

[9] L.Y. Jia, M. Raad, S. Hamieh, J. Toufaily, T. Hamieh, M. Bettahar, G. Mauviel, M. Tarrighi, L. Pinard, A. Dufour, Catalytic fast pyrolysis of biomass : superior selectivity of hierarchical zeolite to aromatics, Green Chem. 19 (2017) 5442–5459. https://doi.org/10.1039/C7GC02309J.

[10] I. Graça, J.-D. Comparot, S. Laforge, P. Magnoux, J.M. Lopes, M.F. Ribeiro, F.R. Ribeiro, Effect of phenol addition on the performances of H–Y zeolite during methylcyclohexane transformation, Applied Catalysis A: General 353 (2009) 123–129. https://doi.org/10.1016/j.apcata.2008.10.032.

[11] I. Graça, A. Fernandes, J.M. Lopes, M.F. Ribeiro, S. Laforge, P. Magnoux, F. Ramôa Ribeiro, Effect of phenol adsorption on HY zeolite for n-heptane cracking: Comparison with methylcyclohexane, Applied Catalysis A: General 385 (2010) 178–189. https://doi.org/10.1016/j.apcata.2010.07.011.

[12] I. Graça, J.-D. Comparot, S. Laforge, P. Magnoux, J.M. Lopes, M.F. Ribeiro, F. Ramôa Ribeiro, Influence of Phenol Addition on the H-ZSM-5 Zeolite Catalytic Properties during Methylcyclohexane Transformation, Energy Fuels 23 (2009) 4224–4230. https://doi.org/10.1021/ef9003472.

[13] I. Graça, J.M. Lopes, M.F. Ribeiro, F. Ramôa Ribeiro, H.S. Cerqueira, M.B.B. de Almeida, Catalytic cracking in the presence of guaiacol, Applied Catalysis B: Environmental 101 (2011) 613–621. https://doi.org/10.1016/j.apcatb.2010.11.002.

[14] I. Graça, F.R. Ribeiro, H.S. Cerqueira, Y.L. Lam, M.B.B. de Almeida, Catalytic cracking of mixtures of model bio-oil compounds and gasoil, Applied Catalysis B: Environmental 90 (2009) 556–563. https://doi.org/10.1016/j.apcatb.2009.04.010.

[15] I. Graça, J.M. Lopes, M.F. Ribeiro, M. Badawi, S. Laforge, P. Magnoux, F. Ramôa Ribeiro, n-Heptane cracking over mixtures of HY and HZSM-5 zeolites: Influence of the presence of phenol, Fuel 94 (2012) 571–577. https://doi.org/10.1016/j.fuel.2011.11.033.

[16] S. Du, D.P. Gamliel, M.V. Giotto, J.A. Valla, G.M. Bollas, Coke formation of model compounds relevant to pyrolysis bio-oil over ZSM-5, Applied Catalysis A: General 513 (2016) 67–81. https://doi.org/10.1016/j.apcata.2015.12.022.

[17] X. Zhu, R.G. Mallinson, D.E. Resasco, Role of transalkylation reactions in the conversion of anisole over HZSM-5, Applied Catalysis A: General 379 (2010) 172–181. https://doi.org/10.1016/j.apcata.2010.03.018.

[18] T. Prasomsri, A.T. To, S. Crossley, W.E. Alvarez, D.E. Resasco, Catalytic conversion of anisole over HY and HZSM-5 zeolites in the presence of different hydrocarbon mixtures, Applied Catalysis B: Environmental (2011) S0926337311002347. https://doi.org/10.1016/j.apcatb.2011.05.026.

[19] N. Pichot, J.W. Hounfodji, M. Badawi, V. Valtchev, S. Mintova, J.-P. Gilson, A. Dufour, L. Pinard, Products and coke shape-selectivity during anisole disproportionation over HZSM-5, Applied Catalysis A: General 665 (2023) 119352. https://doi.org/10.1016/j.apcata.2023.119352.

[20] T. Zhang, C. Bhattarai, Y. Son, V. Samburova, A. Khlystov, S.A. Varganov, Reaction Mechanisms of Anisole Pyrolysis at Different Temperatures: Experimental and Theoretical Studies, Energy Fuels 35 (2021) 9994–10008. https://doi.org/10.1021/acs.energyfuels.1c00858.

[21] Y.-T. Cheng, G.W. Huber, Chemistry of Furan Conversion into Aromatics and Olefins over HZSM-5: A Model Biomass Conversion Reaction, ACS Catal. 1 (2011) 611–628. https://doi.org/10.1021/cs200103j.
[22] J.-L. Grandmaison, P.D. Chantal, S.C. Kaliaguine, Conversion of furanic compounds over H-ZSM-5 zeolite, Fuel 69 (1990) 1058–1061. https://doi.org/10.1016/0016-2361(90)90020-Q.
[23] P.D. Chantal, S. Kaliaguine, J.L. Grandmaison, Reactions of phenolic compounds over HZSM-5, Applied Catalysis 18 (1985) 133–145. https://doi.org/10.1016/S0166-9834(00)80304-8.
[24] Q. Meng, H. Fan, H. Liu, H. Zhou, Z. He, Z. Jiang, T. Wu, B. Han, Efficient Transformation of Anisole into Methylated Phenols over High-Silica HY Zeolites under Mild Conditions, ChemCatChem 7 (2015) 2831–2835. https://doi.org/10.1002/cctc.201500479.
[25] M. Guisnet, P. Magnoux, Coking and deactivation of zeolites: Influence of the Pore Structure, Applied Catalysis 54 (1989) 1–27. https://doi.org/10.1016/S0166-9834(00)82350-7.
[26] P. Magnoux, P. Roger, C. Canaff, V. Fouche, N.S. Gnep, M. Guisnet, New Technique for the Characterization of Carbonaceous Compounds Responsible for Zeolite Deactivation, in: Studies in Surface Science and Catalysis, Elsevier, 1987: pp. 317–330. https://doi.org/10.1016/S0167-2991(09)60370-0.
[27] M. Guisnet, L. Costa, F.R. Ribeiro, Prevention of zeolite deactivation by coking, Journal of Molecular Catalysis A: Chemical 305 (2009) 69–83. https://doi.org/10.1016/j.molcata.2008.11.012.
[28] M. Argyle, C. Bartholomew, Heterogeneous Catalyst Deactivation and Regeneration: A Review, Catalysts 5 (2015) 145–269. https://doi.org/10.3390/catal5010145.
[29] A. Bonnin, Y. Pouilloux, V. Coupard, D. Uzio, L. Pinard, Deactivation mechanism and regeneration study of Zn/HZSM-5 catalyst in ethylene transformation, Applied Catalysis A: General 611 (2021) 117976. https://doi.org/10.1016/j.apcata.2020.117976.
[30] J. Oudar, Deactivation and Poisoning of Catalysts, Taylor & Francis, 1985. https://books.google.fr/books?id=FSa1zLeJL1sC.
[31] S. Laforge, D. Martin, M. Guisnet, m-Xylene transformation over H-MCM-22 zeolite. 2. Method for determining the catalytic role of the three different pore systems, Microporous and Mesoporous Materials 67 (2004) 235–244. https://doi.org/10.1016/j.micromeso.2003.11.008.
[32] M. Guisnet, P. Magnoux, Organic chemistry of coke formation, Applied Catalysis A: General 212 (2001) 83–96. https://doi.org/10.1016/S0926-860X(00)00845-0.
[33] M. Guisnet, F.R. Ribeiro, eds., Deactivation and regeneration of zeolite catalysts, Imperial College Press ; Distributed by World Scientific, London : Singapore, 2011.
[34] R. Setton, ed., Chemical Reactions in Organic and Inorganic Constrained Systems, Springer Netherlands, Dordrecht, 1986. https://doi.org/10.1007/978-94-009-4582-1.
[35] N. Chaouati, A. Soualah, M. Chater, M. Tarighi, L. Pinard, Mechanisms of coke growth on mordenite zeolite, Journal of Catalysis 344 (2016) 354–364. https://doi.org/10.1016/j.jcat.2016.10.011.
[36] R.F. Sullivan, C.J. Egan, G.E. Langlois, R.P. Sieg, A New Reaction That Occurs in the Hydrocracking of Certain Aromatic Hydrocarbons, J. Am. Chem. Soc. 83 (1961) 1156–1160. https://doi.org/10.1021/ja01466a036.
[37] R. Sullivan, Hydrocracking of alkylbenzenes and polycyclic aromatic hydrocarbons on acidic catalysts. Evidence for cyclization of the side chains, Journal of Catalysis 3 (1964) 183–195. https://doi.org/10.1016/0021-9517(64)90126-5.
[38] L. Pinard, S. Hamieh, C. Canaff, F. Ferreira Madeira, I. Batonneau-Gener, S. Maury, O. Delpoux, K. Ben Tayeb, Y. Pouilloux, H. Vezin, Growth mechanism of coke on HBEA zeolite during ethanol transformation, Journal of Catalysis 299 (2013) 284–297. https://doi.org/10.1016/j.jcat.2012.12.018.
[39] Z. Ma, E. Troussard, J.A. van Bokhoven, Controlling the selectivity to chemicals from lignin via catalytic fast pyrolysis, Applied Catalysis A: General 423–424 (2012) 130–136. https://doi.org/10.1016/j.apcata.2012.02.027.
[40] P. Sirous Rezaei, H. Shafaghat, W.M.A.W. Daud, Suppression of coke formation and enhancement of aromatic hydrocarbon production in catalytic fast pyrolysis of cellulose over different zeolites: effects of pore structure and acidity, RSC Adv. 5 (2015) 65408–65414. https://doi.org/10.1039/C5RA11332F.
[41] Z. Liu, X. Dong, X. Liu, Y. Han, Oxygen-containing coke species in zeolite-catalyzed conversion of methanol to hydrocarbons, Catal. Sci. Technol. 6 (2016) 8157–8165. https://doi.org/10.1039/C6CY01463A.
[42] N. Pichot, J.W. Hounfodji, H. El Siblani, M. Badawi, V. Valtchev, S. Mintova, J.-P. Gilson, A. Dufour, L. Pinard, Anisole disproportionation on HZSM-5: the key role of Si/Al ratio on auto-inhibition effect, Applied Catalysis A: General (2024) 119565. https://doi.org/10.1016/j.apcata.2024.119565.
[43] Q.-F. Lin, Z.R. Gao, C. Lin, S. Zhang, J. Chen, Z. Li, X. Liu, W. Fan, J. Li, X. Chen, M.A. Camblor, F.-J. Chen, A stable aluminosilicate zeolite with intersecting three-dimensional extra-large pores, Science 374 (2021) 1605–1608. https://doi.org/10.1126/science.abk3258.

[44] M. Fahda, J. Fayek, E. Dib, H. Cruchade, N. Chaouati, L. Pinard, P. Petkov, A. Mayoral, B. Witulski, L. Lakiss, V. Valtchev, Optimizing the synthesis and probing the acidic properties of an extra-large pore aluminosilicate, Submitted for publication (2024).
[45] J. Ward, The nature of active sites on zeolites IX. Sodium hydrogen zeolite, Journal of Catalysis 13 (1969) 364–372. https://doi.org/10.1016/0021-9517(69)90445-X.
[46] C. Miranda, J. Urresta, H. Cruchade, A. Tran, M. Benghalem, A. Astafan, P. Gaudin, T.J. Daou, A. Ramírez, Y. Pouilloux, A. Sachse, L. Pinard, Exploring the impact of zeolite porous voids in liquid phase reactions: The case of glycerol etherification by tert-butyl alcohol, Journal of Catalysis 365 (2018) 249–260. https://doi.org/10.1016/j.jcat.2018.07.009.
[47] A. Beuque, M. Barreau, E. Berrier, J.-F. Paul, N. Batalha, A. Sachse, L. Pinard, Transformation of Dilute Ethylene at High Temperature on Micro- and Nano-Sized H-ZSM-5 Zeolites, (2021).
[48] MFI: Framework Type, (n.d.). https://europe.iza-structure.org/IZA-SC/framework.php?STC=MFI (accessed February 6, 2024).
[49] Beta: DO Family, (n.d.). https://europe.iza-structure.org/IZA-SC/DO_structures/DO_material_rm.php?IFN=Beta (accessed February 6, 2024).
[50] MOR: Framework Type, (n.d.). https://europe.iza-structure.org/IZA-SC/framework.php?STC=MOR (accessed February 6, 2024).
[51] FAU: Framework Type, (n.d.). https://europe.iza-structure.org/IZA-SC/framework.php?STC=FAU (accessed February 6, 2024).
[52] JZO: Framework Type, (n.d.). https://europe.iza-structure.org/IZA-SC/framework.php?STC=JZO (accessed February 6, 2024).
[53] K.S.W. Sing, Reporting physisorption data for gas/solid systems with special reference to the determination of surface area and porosity (Recommendations 1984), Pure and Applied Chemistry 57 (1985) 603–619. https://doi.org/10.1351/pac198557040603.
[54] K.S.W. Sing, R.T. Williams, Physisorption Hysteresis Loops and the Characterization of Nanoporous Materials, Adsorption Science & Technology 22 (2004) 773–782. https://doi.org/10.1260/0263617053499032.
[55] S. Bordiga, C. Lamberti, F. Bonino, A. Travert, F. Thibault-Starzyk, Probing zeolites by vibrational spectroscopies, Chemical Society Reviews 44 (2015) 7262–7341. https://doi.org/10.1039/C5CS00396B.
[56] A. Bonnin, J.-D. Comparot, Y. Pouilloux, V. Coupard, D. Uzio, L. Pinard, Mechanisms of aromatization of dilute ethylene on HZSM-5 and on Zn/HZSM-5 catalysts, Applied Catalysis A: General 611 (2021) 117974. https://doi.org/10.1016/j.apcata.2020.117974.
[57] M. Huang, S. Kaliaguine, A. Auroux, Lewis basic and Lewis acidic sites in zeolites, in: Studies in Surface Science and Catalysis, Elsevier, 1995: pp. 311–318. https://doi.org/10.1016/S0167-2991(06)81903-8.
[58] M. Guisnet, “Coke” molecules trapped in the micropores of zeolites as active species in hydrocarbon transformations, Journal of Molecular Catalysis A: Chemical 182–183 (2002) 367–382. https://doi.org/10.1016/S1381-1169(01)00511-8.
[59] H. Issa, J. Toufaily, T. Hamieh, J.D. Comparot, A. Sachse, L. Pinard, Mordenite etching in pyridine: Textural and chemical properties rationalized by toluene disproportionation and n-hexane cracking, Journal of Catalysis 374 (2019) 409–421. https://doi.org/10.1016/j.jcat.2019.05.004.
[60] G. Froment, Deactivation of zeolite catalysts by coke formation, Journal of Catalysis 124 (1990) 391–400. https://doi.org/10.1016/0021-9517(90)90187-O.
[61] L. Rollmann, Shape selectivity and carbon formation in zeolites, Journal of Catalysis 56 (1979) 139–140. https://doi.org/10.1016/0021-9517(79)90099-X.

Chapitre VI

Pyrolyse catalytique de biomasse sur zéolithes hiérarchisées: comparaison entre mordenite, beta et ZSM-5.

Le chapitre suivant est une étude en collaboration entre les laboratoires de Nancy (LRGP) et Poitiers (IC2MP). Les auteurs et la distribution de leurs contributions sont indiqués ci-après (**candidat en gras**):

Ludovic Pinard: Supervision, design of experimental work, data exploitation, funding, review and editing, writing.

Liangyuan Jia: Experimental work, data exploitation (pyrolysis, SPI-TOF, PCA).

Nathan Pichot: Review, editing, data exploitation (catalysis).

Amir Astafan: Experimental work, data exploitation (catalysis).

Anthony Dufour: Supervision, design of experimental work, supervision of experiments, data exploitation, funding, review and editing, writing.

Abstract

La pyrolyse catalytique de biomasse (CFP) est un procédé prometteur mais son développement est ralenti par la désactivation du catalyseur via plusieurs mécanismes, notablement celui de la formation de coke. Il est essentiel de mieux comprendre l'effet de la structure des catalyseurs zéolithiques sur le mécanisme de formation du coke, et comment ce coke empoisonne les sites actifs (acides de Brønsted). Dans cette étude, nous proposons une comparaison systématique de plusieurs zéolithes : la mordénite (MOR), la beta (*BEA), et la ZSM-5 (MFI), avec différentes méthodes de hiérarchisation (NaOH, HF, NH_4F). L'effet des tailles de cristaux est également abordé pour la zéolithe *BEA. Ces zéolithes ont été testées avec un ratio biomass/catalyseur de 0.8 dans un montage expérimental à deux lits fixes, ce qui permet la séparation des procédés de pyrolyse et de catalyse (CFP ex-situ). La formation d'espèces volatiles a été suivie on-line par spectrométrie de masse (photoionisation). Ces espèces ont aussi été identifiées par GC/MS-FID. Les catalyseurs désactivés ont été analysés via FTIR (avec molécule sonde pyridine), et leur structure poreuse par N_2-physisorption. La structure bidimensionnelle de la MOR, faiblement interconnectée, mène à une désactivation rapide par bouchage des pores, même après hiérarchisation. La MFI hiérarchisée (avec NaOH) est la plus sélective envers les monoaromatiques. Les BAS sont présents aux intersections des canaux, dans des arrangements sphériques de diamètres d'à peu près 7 Å pour les 3 types de zéolithes. Ainsi, la sélectivité envers les aromatiques et la formation du coke dépend sur la forme des canaux des zéolithes, mais pas de l'environnement des H^+. Les plus larges pores de *BEA aident à la diffusion des espèces, mais ils annulent la sélectivité de forme fournie par la MFI envers les aromatiques, en particulier après désactivation partielle par le coke.

Mots clés : Zéolithes Hiérarchisées, CFP, Sélectivité de forme, Primary component analysis, Biomasse.

I – Introduction

Aromatics (benzene, toluene, xylenes, BTX) are key building blocks for the chemistry and they are produced from crude oil by catalytic reforming and fluid catalytic cracking (FCC) units in refineries. The catalytic fast pyrolysis (CFP) of biomass represents an interesting route for producing green aromatics and olefins by mimicking the FCC of crude oil. In this process, the oxygenated volatiles formed by biomass pyrolysis diffuse within the catalyst particles (like zeolites) and contact the catalytic acid sites to form the targeted products (aromatics, olefins) but also coke and gas (mainly CO, CO_2). Zeolites are the main catalysts proposed for biomass CFP [1,2]. Various zeolites have been tested and tailored for biomass CFP. The addition of a metal (Co, Mo, Ga, Fe, Ni, etc.), the acidity (mainly silica-to-alumina ratio), the size and shape of pores, binders (etc.) are the main studied parameters [3–12].

Despite all the numerous studies on materials synthesis, the catalysts still suffer from deactivation during biomass CFP. **Figure VI.1** presents the main mechanisms of deactivation applied to biomass CFP.

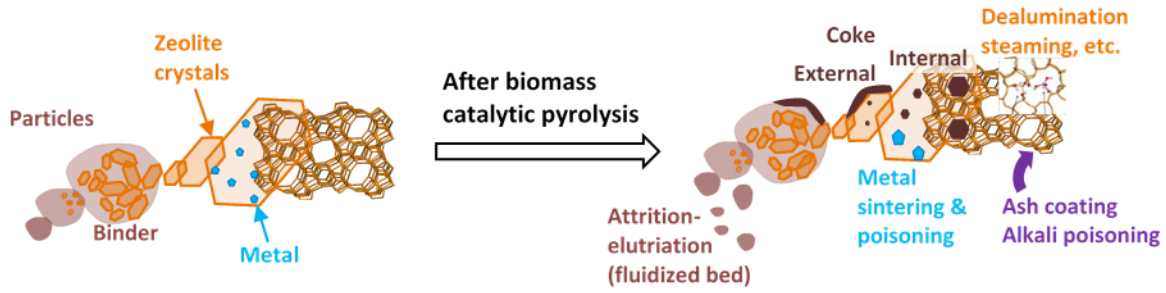

Figure VI.1 : Main mechanisms of catalysts deactivation applied to biomass pyrolysis, here displayed with a HZSM-5 (MFI structure) assumed as doped with metallic nanoparticles, such as Co, Ga, etc.

A first deactivation mechanism is alkali poisoning. It is an irreversible deactivation of the catalysts. Alkali present in ashes can coat the catalyst after the burn-off of char or even react with active sites (notably potassium and sodium) [7,13–16]. Different process configurations are envisioned in order to reduce catalysts deactivation notably by alkali species. “In-situ” CFP means that biomass (and then char/ashes) are in contact with zeolite in a dual fluidized bed (DFB) reactor. “Ex-situ” means that biomass pyrolysis is conducted in a first

reactor and only the vapours are in contact with the zeolite in a second reactor. This second reactor can be a fluidized bed or sequential fixed beds [17]. One potential benefit of fixed bed upgrading over fluidized bed upgrading is catalyst flexibility, providing greater control over chemistry and product composition [17]. Obviously, ex-situ pyrolysis in a fixed bed solves the attrition problem of zeolite particles when operated in fluidized beds. Attrition is another source of zeolites deactivation and loss [18,19]. For these reasons, this present study deals with the ex-situ CFP in a fixed bed reactor.

Another deactivation phenomenon is the dealumination (**Figure VI.1**) of zeolites by steam in the regenerator or stripper zone [14]. Metals have been added to improves zeolites performances [2,5,8,20]. The main challenge is to maintain small nanoparticles of reduced metals which are prone to oxidation (during coke/char oxidation) and sintering (**Figure VI.1**). Metals can be reduced during the pyrolysis of biomass (by coke and pyrolysis gas) and reduced metallic nanoparticles may enhance some hydrogenation reactions. Co in ZSM-5 (**MFI**) was suggested to strongly enhance aromatization reactions [21]. Oxidized Ga/ZSM-5 continued to exhibit improved decarbonylation and decarboxylation activities [22].

Another key deactivation presented in **Figure VI.1** is the formation of coke. The zeolite shape selectivity governs the nature and location of coke. For example, many oxygenate volatiles formed during the pyrolysis of biomass (syringyl-aromatics, levoglucosan, etc.) [23–26] cannot enter the micropores of ZSM-5 (**MFI**) and produce coke on the crystal surface (“external coke”, see **Figure VI.1**). Precoking on the surface of zeolites or MgO addition could be an effective way to reduce coke formation [27].

The light alcohols, acids and furans, etc., formed by biomass pyrolysis have access to active sites located in the micropores and can be converted into aromatics and coke precursors. The latter grows up to be trapped by steric constraints. The coke formation is a genuine shape selectivity reaction. An efficient way to mitigate the internal coke is the shortening of the diffusion path length of molecules in the micropores at few nanometres, which can be achieved through the synthesis of nanocrystal or by the creation of intragranular mesopores connected to the microporous network [28,29]. The formation of mesopores promotes the outwards diffusion of coke precursors from the zeolite channel network and also the accessibility of reactants to the active sites [2,20,30]. Different approaches have been developed for producing additional

mesoporosity in zeolites, either by demetallation (“top-down” approach) or by hydrothermal synthesis (“bottom-up” approach) [31]. Zeolite hierarchization through demetallation treatments (acid treatment for dealumination or alkaline for desilication) is an efficient approach to mitigate catalyst deactivation [31]. Desilication by alkaline treatment leads to higher mesoporous surface area and larger amounts of protonic active sites, when compared to dealumination [32], which can also lead to extra-framework aluminium, partially occupying the channels.

Various types of hierarchical zeolites produced by bottom-up or top-down approaches have been tested for the catalytic pyrolysis of biomass [2,11,20,30,33]. References are reviewed in supplementary material.

Hernando et al. [34] have shown that MgO-loaded hierarchical HZSM-5 provided bio-oil with enhanced energy yields and lower oxygen content, probably due to the adequate balance of acid and basic sites.

Y. Yu et al. [23] demonstrated that, in terms of aromatics selectivity, **MFI** was the best catalyst towards aromatics formation, among those they tested, followed by ***BEA**, **MOR**, and **FAU** zeolites. But **MFI** presents a fast deactivation by coke [23]. Mihalcik et al. [35] have studied **MOR**, ***BEA**, and **MFI** zeolites and came to similar conclusions. The Si/Al ratio has also been shown to have its impact through acidity (number and strength of active sites) [35].

MFI and ***BEA** hierarchization have been extensively studied by Bi et al. [36]. A significant increase in activity, compared to parent zeolites, was attributed to promoted mass transfers of heavier molecules in mesopores [36]. Furthermore, hierarchization seems very promising to reduce pore blockage and active site deactivation [37–39]. Stefanidis et al. found that alkaline treatment of high Si/Al **MOR** resulted in enhanced catalytic activity and led to a noticeable decrease in oxygenated content in the bio-oils [40]. The present authors have studied a hierarchical **MFI** zeolite in micro-fluidized bed [41]. We have also analysed heavy products by high resolution mass spectrometry [42].

Many different zeolites were studied but some results are based on small scale pyrolysis (in micro-pyrolysis reactor combined to GC/MS) with uncontrolled mass transfers of volatiles in the zeolite beds and some of these studies are based on %area (of GC/MS), which does not describe the mass yields selectivity in the targeted species (BTX).

Therefore, the present study aims to complete the literature by comparing three families of zeolites (after different hierarchization methods): mordenite, beta and ZSM-5.

1) Mordenite (**MOR**) features one-dimensional 12-membered-rings 5 (MR) channels (6.7 x 7.0 Å) that are connected to one 8-MR channel (2.6 x 5.7 Å) along the [001] plan, and one 8-MR (3.4 x 4.8 Å) side pocket along the [010] plan. In heterogeneous catalysis, the acid sites within the 12-MR participate in the catalytic event, as most reactants are sterically hindered from accessing Brønsted acid sites (BAS) in 8-MR. Hence, mordenite can be described as featuring a pseudo-one-dimensional structure.

2) Beta (***BEA**) is a large pore zeolite (12-MR) with a 3-dimensional porous network composed of two interconnected different channel systems: (12 6.6 x 6.7** ↔ 12 5.6 x 5.6*). The pore-limiting diameter and the largest cavity diameter are 6.7 and 6.9 Å, respectively.

3) ZSM-5 (**MFI**) is a medium pore zeolite (10 –MR) with a structure based on straight channels (5.3 x 5.6 Å) with sinusoidal channels (5.1 x 5.5 Å). The channel intersections lead to cage-like voids with a diameter of 7.0 Å.

In this work, a wide range of catalysts (10) with various acid site concentrations (Si/Al: 12-40) and textural characteristics (crystal size of 20-800 nm with and without mesopores) is used to compare the performances of these three zeolite frameworks and to highlight the main characteristics that determine their selectivity and stability (towards coke) in the fast pyrolysis of wood. Our pyrolysis method allows for the decoupling of 1) the primary pyrolysis of biomass and 2) the ex-situ catalytic conversion of vapours. Volatiles are analysed on-line by photo-ionisation mass spectrometry (PI-MS) and also quantified by GC/MS-FID. Characterizations of coke and of porous structure after deactivation are provided and they are related to products formation.

II – Experimental section

II.1 – Zeolites production and characterizations

Table VI.1 shows the pore volume dimensions for the three zeolite frameworks: **MOR**, ***BEA** and **MFI**. Various post-treatments were carried out on commercial zeolites from Zeolyst or Süd Chemie to create intracrystalline mesopores. Protocols for treatment by leaching with NaOH, HF or NH_4F are described in the supplementary information**.** The catalysts are labelled as follows: the capital letter indicates the origin of the material: C for commercial, S for synthesised and Hx for hierarchical (post-modification), in brackets the IZA (International Zeolite Association) structural code and in subscripts the crystal size: S (50<ø<500 nm), N <50 nm and M >500 nm). H_A (and H'_A) H_B, and H_{uB} mean hierarchized through alkaline (NaOH), biased (HF), and unbiased (NH_4F) treatments, respectively. The detailed hierarchization procedures are reported in the supporting information.

Table VI.1 Nomenclature of the zeolites tested in this work.

In bracket the zeolite framework; the subscript indicates the crystal size; for hierarchization, H_A and H'_A : alkaline treatment (NaOH at), H_B and H_{uB} : biased (HF) and unbiased (NH_4F) fluorine treatments respectively.

Structure	Parent	Post-synthesis treatment	Crystal size range[a]	Code	Reference
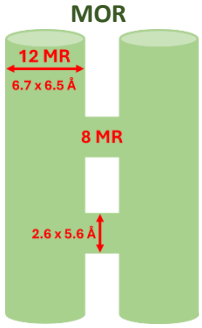	C: Commercial (Süd Chemie)	/	S	C-(MOR)$_S$	/
		H_A: Alkaline (NaOH), 343K	S	H_A-(MOR)$_S$	Issa et al. (2019)[29]
		H'_A: Alkaline (NaOH), 358K	S	H'_A-(MOR)$_S$	
		H_B: Biased (HF), 298K	S	H_B-(MOR)$_S$	
		H_{uB}: Unbiased (NH_4F), 298K	S	H_{uB}-(MOR)$_S$	
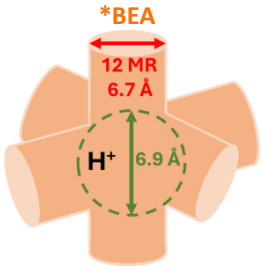	C: Commercial CP814e (Zeolyst)	/	N	C-(*BEA)$_N$	/
		H_A: Alkaline (NaOH), 343K	N	H_A-(*BEA)$_N$	Sammoury et al. (2018)[43]
	S: Synthesized	/	M	S-(*BEA)$_M$	Borade et al. (1996)[44]
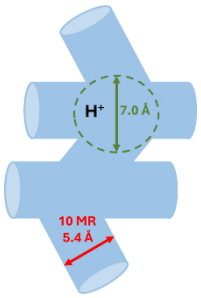	C: Commercial CBV8014 (Zeolyst)	/	S	C-(MFI)$_S$	/
		H_A: Alkaline (NaOH), 343K	S	H_A-(MFI)$_S$	Raad et al. (2018)[28]

[a] N = Nanometer (ø<50 nm), S = Sub-micrometer (50<ø<500 nm), M = Micrometer (ø>500 nm)

II.2 – Characterization of the fresh and spent catalysts

Si/Al ratio assessed via ICP-OES (**Chapter II** part **I.2.a**)

Crystal sizes determined using a scanning electron microscope (**Chapter II** part **I.2.d**).

Nitrogen physisorption (**Chapter II** part **I.2.e**)

Pyr-FTIR (**Chapter II** part I.2.f**)** [45,46].

Beer-Lambert-Bouguer's law:

$$C = \frac{A}{\varepsilon} * \frac{S}{m} * 1000 \qquad \textbf{(Eq. VI.1)}$$

where C is the acid sites concentration (µmol/g), A the band's area (absorption/cm), S the wafer's surface (2 cm^2), m the mass of the wafer (mg), and ε the molar extinction coefficient (cm/µmol).

Molar extinction coefficients were previously determined to be respectively 1.13 cm/µmol and 1.28 cm/µmol for Brønsted and Lewis acid sites [46].

II.3 – Catalytic pyrolysis in a double fixed-bed reactor combined with SPI-MS

A double fixed bed micro-reactor was designed at CNRS Nancy to test these various zeolites by ex-situ pyrolysis. It is composed of 2 interconnected U-shape quartz reactors as presented in **Figure VI.2**.

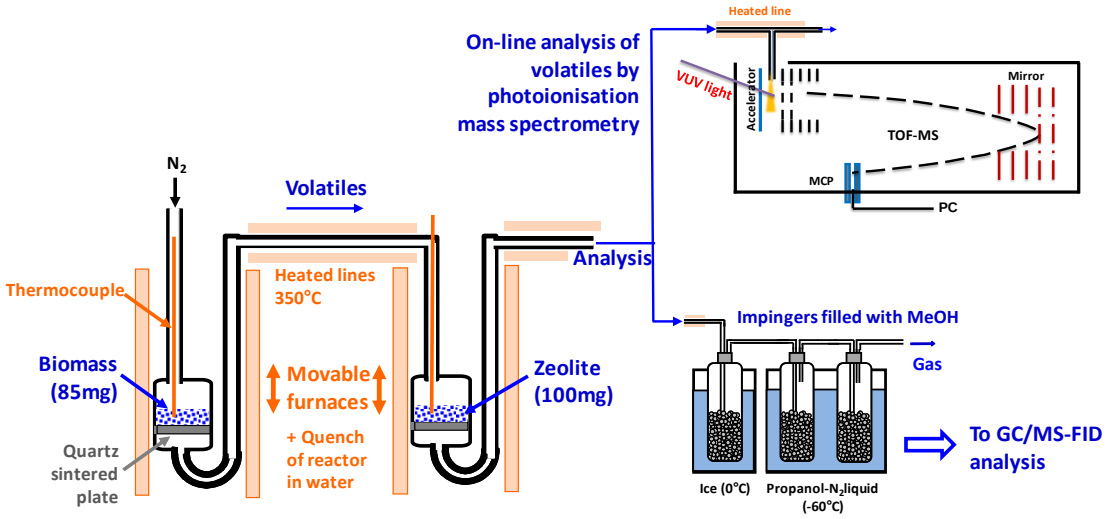

Figure VI.2. Scheme of the double fixed-bed reactors developed at CNRS Nancy combined with photo-ionization mass spectrometry (PI-MS) and impingers for GC/MS-FID quantification of volatiles

The first fixed bed is used to perform the pyrolysis of biomass and the 2nd one to convert ex-situ the volatiles over the zeolite. A similar U-shape reactor was introduced in our previous work for biomass primary pyrolysis and it was shown to give a good control of pyrolysis conditions: final temperature, quenching of the solid, mass transfers, etc. [47–49]. In this present work, the 2nd fixed bed of zeolites allows for an interesting decoupling between biomass pyrolysis and volatiles conversion, for instance by conducting these 2 reactions at different temperatures, quenching times, solid mass, etc.

The dimensions of the 2 quartz reactors are: 3.5 mm (internal diameter, I.D.), 80 mm length (for inlet tubes) and 110 mm length (four outlet tubes); the

biomass and zeolite are positioned in 10 mm I.D., 25 mm length quartz (with a sintered plate).

85 mg (7% water content, 79 mg anhydrous, powder 100-200 µm) of oak wood (complete analysis previously presented in ref. [47]) was pyrolyzed and the mass of zeolite was set at 100 mg. The biomass to catalyst ratio was kept at 0.8 (wt.). 100 mg of zeolite enables the testing of advanced materials (low mass required), a good control of mass transfers through the fixed bed of zeolite (lower than 10 mm height) and extensive characterization of the spent catalyst (acidity, coke, N_2 sorption).

The flow rate of N_2 as carrier gas was set at 120mL/min (measured at atmospheric pressure and 293 K). Therefore, the residence time (at 773 K) of biomass volatiles from the first sintered plate to the inlet of the first impinger was as low as 0.8 sec (calculated with an empty 2nd reactor). All the heated lines between the 2 reactors and before the impingers were heated at 623 K.

At the outlet of the heated lined, the analytical method was the same as the one previously presented [41]. Briefly, a heated capillary line transfers a small fraction of the volatiles to a custom photo-ionization mass spectrometer (Photonion, Germany) operated with a laser and a Xenon cell to ionize the volatiles at 10.5 eV. This soft ionization method is of tremendous importance to monitor on-line biomass volatiles [50].

A major part of the volatiles was condensed in 3 impingers, filled with 10 mL methanol and glass beads in order to break the aerosols. The first impinger was cooled by water ice and the 2 other ones by a mix of isopropanol and liquid nitrogen at 213 K. The last impinger was analysed separately in order to check the efficient trapping of volatiles (no breakthrough). The solution of methanol was analysed by GC/MS-FID and internal calibration as in our previous work [41,51].

The pyrolysis procedure was the following:

1) oak and zeolite were positioned in the 2 reactors;

2) the 2nd furnace was moved on the zeolite (flushed by N_2) and heated to 383 K at 5 K/min, then let 1 hour at 383 K and heated from 383 K to 773 K in 10 K/min;

3) during this time the 2nd furnace was preheated at 773 K (wood was dried at 393 K during 10 min.);

4) impingers and sampling lines were connected, mass spectrometer acquisition started;

5) then the preheated first furnace was quickly moved up on the dried wood reactor. The pyrolysis products were analysed by our on-line PI-MS. Pyrolysis time was around 90 sec (see supplementary material). The reproducibility of the device and procedure is shown in the supplementary material for 4 different experiments on the HZSM-5 (C-(MFI)$_S$) (**Figure VI.S1**).

III – Results and Discussion

III.1 – Characterization of fresh zeolites

Three types of zeolite were used: **MOR**, ***BEA** and **MFI**, with a wide range of acid and textural properties. The catalysts properties (crystal size, micropore and mesopore volumes, concentrations of Brønsted and Lewis acid sites, Si/Al), which were previously synthetized and characterized in other studies [43,44] are presented in **Table VI.2**.

Table VI.2. Textural and acidic properties of the fresh catalysts

Catalyst code	Si/Al[a] mol/mol	Crystal size[b] (nm)	V_{micro}[c] cm^3/g	V_{meso}[c] cm^3/g	DH $\left(\frac{V_{meso}+V_{micro}}{V_{micro}}\right)$	$[P_YH^+]$[d] µmol/g	[PyL][d] µmol/g
C-(MOR)$_S$	20	100-500	0.18	0.11	1.6	552	47
H$_A$-(MOR)$_S$	19	100-500	0.12	0.36	4	382	118
H'$_A$-(MOR)$_S$	18		0.09	0.27	4	329	59
H$_B$-(MOR)$_S$	35.6	100-500	0.18	0.14	1.8	220	50
H$_{uB}$-(MOR)$_S$	15	100-500	0.17	0.15	1.9	497	68
C-(*BEA)$_N$	12	20	0.25	0.75	4.0	346	349
H$_A$-(*BEA)$_N$	8.9	15	0.22	0.44	3.0	334	442
S-(*BEA)$_M$	36	780	0.21	0.02	1.1	523	100
C-(MFI)$_S$	40	250	0.17	0.07	1.4	304	44
H$_A$-(MFI)$_S$	32	250	0.15	0.38	3.5	231	63

[a] by ICP-AES, [b] SEM, [c] N_2 physorption, [d] Pyridine adsorption followed by FTIR

The zeolite microporous volume (V_{micro}) is a "fingerprint" of the framework type. Commercial **MFI**, **MOR**, and ***BEA** zeolites feature V_{micro} of 0.17, 0.18, and 0.25 cm^3/g, respectively, which are the micropore volumes expected for conventional well-crystallized zeolites for these structures. Commercial **MOR** and **MFI** and synthetized ***BEA** with micrometre crystal S-(*BEA)$_M$ can be assimilated as purely microporous materials. The alkaline treatment causes a local collapse of the zeolite framework through its desilication, creating intracrystalline mesopores, which decreases both V_{micro} and the concentration of the Brønsted acid sites (BAS) slightly. Desilication (with NaOH), unlike fluorine treatment, preserves a large part of the microporosity and acidity of the zeolite (**Table VI.2**). The commercial ***BEA** zeolite (C-(*BEA)$_N$) is already a hierarchical material with a significant mesoporous volume resulting from the aggregation of the nanocrystals (20 nm). After alkaline treatment on **MOR** and **MFI**, the mesopores are intracrystals.

It is possible to estimate the degree of hierarchization (DH, **Table VI.2**) of all these materials by the ratio:

$$DH = \frac{V_{meso} + V_{micro}}{V_{micro}}.$$

It is worth noting that the DH factor is the inverse of the relative micropore volume. A DH value of 1 corresponds to a purely microporous material. An alkaline treatment on **MFI** and **MOR** zeolites doubles the degree of hierarchization, while the impact of acid leaching is somewhat limited (an increase of 0.3). DH increases significantly up to 4 by decreasing the zeolite crystal size to the nanometric scale through the aggregation of particles for C -(*BEA)$_N$ [52].

The BAS concentration depends on both the Si/Al molar ratio and on their accessibility to the pyridine probe. Hence, the rate between the probed acid sites to the theoretical, calculated from the Si/Al ratio the zeolite ($[PyH^+]_{423K}/[H^+]_{Theoretical}$), depends strongly on the zeolite framework. On ***BEA** and **MFI** zeolites, this ratio is close to 1 (**Table VI.2**). It is only 0.8 for **MOR** due to acid sites located on the sodalite cages and side pockets, which are inaccessible to the basic pyridine probe.

Five catalysts: C-(*BEA)$_N$, H$_A$-(*BEA)$_N$, C-(MFI)$_S$, H$_A$-(MOR)$_S$, H$_A$'-(MOR)$_S$ feature a comparable concentration of Brønsted acid sites (ca 300-380 µmol/g). ***BEA** zeolite has a larger number of defects than **MFI** and **MOR** zeolites, leading to higher concentrations of Lewis acid sites.

III.2 – Dynamics of volatiles formation as studied by on-line SPI-MS

The SPI-MS enables to monitor on-line the formation of volatiles. The SPI-MS profile of some main markers of cellulose, hemicelluloses and lignin and with an empty 2nd reactor is presented in supplementary material (**Figure VI.S2**). We have previously discussed in details the formation of biomass primary volatiles as analysed by SPI-MS.[41,53] It is out of the scope of this present work to discuss biomass primary pyrolysis in details. Briefly, the first step is the formation of *m/z* 114 (4-hydroxy-5,6-dihydro-2H-pyran-2-one, a typical marker of hemicelluloses pyrolysis) and furans (*m/z* 96 and 68*)* furfural. Then, lignin primary markers are formed (like *m/z* 180 4-vinyl-syringol, *m/z* 154 2,6-dimethoxy-phenol, *m/z* 168 4-methyl-syringol). *m/z* 126 can be assigned to 5-hydroxymethyl-furfural and photoionization fragment from levoglucosan (LVG, from cellulose pyrolysis).

When a zeolite catalyst was positioned in the 2nd reactor (at 773K), the composition of volatiles was completely modified and the species can be classified in 3 main families, with some of the most important species being [41,54]:

1) catalytic hydrocarbons (*m/z* 78 benzene, *m/z* 106 xylenes, *m/z* 42 propylene and fragment of 2,5-dihydrofuran);

2) intermediate products formed by partly deactivated zeolites (*m/z* 82 furan, *m/z* 94 phenol);

3) primary products formed from a deactivated catalyst (*m/z* 98 LVG fragments, *m/z* 114, etc.).

All the zeolites formed in the early step hydrocarbons (**Figure VI.3** and other results presented in supplementary material – **Figure VI.S4**), but only the **MFI** exhibit xylenes as the major products during the whole conversion of biomass.

Concerning mordenite, C, H_B, H_{uB} exhibit mainly fully deactivated products. H_A and H_A' mordenites present a higher peak of partly deactivated zeolites (furans). The alkaline treatment (by NaOH) of these 2 zeolites lead to a higher mesopores volumes and hierarchization degree (**Table VI.2**) and therefore a relative better stability compared to the other 3 mordenites. As shown by Chaouati and al.[55], the generation of mesopores connected to the micropores through alkaline treatment on **MOR** zeolite mitigates the coke toxicity.

Regardless of the crystal size, the 3 ***BEA** present a similar pattern which is very different than **MOR**. The hydrocarbons (notably m/z 42) are the major contribution all along biomass conversion, then furans and phenols are formed (notably during cellulose and lignin main devolatilization steps). The hierarchization of ***BEA** (H_A-(*BEA)$_N$) or a larger crystal size (S -(*BEA)$_M$) does not significantly impact the profile in products formation. As indicated by the large number of Lewis sites probed (Table VI.2), the ***BEA** zeolites contain a large number of EFAl species. Thus, the higher cracking activity on these three zeolites could be attributed to an enhancement of the BAS strength by EFAl species[56]. Indeed, a study combining MAS NMR with DFT calculations[57] showed the existence of a clear interaction between the Brønsted and Lewis acid sites (LAS) leading to an increase in the acid site strength in the zeolite framework.

The **MFI** is the only zeolite to present 2 peaks of catalysed hydrocarbons products (like xylenes) as the major products. The 2 peaks correspond to the conversion of hemicelluloses and cellulose volatiles (cf. the time profile shown in the supplementary material without catalyst – **Figure VI.S2**). The profile is always dominated by hydrocarbons, but deactivated products are also formed. **MFI** converts primary volatiles to hydrocarbons more efficiently than ***BEA** zeolite, not because of the strength of the BAS acid site and the length of diffusion paths, but mostly because of the shape of canals around the acid sites.[4,11,23]

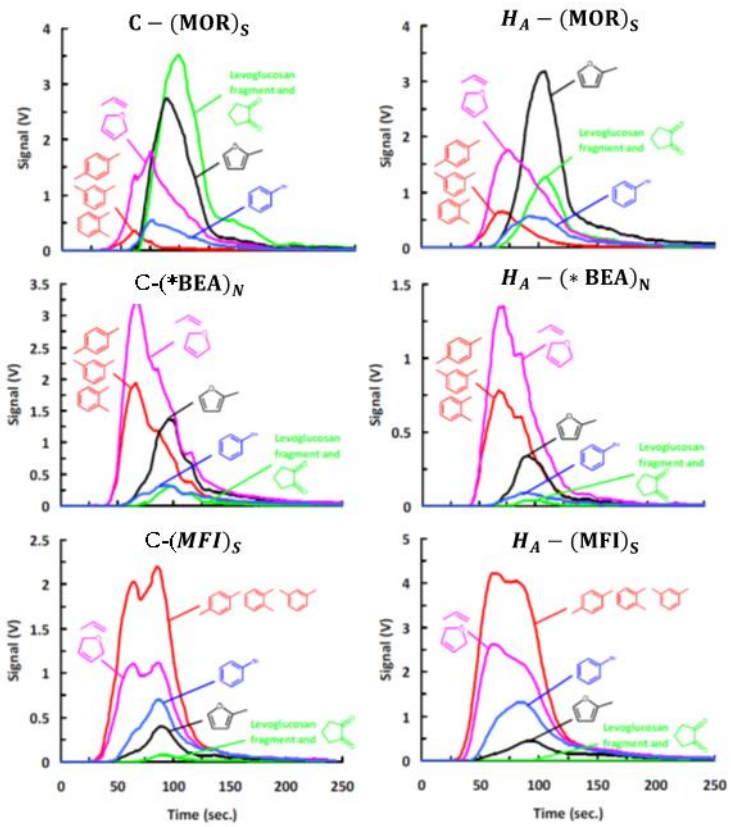

Figure VI.3. Evolution of some important markers: m/z 106 (xylenes), 82 (2-methyl furan), 42 (propylene and fragments of 2,5-dihydrofuran), 94 (phenol), 98 (levoglucosan fragments and 1,2 cyclopentanedione) as a function of time (analysed by on-line SPI-MS). The time "0 sec." corresponds to when the furnace (preheated) is in its final position (after its lift out) on the biomass bed.

III.3 – Comparison of the zeolites based on SPI mass spectra and statistical analysis

The accumulated mass spectra of SPI-MS during the whole conversion of biomass are presented in **Figure VI.4** (and in supplementary material – **Figure VI.S5**).

For all mordenites, the major contributions are *m/z* corresponding to oxygenated products (furans, primary pyrolysis products as levoglucosan markers, etc.). For all ***BEA**, the major contribution is *m/z* 42 (propylene and dihydrofuran fragments) and aromatic hydrocarbons. For the 2 **MFI**, the major peaks are the contributions of aromatics hydrocarbons.

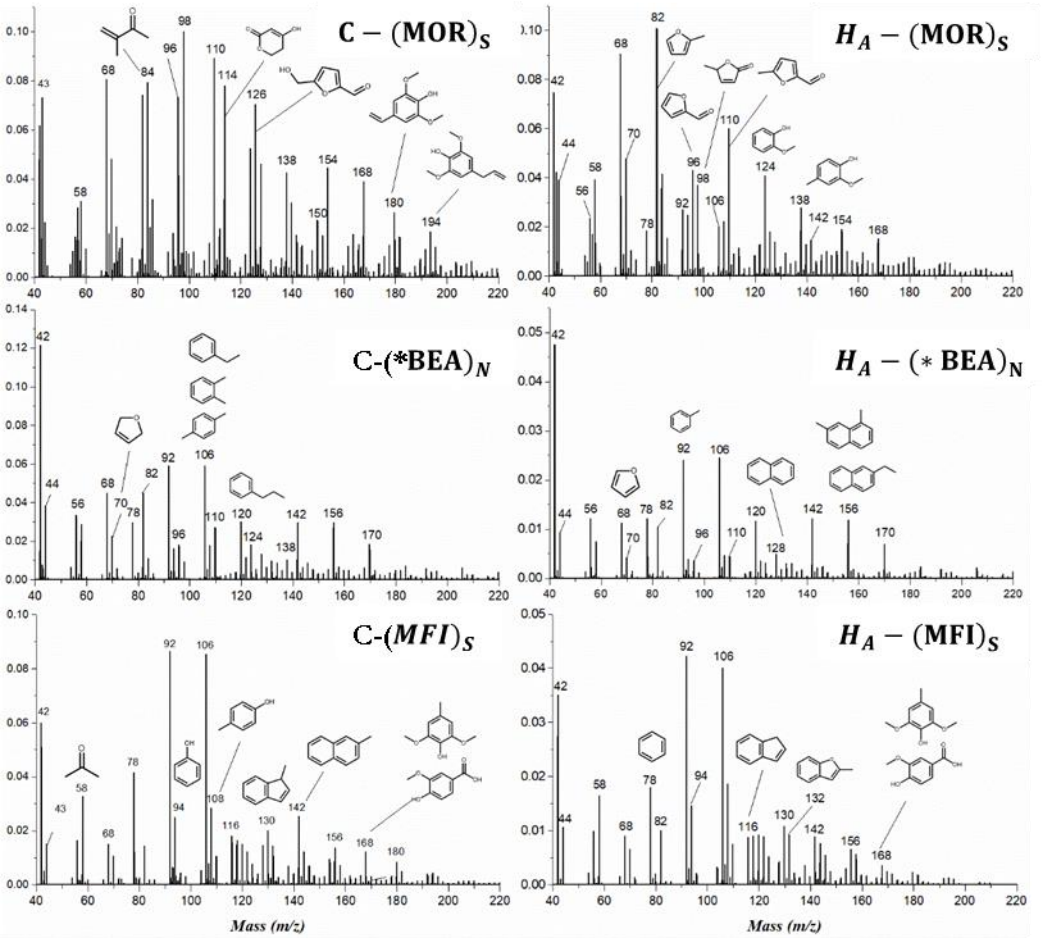

Figure VI.4. SPI total mass spectra (averaged along the whole pyrolysis time) of the catalytic products with different zeolites (other zeolites presented in supplementary materials – **Figure VI.S5**)

We have previously shown the interest to treat the mass spectra by statistical analysis in order to better unravel the significant differences between the pyrolysis conditions [41,53]. **Figure VI.5** presents the principal component analysis (PCA) of all the mass spectra (accumulated during the whole pyrolysis time) obtained with the various tested catalysts. PC1 and PC2 explain 91% of the variance. **Figure VI.5** displays a very clear separation between the 3 types of zeolites. This is despite the high variability in crystal size, texture and acidity within each zeolite type.

Xylenes and ethylbenzene are clear **MFI** markers. The 3 ***BEA** zeolites are clearly differentiated from the other type of zeolites by *m/z* 42 (propylene and dihydrofuran fragments).

Furan and methyl furan (*m/z* 68, 82) are marker for hierarchical mordenites produced by alkaline treatment (H_A-$(MOR)_S$ and H_A'-$(MOR)_S$). The higher mesoporosity and added connectivity between channels (2D to ~3D) induced by this treatment when compared to commercial and fluorine treatments (see DH in Table VI.2) promote some partial deoxygenation of primary products. It reduces the deactivation rate of **MOR**. Desilication is the method of choice for the development of intracrystalline mesoporosity. The generation of mesoporosity leads to an improved resistance to coking through a reduction in the diffusion path length of coke precursors.[29] Primary products from oak pyrolysis (*m/z* 114, 98, 126) are markers for the 3 other mordenites, which present a very weak deoxygenation activity.

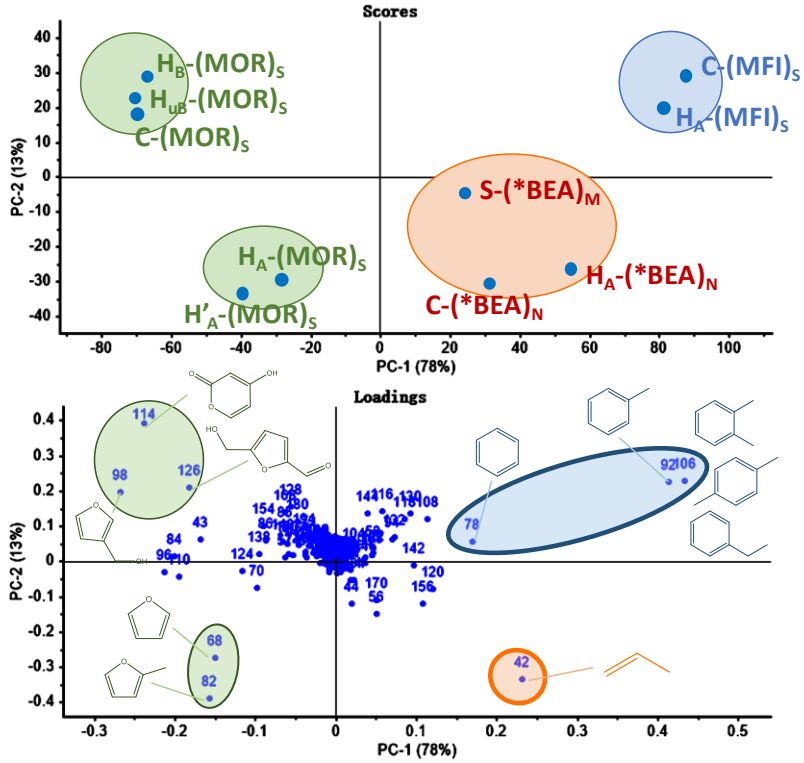

Figure VI.5. PCA of SPI-MS analysis of the volatiles produced by the various zeolites: groups per type of catalysts are clearly evidenced.

III.4 – Comparison of the zeolites based on GC/MS quantification of aromatic hydrocarbons

SPI-MS is an interesting method to monitor in real time the volatiles, but it is semi-quantitative. Therefore, it is required to compare the zeolites by quantitative GC/MS analysis. Figure VI.6 displays the mass yields (based on anhydrous biomass) of the targeted aromatic hydrocarbons.

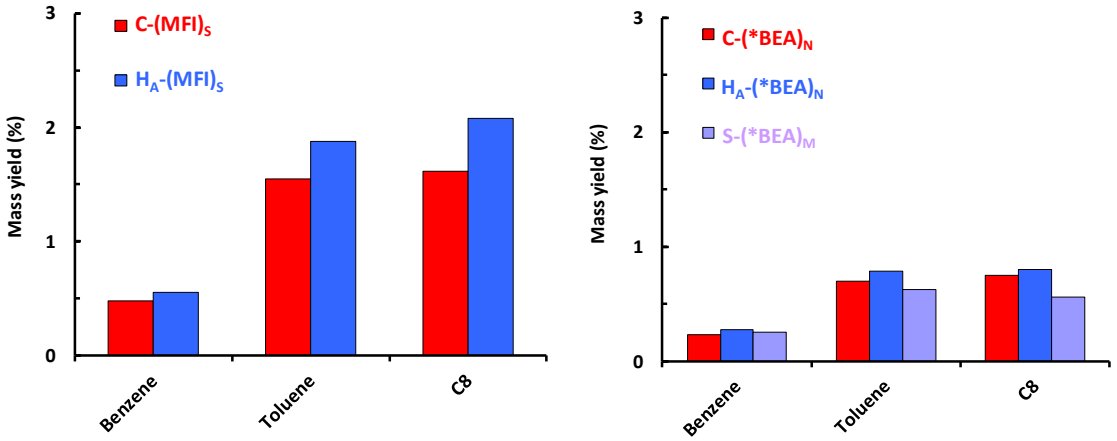

Figure VI.6. Mass yields (% mass of product/mass of anhydrous wood) as quantified by GC/FID-MS for **MFI** and ***BEA** zeolites.

The mass yields of BTX were too small for mordenite-types zeolites (not presented). **Figure VI.6** clearly shows that **MFI** presents a much higher yield in aromatic hydrocarbons compared to the 3 ***BEA** zeolites in agreement with previous work [34,58,59] (conducted under different pyrolysis conditions). Despite the numerous studies on biomass CFP, the quantitative data (mass yields) comparing **MFI** and ***BEA** on wood pyrolysis are scarce (see our table of literature analysis in supplementary material – **Table VI.S1**). The hierarchization of ***BEA** does not improve the mass yield in aromatic hydrocarbons whereas the hierarchization of **MFI** (by NaOH) increases the mass yields in aromatic hydrocarbons, in agreement with our previous work in fluidized bed conditions [41]. Therefore, the hierarchization of **MFI** improves the selectivity in aromatics for both reactor configurations (ex-situ fixed bed or in-situ fluidized bed).

III.5 – Characterization of the spent zeolites

The catalytic transformation of volatiles at 773 K leads to both a fast and high coke content (> 7.5 wt. %) whatever the zeolite framework, as well as the hierarchization degree of the material (**Figure VI.7a**). The high reaction temperature favours the kinetic rate of coke formation much more than the diffusion of coke precursors, even after enhancing the diffusion in crystals, by reducing the crystals size or by hierarchization, by mesopores formation in crystals (see **Table VI.2**).

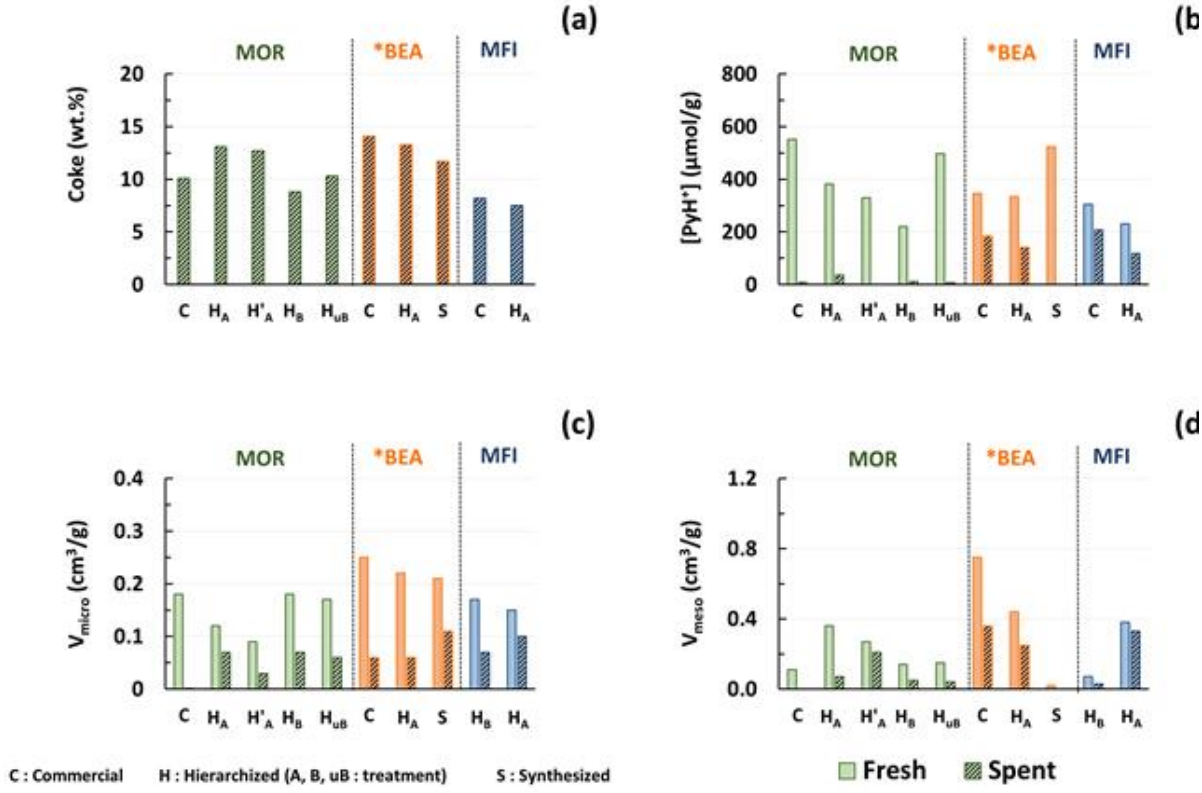

Figure VI.7. Coke content (a, after deactivation, for spent catalysts) and concentration of Brønsted acid sites (b), micropores (c) and mesopores (d) volumes for fresh and spent catalysts

However, the medium-pore zeolite (**MFI**) is more resistant to coking than the large pore pseudo-mono -(**MOR**)- and tri-dimensional-(***BEA**) zeolites. This result means that steric constraints also limit coke formation: the large pore zeolites promote the growth of coke contrariwise to medium pores ones (**MFI**). The higher content of coke in the ***BEA** than in the **MFI** could also be related both

to a higher acid strength and to the nature of the products formed. Olefins produce more coke than aromatics.

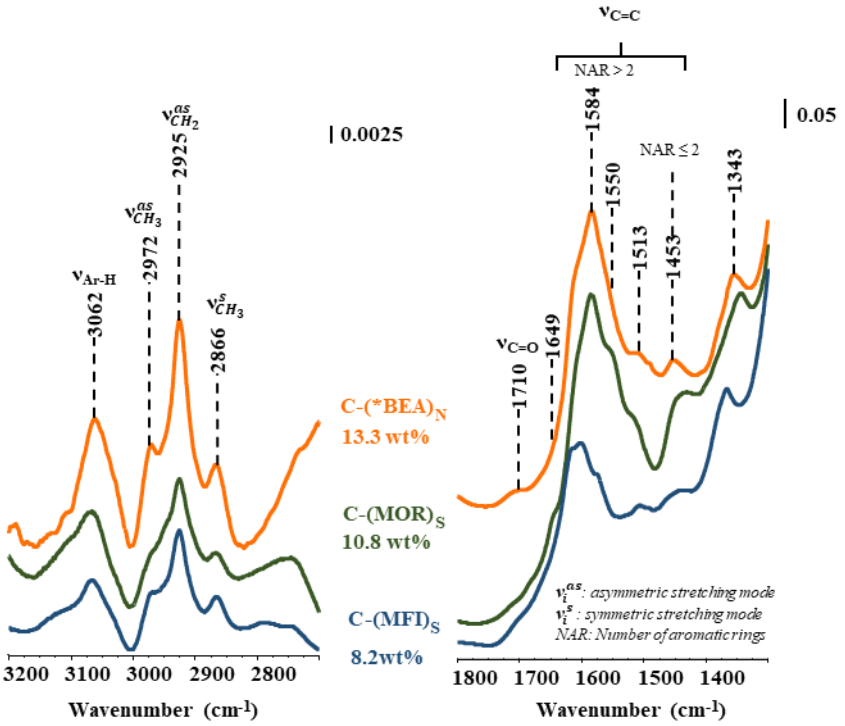

Figure VI.8. Bands of coke molecules in regions 3200-2700 cm^{-1} (a) and 1800-1300 cm^{-1} (b).
Weight fractions of coke based on catalyst initial mass are also recalled.

The coked zeolites were analysed by FTIR (**Figure VI.8**). The bands of carbonaceous compounds deposited on commercial zeolites are observed on two IR spectra domains:

1) 2700-3200 cm^{-1}: CH stretching modes of aromatic and paraffinic groups;

2) 1400-1800 cm^{-1}: C=C stretching modes of unsaturated (olefin, polyenyl, aromatic and polyaromatic) groups and CH bending of paraffinic groups.

The band at 3062 cm^{-1} corresponds to aromatic CH stretching modes, 2972 and 2925 cm^{-1} to the asymmetric stretching mode of CH_3 and CH_2 groups, respectively and 2972 and 2866 cm^{-1} are related to symmetric stretching mode of CH_3 in hydrocarbons chains [60]. Attribution of bands in region between 1300-1800 cm^{-1} is more complex, because it could be attributed to different stretching modes of C=C condensed and non-condensed aromatics and also bending vibrations of CH. Bands at 1600, 1575, 1510, are usually assigned to polyaromatic coke with a

number of aromatic rings superior to 3 (NAR>3) [61]. The band at 1710 cm^{-1} (v_{CO}) indicated the presence of a low content of oxygenated compounds. The coke bands are almost identical regardless of the zeolite framework. Indeed, the transformation of hydrocarbons at high temperature leads to the formation of polyaromatic compounds replicating the shape of micropores [62].

About the pseudo mono-dimensional zeolite (**MOR**), even on those with intracrystalline mesopores (**Figure VI.7d**), the coke completely neutralizes the Brønsted acid sites (**Figure7b**), which indicates a pore blocking by molecules having a size similar to pyridine. The IR spectra of the OH region on the spent catalysts confirms the inaccessibility of the bridged OH groups to organic molecules (see supplementary material – **Figure VI.S6**). Alkaline and fluorine treatments have created connections between the main channel and the mesopores as evidenced by the presence of residual micropore volumes after deactivation (**Figure VI.7c**). Yet, the opening generated by post-treatments are too small to allow the diffusion of organic molecules in the main channels. The structure of mordenite with 1D channels lead to a fast deactivation, plugging by coke even after different hierarchization methods.

Concerning the three-dimensional zeolites (**MFI** and ***BEA**), the losses of BAS and microporosity are partial (**Figure VI.7b** and **7c**) which means that deactivation occurs mainly by poisoning rather than pores blockage. The loss of mesoporous volumes in all the samples suggests that a part of the coke is retained on the mesopores, regardless of whether they are intergranular (***BEA** samples) or intracrystalline (**MOR** and **MFI** zeolites)-(**Figure VI.7d**).

Figure VI.9 presents relations between coke content and BAS and degree of hierarchization.

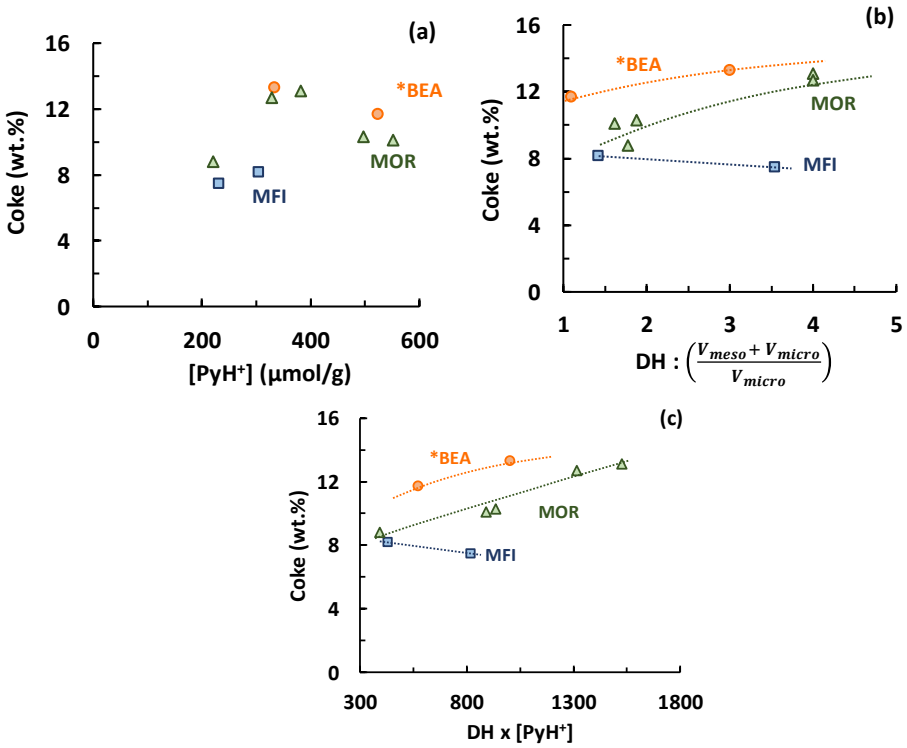

Figure VI.9. Coke content as a function of the initial concentration of Brønsted acid sites (a), degree of hierarchization (DH) of zeolite (b) and the multiplication of these two parameters (c)

The higher coke content of the hierarchical catalysts (at the same concentration of BAS) is due to an additional trapping of carbonaceous compounds in the generated mesopores (**Figure VI.9a**) It is interesting to notice that the reduction in mesopores due to coke deposit is much lower in the hierarchical **MFI** than in the hierarchical ***BEA** zeolites (**Figure VI.7d**). The most important accumulation of coke being observed for the caustic leached zeolite and/or nanosized zeolite, it is likely related to the increased number of silanols, and Lewis acid sites (as for ***BEA** samples) as these are prone to trap desorbed products [32,63,64].

On the larger pore zeolites (***BEA**, **MOR**), the coke content increases with the degree of hierarchization (**Figure VI.9b**) and the trend is clearer when taking into account the acidity (**Figure VI.9c**), while on **MFI** it seems independent of DH.

III.6 – Relationship between aromatics' selectivity, coke deposit and zeolite structures

Figure VI.10a presents the mass yields in monoaromatic hydrocarbons as a function of coke deposit. It highlights a much higher total of monoaromatic hydrocarbons for **MFI** and notably for the hierarchical **MFI** with a lower coke content than all the ***BEA** and **MOR** zeolites. HZSM-5 presents a better compromise to HC selectivity and stability towards coke.

Figure VI.10b clearly shows an increase in aromatic yields as a function of the hierarchization for **MFI**. The increase is much weaker for ***BEA** and **MOR** upon hierarchization, whatever the hierarchization methods used.

Figure VI.10c presents the aromatic yields as a function of the consumed BAS. It confirms a more efficient utilization of BAS in **MFI** to produce aromatics than in ***BEA** and **MOR**. BAS are present in a similar cage-like voids with a diameter of 7.0 Å for the 3 types of zeolites (see **Table VI.1** for zeolites structure). Therefore, the selectivity towards aromatics and coke formation depends on the shape of canals but not on the H^+ cage environment. ***BEA** promotes the diffusion of species in larger pores than **MFI**, but it leads to a lower shape-selectivity than **MFI**.

Figure VI.10d presents another information about the initial activity of the zeolites and not after the complete wood pyrolysis. The signal of m/z 106 obtained by SPI-MS has been integrated during the first 60 seconds (and divided by the total ionic current TIC). This is a relative information about the abundance of C_8 aromatic hydrocarbons vs. the other ions. This data is only semi-quantitative, but it presents a high interest to assess the activity of fresh zeolites. These first 60 seconds of experiments represent mostly the catalytic products formed from hemicellulose primary species (see supplementary data on SPI-MS results without catalyst). This relative signal of C_8 abundance is plotted as a function of the initial BAS and hierarchization degree. Based on **Figure VI.10d**, ***BEA** competes with **MFI** during these early stages of volatiles conversion. This point may explain some conflicting results obtained in the literature when comparing different zeolites (see **Table VI.S1** in supplementary material). The performance of zeolites depends on the amount of coke deposit and of the biomass to catalyst ratio (bcr) studied. The composition of primary volatiles is also a concern: the volatiles from hemicelluloses are easier to be converted to

aromatic hydrocarbons than lignin primary products. For instance, ***BEA** zeolites present better selectivity to aromatic hydrocarbons on lignin vapours than ZSM-5 [23]. Consequently, this work may be extended to a dual fluidized bed configuration where the bcr is much lower than in a fixed bed and where biomass volatiles are in contact with a regenerated zeolite (although potentially deactivated by alkali species).

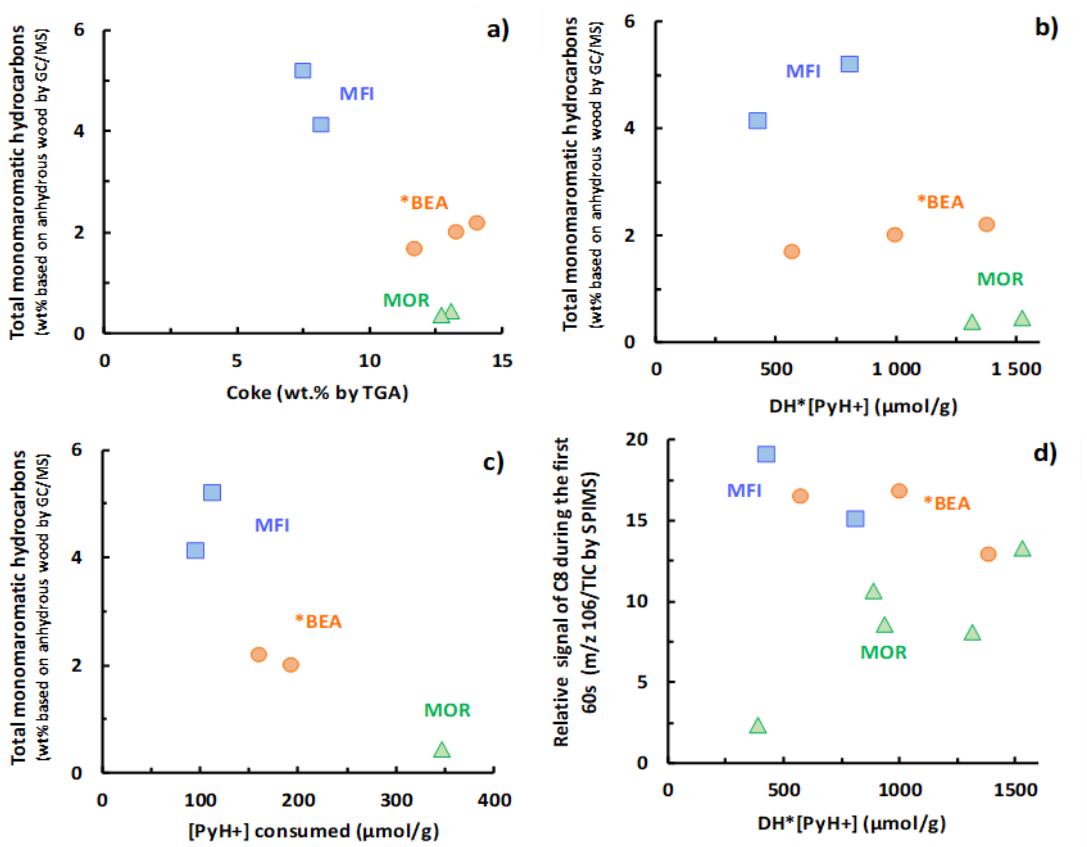

Figure VI.10. Relations between monoaromatic hydrocarbons (wt.%) and a) coke deposit, b) zeolite initial acidity (BAS * degree of hierarchization), c) consumed BAS and d) relative signal of C8 hydrocarbons (m/z 106) obtained by SPI-MS during the first 60sec. as a function of the initial acidity (BAS * degree of hierarchization)

IV – Conclusions

This work presents 2 methodologies of potential interest for studying biomass catalytic pyrolysis:

A double fixed bed reactor where biomass pyrolysis is decoupled from ex-situ conversion of volatiles.

A combination of on-line SPI-MS with GC/MS and advanced characterization of the coked zeolites.

This methodology has been applied to various zeolites presenting complementary porous structures: mordenite, ***BEA** and **MFI**. Furthermore, these zeolites have been hierarchized with different methods (NaOH, HF, NH_4F, etc.). The effect of crystal size has been also studied for ***BEA**. The spent catalysts were analysed by pyridine probe (acidity), coke composition by FTIR (without pyridine) and porous structure by N_2 sorption.

Our main findings are summarized in **Figure VI.11**.

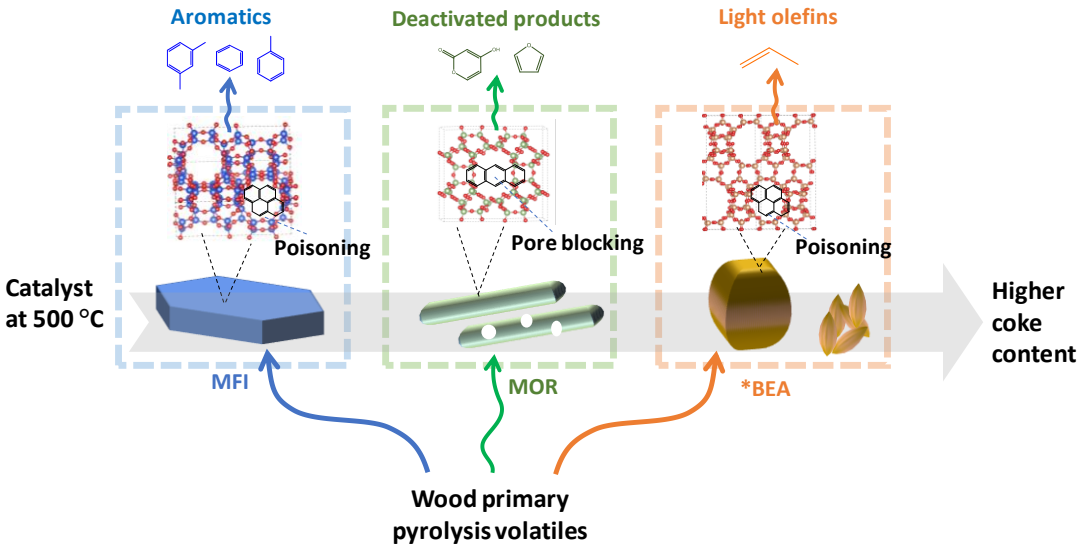

Figure VI.11. Simplified representation of some findings of this study (fixed bed, biomass to catalyst ratio of 0.8)

The hierarchical **MFI** (obtained by mild desilication with NaOH) is the best zeolites among the ones tested under our studied bcr ratio (0.8). BAS were present in a similar cage-like voids with a diameter of 7.0 Å for the 3 types of

zeolites. Therefore, the selectivity towards aromatics and coke formation depends on the shape of canals but not on the H^+ cage environment. ***BEA** promotes the diffusion of species to BAS in larger pores than **MFI**, but it leads to a lower shape-selectivity than **MFI** after partial deactivation by coke. The structure of mordenite with 2D channels and low channel interconnectivity lead to a fast deactivation by pores blocking even after different hierarchization methods. We did not succeed to improve the selectivity and stability of MOR zeolites by hierarchization.

Other catalysts (formulated with binders, additives, metals, etc.) may be tested by following the same methodology and under different configurations, as for instance in a dual fluidized bed or in sequential fixed beds fed by a continuous pyrolysis reactor.

References

[1] P.D. Chantal, S. Kaliaguine, J.L. Grandmaison, Reactions of phenolic compounds over HZSM-5, Applied Catalysis 18 (1985) 133–145. https://doi.org/10.1016/S0166-9834(00)80304-8.

[2] A.J. Foster, J. Jae, Y.-T. Cheng, G.W. Huber, R.F. Lobo, Optimizing the aromatic yield and distribution from catalytic fast pyrolysis of biomass over ZSM-5, Applied Catalysis A: General 423–424 (2012) 154–161. https://doi.org/10.1016/j.apcata.2012.02.030.

[3] P.T. Williams, N. Nugranad, Comparison of products from the pyrolysis and catalytic pyrolysis of rice husks, (2000).

[4] T.R. Carlson, G.A. Tompsett, W.C. Conner, G.W. Huber, Aromatic Production from Catalytic Fast Pyrolysis of Biomass-Derived Feedstocks, Top Catal 52 (2009) 241–252. https://doi.org/10.1007/s11244-008-9160-6.

[5] R. French, S. Czernik, Catalytic pyrolysis of biomass for biofuels production, Fuel Processing Technology 91 (2010) 25–32. https://doi.org/10.1016/j.fuproc.2009.08.011.

[6] R.H. Venderbosch, A Critical View on Catalytic Pyrolysis of Biomass, ChemSusChem 8 (2015) 1306–1316. https://doi.org/10.1002/cssc.201500115.

[7] G. Yildiz, F. Ronsse, R. van Duren, W. Prins, Challenges in the design and operation of processes for catalytic fast pyrolysis of woody biomass, Renewable and Sustainable Energy Reviews 57 (2016) 1596–1610. https://doi.org/10.1016/j.rser.2015.12.202.

[8] E. Yaman, A.S. Yargic, N. Ozbay, B.B. Uzun, K.G. Kalogiannis, S.D. Stefanidis, E.P. Pachatouridou, E.F. Iliopoulou, A.A. Lappas, Catalytic upgrading of pyrolysis vapours: Effect of catalyst support and metal type on phenolic content of bio-oil, Journal of Cleaner Production 185 (2018) 52–61. https://doi.org/10.1016/j.jclepro.2018.03.033.

[9] A. Margeriat, A. Bouzeggane, C. Lorentz, D. Laurenti, N. Guilhaume, C. Mirodatos, C. Geantet, Y. Schuurman, Catalytic conversion of beech wood pyrolytic vapors, Journal of Analytical and Applied Pyrolysis 130 (2018) 149–158. https://doi.org/10.1016/j.jaap.2018.01.015.

[10] E.F. Iliopoulou, K.S. Triantafyllidis, A.A. Lappas, Overview of catalytic upgrading of biomass pyrolysis vapors toward the production of fuels and high-value chemicals, WIREs Energy and Environment 8 (2019) e322. https://doi.org/10.1002/wene.322.

[11] R. Cai, X. Pei, H. Pan, K. Wan, H. Chen, Z. Zhang, Y. Zhang, Biomass Catalytic Pyrolysis over Zeolite Catalysts with an Emphasis on Porosity and Acidity: A State-of-the-Art Review, Energy Fuels 34 (2020) 11771–11790. https://doi.org/10.1021/acs.energyfuels.0c02147.

[12] A. Aho, N. Kumar, K. Eränen, T. Salmi, M. Hupa, D.Yu. Murzin, Catalytic pyrolysis of woody biomass in a fluidized bed reactor: Influence of the zeolite structure, Fuel 87 (2008) 2493–2501. https://doi.org/10.1016/j.fuel.2008.02.015.

[13] K.G. Kalogiannis, S.D. Stefanidis, S.A. Karakoulia, K.S. Triantafyllidis, H. Yiannoulakis, C. Michailof, A.A. Lappas, First pilot scale study of basic vs acidic catalysts in biomass pyrolysis: Deoxygenation mechanisms and catalyst deactivation, Applied Catalysis B: Environmental 238 (2018) 346–357. https://doi.org/10.1016/j.apcatb.2018.07.016.

[14] S.D. Stefanidis, E. Heracleous, D.Th. Patiaka, K.G. Kalogiannis, C.M. Michailof, A.A. Lappas, Optimization of bio-oil yields by demineralization of low quality biomass, Biomass and Bioenergy 83 (2015) 105–115. https://doi.org/10.1016/j.biombioe.2015.09.004.

[15] C.A. Mullen, A.A. Boateng, Accumulation of Inorganic Impurities on HZSM-5 Zeolites during Catalytic Fast Pyrolysis of Switchgrass, Ind. Eng. Chem. Res. 52 (2013) 17156–17161. https://doi.org/10.1021/ie4030209.

[16] V. Paasikallio, C. Lindfors, E. Kuoppala, Y. Solantausta, A. Oasmaa, J. Lehto, J. Lehtonen, Product quality and catalyst deactivation in a four day catalytic fast pyrolysis production run, Green Chem. 16 (2014) 3549–3559. https://doi.org/10.1039/C4GC00571F.

[17] A. Dutta, J.A. Schaidle, D. Humbird, F.G. Baddour, A. Sahir, Conceptual Process Design and Techno-Economic Assessment of Ex Situ Catalytic Fast Pyrolysis of Biomass: A Fixed Bed Reactor Implementation Scenario for Future Feasibility, Top Catal 59 (2016) 2–18. https://doi.org/10.1007/s11244-015-0500-z.

[18] R. Von Ballmoos, C.-M.T. Hayward, Matrix vs Zeolite Contributions to the Acidity of Fluid Cracking Catalysts, in: G. Öhlmann, H. Pfeifer, R. Fricke (Eds.), Studies in Surface Science and Catalysis, Elsevier, 1991: pp. 171–183. https://doi.org/10.1016/S0167-2991(08)62905-5.

[19] C.H. Bartholomew, Mechanisms of catalyst deactivation, Applied Catalysis A: General 212 (2001) 17–60. https://doi.org/10.1016/S0926-860X(00)00843-7.
[20] B. Puértolas, A. Veses, M.S. Callén, S. Mitchell, T. García, J. Pérez-Ramírez, Porosity-Acidity Interplay in Hierarchical ZSM-5 Zeolites for Pyrolysis Oil Valorization to Aromatics, ChemSusChem 8 (2015) 3283–3293. https://doi.org/10.1002/cssc.201500685.
[21] E.F. Iliopoulou, S. Stefanidis, K. Kalogiannis, A.C. Psarras, A. Delimitis, K.S. Triantafyllidis, A.A. Lappas, Pilot-scale validation of Co-ZSM-5 catalyst performance in the catalytic upgrading of biomass pyrolysis vapours, Green Chem. 16 (2014) 662–674. https://doi.org/10.1039/C3GC41575A.
[22] C.A. Mullen, P.C. Tarves, L.M. Raymundo, E.L. Schultz, A.A. Boateng, J.O. Trierweiler, Fluidized Bed Catalytic Pyrolysis of Eucalyptus over HZSM-5: Effect of Acid Density and Gallium Modification on Catalyst Deactivation, Energy Fuels 32 (2018) 1771–1778. https://doi.org/10.1021/acs.energyfuels.7b02786.
[23] Y. Yu, X. Li, L. Su, Y. Zhang, Y. Wang, H. Zhang, The role of shape selectivity in catalytic fast pyrolysis of lignin with zeolite catalysts, Applied Catalysis A: General 447–448 (2012) 115–123. https://doi.org/10.1016/j.apcata.2012.09.012.
[24] A.G. Gayubo, A.T. Aguayo, A. Atutxa, B. Valle, J. Bilbao, Undesired components in the transformation of biomass pyrolysis oil into hydrocarbons on an HZSM-5 zeolite catalyst, J. Chem. Technol. Biotechnol. 80 (2005) 1244–1251. https://doi.org/10.1002/jctb.1316.
[25] G. Fogassy, N. Thegarid, Y. Schuurman, C. Mirodatos, From biomass to bio-gasoline by FCC co-processing: effect of feed composition and catalyst structure on product quality, Energy Environ. Sci. 4 (2011) 5068. https://doi.org/10.1039/c1ee02012a.
[26] S. Du, D.P. Gamliel, M.V. Giotto, J.A. Valla, G.M. Bollas, Coke formation of model compounds relevant to pyrolysis bio-oil over ZSM-5, Applied Catalysis A: General 513 (2016) 67–81. https://doi.org/10.1016/j.apcata.2015.12.022.
[27] E.F. Iliopoulou, K.S. Triantafyllidis, A.A. Lappas, Overview of catalytic upgrading of biomass pyrolysis vapors toward the production of fuels and high-value chemicals, WIREs Energy Environ 8 (2019) e322. https://doi.org/10.1002/wene.322.
[28] M. Raad, S. Hamieh, J. Toufaily, T. Hamieh, L. Pinard, Propane aromatization on hierarchical Ga/HZSM-5 catalysts, Journal of Catalysis 366 (2018) 223–236. https://doi.org/10.1016/j.jcat.2018.07.035.
[29] H. Issa, N. Chaouati, J. Toufaily, T. Hamieh, A. Sachse, L. Pinard, Toolbox of Post-Synthetic Mordenite Modification Strategies: Impact on Textural, Acidic and Catalytic Properties, ChemCatChem 11 (2019) 4581–4592. https://doi.org/10.1002/cctc.201900927.
[30] H.J. Park, H.S. Heo, J.-K. Jeon, J. Kim, R. Ryoo, K.-E. Jeong, Y.-K. Park, Highly valuable chemicals production from catalytic upgrading of radiata pine sawdust-derived pyrolytic vapors over mesoporous MFI zeolites, Applied Catalysis B: Environmental 95 (2010) 365–373. https://doi.org/10.1016/j.apcatb.2010.01.015.
[31] D. Verboekend, J. Pérez-Ramírez, Design of hierarchical zeolite catalysts by desilication, Catal. Sci. Technol. 1 (2011) 879. https://doi.org/10.1039/c1cy00150g.
[32] F. Ngoye, L. Lakiss, Z. Qin, S. Laforge, C. Canaff, M. Tarighi, V. Valtchev, K. Thomas, A. Vicente, J.P. Gilson, Y. Pouilloux, C. Fernandez, L. Pinard, Mitigating coking during methylcyclohexane transformation on HZSM-5 zeolites with additional porosity, Journal of Catalysis 320 (2014) 118–126. https://doi.org/10.1016/j.jcat.2014.10.001.
[33] J. Li, X. Li, G. Zhou, W. Wang, C. Wang, S. Komarneni, Y. Wang, Catalytic fast pyrolysis of biomass with mesoporous ZSM-5 zeolites prepared by desilication with NaOH solutions, Applied Catalysis A: General 470 (2014) 115–122. https://doi.org/10.1016/j.apcata.2013.10.040.
[34] H. Hernando, I. Moreno, J. Fermoso, C. Ochoa-Hernández, P. Pizarro, J.M. Coronado, J. Čejka, D.P. Serrano, Biomass catalytic fast pyrolysis over hierarchical ZSM-5 and Beta zeolites modified with Mg and Zn oxides, Biomass Conv. Bioref. 7 (2017) 289–304. https://doi.org/10.1007/s13399-017-0266-6.
[35] D.J. Mihalcik, C.A. Mullen, A.A. Boateng, Screening acidic zeolites for catalytic fast pyrolysis of biomass and its components, Journal of Analytical and Applied Pyrolysis 92 (2011) 224–232. https://doi.org/10.1016/j.jaap.2011.06.001.
[36] Y. Bi, X. Lei, G. Xu, H. Chen, J. Hu, Catalytic Fast Pyrolysis of Kraft Lignin over Hierarchical HZSM-5 and Hβ Zeolites, Catalysts 8 (2018) 82. https://doi.org/10.3390/catal8020082.
[37] S. Soltanian, C.L. Lee, S.S. Lam, A review on the role of hierarchical zeolites in the production of transportation fuels through catalytic fast pyrolysis of biomass, Biofuel Res. J. 7 (2020) 1217–1234. https://doi.org/10.18331/BRJ2020.7.3.5.
[38] A.M. Hernández-Giménez, E. Heracleous, E. Pachatouridou, A. Horvat, H. Hernando, D.P. Serrano, A.A. Lappas, P.C.A. Bruijnincx, B.M. Weckhuysen, Effect of Mesoporosity, Acidity and Crystal Size of Zeolite

ZSM-5 on Catalytic Performance during the Ex-situ Catalytic Fast Pyrolysis of Biomass, ChemCatChem 13 (2021) 1207–1219. https://doi.org/10.1002/cctc.202001778.
[39] H. Chen, X. Shi, J. Liu, K. Jie, Z. Zhang, X. Hu, Y. Zhu, X. Lu, J. Fu, H. Huang, S. Dai, Controlled synthesis of hierarchical ZSM-5 for catalytic fast pyrolysis of cellulose to aromatics, J. Mater. Chem. A 6 (2018) 21178–21185. https://doi.org/10.1039/C8TA08930B.
[40] S. Stefanidis, K. Kalogiannis, E.F. Iliopoulou, A.A. Lappas, J.M. Triguero, M.T. Navarro, A. Chica, F. Rey, Mesopore-modified mordenites as catalysts for catalytic pyrolysis of biomass and cracking of vacuum gasoil processes, Green Chem. 15 (2013) 1647. https://doi.org/10.1039/c3gc40161h.
[41] L.Y. Jia, M. Raad, S. Hamieh, J. Toufaily, T. Hamieh, M. Bettahar, G. Mauviel, M. Tarrighi, L. Pinard, A. Dufour, Catalytic fast pyrolysis of biomass : superior selectivity of hierarchical zeolite to aromatics, Green Chem. 19 (2017) 5442–5459. https://doi.org/10.1039/C7GC02309J.
[42] J. Hertzog, V. Carré, L. Jia, C.L. Mackay, L. Pinard, A. Dufour, O. Mašek, F. Aubriet, Catalytic Fast Pyrolysis of Biomass over Microporous and Hierarchical Zeolites: Characterization of Heavy Products, ACS Sustainable Chem. Eng. 6 (2018) 4717–4728. https://doi.org/10.1021/acssuschemeng.7b03837.
[43] H. Sammoury, J. Toufaily, K. Cherry, T. Hamieh, Y. Pouilloux, L. Pinard, Desilication of *BEA zeolites using different alkaline media: Impact on catalytic cracking of n-hexane, Microporous and Mesoporous Materials 267 (2018) 150–163. https://doi.org/10.1016/j.micromeso.2018.03.022.
[44] R.B. Borade, A. Clearfield, Preparation of aluminum-rich Beta zeolite, Microporous Materials 5 (1996) 289–297. https://doi.org/10.1016/0927-6513(95)00064-X.
[45] J. Ward, The nature of active sites on zeolites IX. Sodium hydrogen zeolite, Journal of Catalysis 13 (1969) 364–372. https://doi.org/10.1016/0021-9517(69)90445-X.
[46] C. Miranda, J. Urresta, H. Cruchade, A. Tran, M. Benghalem, A. Astafan, P. Gaudin, T.J. Daou, A. Ramírez, Y. Pouilloux, A. Sachse, L. Pinard, Exploring the impact of zeolite porous voids in liquid phase reactions: The case of glycerol etherification by tert-butyl alcohol, Journal of Catalysis 365 (2018) 249–260. https://doi.org/10.1016/j.jcat.2018.07.009.
[47] Y. Le Brech, L. Jia, S. Cissé, G. Mauviel, N. Brosse, A. Dufour, Mechanisms of biomass pyrolysis studied by combining a fixed bed reactor with advanced gas analysis, Journal of Analytical and Applied Pyrolysis 117 (2016) 334–346. https://doi.org/10.1016/j.jaap.2015.10.013.
[48] Y. Le Brech, J. Raya, L. Delmotte, N. Brosse, R. Gadiou, A. Dufour, Characterization of biomass char formation investigated by advanced solid state NMR, Carbon 108 (2016) 165–177. https://doi.org/10.1016/j.carbon.2016.06.033.
[49] Y. Le Brech, T. Ghislain, S. Leclerc, M. Bouroukba, L. Delmotte, N. Brosse, C. Snape, P. Chaimbault, A. Dufour, Effect of Potassium on the Mechanisms of Biomass Pyrolysis Studied using Complementary Analytical Techniques, ChemSusChem 9 (2016) 863–872. https://doi.org/10.1002/cssc.201501560.
[50] L. Jia, Y. Le Brech, G. Mauviel, F. Qi, M. Bente-von Frowein, S. Ehlert, R. Zimmermann, A. Dufour, Online Analysis of Biomass Pyrolysis Tar by Photoionization Mass Spectrometry, Energy Fuels 30 (2016) 1555–1563. https://doi.org/10.1021/acs.energyfuels.5b02274.
[51] R. Olcese, V. Carré, F. Aubriet, A. Dufour, Selectivity of Bio-oils Catalytic Hydrotreatment Assessed by Petroleomic and GC*GC/MS-FID Analysis, Energy Fuels 27 (2013) 2135–2145. https://doi.org/10.1021/ef302145g.
[52] N. Batalha, A. Soualah, L. Pinard, Y. Pouilloux, F. Lemos, T. Belin, Impact of the BEA zeolite morphology on isobutane adsorption followed by Reversed-Flow Inverse Gas Chromatography, Journal of Chromatography A 1260 (2012) 206–214. https://doi.org/10.1016/j.chroma.2012.08.079.
[53] L. Jia, Y. Le-Brech, B. Shrestha, M.B. Frowein, S. Ehlert, G. Mauviel, R. Zimmermann, A. Dufour, Fast Pyrolysis in a Microfluidized Bed Reactor: Effect of Biomass Properties and Operating Conditions on Volatiles Composition as Analyzed by Online Single Photoionization Mass Spectrometry, Energy Fuels 29 (2015) 7364–7374. https://doi.org/10.1021/acs.energyfuels.5b01803.
[54] C. Mukarakate, M.J. Watson, J. ten Dam, X. Baucherel, S. Budhi, M.M. Yung, H. Ben, K. Iisa, R.M. Baldwin, M.R. Nimlos, Upgrading biomass pyrolysis vapors over β-zeolites: role of silica-to-alumina ratio, Green Chem. 16 (2014) 4891–4905. https://doi.org/10.1039/C4GC01425A.
[55] N. Chaouati, A. Soualah, L. Pinard, Coke toxicities, descriptors of the deactivating effect of coke on microporous and desilicated mordenite zeolite, Reac Kinet Mech Cat 136 (2023) 2243–2257. https://doi.org/10.1007/s11144-023-02447-3.
[56] C. Mirodatos, D. Barthomeuf, Superacid sites in zeolites, J. Chem. Soc., Chem. Commun. (1981) 39–40. https://doi.org/10.1039/C39810000039.

[57] S. Li, A. Zheng, Y. Su, H. Zhang, L. Chen, J. Yang, C. Ye, F. Deng, Brønsted/Lewis Acid Synergy in Dealuminated HY Zeolite: A Combined Solid-State NMR and Theoretical Calculation Study, J. Am. Chem. Soc. 129 (2007) 11161–11171. https://doi.org/10.1021/ja072767y.

[58] N. Chaihad, S. Karnjanakom, I. Kurnia, A. Yoshida, A. Abudula, P. Reubroycharoen, G. Guan, Catalytic upgrading of bio-oils over high alumina zeolites, Renewable Energy 136 (2019) 1304–1310. https://doi.org/10.1016/j.renene.2018.09.102.

[59] Y.-M. Kim, J. Jeong, S. Ryu, H.W. Lee, J.S. Jung, M.Z. Siddiqui, S.-C. Jung, J.-K. Jeon, J. Jae, Y.-K. Park, Catalytic pyrolysis of wood polymer composites over hierarchical mesoporous zeolites, Energy Conversion and Management 195 (2019) 727–737. https://doi.org/10.1016/j.enconman.2019.05.034.

[60] L. Pinard, P. Bichon, A. Popov, J.L. Lemberton, C. Canaff, F. Maugé, P. Bazin, E.F. S.-Aguiar, P. Magnoux, Identification of the carbonaceous compounds present on a deactivated cobalt based Fischer–Trospch catalyst resistant to “rejuvenation treatment,” Applied Catalysis A: General 406 (2011) 73–80. https://doi.org/10.1016/j.apcata.2011.08.012.

[61] N. Chaouati, A. Soualah, M. Chater, M. Tarighi, L. Pinard, Mechanisms of coke growth on mordenite zeolite, Journal of Catalysis 344 (2016) 354–364. https://doi.org/10.1016/j.jcat.2016.10.011.

[62] K. Ben Tayeb, S. Hamieh, C. Canaff, H. Nguyen, H. Vezin, L. Pinard, The radical internal coke structure as a fingerprint of the zeolite framework, Microporous and Mesoporous Materials 289 (2019) 109617. https://doi.org/10.1016/j.micromeso.2019.109617.

[63] F. Thibault-Starzyk, A. Vimont, J.-P. Gilson, 2D-COS IR study of coking in xylene isomerisation on H-MFI zeolite, Catalysis Today 70 (2001) 227–241. https://doi.org/10.1016/S0920-5861(01)00420-5.

[64] L. Lakiss, F. Ngoye, C. Canaff, S. Laforge, Y. Pouilloux, Z. Qin, M. Tarighi, K. Thomas, V. Valtchev, A. Vicente, L. Pinard, J.-P. Gilson, C. Fernandez, On the remarkable resistance to coke formation of nanometer-sized and hierarchical MFI zeolites during ethanol to hydrocarbons transformation, Journal of Catalysis 328 (2015) 165–172. https://doi.org/10.1016/j.jcat.2014.12.030.

Conclusion Générale et perspectives

Au fil des chocs pétroliers, et plus l'urgence écologique croît, plus le recours à des sources alternatives des hydrocarbures tant convoités devient impératif. La biomasse lignocellulosique est une source très prometteuse de ces hydrocarbures. Concomitamment, la pyrolyse catalytique de cette biomasse promet une production « verte » (source renouvelable, faible pression) d'hydrocarbures à haute valeur ajoutée tels que les BTX. Surmonter l'obstacle de la désactivation rapide du catalyseur reste l'obstacle majeur à l'industrialisation à grande échelle du procédé. L'étude en laboratoire de molécules modèles apporte une meilleure compréhension des mécanismes gouvernant cette désactivation. L'anisole permet l'étude des mécanismes régissant les groupes methoxy, ainsi que les phénols, produits majoritaires de sa dismutation.

Le travail de cette thèse a permis la mise en évidence de plusieurs phénomènes remarquables liés à la dismutation de l'anisole sur catalyseur zéolithique, des conditions régissant son activité initiale à l'inhibition de la désactivation classique par dépôt de coke.

Dans la première partie, l'étude de l'impact du temps de contact et de la conversion sur les rendements des produits a permis de valider les résultats déjà présents dans la littérature, en particulier les différentes réactions de transalkylation bimoléculaires responsables de la production de la plupart des produits primaires (méthylanisole, phénol), secondaires (m-, o-, p-crésol) et tertiaires (2,3-, 2,4- 2,5-, 2,6-, 3,4-, 3,5-xylénol). L'étude cinétique de la désactivation, d'une part en suivant l'activité, et d'autre part en suivant le dépôt de coke a permis la mise en évidence d'un état d'activité stationnaire sur la zéolithe MFI. Cet état stationnaire est produit après une rapide désactivation, et n'est pas affecté par la masse d'espèces désactivantes (coke) qui s'ajoute encore au catalyseur.

L'étude du coke, par analyse élémentaire et par extraction puis injection en spectrométrie de masse, a mis au jour la grande proportion d'espèces oxygénées (les produits de réaction eux-mêmes) dans ce coke, ainsi que l'absence des composés polyaromatiques habituels dans les procédés de catalyse hétérogène en chimie organique. L'étude calculatoire (DFT) des énergies d'adsorption des composés a montré la forte rétention par adsorption des produits de réaction sur les sites acides de Brønsted, ainsi que l'importance des

énergies de dispersion et donc des contraintes stériques imposées par la taille des réactifs et les canaux de la zéolithe dans cette rétention. Enfin, cette première partie a mis en évidence le mode de désactivation du catalyseur, qui n'est pas empoisonné (car l'activité stationnaire reste, et il y a dans la structure jusqu'à 2,5 fois plus de molécules de coke que de sites acides disponibles pour les adsorber), et dont les canaux ne sont pas bloqués : la zéolithe subit un « fouling », soit la couverture de la surface disponible par ses produits de réaction, adsorbés partout dans la structure (et pas uniquement sur les sites actifs).

L'effet de l'acidité d'une zéolithe sur la réaction qu'elle catalyse étant normalement important, la seconde partie a comparé 9 zéolithes MFI, d'acidités variant entre 67 et 1038 $\mu mol.g^{-1}$. L'étude de l'activité et de la fréquence rotationnelle (Turnover Frequency, TOF) initiales a mis en évidence l'augmentation constante de l'activité en fonction de l'acidité, jusqu'à un maximum, puis un soudain anéantissement de l'activité initiale et du TOF_0 aux alentours d'une concentration de sites acides de 500 $\mu mol.g^{-1}$. Cette soudaine chute d'activité marque la mise en place d'un effet auto-inhibiteur, signalé dans la littérature pour des réactions en phase liquide. Cet effet a été confirmé par l'étude calculatoire (DFT) des énergies d'adsorption des différents réactifs et produits sur des sites acides isolés ou appariés (NNN, NNNN, opposés sur l'anneau 10 MR), où l'énergie d'adsorption se voit augmenter drastiquement avec l'ajout d'un site acide au voisinage d'un premier, soulignant la difficulté accrue pour les produits de désorber hors de la zéolithe. A partir d'une certaine acidité, l'étape de désorption des produits devient limitante selon le principe de Sabatier, et le catalyseur est presque totalement désactivé dès le début de la réaction.

La troisième partie a conclu l'étude sur l'anisole, en étendant les phénomènes remarquables à d'autres zéolithes (*BEA, MOR, FAU et JZO). L'état d'activité stationnaire est toujours présent, et une étude détaillée de la désactivation a mis en évidence l'effet limité de l'adsorption espèces « cokantes » sur les sites actifs sur cet état stationnaire, et la dépendance quasi exclusive de l'activité et son maintien sur le volume poreux d'une zéolithe. En effet, il apparaît que les espèces cokantes (les produits de réaction : méthylphénols) participent à l'état stationnaire en étant disponibles pour les réactions de transalkylation avec l'anisole présent en phase gaz. Cette étude a également mis en évidence l'importance de l'interconnectivité des canaux des zéolites : la zéolithe MOR (2D) est facilement désactivée, la faible interconnectivité aggravant l'effet auto-inhibiteur montré pour la MFI. Cet effet auto-inhibiteur de l'acidité est présent peu importe la structure de la zéolithe, et est mitigé par les pores larges et extra

larges dans les zéolithes 3D, qui facilitent les réactions bimoléculaires (de transalkylation) et la diffusion des espèces en phase gaz, même après adsorption d'un grand nombre de produits.

L'étude de l'évolution de la sélectivité au cours du temps de réaction a mis en évidence un changement de prévalence d'un chemin réactionnel pour la production des crésol (produit secondaire) sur un autre, ainsi qu'un effet d'exclusion de taille de la zéolithe MOR, au moyen de ses « poches latérales », et à l'encontre du méthylanisole.

Enfin, la troisième étude a aussi étendu aux zéolithes à large pores la composition remarquable du coke, là encore composé des produits de réaction et exempt des hydrocarbures polyaromatiques. Cette absence est expliquée par les effets électroniques des groupements methoxy et hydroxyle, tous deux mésomères donneurs, qui enrichissent le cycle aromatique en densité électronique, prévenant la formation des ions carbénium, point de départ de la réaction « d'épluchage » d'un cycle alkylé et du mécanisme de Sullivan, responsable de la production classique du coke à haute température. Exception à cela, la zéolithe MFI avec une haute acidité (Si/Al = 12 dans l'étude), présente des polyaromatiques oxygénés dans son coke. Leur formation est probablement due à l'autre mécanisme de formation du coke, rendu possible seulement à basse pression partielle de réactif, qui consiste en la condensation des composés adsorbés entre eux pour former des espèces plus volumineuses.

Après l'étude du comportement de l'anisole, des tests de différentes zéolithes hiérarchisées (*BEA, MFI, MOR, hiérarchisation par désilication et désalumination) sur la pyrolyse catalytique de biomasse lignocellulosique ont été réalisés. La faible connectivité de la zéolithe MOR a mené, une fois encore, à une rapide désactivation, cette fois par bloquage des pores, et la hiérarchisation n'a que peu aidé à la stabilité du matériau. La MFI hiérarchisée a montré une grande sélectivité envers les hydrocarbures aromatiques. Cette étude a montré que la sélectivité envers différents produits dépend de la forme des canaux de la zéolithe, et les larges pores de la *BEA aident à la diffusion des espèces vers les sites actifs. Les différentes zéolithes produisent, par sélectivité de forme, des espèces « marqueurs » qui leur sont propres. Le coke est constitué des espèces classiques polyaromatiques.

En conclusion, le travail de cette thèse a mis en évidence une bonne quantité de phénomènes propres à l'anisole et aux composés méthoxy et phénoliques, soulignant l'importance de la structure et de l'acidité de la zéolithe pour son activité et sa sélectivité. Cependant, ces phénomènes n'ont pas été retrouvés lors des tests en pyrolyse catalytique de biomasse, dû à la complexité du mélange réactionnel. Ainsi, les prochaines études devraient complexifier le système en apportant un co-feeding en plus de l'anisole, tel que le méthanol ou le gaïacol, car la transformation de l'anisole seul ne permet pas de comprendre, dans leur intégralité, les mécanismes en jeu lors de la pyrolyse catalytique de biomasse lignocellulosique.

Annexes

Annexes – Chapitre IV

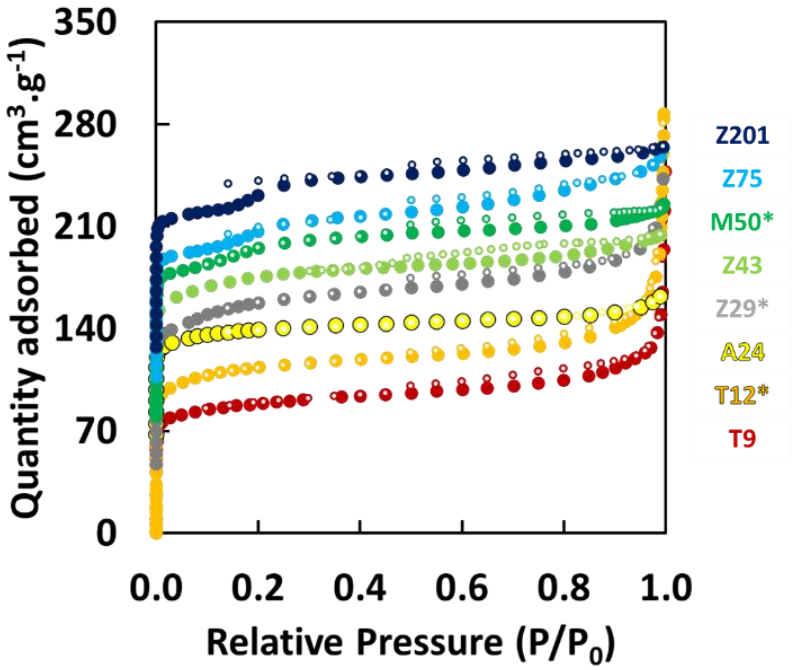

Figure IV.S1: Isothermes de N_2-physisorption (77 K) des catalyseurs utilisés dans l'étude du chapitre.
(Les valeurs de l'axe des ordonnées sont incrémentées pour améliorer la lisibilité)

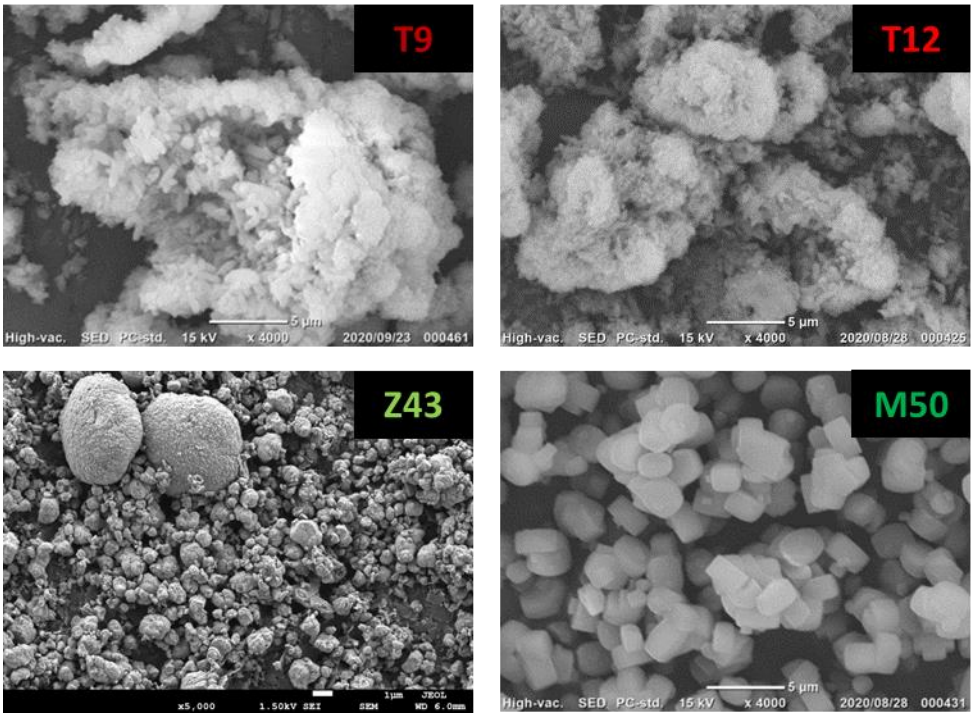

Figure IV.S2: Clichés SEM pour les catalyseurs T9, T12, Z43 et M50

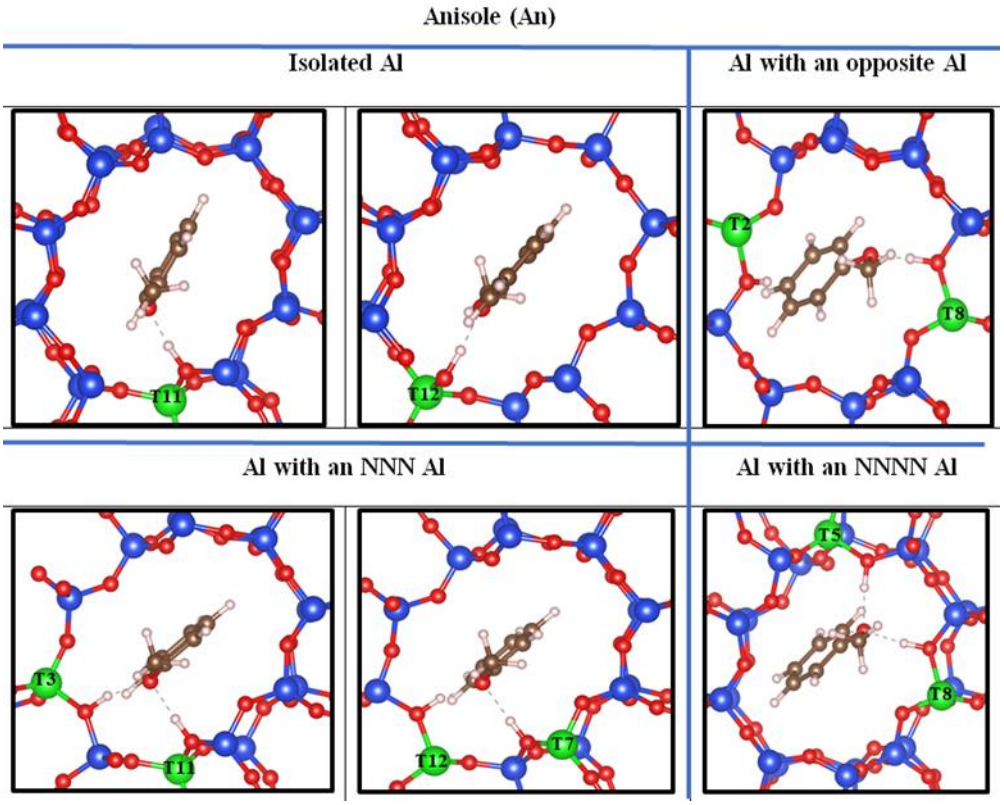

Figure IV.S3: Géométries finales de l'anisole adsorbé sur les aluminium isolés et appariés.

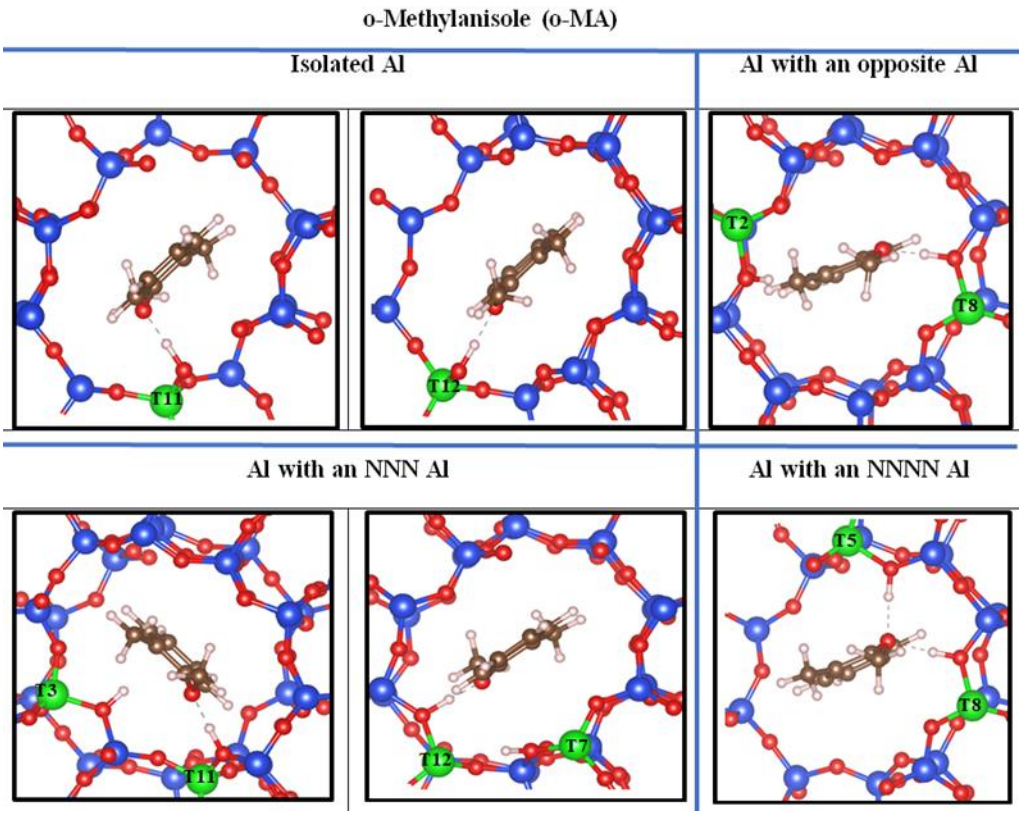

Figure IV.S4: Géométries finales du o-méthylanisole adsorbé sur les aluminiums isolés et appariés.

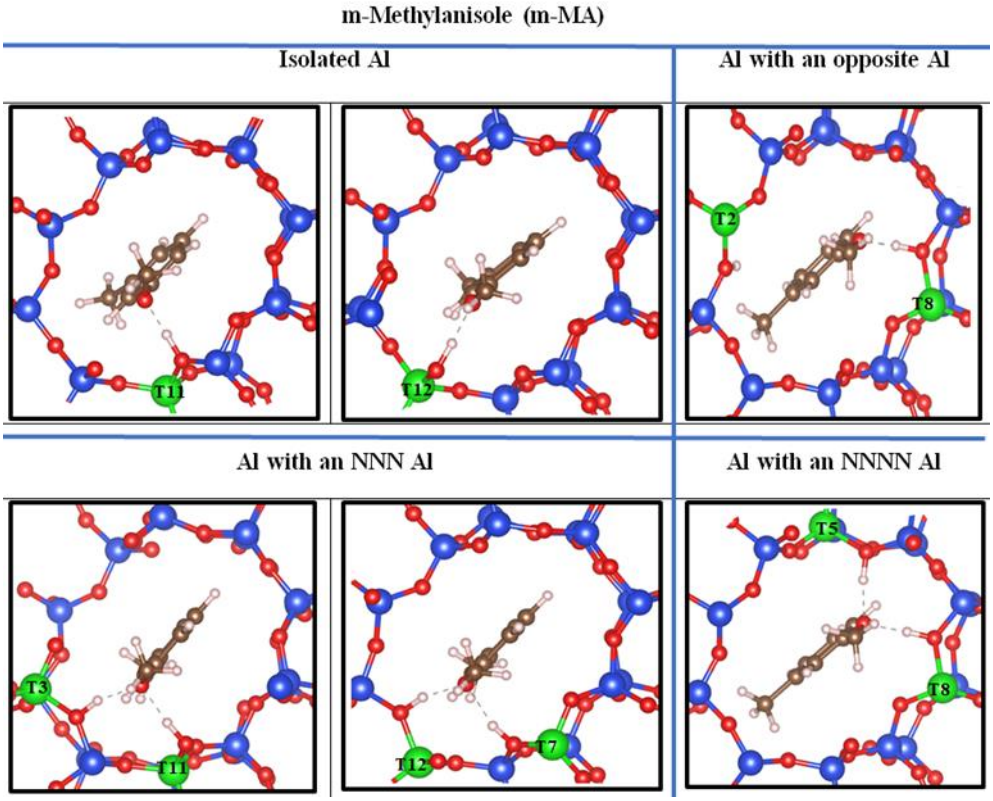

***Figure IV.S5*:** Géométries finales du m-méthylanisole adsorbé sur les aluminiums isolés et appariés.

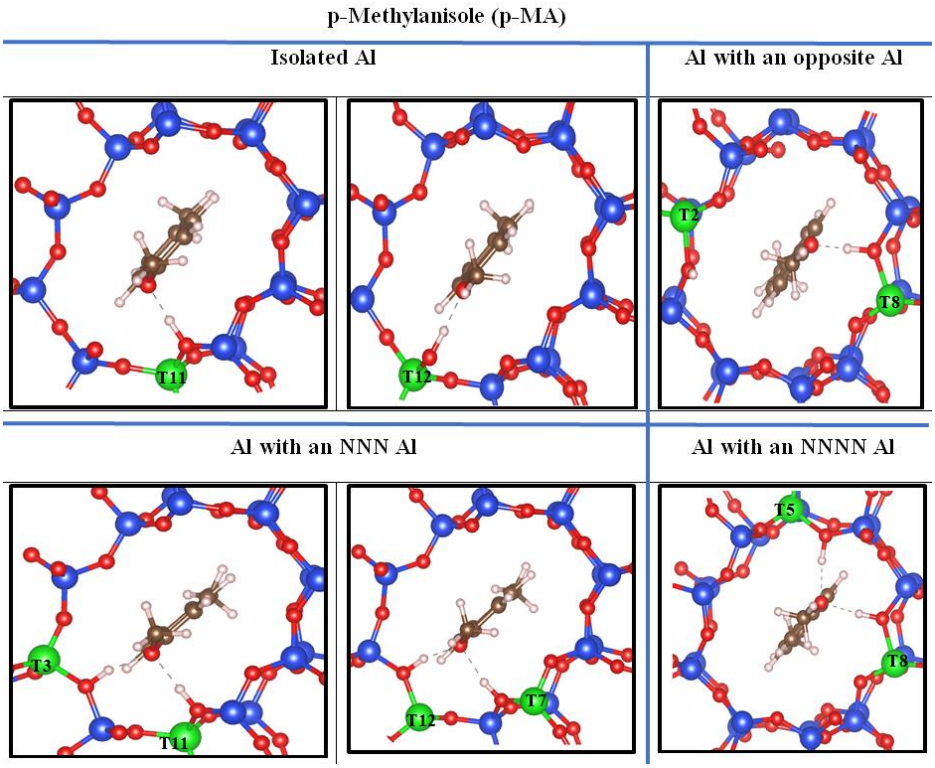

Figure IV.S6: Géométries finales du p-méthylanisole adsorbé sur les aluminiums isolés et appariés.

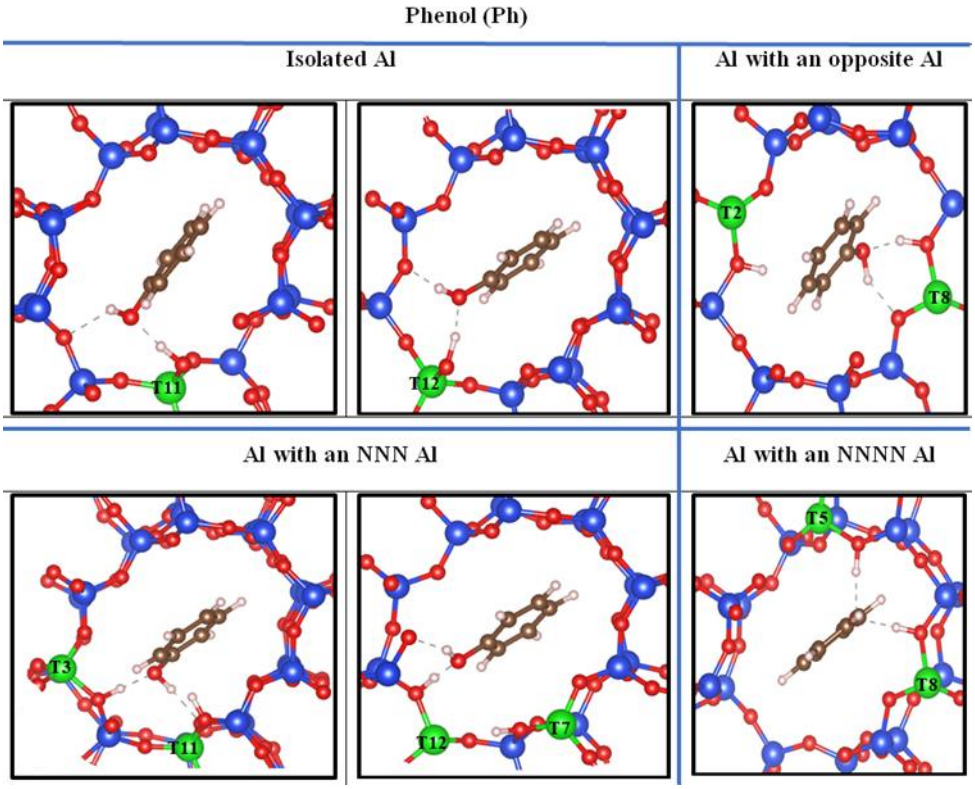

Figure IV.S7: Géométries finales du phénol adsorbé sur les aluminiums isolés et appariés.

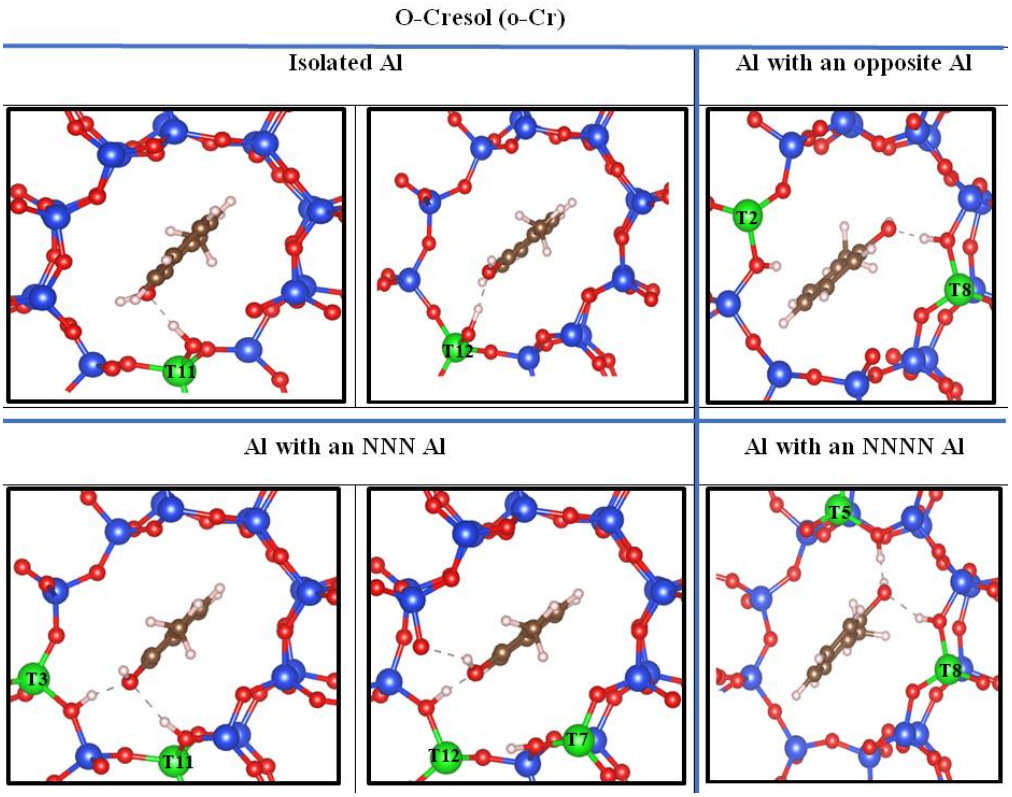

Figure IV.S8: Géométries finales du o-crésol adsorbé sur les aluminiums isolés et appariés.

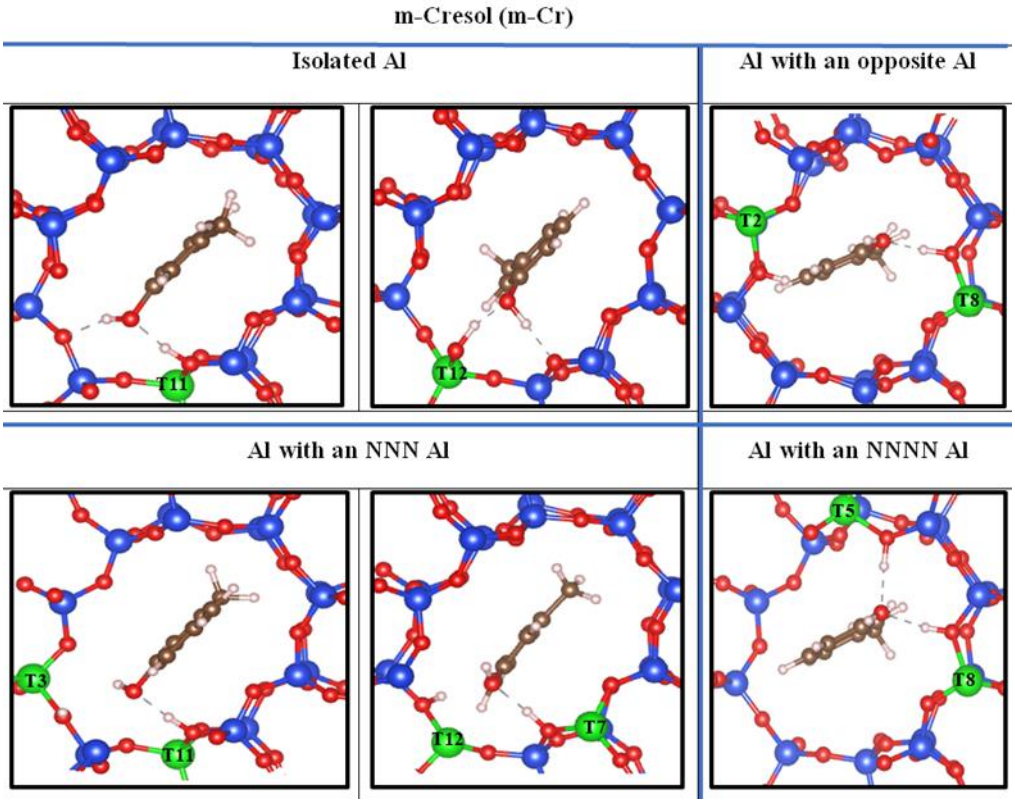

Figure IV.S9: Géométries finales du m-crésol adsorbé sur les aluminiums isolés et appariés.

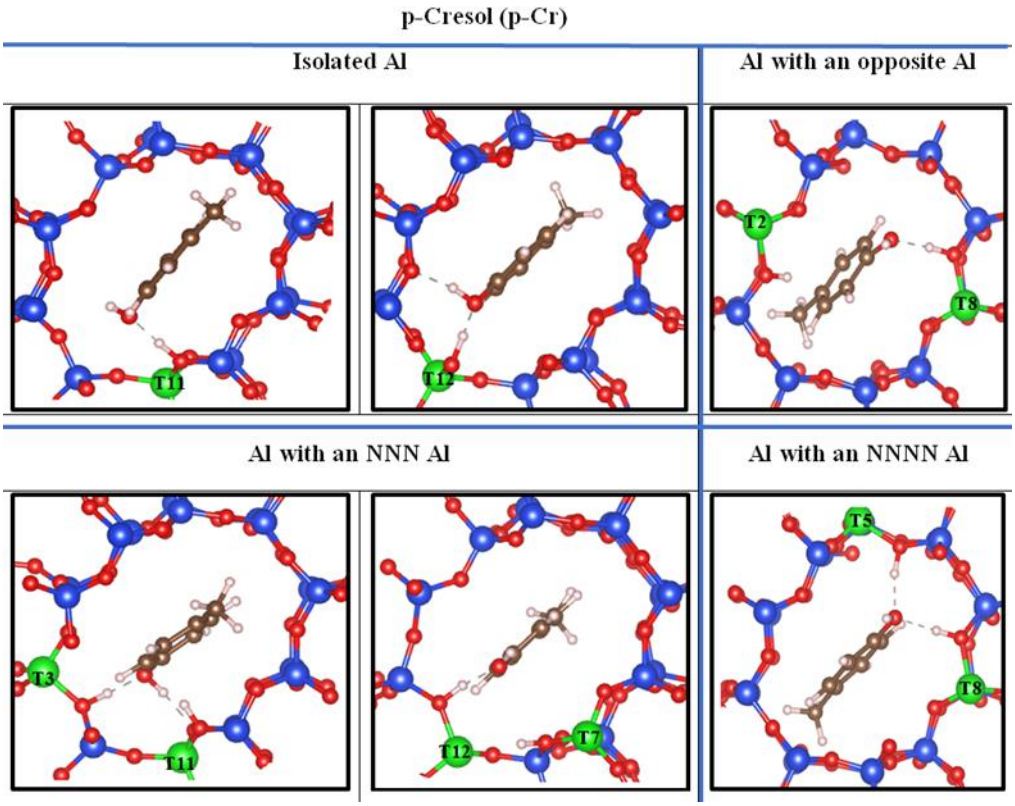

***Figure IV.S10*:** Géométries finales du p-crésol adsorbé sur les aluminiums isolés et appariés.

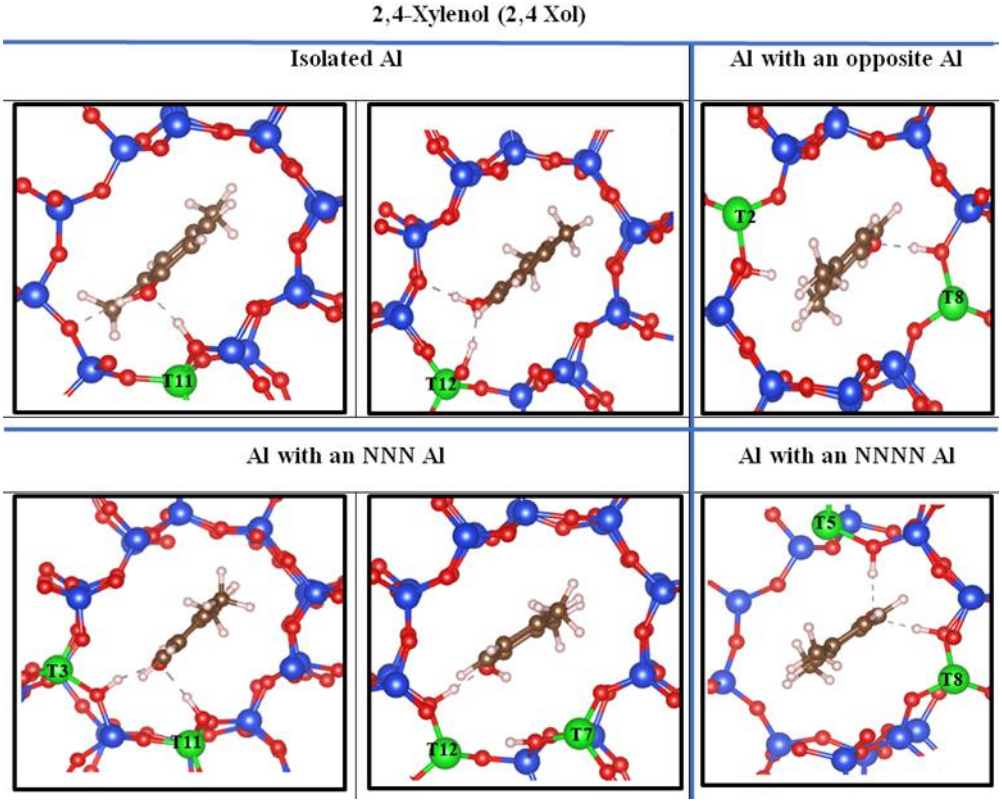

***Figure IV.S11*:** Géométries finales du 2,4-xylénol adsorbé sur les aluminiums isolés et appariés.

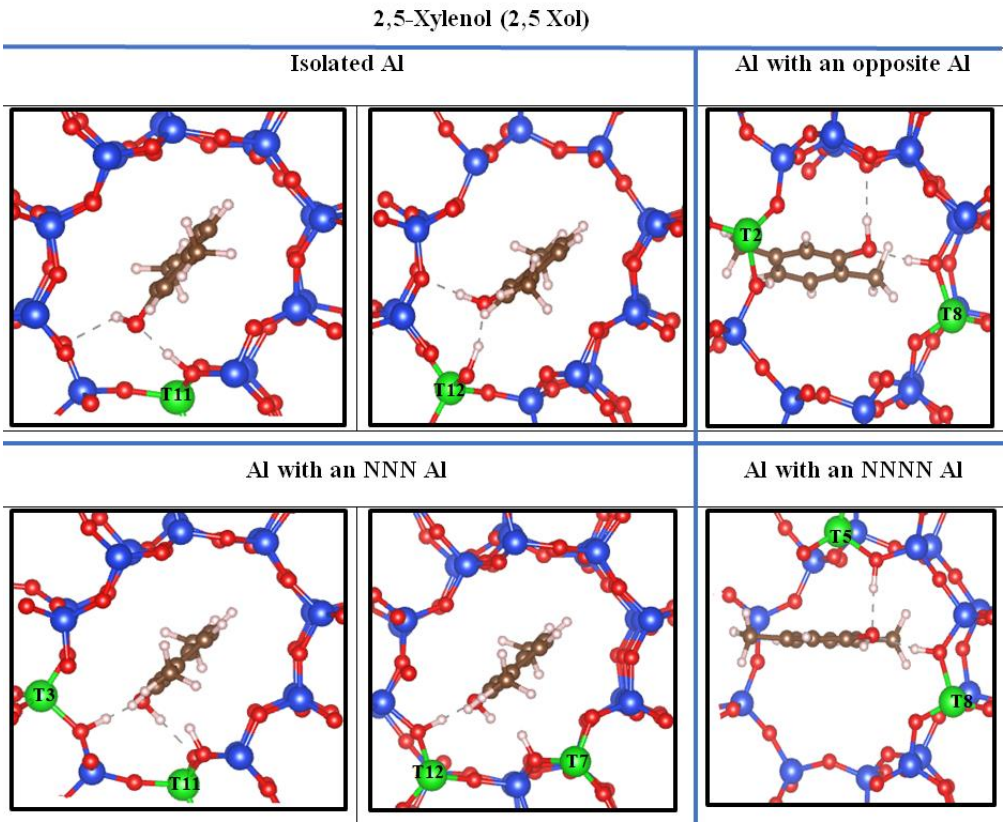

Figure IV.S12**:** Géométries finales du 2,5-xylénol adsorbé sur les aluminiums isolés et appariés.

Annexes – Chapitre V

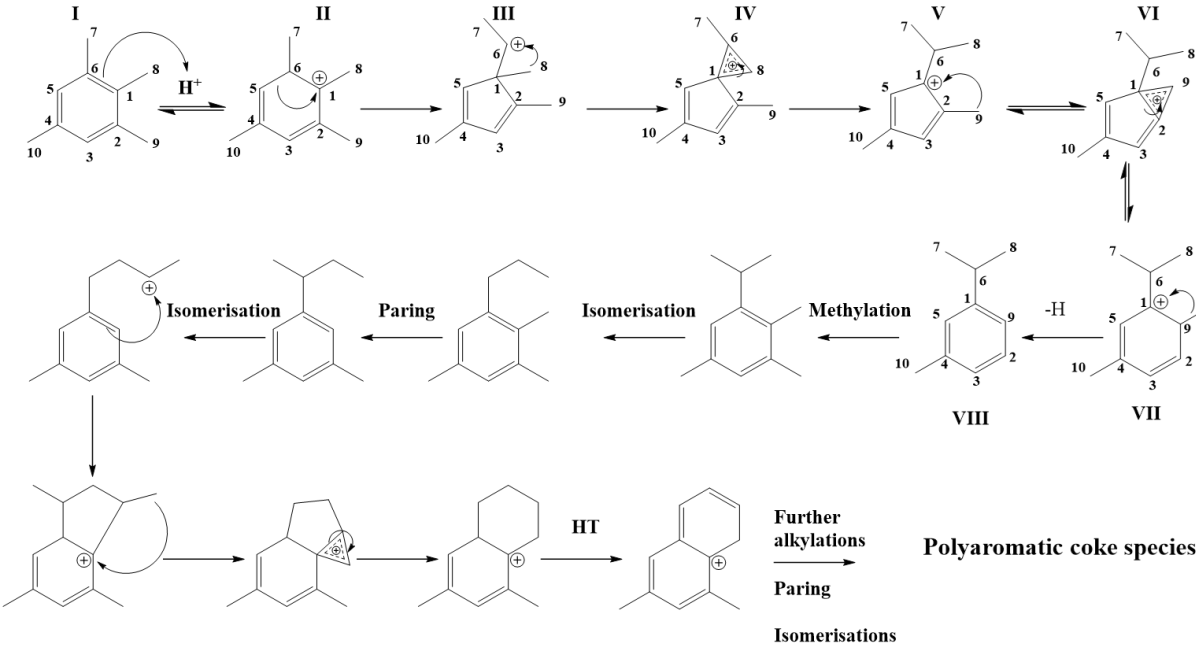

Scheme V.S1: Mécanisme de Sullivan: croissance du coke par contraction-expansion du cycle aromatique.

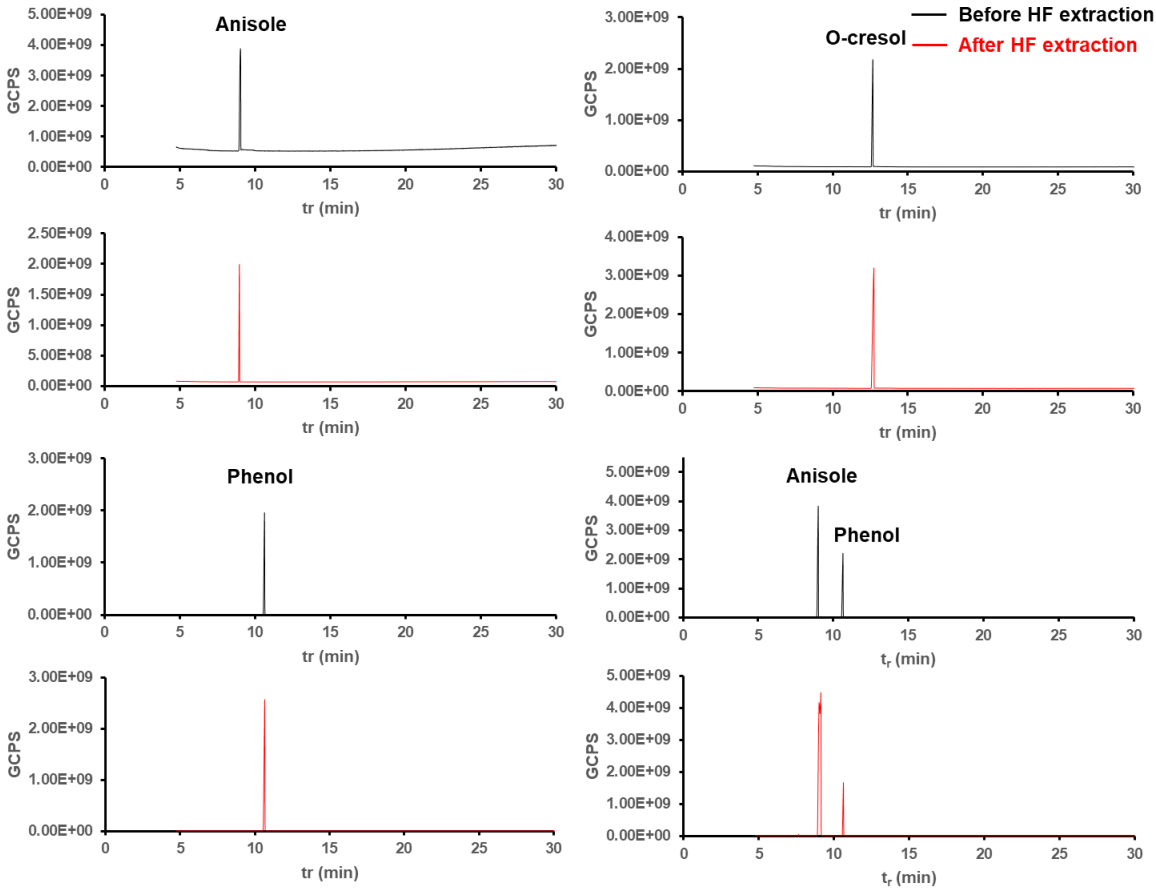

Figure V.S1: Tests à blanc démontrant l'absence d'activité des composes oxygénés dans les conditions de l'extraction du coke par HF. (Chromatogrammes de l'anisole, du phenol et de leur mélange avant et après extraction par HF)

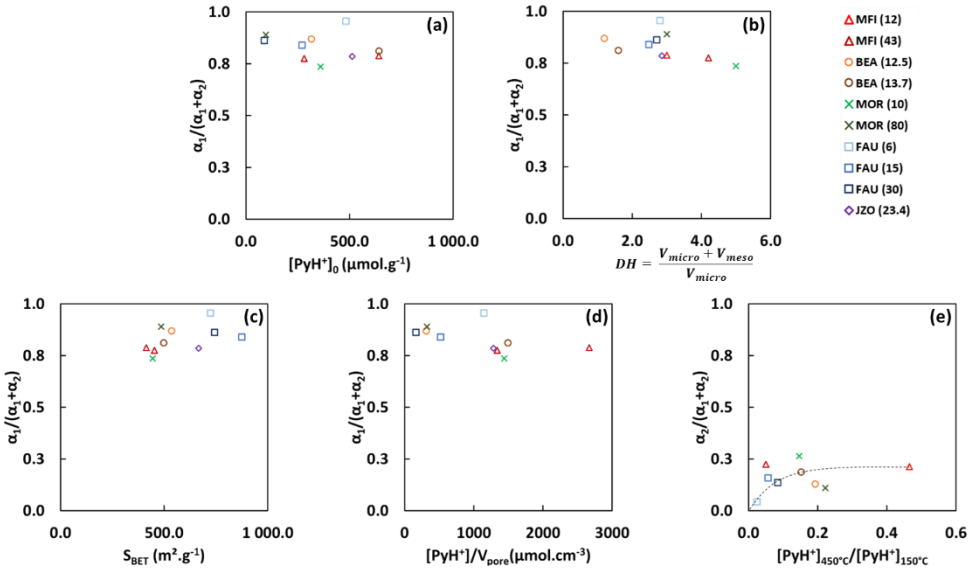

Figure V.S2: Ratio entre activité de l'état stationnaire/activité initiale($\frac{\alpha_2}{\alpha_1+\alpha_2}$) en fonction de différents facteurs.

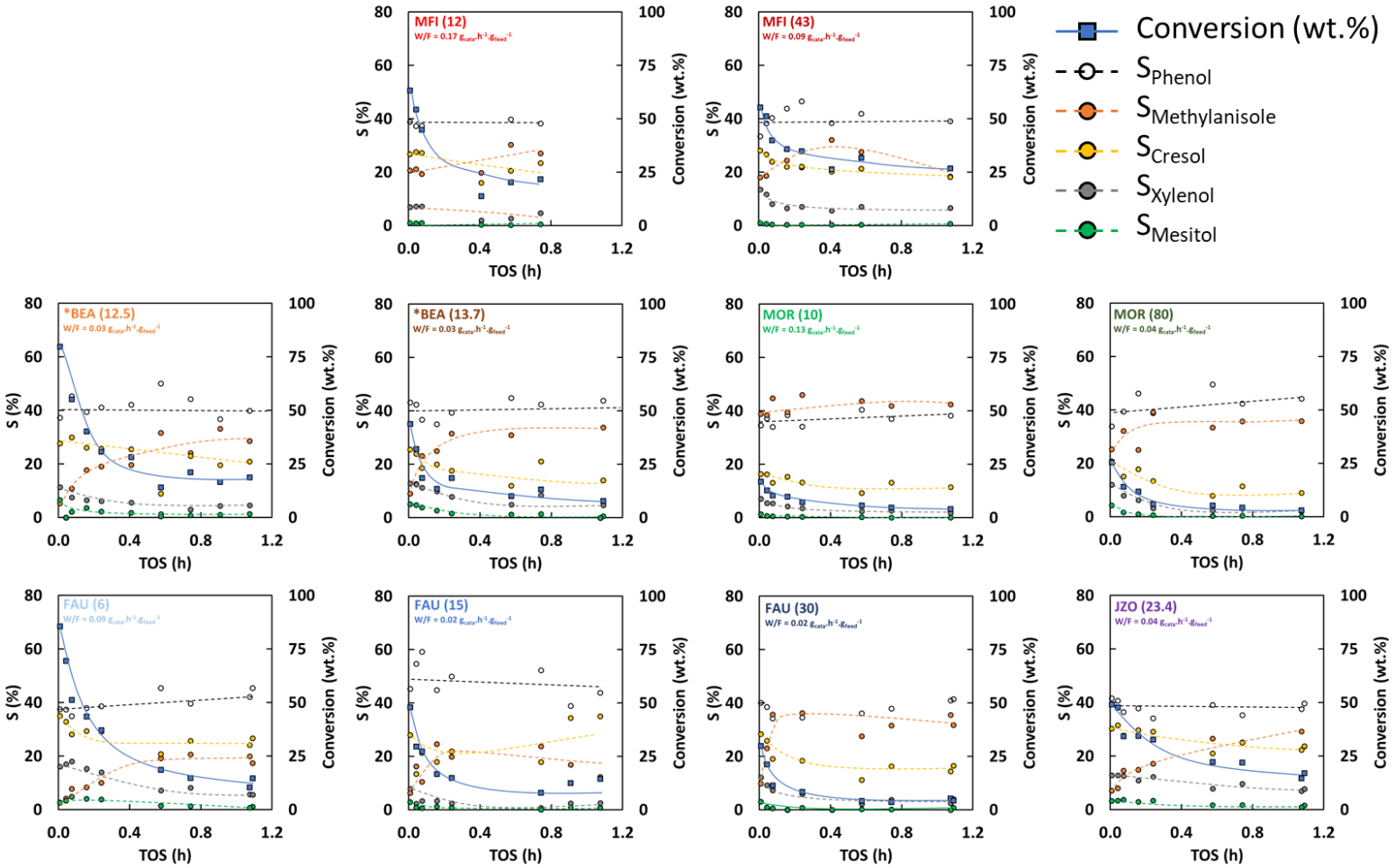

Figure V.S3: Conversion de l'anisole et sélectivité envers les produits pour les catalyseurs du chapitre V en fonction du temps de réaction.

T = 673 K; P_{An} = 0.048 atm; P_{tot} = 1 atm.

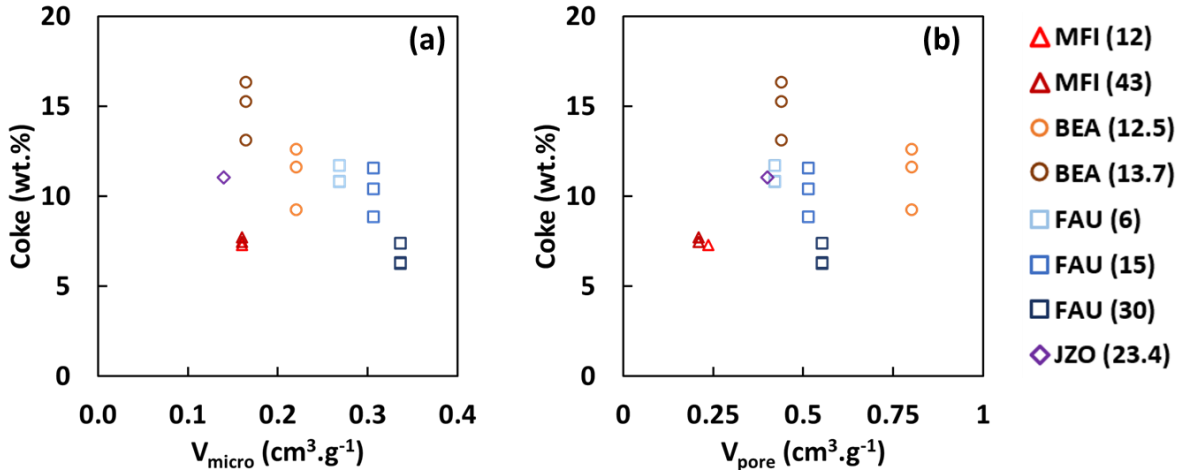

Figure V.S4 : Quantité de coke dans les zéolithes en fonction de (a) leur volume microporeux et (b) leur volume poreux total.

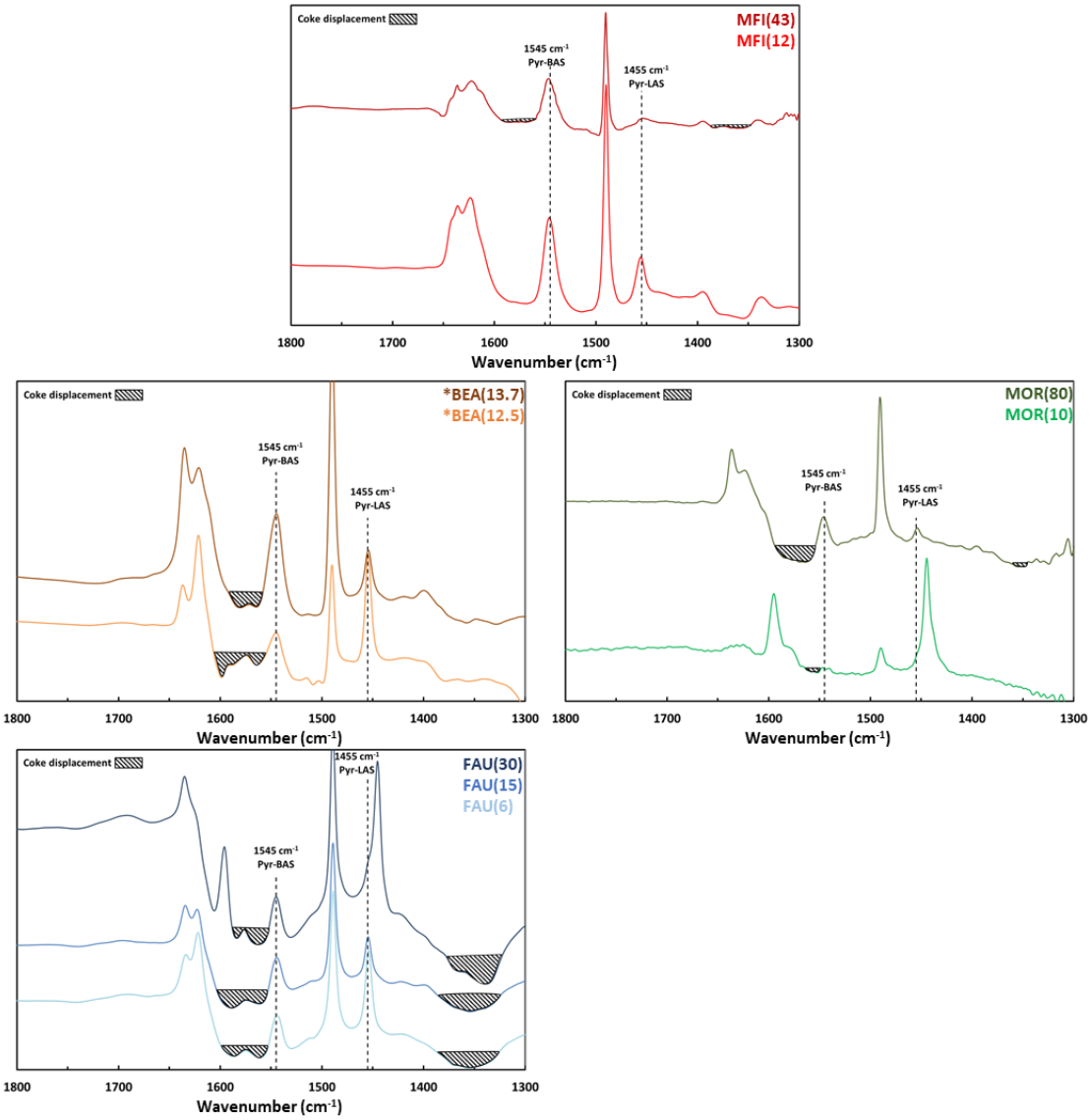

Figure V.S5: Déplacement du coke par la pyridine lors de l'analyse Pyr-FTIR.

Tableau V.S1: Composants du coke identifies dans la MFI(12) et leurs caractéristiques. (ordre des lignes : ordre d'élution sur une colonne SC-5MS).

ID	Formula	M $g.mol^{-1}$	ρ $g.cm^{-3}$
Methylindan-1-one	$C_{10}H_{10}O$	146.19	1.075
Coumarin	$C_9H_6O_2$	146.15	0.935
Dimethylindan-1-one	$C_{11}H_{12}O$	160.21	1.000
Naphtalenol	$C_{10}H_8O$	144.17	1.220
i-Naphtalenol	$C_{10}H_8O$	144.17	1.220
Methylbiphenylol	$C_{13}H_{12}O$	184.23	1.087
Methylnaphthalenol	$C_{11}H_{10}O$	158.20	0.989
Methylbiphenylol	$C_{13}H_{12}O$	184.23	1.087
Fluoren/phenalene	$C_{13}H_{10}$	166.22	1.200
Biphenylol	$C_{12}H_{10}O$	170.21	1.270
Me-fluorene	$C_{14}H_{12}$	180.25	1.100
9-MeO-fluorene	$C_{14}H_{12}O$	196.25	1.400
9,10-dihydroanthracene	$C_{14}H_{12}$	180.25	1.190
Anthracene/phenanthrene	$C_{14}H_{10}$	178.23	1.250
9,10-dihydro-2-methylanthracene	$C_{15}H_{14}$	194.28	1.100
Dimethylbenzophenone	$C_{15}H_{14}O$	210.28	1.023
Fluorenol	$C_{13}H_{10}O$	182.22	1.151
Phenylanisole	$C_{13}H_{12}O$	184.23	1.000
Methylphenanthrene	$C_{15}H_{12}$	192.26	1.100
Phenalenone	$C_{13}H_8O$	180.20	1.300
Fluorenal	$C_{14}H_{10}O$	194.23	1.200
Tetramethylacenaphthylene	$C_{16}H_{16}$	208.30	1.100
Naphtho[2,1-b]furan, 1,2-dimethyl-	$C_{14}H_{12}O$	196.25	1.134
Phenanthrenol	$C_{14}H_{10}O$	194.23	1.200
i-Phenanthrenol	$C_{14}H_{10}O$	194.23	1.200
Fluorene-propyl	$C_{16}H_{16}$	208.30	1.202
Dimethylfluorenone	$C_{15}H_{12}O$	208.26	1.200
2-Methoxy-6methylanthracene	$C_{16}H_{14}O$	222.28	1.100
7H-Benzanthrene	$C_{17}H_{12}$	216.28	1.200
Dimethylpyrene	$C_{18}H_{14}$	230.30	1.200

Annexes – Chapitre VI

Tableau VI.S1 Vue d'ensemble d'études précédentes en pyrolyse catalytique, avec emphase sur la comparaison entre les zéolithes classiques et hiérarchisées (*BEA, MFI).

Feedstock	Catalysts	Acidity (fresh, method) (µmol/g)	Acidity (spent, method) (µmol/g)	Si/Al	Reactor type	Biomass/catalyst ratio	Results (Qualitative)	Aromatic Hydrocarbons (AH) production Results (Quantitative)	Reference
Milled Wood Lignin-derived monomeric phenols	HY	1837 (Total, NH3-TPD)	None	5.2	Coil-type CDS Pyroprobe 5000 (CDS Analytical Inc., Oxford, PA, USA)-GC-MS/FID	0,15mg/0,6mg	Y produced more aromatic hydrocarbons; BEA produced more naphtalenes; ZSM-5 had better results with oxygen-saturated phenols for AH production; temperature (600-700-800°C) and structure (saturation or not of the phenols) were shown to have great impact on the formation of AH.	AH Yields : - from phenol : 7wt%; -from guaiacol : 8,5wt%; - from syringol : 4,5wt%; - from methylphenol : 8,6wt%; - from ethylguaiacol : 14wt%; - from propylguaiacol : 13,4wt%; from methylsyringol : 6,3wt%; -from vanillin : 4,2wt%; - from syringaldehyde : 2,8wt%; - from acetosyringone : 4,8wt%	J-Y Kim et al.(2020) [1]
	HBEA	1307		25				AH Yields : - from phenol : 5,7wt%; -from guaiacol :5,1wt%; - from syringol : 2,2wt%; - from methylphenol : 9,3wt%; - from ethylguaiacol : 8,5wt%; - from propylguaiacol : 12,9wt%; from methylsyringol :5,5wt%; -from vanillin : 3,2wt%; - from syringaldehyde : 2,7wt%; - from acetosyringone : 6,2wt%	
	HZSM-5	1141		23				AH Yields : - from phenol : 5,1wt%; -from guaiacol : 1,6wt%; - from syringol : 1,1wt%; - from methylphenol : 4,1wt%; - from ethylguaiacol : 2,9wt%; - from propylguaiacol : 3wt%; from methylsyringol : 4,5wt%; -from vanillin : 5,2wt%; - from syringaldehyde : 5,4wt%; - from acetosyringone : 5,5wt%	
Wood polymer composites (Wood powder + Polyethylene, Polyethylene + CaCO3 + others)	Hierarchical HZSM-5	Qualitative (NH3-TPD)	None	<15	Tandem Micro Reactor-GC-MS	1mg/1mg	Hierarchised BEA had a lower decomposition temperature for plastics (polyethylene and polypropylene), and a higher elimination efficiency of large molecules, due to its large pore size. Hierarchised ZSM-5 showed the best activity, with its strong acidity, its mesoporosity and shape selectivity for AH formation. It also had better stability compared to standard µporous ZSM-5.	AH Yields (MS peak area*10^6): -from WPC1 : ~875; -from WPC2 : ~900.	Y-M Kim et al. (2019) [2]
	Hierarchical HBEA	Qualitative (NH3-TPD)		<19				AH Yields (MS peak area*10^6): -from WPC1 : ~600; -from WPC2 : ~580.	
Sunflower stalk, knotweed, cedar, apple tree stem	HZSM-5	1230 (Total, NH3-TPD)	None, but XRD of spent zeolites	24	In-situ catalytic upgrading, quartz fixed bed reactor-GC-MS	0,5g/1g	H-ZSM-5 is the most effective catalyst, for producing more AH; USY has the most coke deposition, all 3 are easy to regenerate and were active after 3 cycles. Zeolite structure and biomass origin have a high impact on the resulting products' distribution	AH yields : - 1st cycle : 6,88wt%; - 2nd cycle : 5,88wt%; - 3rd cycle : 4,59wt%	N. Chaihad et al. (2019) [3]
	HBEA	750		28				AH yields : - 1st cycle : 2,96%; - 2nd cycle :2,52wt%; - 3rd cycle : 2,16wt%	
	HUSY	930		6				AH yields : - 1st cycle : 3,77wt%; - 2nd cycle : 3,49wt%; - 3rd cycle : 3,53wt%	

Feedstock	Catalysts	Acidity (fresh, method) (µmol/g)	Acidity (spent, method) (µmol/g)	Si/Al	Reactor type	Biomass/catalyst ratio	Results (Qualitative)	Aromatic Hydrocarbons (AH) production Results (Quantitative)	Reference
Eucalyptus Woodchips	Hierarchical HZSM-5	360 (Total, NH3-TPD); 100 ($B_{350°C}$, Pyr-FTIR)	/	58	Fixed-bed stainless steel reactor-µGC-TCD	5g/1g	ZnO and MgO-loaded materials had better deoxygenation activity, better bio-oil yield, and lower gas and coke formation (the two latter, due to lower Bronsted acidity). MgO was more effective than ZnO. H-ZSM-5 was even better than HBEA, with these loadings. (MgO/HZSM-5 being the best catalyst out of those tested).	AH Yields (GC/MS %relative Area) : 12% of the 26,5wt% of bio-oil yield	H. Hernando et al. (2017) [4]
	Hierarchical HBEA	578 ; 90		24				AH Yields (GC/MS %relative Area) : 5% of the 31,8wt% of bio-oil yield	
	Hier-HZSM-5 MgO	660 ; 20		58				AH Yields (GC/MS %relative Area) : 4% of the 28,4wt% of bio-oil yield	
	Hier-HZSM-5 ZnO	704 ; <20		58				AH Yields (GC/MS %relative Area) : 3% of the 25,4wt% of bio-oil yield	
	Hier-HBEA MgO	662 ; <20		24				AH Yields (GC/MS %relative Area) : 1,5% of the 34,6wt% of bio-oil yield	
	Hier-HBEA ZnO	871 ; <<20		24				AH Yields (GC/MS %relative Area) : 1,5% of the 32wt% of bio-oil yield	
Dealkalined Lignin	HFER	1440 (Total, NH3-TPD)	/	18	Fixed-bed reactor-GCMS/Karl-Fischer analyzer	1 : 1	HZSM-5 produced the most AH (mono and poly), while BEA was more selective towards mono AH.	AH Yields : 0,81% of the 22,6wt% of bio-oil yield	I. Kurnia et al. (2017) [5]
	HMOR	1220		15				AH Yields : 2,67% of the 17,4wt% of bio-oil yield	
	HZSM-5	1230		24				AH Yields : 8,87% of the 17,2wt% of bio-oil yield	
	HBEA	750		28				AH Yields : 5,26% of the 15,8wt% of bio-oil yield	
	HUSY	930		6				AH Yields : 5,08% of the 13,5wt% of bio-oil yield	
Pine wood	HZSM-5	395 ($B_{350°C}$, Pyr-FTIR)	/	11.5	(Auger fed reactor for pyrolysis and packed bed reactor for upgrading)-GC-TCD/FID-MS	50g cata and WHSV = $10h^{-1}$ of pyrolysis vapors	HZSM-5 produced more Hydrocarbons, and more AH, with HBEA being far behind. HZSM-5 was also more efficient in deoxygenation (O/C=0,33 against 0,75 for non-catalytic pyrolysis, and 0,43 at minimum for HMOR)	AH Yields (GC %relative Area) : 24,03%	V.K. Guda et al.(2016) [6]
	HMOR	305		10				AH Yields (GC %relative Area) : 6,75%	
	HFER	/		10				AH Yields (GC %relative Area) : 5,14%	
	HY	205		6				AH Yields (GC %relative Area) : 7,63%	
	HBEA	187		19				AH Yields (GC %relative Area) : 10,62%	
Jatropha husk and Cedar	HUSY	620 (strong, NH3-TPD)	/	5	Single-shot microfurnace pyrolyzer-GC/MS	1 : 1 & 1 : 5	HBEA produced the most HC and less PAH than HUSY, for example. HUSY seemed the most effective for reducing O in the pyrolysis vapor. Reducing the biomass to catalyst ratio significantly increased HC production for HBEA.	Hydrocarbons Yields (GC %relative Area) : From Jatropha 31,1% (1:1) et 50,7% (1:5) - From Cedar 4,7% (1:1)	T. Mochizuki et al. (2013) [7]
	HBEA	120		20				Hydrocarbons Yields (GC %relative Area) : From Jatropha 26,4% (1:1) et 46,8% (1:5) - From Cedar 1,8% (1:1)	
	HMOR	460		9				Hydrocarbons Yields (GC %relative Area) : From Jatropha 32,5% (1:1) et 42,9% (1:5) - From Cedar 2% (1:1)	
	HZSM-5	510		11.5				Hydrocarbons Yields (GC %relative Area) : From Jatropha 31,3% (1:1) et 48,2% (1:5) - From Cedar 3,9% (1:1)	

Feedstock	Catalysts	Acidity (fresh, method) (µmol/g)	Acidity (spent, method) (µmol/g)	Si/Al	Reactor type	Biomass/catalyst ratio	Results (Qualitative)	Aromatic Hydrocarbons (AH) production Results (Quantitative)	Reference
Eucalyptus and Oak-derived Lignin	HZSM-5	/	/	12.75	Pyroprobe 5200 analytical pyrolyzer (CDS Analytical Inc.)-GC/MS	1 : 20	HZSM-5 produced the most AH, then HBEA, HMOR, and HY. BEA and Y were best at deoxygenation, but HZSM-5 is not far behind, and thus overall, a better choice.	AH Yields (GC peak Area) : 1,54*10^9	Y. Yu et al. (2012) [8]
	HMOR			8.2				AH Yields (GC peak Area) : 9,09*10^8	
	HBEA			12.75				AH Yields (GC peak Area) : 2,08*10^9	
	HY			2.55				AH Yields (GC peak Area) : 4,55*10^8	
Glucose	ZK-5	/	/	2.75	Pyroprobe reactor (CDS 2000 Analytical Inc.)-GC/MS	1 : 19	ZSM-5 and ZSM-11 have the highest aromatic yield and the least amount of coke; High coke yield, low aromatic yields, and low oxygenate yields were observed with large pore zeolites. Aromatic yield was a function of zeolite pore size (none with small pores, max with medium pores, large pores having higher coke formation)	AH Yields (Carbon%) : 0%	J. Jae et al. (2011) [9]
	SAPO-34			0.28				AH Yields (Carbon%) : 0%	
	FER			10				AH Yields (Carbon%) : 2,5%	
	ZSM-23			80				AH Yields (Carbon%) : 12%	
	MCM-22			15				AH Yields (Carbon%) : 3,6%	
	SSZ-20			45				AH Yields (Carbon%) : 10,3%	
	ZSM-11			15				AH Yields (Carbon%) : 25,3%	
	ZSM-5			15				AH Yields (Carbon%) : 35,5%	
	IM-5			20				AH Yields (Carbon%) : 17,3%	
	TNU-9			20				AH Yields (Carbon%) : 2,3%	
	BEA			19				AH Yields(Carbon%) : 4,3%	
	SSZ-55			27				AH Yields (Carbon%) : 2,7%	
	Y			2.6				AH Yields (Carbon%) : 1,6%	
Glucose, Xylitol, Cellobiose, Cellulose	HZSM-5	/	/	60	Pyroprobe analytical pyrolyzer (CDS 2000 Analytical Inc.)-GC/MS	1 : 19 ; 1 : 9 ; 1 : 4 ; 1 : 2,3 ; 1 : 1,5; 1 : 19 was common to all the feeds	Coke formation can be minimized by: fast heating rates ; high catalyst to feed ratios; proper catalyst selection (active sites and pore structure); (molar carbon yield where the moles of carbon in the product are divided by the moles of carbon in the reactant.)	AH Yields (Carbon%, for 1:19) : 30,95%	T.R. Carlson et al. (2009) [10]
	Silicalite			?				AH Yields (Carbon%, for 1:19) : 5,95%	
	HBEA			?				AH Yields (Carbon%, for 1:19) : 4,29%	
	HY			50				AH Yields (Carbon%, for 1:19) : 0%	
	Silica-Alumina			8				AH Yields (Carbon%, for 1:19) : 1,19%	

Feedstock	Catalysts	Acidity (fresh, method) (µmol/g)	Acidity (spent, method) (µmol/g)	Si/Al	Reactor type	Biomass/catalyst ratio	Results (Qualitative)	Aromatic Hydrocarbons (AH) production Results (Quantitative)	Reference
Wood(poplar)-Polypropylene composite	ZnO	/	/	/	CDS5200 pyroprobe analytical pyrolyzer (CDS Analytical Inc.)-GC/MS	1 : 4	CaO was good for deoxygenation, eliminating phenols and carboxylic acids; MgO increased alkene yield; ZnO had the best alkene yield, while increasing ketones and phenols; only Fe_2O_3 produced aromatics.	AH Yields (GC peak Area%) : 0%	X. Lin et al. (2018) [11]
	CaO							AH Yields (GC peak Area%) : 0%	
	MgO							AH Yields (GC peak Area%) : 0%	
	Fe_2O_3							AH Yields (GC peak Area%) : 4,89%	
Oak	ZSM-5-ATP 0.7:0.3 wt. (ATP = Attapulgite)	118 (Brønsted, Pyr-FTIR. Very detailed with strength and type)	43	18	Continuous biomass pyrolysis bench scale unit: Fluidized bed for pyrolysis and fixed bed for zeolites	Wood: 5g.min^{-1}, 10, 15, 20 and 25min feeding over a bed of 25g of zeolite/binder.	ZrO2 in desilicated ZSM-5/ATP decreases cracking activity, improving bio-oil yields, and coke was softer (less PAH); deactivation by site coverage. Nanocrystalline ZrO2/n-(ZSM-5)-ATP was better for deoxygenation, bio-oil yields, and retaining textural properties. Nice imaging and characterization of coke location in particles (with binder).	Mass yields in aromatic hydrocarbons not provided. Best reduction of O in organics for ZrO_2/nZSM-5-ATP (nanosized ZSM-5 crystals (30-100nm) with ZrO_2	A.M. Hernández-Giménez et al. (2020) [12]
	ds-(ZSM-5)-ATP 0.7:0.3 wt. (ds = desilicated)	94	32	9					
	ZrO_2/ds-(ZSM-5)-ATP 0.07:0.63:0.3 wt.	98	8	9					
	ZrO2/n-(ZSM-5)-ATP 0.07:0.63:0.3 wt. (n = nanosized)	67	35	42					

Protocoles de synthèse des catalyseurs

Synthesis of *BEA-type zeolite micron-sized crystal, S-(*BEA)$_{MC}$ [13]

The synthesis mixture was prepared by hydrolysing tetraethylorthosilicate (TEOS) (98 wt%, Aldrich) in an aqueous solution of tetraethylammonium hydroxide (TEAOH) (35 wt% in aqueous solution, Aldrich). Then a solution made by dissolving metal aluminium (99.95%, Aldrich) in aqueous TEAOH was added and the mixture was kept under stirring until the complete evaporation of ethanol formed upon hydrolysis of TEOS. Finally, hydrofluoric acid (40 wt% in H_2O) was added. The obtained gel was hydrothermally treated at 1343 K for 14 days in a Teflon lined stainless steel autoclave. After the required crystallization time, the autoclave was cooled down to room temperature. The pH of the mother liquor was in the range 8–9.5. The product was filtered and washed extensively with distilled water. Finally, the sample was calcined under air at 823 K during 5 h with a temperature ramp of 20 K/min in order to remove the organic template.

Alkaline treatment on BEA zeolite, H_A-(*BEA)$_N$[14]

The creation of mesopores inside a commercial *BEA zeolite (CP814E zeolite, Zeolyst) was carried out by using a 0.13 M solution formed of NaOH & tetrabutylammonium hydroxide (TBAOH), with a 0.6 molar ratio of TBAOH. Desilication treatments were carried out at 338 K for 30 minutes. After each desilication, the suspension was cooled down in an ice-bath, filtered and washed with distilled water to reach neutral pH. Threefold successive Na^+ / NH_4^+ ion exchanges were done after with 0.5M NH_4NO_3 solution at 353 K for 1 hour. The final materials were calcined at 823 K for 6 hours. The conditions of desilications are reported in **Table VI.S2**.

Alkaline treatment on MFI zeolite, H_A-(MFI)$_S$ [15]

The generation of mesopores inside a commercial NH_4-ZSM-5 zeolite (CBV 8014) was carried out by using NaOH (0.2M, pH=13.3 at 298 K) at 338 K for 30 min. The pH of solution after the alkaline treatment is around 12. The solution is cooled in ice in order to stop the zeolite modification. The desilicated zeolite was calcined at 773 K for 12 h, then exchanged by a solution of NH_4NO_3 at 333 K for 1 h (three

times), dried and calcined at 773 K for 12 h. Finally, the zeolite washed with a solution of 0.1 M HCl at 343 K for 6 h, then washed with distilled water, dried and calcined at 773 K.

Alkaline treatment on MOR zeolite, H_A-(MOR)$_S$ and H'_A-(MOR)$_S$[16]

The zeolite used as a starting material was a commercial protonic mordenite (MOR, Süd Chemie) with a molar ratio Si/Al of 20. Alkaline treatment was carried out using NaOH as desilicating agent following operating conditions reported in **Table VI.S2**. Briefly, 10 grams of **MOR** were stirred at 400 rpm in 300 ml alkaline solution (0.2 M) at 343 K (H_A) and 358 K (H'_A) respectively for 2 h. Then, zeolite suspension was centrifuged (6000 rpm) after being cooled down in ice–water mixture. The decantation of the liquid was followed by re-suspension with demineralized water. This procedure was repeated until the pH was 7. Samples were subsequently treated with 0.5 M of HCl under stirring at 303 K for 10 min using the proportion of 10 ml per gram of sample. All samples were converted into their correspondent protonic form by three consecutive exchanges with 2M, NH_4NO_3 using the proportion: 20 cm^3/g of zeolite. The exchange was carried out at 333 K for 4 h. After a careful wash up to pH 7, solid was calcined under air flow (100 ml/min per g of zeolite) at 823 K for 5 h.

Fluoride etching on MOR zeolite, H_B-(MOR)$_S$ and H_{uB}-(MOR)$_S$ [16]

Fluoride etching on mordenite was carried out through the use of an aqueous HF solution (0.7 M, (H_B-(MOR)$_S$, biased) **or** ammonium fluoride (4.5 M, H_{uB}-(MOR)$_S$, unbiased) on commercial mordenite (Süd Chemie). 1 g of the parent mordenite was placed in 100mL Teflon vessel. 20 mL of the HF solution was added at 298 K for 6 min under mechanical stirring (500 rpm). Thereafter the zeolite suspensions were centrifuged at 6000 rpm for 10 min. The residue was washed with 40 mL of demineralized water. Washing cycles were performed until neutral pH. Solids were dried at 373 K for 12 h and calcined under air flow (100 ml/min per 1 g of zeolite) at 823 K for 8h.

Les résultats de 4 expériences différentes sont présentées en **Figure VI.S1**. La bonne reproductibilité s'explique par la procédure optimisée de pyrolyse (et le design du réacteur) et pas la méthode de calibration interne pour la GC/MS-FID.

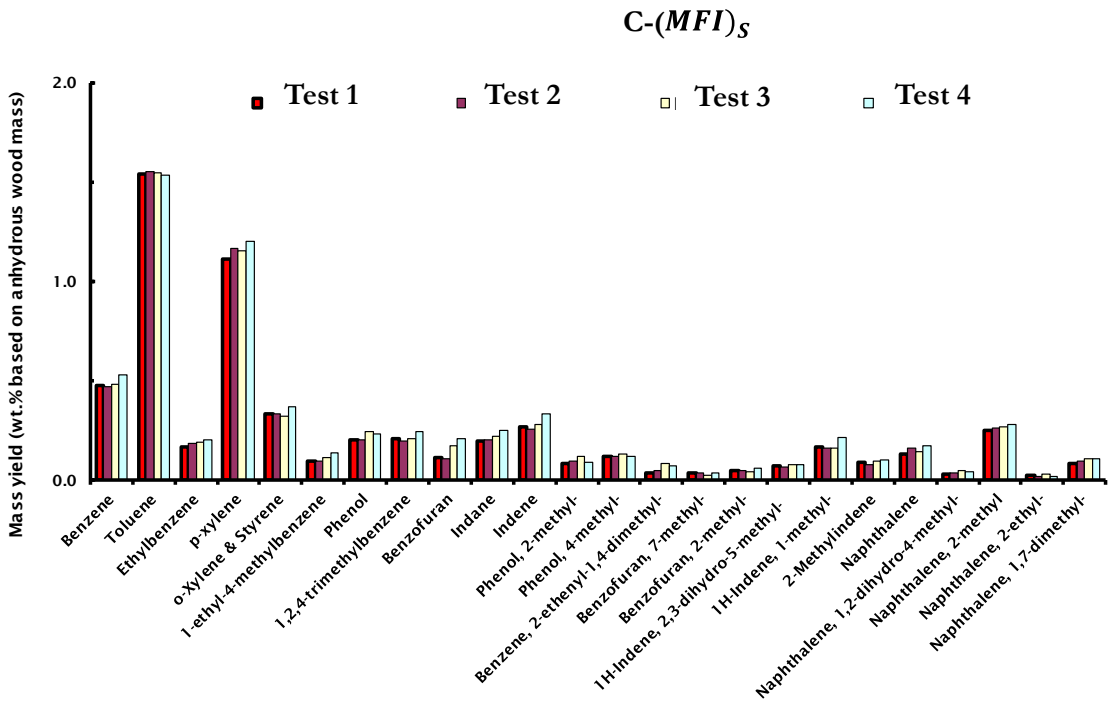

Figure VI.S1 : Reproductibilité pour 4 expériences différentes menées avec le catalyseur C-$(MFI)_S$, quantification des molécules par GC/MS-FID

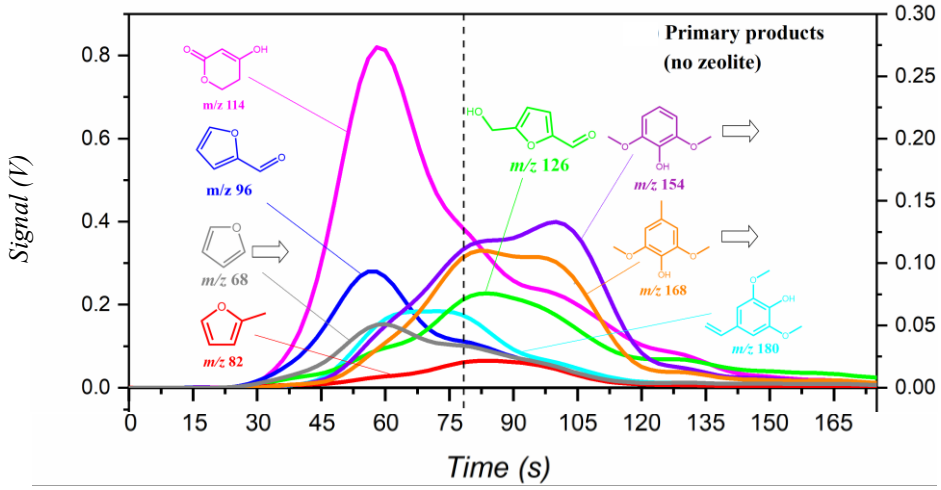

Figure VI.S2 : Marqueurs principaux en fonction du temps pour la pyrolyse de biomasse sans catalyseur dans le deuxième réacteur à 773 K.

(A noter : les intensités de signal des m/z 68, 154 et 168 sont présentées sur l'axe des ordonnées de droite).

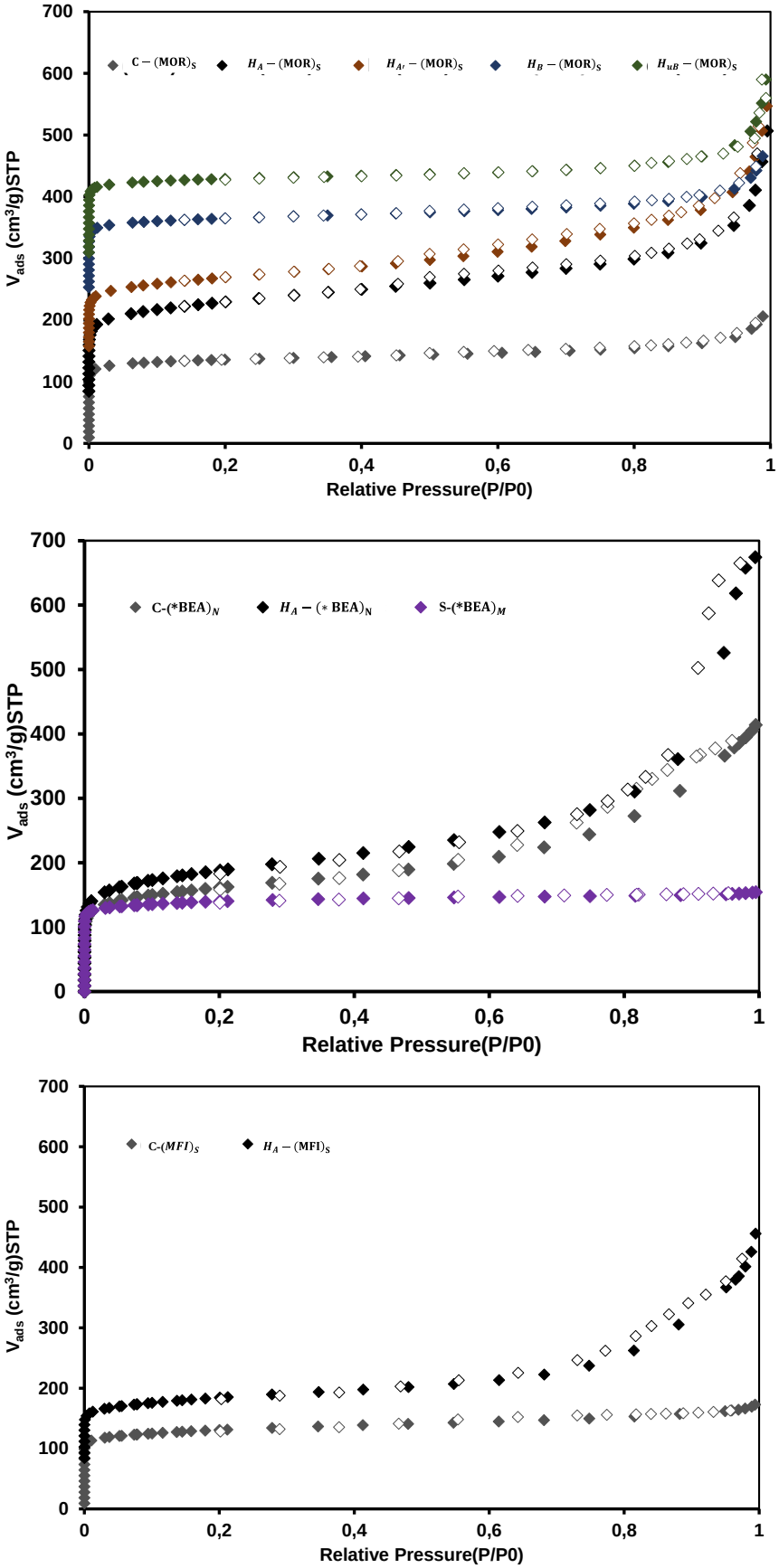

Figure VI.S3 : Isothermes de N_2-physisorption (77 K)
Symboles pleins: adsorption; symboles vides: désorption.

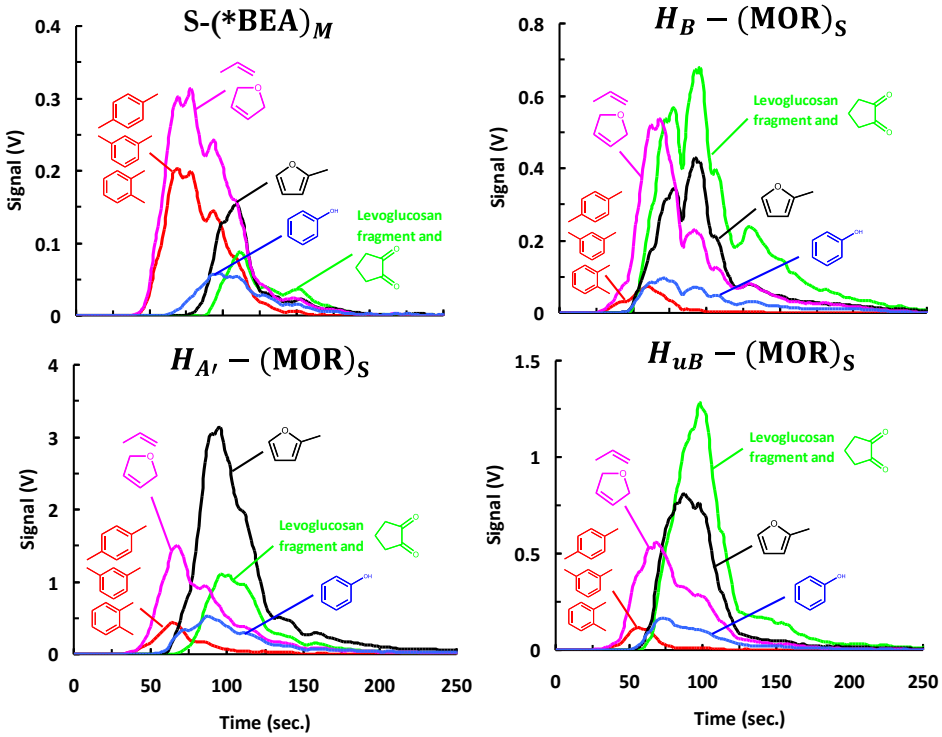

Figure VI.S3 : Evolution de certains marqueurs importants: m/z 106 (xylènes), 98 (fragments de levoglucosane et 1,2 cyclopentanedione), 82 (2-méthyl furane), 42 (propylène et fragments de 2,5-dihydrofurane), 94 (phénol) en fonction du temps (analysé par SPI-MS on-line).

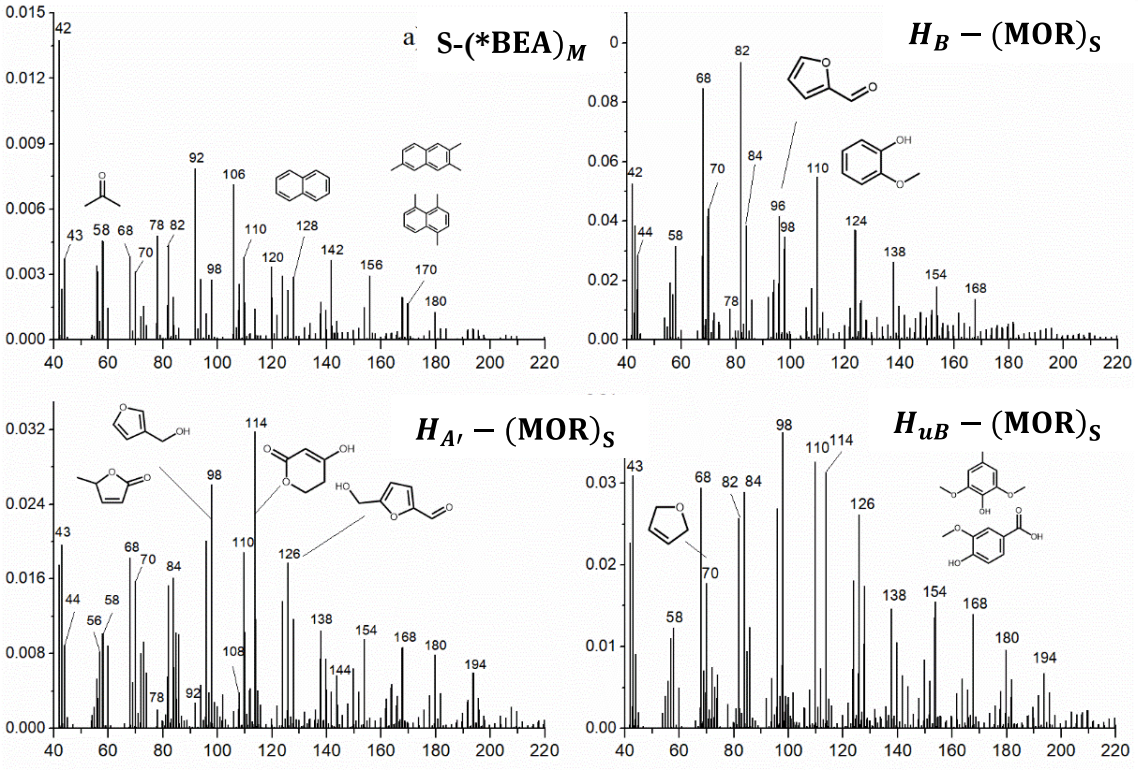

Figure VI.S5 **: Spectres de masse complets acquis en SPI (Moyenne sur tout le temps de la pyrolyse) des produits catalytiques avec différentes zéolithes.**

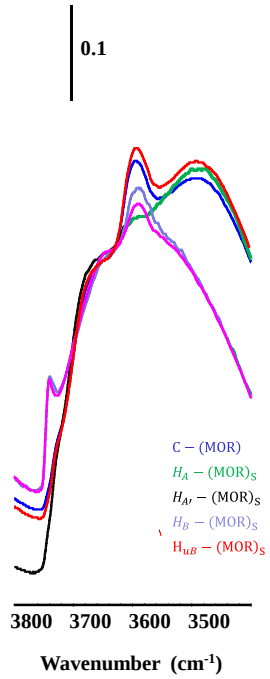

Figure VI.S6 : Spectres FTIR de la region des hydroxyls (3800-3400 cm^{-1}) pour les MOR cokées.

Références

[1] J.-Y. Kim, J. Moon, J.H. Lee, X. Jin, J.W. Choi, Conversion of phenol intermediates into aromatic hydrocarbons over various zeolites during lignin pyrolysis, Fuel 279 (2020) 118484. https://doi.org/10.1016/j.fuel.2020.118484.

[2] Y.-M. Kim, J. Jeong, S. Ryu, H.W. Lee, J.S. Jung, M.Z. Siddiqui, S.-C. Jung, J.-K. Jeon, J. Jae, Y.-K. Park, Catalytic pyrolysis of wood polymer composites over hierarchical mesoporous zeolites, Energy Conversion and Management 195 (2019) 727–737. https://doi.org/10.1016/j.enconman.2019.05.034.

[3] N. Chaihad, S. Karnjanakom, I. Kurnia, A. Yoshida, A. Abudula, P. Reubroycharoen, G. Guan, Catalytic upgrading of bio-oils over high alumina zeolites, Renewable Energy 136 (2019) 1304–1310. https://doi.org/10.1016/j.renene.2018.09.102.

[4] H. Hernando, I. Moreno, J. Fermoso, C. Ochoa-Hernández, P. Pizarro, J.M. Coronado, J. Čejka, D.P. Serrano, Biomass catalytic fast pyrolysis over hierarchical ZSM-5 and Beta zeolites modified with Mg and Zn oxides, Biomass Conv. Bioref. 7 (2017) 289–304. https://doi.org/10.1007/s13399-017-0266-6.

[5] I. Kurnia, S. Karnjanakom, A. Bayu, A. Yoshida, J. Rizkiana, T. Prakoso, A. Abudula, G. Guan, *In-situ* catalytic upgrading of bio-oil derived from fast pyrolysis of lignin over high aluminum zeolites, Fuel Processing Technology 167 (2017) 730–737. https://doi.org/10.1016/j.fuproc.2017.08.026.

[6] V.K. Guda, H. Toghiani, Altering bio-oil composition by catalytic treatment of pinewood pyrolysis vapors over zeolites using an auger - packed bed integrated reactor system, Biofuel Research Journal 3 (2016) 448–457. https://doi.org/10.18331/BRJ2016.3.3.4.

[7] T. Mochizuki, S.-Y. Chen, M. Toba, Y. Yoshimura, Pyrolyzer–GC/MS system-based analysis of the effects of zeolite catalysts on the fast pyrolysis of Jatropha husk, Applied Catalysis A: General 456 (2013) 174–181. https://doi.org/10.1016/j.apcata.2013.02.022.

[8] Y. Yu, X. Li, L. Su, Y. Zhang, Y. Wang, H. Zhang, The role of shape selectivity in catalytic fast pyrolysis of lignin with zeolite catalysts, Applied Catalysis A: General 447–448 (2012) 115–123. https://doi.org/10.1016/j.apcata.2012.09.012.

[9] J. Jae, G.A. Tompsett, A.J. Foster, K.D. Hammond, S.M. Auerbach, R.F. Lobo, G.W. Huber, Investigation into the shape selectivity of zeolite catalysts for biomass conversion, Journal of Catalysis 279 (2011) 257–268. https://doi.org/10.1016/j.jcat.2011.01.019.

[10] T.R. Carlson, G.A. Tompsett, W.C. Conner, G.W. Huber, Aromatic Production from Catalytic Fast Pyrolysis of Biomass-Derived Feedstocks, Top Catal 52 (2009) 241–252. https://doi.org/10.1007/s11244-008-9160-6.

[11] X. Lin, Z. Zhang, Z. Zhang, J. Sun, Q. Wang, C.U. Pittman, Catalytic fast pyrolysis of a wood-plastic composite with metal oxides as catalysts, Waste Management 79 (2018) 38–47. https://doi.org/10.1016/j.wasman.2018.07.021.

[12] A.M. Hernández-Giménez, E. Heracleous, E. Pachatouridou, A. Horvat, H. Hernando, D.P. Serrano, A.A. Lappas, P.C.A. Bruijnincx, B.M. Weckhuysen, Effect of Mesoporosity, Acidity and Crystal Size of Zeolite ZSM-5 on Catalytic Performance during the Ex-situ Catalytic Fast Pyrolysis of Biomass, ChemCatChem 13 (2021) 1207–1219. https://doi.org/10.1002/cctc.202001778.

[13] R.B. Borade, A. Clearfield, Preparation of aluminum-rich Beta zeolite, Microporous Materials 5 (1996) 289–297. https://doi.org/10.1016/0927-6513(95)00064-X.

[14] H. Sammoury, J. Toufaily, K. Cherry, T. Hamieh, Y. Pouilloux, L. Pinard, Desilication of *BEA zeolites using different alkaline media: Impact on catalytic cracking of *n*-hexane, Microporous and Mesoporous Materials 267 (2018) 150–163. https://doi.org/10.1016/j.micromeso.2018.03.022.

[15] M. Raad, S. Hamieh, J. Toufaily, T. Hamieh, L. Pinard, Propane aromatization on hierarchical Ga/HZSM-5 catalysts, Journal of Catalysis 366 (2018) 223–236. https://doi.org/10.1016/j.jcat.2018.07.035.

[16] H. Issa, N. Chaouati, J. Toufaily, T. Hamieh, A. Sachse, L. Pinard, Toolbox of Post-Synthetic Mordenite Modification Strategies: Impact on Textural, Acidic and Catalytic Properties, ChemCatChem 11 (2019) 4581–4592. https://doi.org/10.1002/cctc.201900927.

Résumé

Les hydrocarbures (HC) sont une ressource irremplaçable dans le monde d'aujourd'hui, étant à l'origine de produits tels que les plastiques, carburants, médicaments, etc. Cependant, leur production à partir des sources fossiles contribue à l'appauvrissement des ressources, ainsi qu'aux phénomènes de pollution, effet de serre, changements climatiques. Il apparaît donc essentiel de diversifier les sources de ces composés. Une méthode prometteuse est la pyrolyse de biomasse, qui permet, à partir de déchets agricoles et sylvicoles, de produire des hydrocarbures oxygénés (« huiles » de pyrolyse), puis, après une étape de traitement sur catalyseurs acides (« upgrading » catalytique), des HC classiques. L'obstacle majeur à la commercialisation de ces procédés est la désactivation rapide des catalyseurs utilisés. L'étude et remédiation à ce phénomène sont donc primordiaux.

Le procédé d' « upgrading » catalytique des huiles de pyrolyse étant complexe (nombreux réactifs et produits), le travail de cette thèse se focalise sur l'étude d'une molécule modèle, le methoxybenzène (anisole), et sa dismutation sur des catalyseurs acides, les zéolithes. L'anisole est une molécule aromatique oxygénée avec une simple fonction -OCH_3 substitué sur son cycle aromatique C_6. Il est représentatif d'une partie des molécules issues de la pyrolyse de biomasse, qui possèdent ce groupe.

La conversion de l'anisole sur zéolithes est une réaction bimoléculaire de dismutation, qui consiste en une transalkylation d'un groupe méthyl d'une molécule d'anisole vers le cycle aromatique de l'autre, formant une molécule de phénol et une de méthylanisole. Des réactions ultérieures forment des phénoliques méthylés (crésol, xylénol, …), notoirement très désactivants pour un catalyseur, car très facilement adsorbés à sa surface.

Cette thèse a établi l'existence, après une première désactivation rapide, d'un état d'activité stationnaire pour la conversion de l'anisole. De plus, les phénoliques produits par cette conversion participent à la désactivation du catalyseur, comme prévu, en s'adsorbant fortement sur les sites actifs, mais participent également à l'activité stationnaire en étant continuellement disponibles pour d'éventuelles réactions de transméthylation avec les réactifs en phase gaz. Ces composés phénoliques, fortement adsorbés à la surface du catalyseur, sont retrouvés dans les espèces extraites du catalyseur après réaction (coke), là où le coke « traditionnel » (HC polyaromatiques lourds : pyrène, anthracène, etc.) n'est pas détecté. Les effets mésomères induits par les groupements oxygénés (methoxy- , hydroxy-) inhibent le mécanisme classique de formation de ces polyaromatiques par contraction-extension des cycles aromatiques méthylés.

Les effets de l'acidité (densité des sites acides) et de la structure (MFI, *BEA, MOR, FAU, JZO) des zéolithes utilisées sur les phénomènes présentés précédemment ont été étudiés. Dans la zéolithe MFI (ouvertures de pores à 10 atomes T), l'augmentation du nombre de sites acides (bas Si/Al) provoque une forte diminution de l'activité et de la fréquence rotationnelle des sites actifs du catalyseur : l'augmentation des énergies d'adsorption des produits (qui peuvent s'adsorber sur deux sites acides adjacents) induit un effet auto-inhibiteur de la réaction. Cet effet de retrouve sur des zéolithes à plus larges pores (*BEA, FAU, JZO), mais est mitigé par la promotion des réactions bimoléculaires des plus larges canaux. L'effet d'auto-inhibition est également promu par la faible interconnectivité des canaux des zéolithes 2D (MOR).

Ces phénomènes peu communs n'étant pas retrouvés lors de la pyrolyse catalytique de biomasse, cela implique que la conversion de l'anisole seul, sans autre réactif, n'est pas une réaction modèle suffisante pour conclure sur l'efficacité d'un catalyseur pour ce procédé, mais permet une meilleure compréhension du comportement des molécules analogues à l'anisole durant l'upgrading catalytique des huiles de pyrolyse.

Mots clés : Anisole, Zéolithes, Pyrolyse Catalytique, Catalyse acide, Désactivation, Coke, Hydrocarbures oxygénés.

Abstract

Hydrocarbons are an irreplaceable resource in today's world, being the basis of products such as plastics, fuels, medicines and so on. However, their production from fossil fuels contributes to resource depletion, pollution, greenhouse effect and climate change. It appears therefore essential to diversify the primary sources of these compounds. One promising method is biomass pyrolysis, which uses agricultural and forestry waste to produce first oxygenated hydrocarbons ("pyrolysis oils") and then, after a treatment stage on acid catalysts (catalytic upgrading), conventional hydrocarbons.
The major obstacle to the commercialization of these processes is the rapid deactivation of the catalysts used. Studying and remedying this phenomenon is therefore of prime importance.
As the catalytic upgrading of pyrolysis oils is a complex process (numerous reagents and products), this thesis focuses on the study of a model molecule, methoxybenzene (anisole), and its disproportionation reaction on acid catalysts, zeolites. Anisole is a simple oxygenated aromatic molecule, with a single -OCH_3 group substituted on its six-carbon aromatic ring. It is representative of some of the molecules derived from biomass pyrolysis, which can possess this function.
Anisole conversion on zeolites is a bimolecular dismutation reaction, involving transalkylation of a methyl group from one anisole molecule to the aromatic ring of the other, producing one molecule of phenol and another of methylanisole. Subsequent reactions produce methylated phenol derivatives (cresol, xylenol, mesitol, etc.), which are known to be extremely deactivating for the activity of a catalyst, as they are easily adsorbed on its surface.

The work in this thesis has established the existence, after an initial stage of rapid deactivation, of a steady-state activity for anisole conversion. Additionaly, the phenolic compounds produced by this conversion participate in catalyst deactivation, as expected, by strong adsorption on the active sites, but also participate to the steady-state by being continuously available for transmethylation reactions with gas-phase reactants. These phenolic compounds, strongly adsorbed in the catalyst channels, are found in the species extracted from the catalyst after reaction (coke), where "traditional" coke compounds (heavy polyaromatic hydrocarbons, such as pyrene, anthracene, etc.) are not detected. The mesomeric effects induced by oxygenated groups (methoxy- , hydroxy-) inhibit the classical mechanism of formation of these polyaromatics by contraction-extension of methylated aromatic rings (Sullivan mechanism).

The effects of acidity (acid site density) and structure (MFI, *BEA, MOR, FAU, JZO) of the zeolites used on the phenomena presented above were investigated. In MFI zeolite (pore openings at 10 atoms T), the increase in the number of acid sites (low Si/Al ratios) leads to a sharp decrease in the activity and turnover frequency of the catalyst's active sites: the increase in the adsorption energies of the products (which can adsorb on two adjacent acid sites) induces an auto-inhibition effect on the reaction. This effect is found with wider-pore zeolites (*BEA, FAU, JZO), but is strongly mitigated by the promotion of bimolecular reactions of the widest channels. The auto-inhibition effect is also promoted by the lack of channel interconnectivity of 2D zeolites (MOR).

The fact that these unusual phenomena are not found during catalytic pyrolysis of biomass shows that the conversion of anisole alone, without any co-feeding of another species, is not a sufficient model reaction to conclude on the efficiency of a catalyst for this process, but allows a better understanding of the behaviour of anisole-like molecules during catalytic upgrading of pyrolysis oils.

Keywords: Anisole, Zeolites, Catalytic Pyrolysis, Acid Catalysis, Deactivation, Coke, oxygenated hydrocarbons.